POLITECNICO
MILANO 1863

SCUOLA DI INGEGNERIA INDUSTRIALE
E DELL'INFORMAZIONE

Simulations of Ti6Al4V milling for assessing different cooling lubrication strategies.

Tesi di Laurea Magistrale in
Mechanical Engineering - Ingegneria Meccanica

Author: **Enrico Buratti**

Student ID: 10543631
Advisor: Prof. Paolo Albertelli
Co-advisors: Luca Bernini
Academic Year: 2020-21

ABSTRACT (ENG)

This work aims at a deeper understanding of the mechanisms that influence the performances of cryogenic milling on Ti6Al4V using high feed strategy, also comparing it with more common approaches as square shoulder milling, and this is done through finite element simulations (software: Forge NxT).

Cryogenically assisted machining (with LN2 or LCO2) has high potentialities and it is one of the most promising technologies for future metal cutting procedures, especially in case of hard to cut materials (Titanium, Nickel, Cobalt alloys and Stainless steels) which find growing utilization in modern society. Anyway, these potentialities must be verified on the field to demonstrate the superiority of this approach over more conventional strategies as flood cooling or dry machining.

Under a manufacturing point of view the first and most intuitive advantage of cryogenic machining is the reduction of the temperature in the cutting zone, fundamental parameter for the tool life. Also a reduction of friction between tool and workpiece is experienced. The manufactured products exhibit superior surface finishing, microhardness and compressive stresses on the surface able to enhance their mechanical performances.

Using LN2 as coolant, no dangerous and pollutant substances contained in conventional metal cutting fluids are dispersed in the ambient and also energy consumption at shop floors' level is reduced, keeping competitive or enhancing the duration of the tools. If the superiority of cryogenic machining is consolidated over wet or dry turning in the majority of scientific works, passing to milling operations this trend is not often verified. In particular the cryogenic coolant applied to square shoulder mills can decrease their life if compared to conventional flood cooling. Passing to high feed milling the cryogenic approach can extend the tool life (especially at high cutting speeds) if compared to wet approach.

From the FE simulations can be noticed that for a cutter of a square shoulder mill the most mechanically stressed zone is also the one in which the highest temperatures are developed during the cut, since it is the farthest zone from the centre of the tool, thus where the maximal tangential speed is experienced. In high feed cutters the most mechanically stressed spot is not on the external edge but is shifted towards the centre

where lower tangential speeds are developed (with same nominal diameter and rotational speed). This spot does not coincide anymore with the maximum temperature spot, and the maximum temperature in case of square shoulder milling is higher.
Another important difference is in the first part of the engagement between tool and workpiece. Square shoulder inserts in wall milling are subjected to intense hammering action when approaching the cut. The whole insert edge is engaged at once, the engagement is sudden and not gradual. Moreover the square shoulder concentrates the load on a thin rake area. This rapid and cyclic mechanical load could be the explanation of the poor results obtained with square shoulder mills, under cryogenic cooling. Largely positive rake angles can be detrimental for cryogenic milling, especially if the cryogenic fluid overhardens the workpiece and decreased the toughness of the cutter.
On the contrary in high feed the engagement is more gradual and the chip thickness increases along the path guaranteeing smoother force profiles/stresses.

In the FE simulations passing from square shoulder to high feed milling some important outputs as maximum cutting temperature, compressive stress on tool, Tool-WP relative tangential speed and tool abrasion index are decreased.

Passing from wet machining to cryogenic machining there is a reduction of the contact area between tool and workpiece, locally increasing the mechanical stress on the tool. This phenomenon can favour two wear modalities as abrasion and fatigue. At the same time the lower temperature experienced in cryogenic machining can limit the effect of other wear modalities as atomic diffusion, oxidation and plastic deformation. The optimization of the cryogenic fluid's delivery system and of the process parameters should be finalized to the minimization of thermo-mechanical fatigue stresses, abrasion and embrittlement on the tool to favour superior tool life over conventional flood cooling, and for the reasons evidenced above high feed milling is more adapt to this scope than square shoulder milling.

ABSTRACT (ITA)

Lo scopo di questo lavoro è fare luce sui meccanismi che determinano le prestazioni della fresatura criogenica ad alto avanzamento del Ti6Al4V, facendo anche una comparazione con tecniche di fresatura più diffuse come la fresatura a spallamento retto; questo è fatto

tramite simulazioni agli elementi finiti (software: Forge NxT).

Le lavorazioni in cui si usa come lubro-refrigerante un fluido criogenico (azoto liquido o anidride carbonica liquida) hanno grandi potenzialità e sono guardate con interesse specialmente per applicazioni future su materiali difficili da tagliare come leghe in titanio, nichel, cobalto o acciai inossidabili, materiali sempre più utilizzati nell'industria moderna. Le potenzialità di questo approccio devono essere verificate sul campo per poterne dimostrare la superiorità rispetto a strategie di lubro-refrigerazione più convenzionali come emulsione o lavorazione a secco.

Il vantaggio più intuitivo delle lavorazioni criogeniche è la riduzione della temperatura nella zona di taglio, parametro fondamentale per la durata dell'utensile. Spesso si evidenzia anche una riduzione della frizione tra pezzo e utensile. I prodotti finiti sono caratterizzati da una migliore finitura superficiale, microdurezza e sforzi residui di compressione sulla superficie che garantiscono migliori prestazioni meccaniche.

Utilizzando l'azoto liquido non vengono liberate nell'ambiente sostanze inquinanti o pericolose per la salute dell'uomo solitamente contenute nei refrigeranti convenzionali, inoltre si riduce il consumo di energia elettrica da parte dei macchinari mantenendo comunque a buon livello o migliorando la durata degli utensili.

In letteratura la superiorità delle lavorazioni criogeniche è ampiamente consolidata se si tratta di tornitura, passando alla fresatura non è possibile affermare lo stesso. In particolare nel caso di utensili con geometria a spallamento retto, l'utilizzo di fluidi criogenici può diminuire anche drasticamente la vita dei taglienti se comparato al lubro-refrigerante tradizionale. Passando però alla fresatura ad alto avanzamento è possibile invertire questa tendenza specialmente ad alte velocità di taglio.

Dai risultati ottenuti nelle simulazioni FEM, si può notare come per un tagliente a spallamento retto la zona più stressata meccanicamente sia anche quella dove si sviluppano le temperature maggiori durante il taglio, poichè è la zona più lontana dal centro dell'utensile, perciò caratterizzata da maggior velocità tangenziale. Nei taglienti ad alto avanzamento la zona più sollecitata meccanicamente non è più sul profilo esterno ma è spostata verso il centro dove a parità di diametro nominale e giri al minuto, si svilupperanno velocità tangenziali minori. Questo punto non coinciderà più con la zona di massima temperatura, e la temperatura massima in caso di utensile a spallamento retto è superiore. Un'altra differenza rilevante tra i due approcci sta nella parte iniziale d'ingaggio

tra pezzo e utensile. Inserti a spallamento retto sono soggetti ad un'intensa azione di "martellamento" quando iniziano il taglio. Tutto il tagliente viene ingaggiato nello stesso istante, in maniera improvvisa e non graduale. Inoltre la geometria a spallamento retto concentra lo sforzo in una sottile porzione del petto dell'inserto. Questo carico ciclico e rapido può essere la spiegazione dei risultati non soddisfacenti ottenuti applicando fluido criogenico a questa tecnica di fresatura. Angoli di spoglia altamente positivi inoltre possono essere dannosi in caso di fresatura criogenica, specialmente nel caso in cui il fluido porti all'indurimento del materiale da tagliare e all'infragilimento del materiale del tagliente.
Al contrario con l'alto avanzamento l'ingaggio è più graduale e lo spessore di truciolo indeformato sul suo cammino cresce gradualmente garantendo un profilo di forze/stress più dolce.

Dai risultati delle simulazioni, passando da spallamento retto ad alto avanzamento alcune grandezze significative come temperatura massima nella zona di taglio, sforzo compressivo sull'utensile, velocità tangenziale relativa tra pezzo/tagliente e indice di abrasione sono ridotte.

Quando si passa da lubro-refrigerante convenzionale a criogenico si nota una riduzione dell'area di contatto tra pezzo e utensile, questo a livello locale si traduce in uno sforzo meccanico superiore sull'utensile. Vengono così favorite due modalità di usura come l'abrasione e la fatica. Allo stesso tempo però una riduzione della temperatura nella zona di taglio può limitare l'effetto usurante di diffusione atomica, ossidazione e deformazione plastica. Da qui ne deriva che l'ottimizzazione del sistema di adduzione del refrigerante e dei parametri di lavorazione deve essere finalizzato alla minimizzazione della fatica termo-meccanica, dell'abrasione e dell'infragilimento dell'utensile per favorire una sua durata superiore rispetto al caso di fluido refrigerante convenzionale e per le ragioni sopra citate la fresatura ad alto avanzamento si presta meglio a questo scopo.

Contents

1 | Introduction

1.1. Aim of the Work

Experimental results show that the application of cryogenic fluid (LN2) as refrigerant for milling operations on Ti6Al4V gives different results depending on the milling strategy adopted. Literature works adress the cryogenic fluid's delivery strategy and parameters as key variables that strongly influence the tool life, but it is also important to notice that keeping fixed these parameters and passing from sqaure shoulder mills to high feed mills the performances of the tools can be enhanced and become comparable or superior if compared to more common and health/environmentally dangerous wet machining. The explanation of this trend is not trivial and Finite Element Analyses capable of reliably reproducing the cutting phase are precious tools for a deeper understanding of the observed phenomena. Cutting forces, temperature profiles, mechanical stresses, wear indexes, heat exchange modalities and requested powers are some of the outputs of the finite element simulations presented in this work, and are the basis for the demonstartion of superiority of high feed strategy over sqaure shoulder in case of cryogenically assisted milling.

1.2. Preview of Concepts

Chapter 1: Introduction to new manufacturing challenges and aim of the thesis work.

STATE OF THE ART

Chapter 2: Main characteristics of Titanium and Ti-alloys.

Chapter 3: Importance of cutting tempreature (fundamental for wear of tools), analytical models for its prediction, experimental and numerical methods for cutting temperature measurement, overview on tool wear and tool materials.

Chapter 4: Ti-Chips: formation and features.

Chapter 5: Overview of most common lubro-refrigeration techniques in industrial scenario: flood cooling = wet machining, dry machining. Health hazards in the application of conventional flood cooling, disposal of cutting fluids.

Chapter 6: Energy consumtion of a machine tool, optimization of cutting processes.

Chapter 7: Presentation of promising anternatives to conventional wet machining as MQL and cryogenic machining. Deepening on cryogenic machining and cryogenic cutting fluid's delivery systems.

Chapter 8: Comparison on energy consumtion basis between dry, wet and cryogenic machining.

Chapter 9: Cutting forces in milling operations, differences between square shoulder and high feed strategies (important for the discussion of the results), application of cryogenic fluid on high feed tools.

Chapter 10: Importance of machining simulations and literature review over useful parameters (fundamental in the creation of FE set up): contact/friction models, material models, damage models, thermal problem. Applications of different material models on Ti6Al4V.
Machining simulations, CFD simulations, cryogenic cutting simulations and thermal analysis.

END OF STATE OF THE ART

FINITE ELEMENT MODEL AND RESULTS

Chapter 11: Generation of CAD high feed milling model and simulation set up on finite element software. Definition of thermal and mechanical properties.
Experimental campaing and its results.
Cryogenic and wet simulations' set up.
Validation of the model.

Chapter 12: Presentation of the results of FEA, differences between sqaure shoulder and high feed milling on FE simulations basis, differences between cryo and wet environ-

ment. Overall comparison of FE results.

Chapter 13: Conclusions and future developments.

1.3. New Manufacturing Challenges

Titanium alloys, because of their excellent properties, find applications in different areas such as aerospace, automotive and petrochemical industries, off-shore equipment and biomedical field. They are characterized by high strength-to-weight ratio, high corrosion resistance and biocompatibility. Ti6Al4V in particular is one of the most commonly used Ti-alloys, it has the same strength as steel with a 40 % lower density. At the same time a stable, protective and strongly adherent oxide film provides it an excellent resistance to seawater where it can resist 15 times longer than steel [89]. In the last two decades the worldwide usage of Ti6Al4V has shown a constant and consistent growth [103], that is still not showing deflection. The following figure reports Percentage of titanium with respect to the total weight in the aircraft manufactured by Boeing in the last decades.

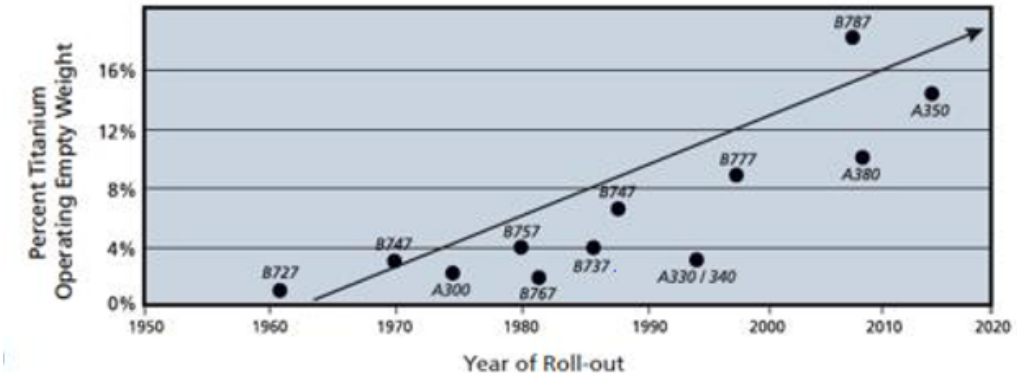

Figure 1.1: Percentage of titanium in the operating empty weight of aircrafts (Boeing) [103].

Contemporary society's challenges, like having lighter and less fuel demanding airplanes, are strictly bounded to new manufacturing challenges. Ti6Al4V is recognized as an "hard to cut" material and, in order to have an efficient production with chip removal approaches, strong developments are required at different levels. Basically, technologies as turning, milling, drilling, grinding etc. are optimized on Steel/Aluminium machining. The new necessity of large scale production of materials like Ti-alloys (or Ni-alloys) calls for enhancements on crucial aspects as: tool design, cutting inserts' materials, machine-tool dynamics and lubrication-refrigeration techniques. Nowadays production throughput of

Ti6Al4V components is way smaller compared to conventional materials. Also the specific tools for Ti-alloys have a non competitive cost with respect to common tools for steel machining and their life-time is not satisfactory. The only large-scale applicable solution to reach an acceptable tool life is the use of conventional cooling with oil or a mixture of oil and water, but many medical studies demonstrate their direct negative impact on the health of workers. Moreover the pumping and recirculating systems of these fluids have a major impact on the overall energy consumption of the machines. The hard machinability of Ti6Al4V bounds it to reduced working parameters during the chip removal operations, to have a rough estimate, a typical cutting speed for Ti-alloys is around 50 m/min while for Steel it is around 200 m/min and 1000 m/min for Aluminium-alloys.

High cutting forces are involved in the machining of Ti6Al4V, as consequence crucial components of the dedicated machine tools as spindles or electro-spindles must be capable of generating high torque and power while maintaining excellent reliability and availability performance indexes. These requirements increase substantially the cost of the working equipment.
Still referring to aerospace/aeronautical field, the material has to exhibit mainly high strength and fatigue resistance. The microstructure must be controlled, so the working procedure starts from big blocks of semi-worked material which have passed a sequence of thermal treatments and accurate quality tests. This is valid also for the production of small / thin components. At the end the so called buy-to-fly ratio (ratio between the mass of the initial workpiece and of the final product) is very high, typically varying from 8:1 to 20:1. In such peculiar conditions the importance of the material removal rate is huge.
One of the biggest problems dealing with Ti6Al4V is its low thermal conductivity and diffusivity (about 1/3 of the values exhibited by steel). So the heat generated during the cutting procedure remains concentrated around the cutting zone, increasing the operative temperature of the tool inserts and drastically reducing their life. This phenomenon is worsened by the adoption of high working parameters, in particular the cutting speed. The necessity of higher (acceptable) material removal rate values (for hard to cut materials) represents an important challenge in the manufacturing scenario and pushes researchers in finding new solutions. Lighter and more resistant materials are necessary for the construction of vehicles / aircrafts and many other applications mentioned above. These technologies are principally requested in order to reduce the consumption of hydrocarbons. The manufacturing world which stands behind should follow the same energetic and environmental conscious approach, otherwise it makes no sense in producing less pollutant systems with much more pollutant (or dangerous for workers' health) processes.

It is important to take into the account that every component adopted in aerospace, petrochemical or energy production field has to undergo a strict series of quality tests since its reliability must be maximized. All its production routine and the process parameters themselves are subject to rigid rules and approval procedures. In this context, every new technology before being adopted must be carefully evaluated/approved and this is done if and only if the benefits are evident and sustained by a long trial background.
The high temperature reached in the cutting process of Ti6Al4V represents the most evident limitation for the tool life, it requires a reduction of process parameters and the material removal rate becomes smaller. One of the most promising technology adopted for the reduction of temperature is the Cryogenic Machining. The idea is to use a cryogenic fluid as liquid Nitrogen or liquid Carbon Dioxide to cool down chips and cutting zone, resulting in an enhancement of tool life, MRR and productivity. These positive trends have been consolidated by many scientific works but in literature some results are in contrast with others and wide areas of knowledge are not covered; so cryogenic technology results to be still far from a robust affirmation in the manufacturing market despite its undisputed potential. Experimental campaigns on cryogenic machining of Ti6Al4V require high investment costs, high operating costs, non trivial and multidisciplinary expertise. Finite Element Analyses in this field may play an important role in reducing the number of tests required, breaking down costs and time of trials. A systematic approach in the model definition, calibration, validation and results analysis can be a precious basis for further developments of this technology.

State of the art

2 | Ti and Ti-alloys

Titanium is the fourth most abundant structural metal in the earth's crust [144], but it hardly exists in concentrated form, so it has a short production history. The chemical element was discovered in England by William Gregor in 1790 and was first purified in the United States by M. A. Hunter at the General Electric Company in 1906. In the 1950s, numbers of companies managed to meet the challenge to produce titanium. The value of aluminium and vanadium as alloy additions was established in the "Workhorse alloy" Ti6Al4V, which was patented by Crucible Steel in 1954. Since then, Ti6Al4V has been widely used for lightweight parts in variety of industrial products. It is appreciated for its good balance of strength, ductility, fatigue and fracture properties. In this table I report its chemical composition.

Chem. Element wt.%	Al	V	Fe	O	N	C	H	Ti
Min.	5.50	3.50	0	0	0	0	0	balance
Max.	6.75	4.50	0.40	0.20	0.05	0.08	0.015	balance

Table 2.1: Chemical composition of Ti6Al4V weight basis.

Ti6Al4V has been used as an important structural material in advanced aircraft since the 1960s. Nippon Steel and the Sumitomo Metal Corporation acquired qualifications in 1985 from Rolls-Royce and started commercial production of titanium alloys for aircraft engines [57]. Furthermore, the company concluded a long-term agreement with Airbus in 2002 and has been consistently supplying titanium for their airframes. In aerospace, this alloy is mainly used for airframe and engine parts. An expansion of the demand on the market is expected due to the requirement of low fuel consumption by aircraft. In airframes, it is used as structural components, such as bolts and seat rails; in engines, due to the relatively low allowable temperature of about 300°C of the material, it is used for fan blades, fan cases and engine suspension, where the working temperatures are lower

than 300°C.

2.1. Structure of Ti-alloys

In nature Titanium shows two different crystal structures: close packed hexagonal alpha phase and a body centered cubic beta phase [78]. Every alloy element is consequently categorized in alpha-stabilizer, beta-stabilizer or neutral addition depending of which phase the element tends to stabilize or if it significantly modifies the alpha-beta transus-temperature.
α-stabilizers, which include also aluminium as substitutional element or Oxygen, Nitrogen, Carbon as interstitial elements, are able to increase the threshold temperature at which the alpha-phase is stable, even with an increment of solute content. β-stabilizers, which include also isomorphous elements as Vanadium, Molybdenum, Niobium and Tantalum or eutectoid elements as Ferrous, Manganese, Chromium and Nickel, stabilize the beta-phase at lower temperatures. On the contrary neutral elements are the ones that do not modify significantly the beta-transus temperature.
$\alpha + \beta$ alloys (i.e. Ti6Al4V) contain 4÷6 wt.% β-stabilizers, which allows a substantial retention of beta-phase from $\alpha + \beta$ phase fields after quenching. Aluminium does not only stabilize the alpha-phase but its contribution is precious in the weight reduction of the alloy, Vanadium on its hand guarantees a considerable amount of beta-phase that promotes a ductile behaviour of the material. With the term 'beta-transus-temperature' is indicated the lowest T at which a 100 % beta-phase can exist. The addition of alloying elements to Ti leads to an increase of the β-transus-temperature from 882°C of pure titanium to 980°C, and approximately 9+/-2 wt.% of the β-phase is retained at room temperature. The majority of the diffusion transformation occurs within the temperature range between 850 and 950°C at a cooling rate between 5 and 50°C/s. In $\alpha + \beta$ alloys, at room-temperature the equilibrium microstructure consists mainly of α-phases with some retained β-phases. During the cooling processes typical of the production routine of these alloys the β-phases are fully or partly transformed into α with a martensitic type, which has two different forms: Hexagonal α (α') and the orthorhombic α (α"). Phase transformations strongly depends on the temperature history of the material: α' martensite forms within a specific cooling rate range between 20 and 410°C/s. The formation of α' martensite phase is beneficially produced by the rapid cooling through diffusionless transformation, on the contrary $\alpha + \beta$ transformation is a diffusional process. The α platelets are thicker and shorter when the cooling rate decreases, they can even transform into a global type with very low cooling rates. The four typical microstructures in $\alpha + \beta$ alloys are:

a. Widmanstätten: primary β grains are coarse and complete. Continuous α particles grow on the grain boundary. The colonies of α lamellae are thick and parallel. After slow cooling (furnace cooling) from β phase zone, Widmanstätten structure shows a low ductility and a high fatigue performance.

b. Duplex microstructure: no more than 50% of the discontinuous equiaxed α particles distribute in transformed β matrix. When alloy is heated or deformed in the upper part of $\alpha+\beta$ phase zone, a duplex microstructure with a comprehensive performance of mechanical properties can be achieved.

c. Basket-weave microstructure: primary grain boundaries are destroyed and the α lamellae become shorter in multiple orientations. When a large deformation is performed near β transus temperature, basket-weave structure with enhanced ductility is formed.

d. Equiaxed structure: more than 50% of the primary α grains and a certain amount of the transformed β grains display an irregular polygon shape. With a higher deformation rate, higher temperature, longer time of temperature holding, the equiaxial level is lifted, with a result of an excellent overall performance.

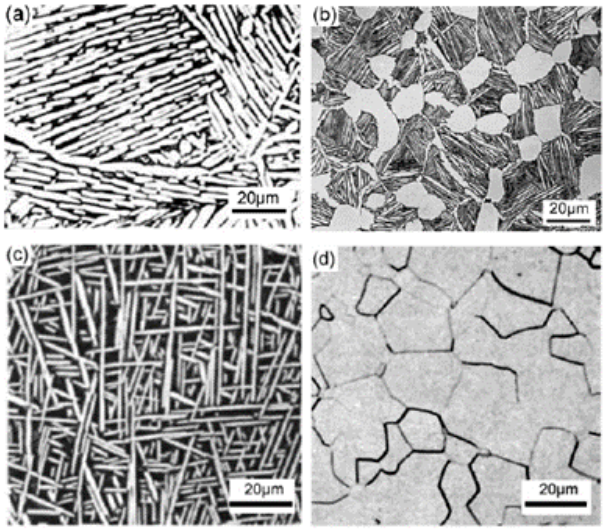

Figure 2.1: Typical microstructures of $\alpha+\beta$ titanium alloys (a)Widmanstätten, (b) duplex microstructure, (c) basket-weave microstructure, (d) equiaxed structure. [78]

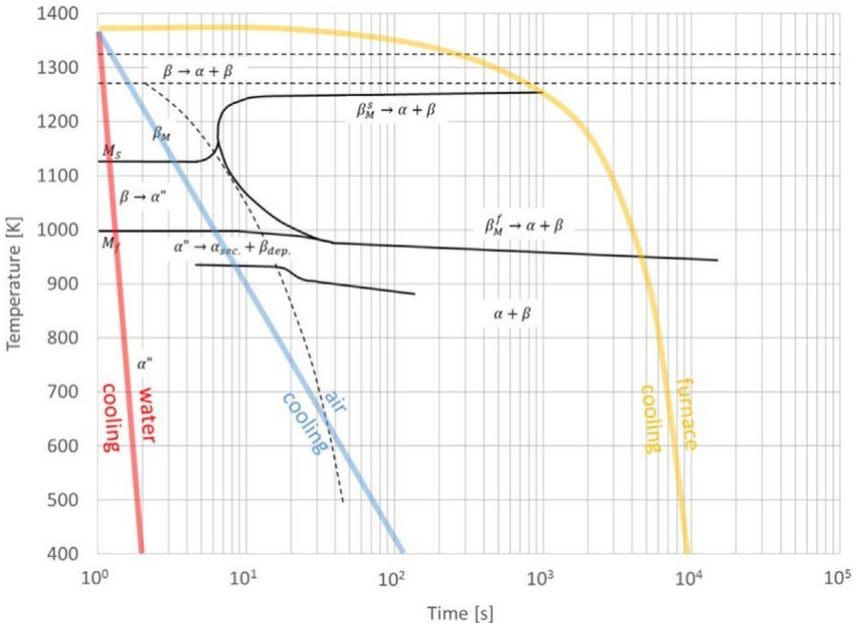

Figure 2.2: relationship between cooling rate and microstructure.

2.2. Machinability of Ti6Al4V

The specifications ASTM F1108 for casted and ASTM F1472 for annealed material for the mechanical properties of Ti6Al4V are reported below, where ASTM stands for American Society for Testing and Materials.

	Cast Material	Annealed Material
Yield Strength ($R_{p0.2}$)	758MPa	860MPa
Ultimate Tensile Strength (R_m)	860MPa	930MPa
Elongation at break (%)	> 8	> 10
Reduction of Area (%)	> 14	> 25

Table 2.2: Mechanical properties of Ti6Al4V.

Here below a comprehensive table of environmental properties proposed by Azom-Materials is reported.

	Resistance Factors 1 = Poor 5 = Excellent
Flammability	5
Fresh Water	5
Organic Solvents	5
Oxidation at 500C	4
Sea Water	5
Strong Acid	4
Strong Alkalis	4
UV	5
Wear	3
Weak Acid	5
Weak Alkalis	5

Table 2.3: Comprehensive table of environmental properties of Ti6Al4V.

Several properties of this material make it suitable for the definition of "hard to cut material".

1. First of all, machining titanium alloys high cutting temperatures are generated, they act close to the cutting edge of the tool and they are the principal reason for a rapid tool wear. A large portion (around 80%) of the heat generated during the machining phase is conducted into the tool because it can not be removed with the fast flowing chips or bed into the workpiece due to the low thermal conductivity of Ti6Al4V that ranges from 1/3 to 1/6 of that of steels. Only the 50% of the heat generated is absorbed into the tool when machining steel.

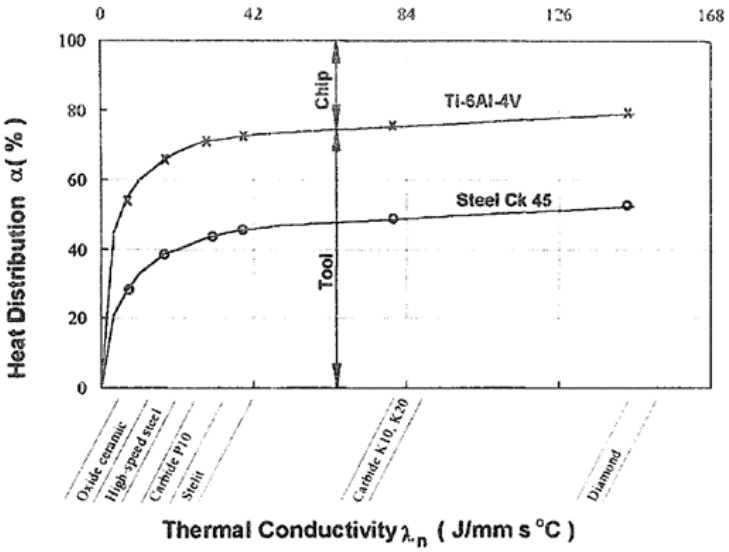

Figure 2.3: Distribution of thermal load when machining Titanium and steel [36].

In case of titanium alloys machining, the temperature gradients are much steeper and the heat affected zone much smaller and much closer to the cutting edge [36]. In case of reduced depth of cut and feed rate this phenomenon is accentuated, the presence of thin flow zone between the chip and the tool causes tool-tip temperatures to rise over 1100°C.

2. Titanium has a low modulus of elasticity, as consequence the workpiece tends to move away from the cutting tool unless heavy cuts are maintained. Slender parts tend to deflect nearly twice as much as carbon steel under the tool pressure [98]. The greater spring-back behind the cutting edge results in premature flank wear, vibrations and higher cutting temperatures. The bouncing action caused by the cutter while approaching the material may also increase the probability of chatter appearance, tool rubbing and consequent tolerance problems.

3. Cutting tools also suffer the strong chemical reactivity of titanium. Ti6Al4V reacts chemically with a wide range of tool materials at cutting temperatures above 500°C. This causes galling, welding and smearing along with rapid destruction of the cutting tool. But also reactivity with common gases such as oxygen and hydrogen leads to formation of oxides and hydrides respectively. These phases cause embrittlement and decrease of the fatigue strength of the alloy. Surface hardening by formation of hard solid solution due to internal diffusion of oxygen causes decrement of the fatigue strength of machined surfaces and increment of tool wear [135].

4. Work-hardening characteristics of titanium are such that titanium alloys demonstrate a complete absence of "built-up edge". Because of the lack of a stationary mass of metal (BUE) ahead of the cutting tool, a high shearing angle is formed. This causes a thin chip in contact with a small area on the cutting tool face and results in high loads per unit area. These high forces, coupled with the friction developed by the chip as it passes over the cutting area result in a great increase of heat on a localized portion of the cutting tool. All this heat (which the titanium is slow to conduct away) and pressure promote craters formation reducing consistently the tool life [98].

5. Ti6Al4V, also in presence of high temperatures as in cutting conditions, exhibits high strength and hardness if compared with steel or aluminium. As consequence high cutting forces are generated. High dynamic shear strength during cutting process induces abrasive saw-tooth edges, generating tool notching [135].

3 | Cutting Temperature and Wear Phenomenon

The cutting temperature is considered a key parameter when dealing with chip removal operations. High temperature reduces the tool life and may cause geometrical errors on the workpiece due to thermal expansion. Moreover, extremely hot chips represent a danger for operators. During metal cutting, almost the 98% of the energy consumed $\left(\dot{Q} = F_c * V_c\right)$ is converted into heat that causes the temperature rising on the contact surface between chip/tool/workpiece. The remaining 2% of energy is kept by the chip under the form of elastic energy [40]. Referring to the simplest example of orthogonal cutting, it is possible to define three zones in which mechanical power of the process is converted into thermal power. The first one is called primary deformation zone or shear zone. It is the section where the actual plastic deformation responsible of the removal of the chip is generated. The heat generated in this zone is principally stored by the chip and evacuated with its detachment from the working zone. The secondary deformation zone or friction zone is located on the tool-chip interface. Here the contact pressure and relative speed lead to heat generation through friction. The portion of heat that remains into the tool is function of several factors such as the relative friction coefficients of the material of chip and tool, the lubrication strategy, the cutting parameters, the geometry of the tool and so on [1]. It is the zone where the maximum temperature is reached, exposing the rake of the tool to quick consumption in case of non optimized cutting procedure. The third is the workpiece-tool contact zone. Here burnishing friction between the flank face of the tool and workpiece is responsible of heat generation. It increases with time because of the increasing wear land on the tool. Surface heating by this mechanism can induce detrimental stress states that lead to anticipate fatigue failure of components under cyclic loading. (immagine da cambiare!)

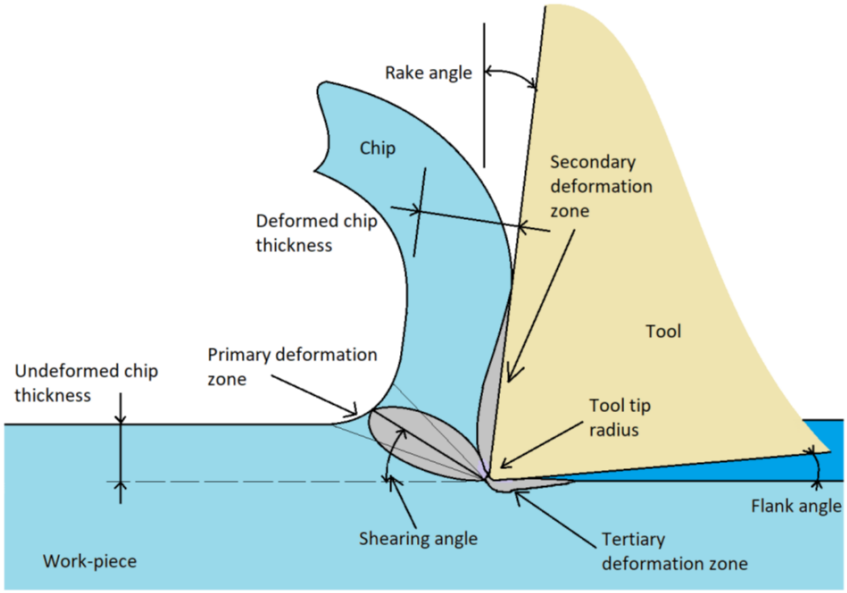

Figure 3.1: Deformation zones visualization (credit to L.Losa)

In literature common percentage of heat partition between tool, chip and workpiece can be found. For carbon steels the heat evacuated by the chip is around the 80%, a fraction of heat between 10÷15% remains in the tool and the remaining 5÷10% is kept by the machined surface. In case of ti-alloys (as mentioned above) the heat evacuated by chips is much smaller, while the heat that flows in the tool surface is much higher. In practice these values are variable depending on material pairs and cutting parameters. For what concerns the heat flowing into the tool the main responsible parameters are: tool and workpiece conductivity, specific heat, and interface conductance (perfect contact or not). Adoption of higher feed rates promotes a temperature increment due to friction zone and shear zone enlargements. Higher cutting speeds promote higher strain rates, major chip flow over the tool and lower time for heat dissipation. At the same time with higher cutting speeds the portion of heat evacuated by the chip increases, especially working with materials with low thermal conductivity.

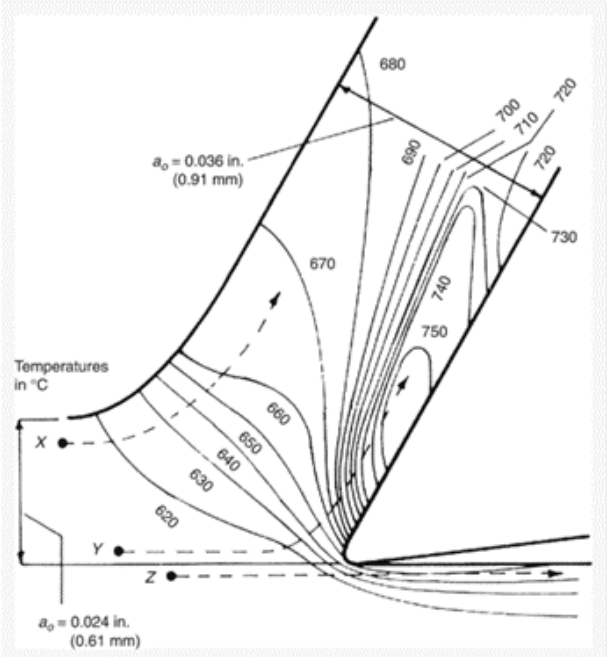

Figure 3.2: Temperature distribution during orthogonal cutting (free-cutting mild steel, cutting speed = 75 f/min width of cut = 0.25 in) [75]

.

During the years many different analytical methods for the cutting temperature estimation have been developed. One of the most important and diffused is the so called Cook's model, developed by the homonym researcher and presented in 1973. The basic formula is:

$$\Delta T = \frac{0.4 k_c}{\rho C} * \left(\frac{v_c * h_D}{K} \right)^{0.333}$$

Where ΔT is the increment of mean temperature on the contact surface between chip and tool in °C, k_c is the cutting pressure of the operation in $\mathrm{Nm/mm^3} = \mathrm{J/mm^3}$, v_c is the cutting speed in m/s, h_D is the undeformed chip thickness in m, ρC is the volumetric specific heat of the workpiece in $\mathrm{J/mm^3} - \mathrm{C}$ and K is the thermal diffusivity in $\mathrm{m^2}/s$. Another important model is the Kronenberg's model, developed on empirical trials in 1966:

$$T = \frac{C_0 K_c v_c^{0.44} A^{0.22}}{K^{0.44} \rho C^{0.56}} = C_1 v_c^{0.44} A^{0.22}$$

where C_0, C_1 are constants, k_c is the specific cutting energy, v_c is the cutting speed, A is the chip cross section, K is the thermal conductivity, ρ is the specific mass, and C is the specific heat. The following figures represent the trend of cutting temperature as function of major process parameters and material characteristic [75].

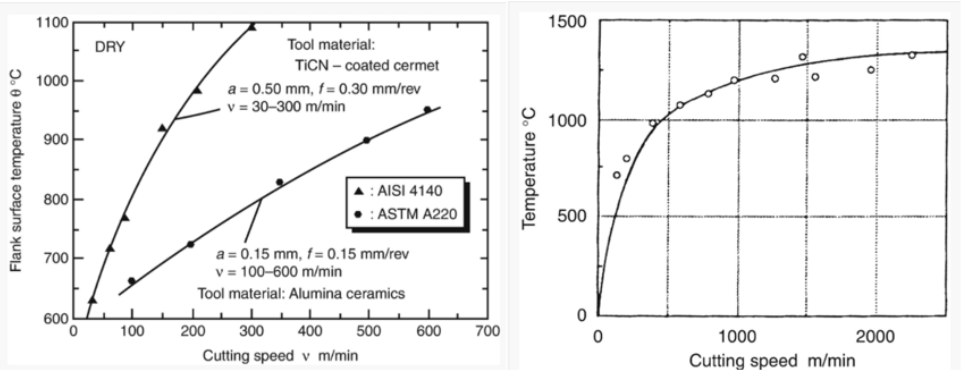

Figure 3.3: Influence of cutting speed on tool-chip interface temperature in turning.

In the first figure it is reported the influence of cutting speed on tool-chip interface temperature in turning (Work: AISI 1055, Cutting tool: Al_2O_3, Depth of cut: 30μm). In case of AISI 4140 the peak of temperature is extremely high and finds a plateau only close to the melting temperature of the material.

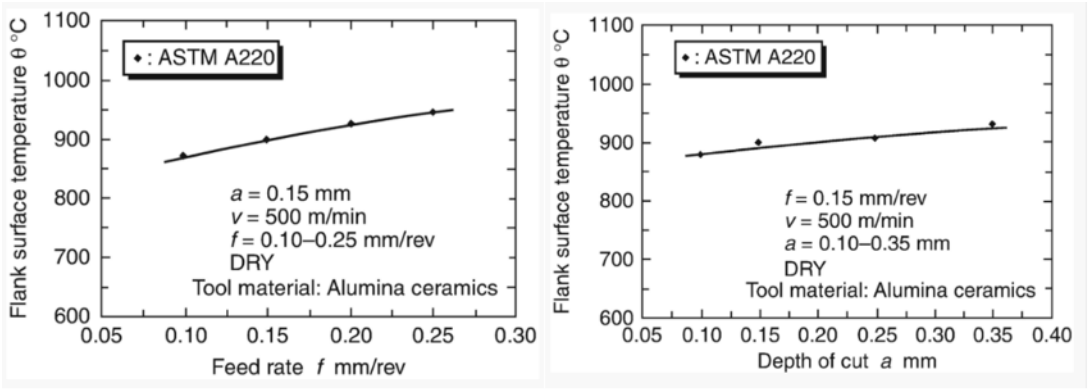

Figure 3.4: Influence of feed rate and depth of cut on tool temperature in turning.

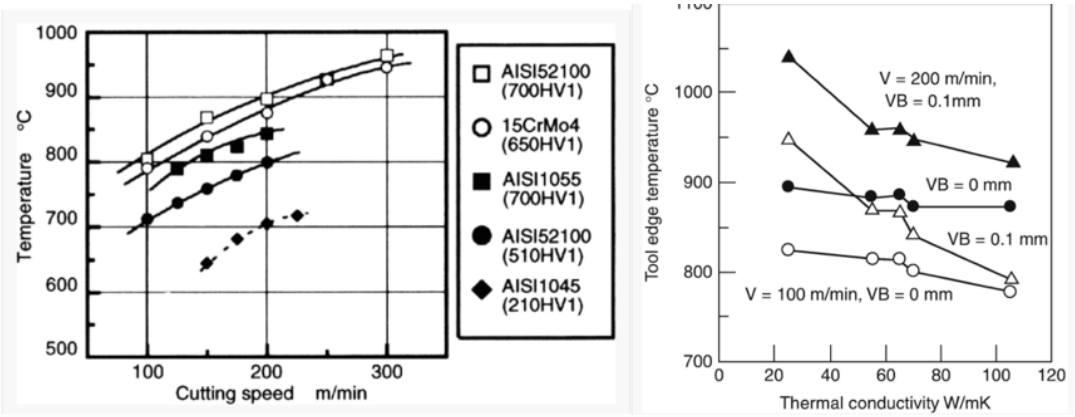

Figure 3.5: Influence of work hardness on tool temperature.

Passing to the analysis of temperatures in milling operations, it is interesting the work exposed in [36] by E.O. Ezugwu and Z.M. Wang. In particular they performed end milling trials experiments on $\alpha+\beta$ phase Ti-6-Al-6V-2Sn alloy using a vertical high-speed machining centre and sintered carbide tool. Tests were repeated until a tool life criterion of flank wear width of V_B=0.22 mm. Then they performed a comparison with a turning operation keeping as similar as possible the working parameters.

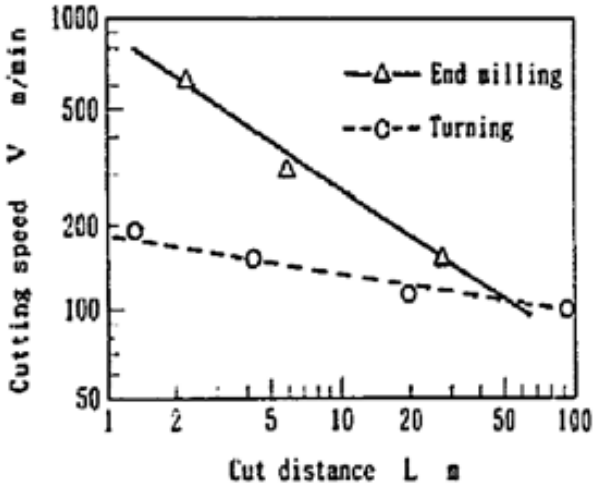

Figure 3.6: Cutting distance comparison between milling and turning for varying speed of cut.

The tool life shows a linear dependency on cutting speed in logarithmic scales, which means that Taylor's tool life equation holds. Existence of a large helix angle is considered one plausible reason for longer tool life in end milling. In order to investigate the reason for differences in tool life between end milling and turning, tool temperature was measured using the so called tool-work thermocouple method. The two different metals of tool and workpiece are considered as junction of the thermocouple. Through a proper connection of electric conductors to the tool and the workpiece it is possible to monitor the voltage generated on the contact surface between tool and chip using a potentiometer. The voltage exiting from the thermocouple, measured in mV, is converted in a correspondent temperature value thanks to the equations of calibration for the particular combination of tool and workpiece. First of all they performed trials on the Ti-alloy during turning operations at different cutting speeds, reaching the following results of mean rake temperature.

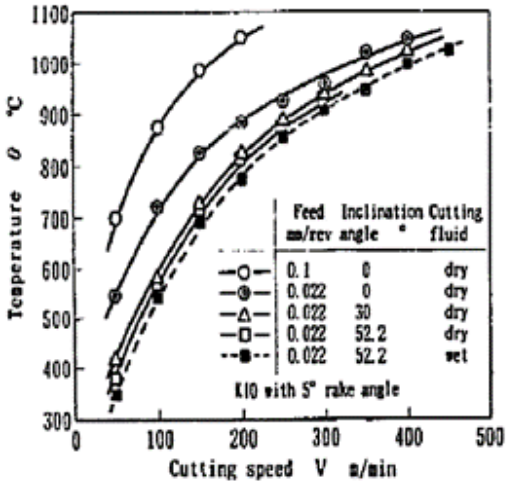

Figure 3.7: Cutting temperature vs cutting speed for Ti-alpha+beta alloy.

Then to simulate the behaviour of temperature in milling operations a particular setup for intermittent cutting was designed as shown in the following figure. The results are compared with continuous cutting both in wet and dry conditions.

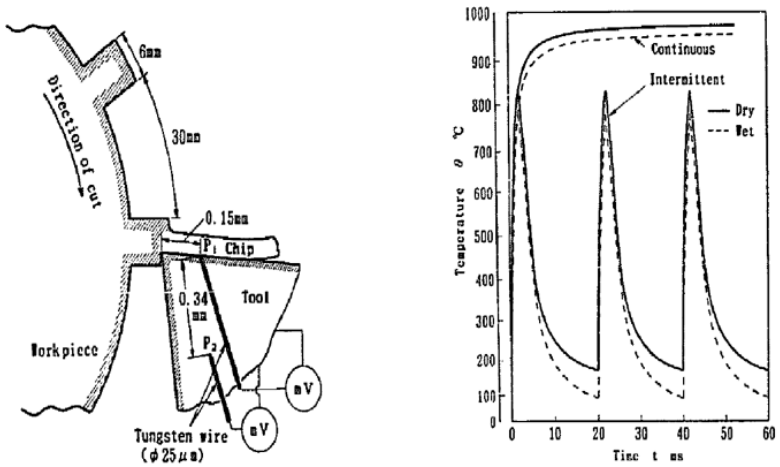

Figure 3.8: Intermittent cutting setup and T measurement.

The last plot reported is meaningful. It clearly points out that a milling insert, even if it does not reach the same maximum temperature nor the same mean temperature of a turning insert, it is subject to multiple heating and cooling cycles. This phenomenon exposes the insert to thermal fatigue, generally reducing its life.

During the last decades, a direct and precise measurement of the temperature in the cutting zone has been a problem faced by many researchers, but a standard and reliable procedure to do that is not available yet. The main problem is a matter of space, the

microscopic scale of the zone of interest makes difficult the direct positioning of measurement instruments. In addition, on tool side, no instrumentation can be placed in the secondary deformation zone (where peak temperatures arise), while on workpiece side no sensors can be placed on the chips. The main signals that can be measured in a metal cutting operation are force, surface roughness, chip dimensions, strain, tool wear and temperature. Among these, temperature is the most difficult to measure, which explains the number of different methods used over the years [9].
In [80] the authors present an overview of the most diffused methods for cutting temperature measurements.

Tool-workpiece thermocouples: are one of the most established methods of temperature measurement. The cutting temperature is related to the emf generated across the hot interface between tool and workpiece, it is unlikely that thermocouples record the highest temperature in the contact area, more likely the emf measured is an average between the tool and workpiece, and also this emf does not correspond to the average interfacial temperature. This is only the case if the temperature is uniform, or if the thermoelectric emf of the tool-work material combination varies linearly with temperature. This method has also many limitations: tools and/or workpieces have to be insulated, so as not to short-circuit the system. With high speed machining, cubic boron nitride (CBN) and polycrystalline cubic boron nitride (PCBN) ceramic, sintered or coated tools may be used. These provide poor electrical contacts and with a rotating tool with numerous cutting points, there is not a permanent electrical contact, hence casting some doubt on the thermocouple's readings. Another difficulty that has to be overcome is the necessity for an accurate calibration of the tool and workpiece materials as a thermocouple pair [96]. In addition, cooling fluids should not be used with this method. However, this is the most widely used method in laboratory environments and has a good dynamic response, but its sensitivity to material properties makes it difficult to implement in production environments

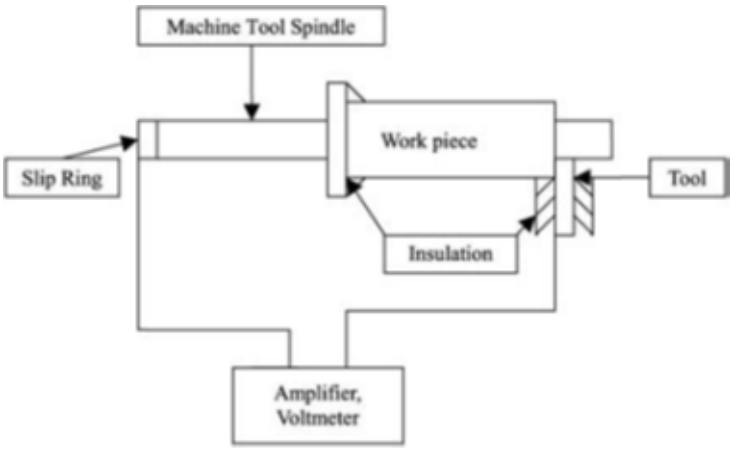

Figure 3.9: Schematic diagram of a tool-work thermocouple, where the tool-workpiece contact is the hot junction of the thermocouple [80].

Embedded thermocouples: another regularly used method is the embedded thermocouple. The thermocouple is placed in a hole drilled in the tool in the case of turning or in the workpiece for milling. The holes have to be placed close to the cutting edge at very precise locations. If the thermocouple is embedded in the workpiece, it will not give the temperature at the surface, which is the point of interest (until it is too late) but will give a temperature deeper into the metal than the cutting point. These thermocouples can be used for finding the temperature distribution within the tool or workpiece, but not for giving the surface temperature. To obtain the temperature at the workpiece surface mathematical heat transfer modelling is required. However, some doubt has been cast on the accuracy of embedded thermocouples due to the presence of the holes that have to be drilled to install the thermocouples and due to the presence of the thermocouples themselves. The error in the embedded thermocouple reading due to the presence of the thermocouple itself has been found to be as large as 50 per cent of the temperature in certain cases. This is caused by the air gap in the hole around the thermocouple and the transient heat conduction of the thermocouple in a solid body [67]. Again, the correct calibration of the embedded thermocouple is difficult at high temperatures and they do not respond to rapid changes of temperature.

Single wire thermocouple: a sample is divided in two across the line of cutting/grinding and a thin insulated conductor is introduced between the two halves. When re-assembled this makes a thermocouple with the main body of the sample being milled or ground. As the inserted conductor is exposed by the cutting action it comes in contact with the sample body and a signal is produced. This method has been shown to work well in grinding experiments. The cutting temperature is measured only for a very short time

(around 0.02 s) and so a high sampling rate is required. Only one brief measurement can be measured in each pass.

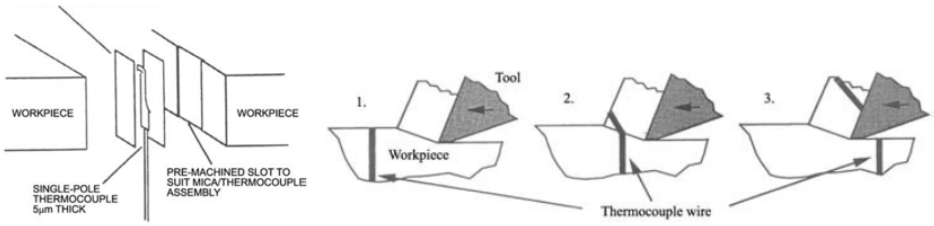

Figure 3.10: Installation and use of single wire thermocouple [80]

Fibre Bragg Gratings: it is a method in which the induced wavelength changes in an optical fibre placed beneath the workpiece is detected. Bragg gratings are made by illuminating the core of a suitable optical fibre with a spatially varying pattern of intense ultraviolet light. Short wavelength UV photons have sufficient energy to break the highly stable silicon-oxygen bonds, damaging the structure of the fibre and increasing its refractive index slightly. This modified fibre acts as a wavelength selective mirror. The reflective wavelength is affected by any variation in the physical or mechanical properties of the grating region. Changes in temperature lead to changes in the effective refractive index via the thermo-optic effect. It is in effect an optical thermocouple. The workpiece has to be placed on the optical tube, or the optical tube has to be placed in a sandwich between the part being cut and a backing component.

PVD film method: a system referred to as physically vapour deposited (PVD) method has been developed and used by [66]. The PVD film method requires the workpiece to be cut into two parts and the mating faces have to be ground and polished to a mirror finish. Materials with known melting points are then vapour deposited on the polished surfaces. One material is deposited on each pair of surfaces. The two halves are then reassembled before cutting. After cutting, the two halves of the workpiece are opened up and the boundaries between the melted and unmelted materials indicate the depth to which the melting temperature has penetrated the workpiece. With a number of different coatings, a profile can be obtained and the temperature extrapolated to the surface. The equipment to carry out the vapour deposition is required for these tests and the materials to be deposited are expensive. There are commercial establishments that will perform the coating operation to order (with very high costs).

Infrared thermometers: infrared pyrometers or thermometers have been used in more

reports than any other method. They are used either to measure the heat radiated directly from the cutting point or through fibre optic cables fitted adjacent to, or through, the tool or workpiece. The advantages of infrared sensors can be summed up: they are non-contact, they can respond to rapid changes in temperature and they enable the easy measurement of high temperatures without disturbing the heat distribution. As the space around the cutting point is limited, the target area is small and the temperature gradients in the target area are steep, a remote and accurate method of temperature measurement has advantages. The setting of the correct emissivity level is one practical problem, which can be overcome by regular calibration for the conditions being measured. There could be problems associated with the target being obscured by flying chips and coolant. It is possible to "see through" the chips and other smoke and dust by using a two-colour pyrometer, where the sensor is measuring on two different but close wavelengths of infrared light. Coolant remains a problem.

Infrared cameras: These devices produce a temperature map of the area studied, thus showing areas of similar temperature. Objects are shown in different colours to illustrate the different temperature zones. It is possible to acquire spot temperatures while filming by directing the cross hairs of the camera at a point of interest and obtaining the read out for that point. The setting of the correct emissivity in the camera is an essential part of the work. With an incorrect emissivity the temperature read out can be too high or too low as the temperature reading is proportional to emissivity. **Remote measuring/inverse methods:** It is a technique that utilises analytical and experimental results to create models for temperature estimation, thus combining the advantages of both approaches. Here the temperature is measured exploiting one of the methods mentioned above, but in a position away from the point of real interest. Then the actual temperature required is calculated using heat transfer equations. Easy to say but not to report into practice, this methodology however is also useful to double check the results of more direct measurements specifically localized in the zone of interest.

Thermographic phosphor thermometry: the item whose temperature has to be measured is coated with a phosphor powder mixed with a high temperature binder and this is sensitive to ultraviolet light. The resulting thermoluminescence indicates the temperature. This method has been developed for use in gas turbines to measure the turbine entry blade temperatures, it is still an open question if it is adaptable to machining world.

Finite Element simulations are a powerful tool for the prediction of temperature in the cutting zone and many works available in literature demonstrate the agreement

of their results with experimental data. One example can be the work [139] in which a finite element model of helix double-edge cutting (uncoated carbide) was developed to study cutting temperature during milling of Ti6Al4V. According to the heat transfer theory and thermal equilibrium relationship, the heat conduction equation is given as follows:

$$\frac{\partial}{\partial x}\left(k\frac{\partial T}{\partial x}\right)+\frac{\partial}{\partial y}\left(k\frac{\partial T}{\partial y}\right)+\frac{\partial}{\partial z}\left(k\frac{\partial T}{\partial z}\right)=\rho c\frac{\partial T}{\partial t}$$

where ρ = the material density $[\mathrm{Kg/m^3}]$, c = specific heat capacity $[\mathrm{J/(kg\cdot K)}]$, k = thermal conductivity coefficient. Imposing the boundary conditions:

$$\begin{cases} T(x,y,z,0)=T_0 \\ k\frac{\partial T}{\partial x}l_x+k\frac{\partial T}{\partial y}l_y+k\frac{\partial T}{\partial z}l_z=-q-\beta\left(T-T_c\right) \\ T=T_B \end{cases}$$

Where T_B = workpiece surface temperature at any point, T_0 = initial temperature of each node in the workpiece, q = heat loss caused by heat conduction, $\beta\left(T-T_c\right)$ = heat loss on the boundary, and l_x, l_y, and I_z the direction cosine in X, Y, and Z direction along outward normal vectors. According to the variational principle, the functional minimum satisfying the equations coupled with the b.c. is:

$$I(T)=\iiint_R\left\{\frac{k}{2}\left[\left(\frac{\partial T}{\partial x}\right)^2+\left(\frac{\partial T}{\partial y}\right)^2+\left(\frac{\partial T}{\partial z}\right)^2\right]+\frac{\partial T}{\partial t}T\right\}dxdydz+ \\ +\iint_c\frac{\beta}{c\rho}\left(\frac{1}{2}T^2-T_cT\right)ds$$

The solution region is divided into many units, in which the unknown temperature T can be expressed as element node temperature T_i. Assuming that $I\left(T^e\right)$ is the functional of unit e, so the functional $I(T)$ becomes functional integration of all units and can be shown as:

$$I=\sum_{e=1}^{n}I^e$$

Functional $I(T)$ takes the minimum value and is given by:

$$\frac{\partial I}{\partial T}=\sum_{e=1}^{n}\sum_{i=1}^{r}\frac{\partial I\left(T^e\right)}{\partial T_i}=0$$

where e is the unit number, r is the element node number. The results of the finite element simulations, representative of the workpiece-tool interface are then compared with the experimental results coming from embedded thermocouples. The two quantities

shows a good agreement:

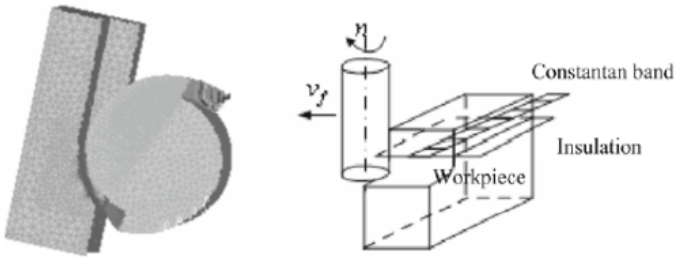

Figure 3.11: Finite element model and experimental model [139]

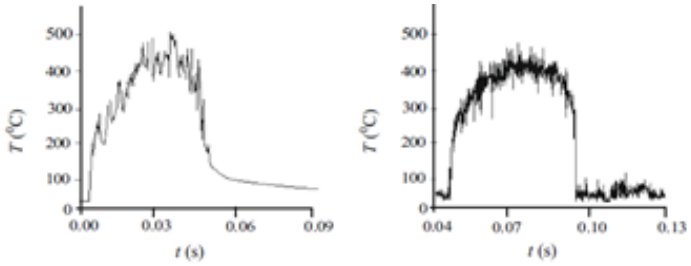

Figure 3.12: Finite element temperature result, experimental result [139]

Another important work in this field is [108]. The paper describes the cyclic temperature variation beneath the rake face of a cutting tool in end milling of Ti6Al4V, both in in up and down milling with a tungsten carbide tool insert at a cutting speed of 214 m/min. A newly developed infrared radiation pyrometer equipped with two optical fibers is used to measure the temperature. In up milling, the temperature beneath the rake face increases gradually during the cutting period and reaches a maximum just after the cutting. In contrast, in down milling, the temperature increases immediately after cutting starts. It reaches a maximum and then begins to decrease during cutting. This suggests that the thermal impact to the cutting tool during heating is larger in down milling than in up milling, whereas that during cooling is larger in up milling than in down milling. Down-Milling is preferable for what concerns thermal loading of the insert.

For the analytical computation of the temperature the authors model the 3D transient heat transfer problem with the help of Green functions, assuming a pulsating heat source as a plane with the dimensions of the feed and the depth of cut. If the material properties are constant and radiation is neglected, the time dependent spatial heat transfer equation and the boundary conditions in the heat generation zone are:

$$\frac{\partial^2 T}{\partial x^2}+\frac{\partial^2 T}{\partial y^2}+\frac{\partial^2 T}{\partial z^2}=\frac{1}{\alpha}\frac{\partial T}{\partial t}$$

$$-K\frac{\partial T}{\partial z}=\dot{q}''(x,y,t)=\dot{q}''(t)\quad 0<x<L_x, 0<y<L_y, z=0$$

The Green function describing the temperature due to an instantaneous point source situated in $\mathrm{x}=\mathrm{x_R}, \mathrm{y}=\mathrm{y_R}, \mathrm{z}=0$ at time t is:

$$\Theta_G\left(x,y,z,x_p,y_p,z=0,D\right)=\frac{2}{\sqrt{\pi D}}e^{\frac{-z^2}{D^2}}\cdot\left\{e^{\frac{-(x+x_p)^2}{D^2}}+e^{\frac{-(x-x_p)^2}{D^2}}\right\}\cdot\left\{e^{\frac{-(y+y_p)^2}{D^2}}+e^{\frac{-(y-y_p)^2}{D^2}}\right\}$$

$$T(x,y,z,t)=\frac{\alpha}{K}\int_0^t\int_0^{L_x}\int_0^{L_y}\Theta_G\left(x,y,z,x_p,y_p,0,D\right)\cdot\dot{q}''\left(x_p,y_p,\tau\right)dx_p dy_p d\tau$$

In case of uniform heat source the Green function has another simplified form and θ_{GR} represents the solution to a spacial uniform heatsource with an instantaneous heat impulse.

$$\Theta_{GR}\left(x,y,z,L_x,L_y,D\right)=\int_0^{L_x}\int_0^{L_y}\Theta_G\left(x,y,z,x_p,y_p,0,D\right)dx_p dy_p=$$

$$=\frac{1}{2\sqrt{\pi D}}e^{\frac{-z^2}{D^2}}\Theta_{GU}\left(x,L_x,D\right)\cdot\Theta_{GU}\left(y,L_y,D\right)$$

$$\Theta_{GU}(u,L,D)=\mathrm{erf}\left(\frac{L+u}{D}\right)+\mathrm{erf}\left(\frac{L-u}{D}\right),\quad D=2\cdot\sqrt{a(t-\tau)}$$

where $D=$ characteristic dimension, $K=$ thermal conductivity and $\alpha=$ thermal diffusivity. The width of the heat sources varies during the cutting arc depending on the strategy adopted (up/down-milling)

$$\begin{aligned}L_x(\tau)&=\tfrac{l_c}{h}f\sin\left\{\left(\tfrac{\tau}{\tau_1}\right)\eta\right\}&&\text{for Up-milling}\\L_x(\tau)&=\tfrac{l_c}{h}f\sin\left\{\left(1-\tfrac{\tau}{\tau_1}\right)\eta\right\}&&\text{for Down - milling}\end{aligned}$$

where τ_1 is the cutting time, f the feed, η the arc engagement angle. The results of the model are in good agreement with experimental measured data for what concerns the bulk body temperature of the insert. Temperature profiles in the skin depend much more on the heat source distribution, so on the contact nature.

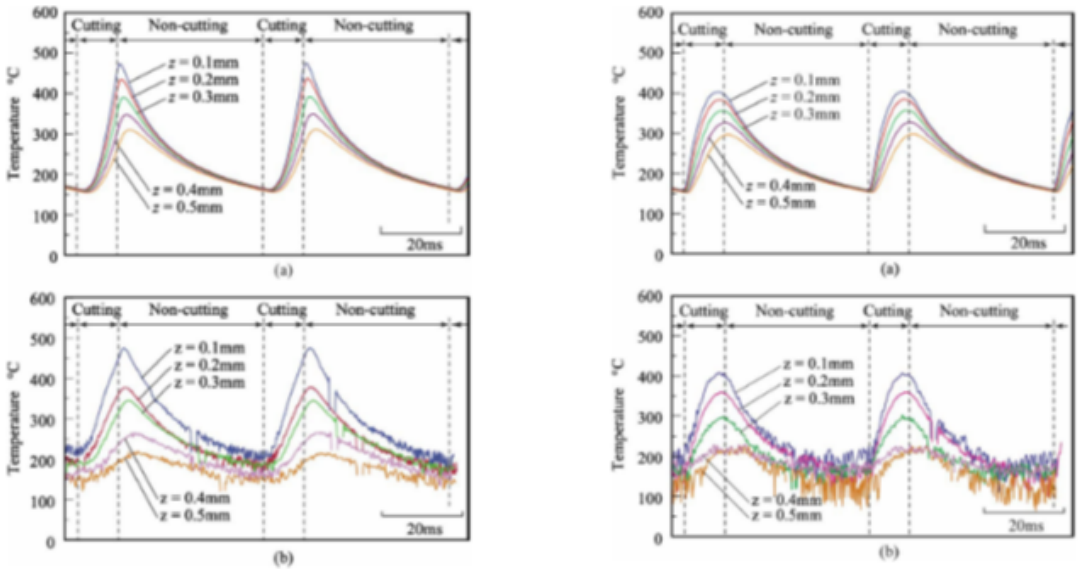

Figure 3.13: Predicted and experimental values of temperature, for up(on the left) and down(on the right) milling approach [108].

In [61] the authors make use always of the Green formulation but considering varying heat intensity. In this case, depending on the uncut chip thickness, the heat flux varies from a minimum toward a maximum. The selected material is 1045 steel. They repeat tests and calculations with different engagements and report the variation of the temperature profiles in the tool. They also propose a model for the temperature distribution in the workpiece. From the results, larger is the engagement higher is the thermal load for the body of the insert, while for the tool skin it is not possible to make considerations not affected by big uncertainties.

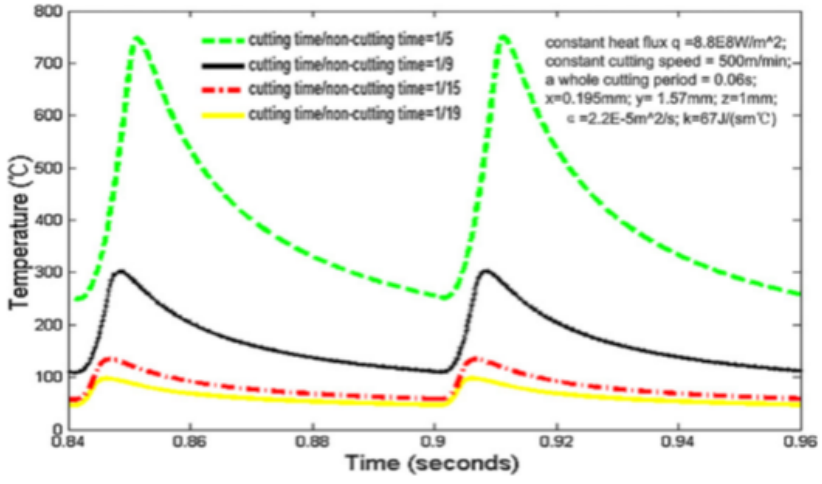

Figure 3.14: Temperature profiles with different engagements [61].

In [64] there is another example of the application of Green functions to calculate the transient thermal fields inside a milling insert cutting AISI 1050. The authors in this case decide to model the heat source intensity as the product between the resulting cutting force and the cutting speed $\left(\dot{Q} = F_c * V_c\right)$. From the results they observe how lowering the engagement both the maximum and the average temperature of thermal cycle for the insert are reduced. Increasing the cutting speed, there is a reduction of the oscillations of temperature but also an increment in the average temperature of the cycle.

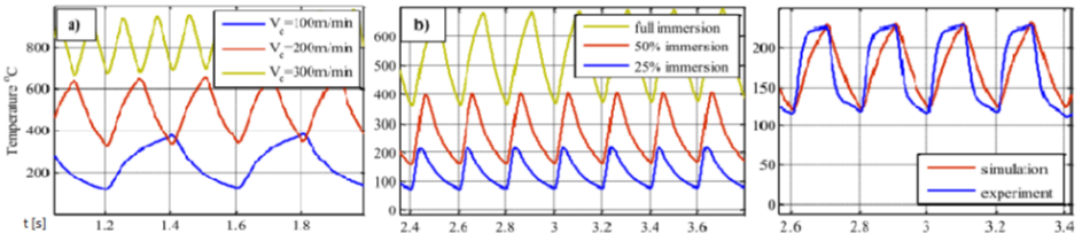

Figure 3.15: Estimated temperature profiles for different cutting speeds, different engagements and comparison between simulated and experimental results [64].

In [7] the authors are interested in the transient temperature of a milling insert while cutting Ti6Al4V. Their choice is to model the heat source as a simple square wave. The heating and cooling power is determined by iteration exploiting experimental acquisitions from thermocouples. Here it is possible to find a comparison of the thermal cycles that the insert faces with the adoption of different lubricating / cooling strategies. In particular the comparison is between minimum quantity lubrication approach and minimum quantity lubrication plus liquid C02 delivery (see next chapters for their deeper explanation). With the use of LCO2 the temperature of the heating cycle is reduced of at least 50°C.

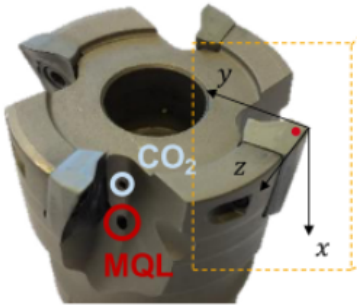

Figure 3.16: Minimum quantity lubrication and cryogenic approach [7].

In successive studies [8] on AISI 1050 they consider the heat generated by the heat source

as a portion of the product of cutting forces and cutting speed through an heat partition coefficient $\left(\dot{Q} = F_c * V_c * \beta\right)$. The proper coefficient β is found through an iterative procedure. The results suggest that increasing the cutting speed the amount of heat transmitted to the tool decreases (the heat partition coefficient decreases), and the physical explanation is that the enhanced dragging action of the chip at high speed is responsible for this effect, since they are able to carry out a large amount of heat generated during cutting. The model proposed is accurate in the predictions of cutting temperature adopting low cutting speeds and it becomes much less accurate if the speed is increased. The authors justify it with a large uncontrollable influence of a tool wear that is more important at high cutting speeds.

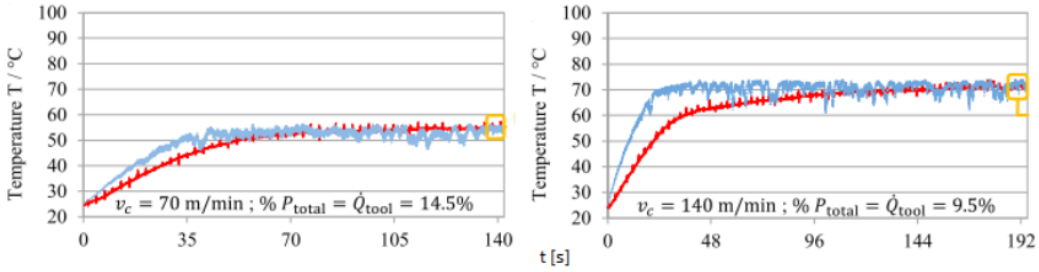

Figure 3.17: Comparison between estimated and measured temperatures [8].

3.1. Wear Phenomenon

Dealing with tool wear phenomenon two parts of the cutting insert must be carefully analysed: the **flank** and the **rake**.

Figure 3.18: Example of milling insert.

It is possible to distinguish three principal wear modalities:

1. Chipping: it affects the rake, it starts with the formation of small cracks growing up until the separation of portion of material and resulting in formation of craters.

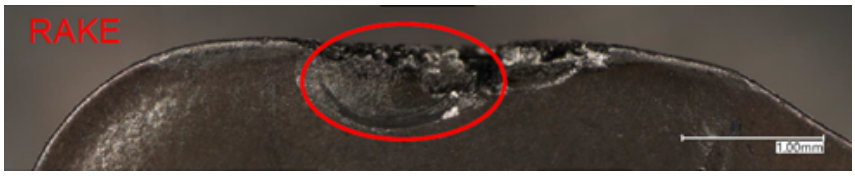

Figure 3.19: Example of chipping.

2. Plastic deformation: it affects the flank, the combination of high forces and high temperatures may plastically deform the shape of the tool.
3. Gradual wear: it affects both the flank and the rake, it is a gradual in time evolution as reported from picture a) to e).

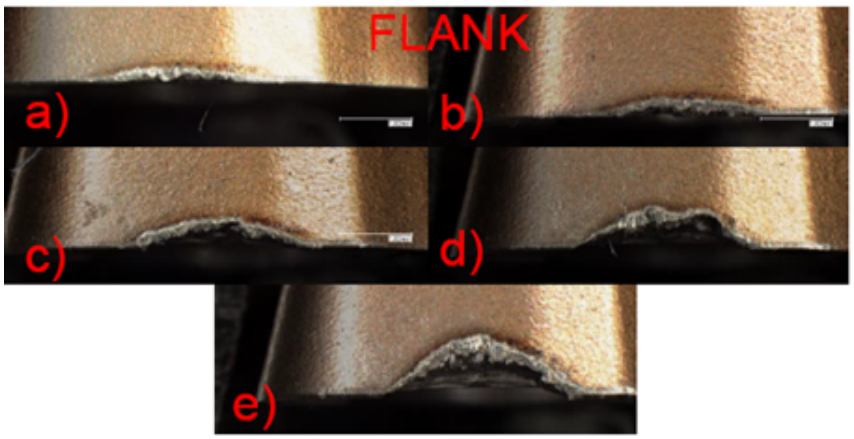

Figure 3.20: Example of gradual wear.

In this case it is also visible an heat affected zone around the worn part of the tool. In this zone the microstructure and the properties of the cutter are slightly different from the initial conditions.

The tool wear is caused mainly by six factors:

1. Abrasion: common wear cause due to friction between metal particles.
2. Atomic diffusion: it is a phenomenon promoted by high temperatures and pressures resulting in a net transport of atoms between tool and workpiece. It is easily experimentable at temperature above 1000 K with diamond tools cutting iron [116].

3. Adhesion: also known as "built up edge" is one of the main wear mechanisms in metal cutting. It shortens the tool life and can have a devastating impact on the machined surface quality. Worn cutting edges affect the surface finish, integrity, flatness and the cutting forces [128].

4. Oxidation: at high temperature the metals involved in cutting and the gases surrounding the cutting zone are more reactive than at ambient temperature. In these conditions the formation of oxidized layers is more likely, oxides are easily removable during the cutting process. The result is an undesired fast wear of the tool.

5. Plastic deformation: one of the most important wear modes in metal cutting, promoted by the lowering of mechanical properties of tool materials at very high temperature. Such deformation changes the geometry of the cutting edge, which often results in accelerated tool wear, increased cutting forces, risk of tool failure, vibrations and poor dimensional accuracy and surface finish [90].

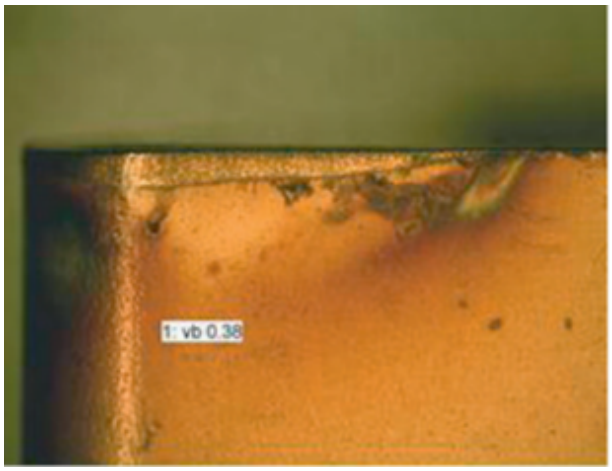

Figure 3.21: Flank view of a deformed cutting edge [90]

6. Fatigue: as showed in previous sections, during a milling operation every insert undergoes a cyclical solicitation both on mechanical and thermal point of view. The surface of the hot tools is damaged under coupled non-isothermal fatigue. The phenomenon starts with crack initiation, goes on with crack propagation and may result also in fatigue-oxidation interaction with detrimental effects on tool life [91].

Tool wear leads to:

1. Increased cutting forces.

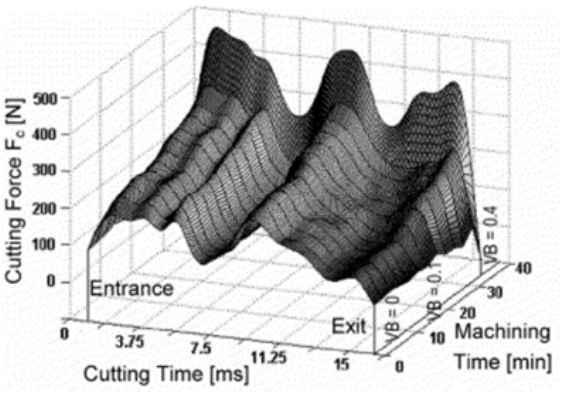

Figure 3.22: Characteristic of cutting force signal against cutting time and machining time [74].

2. Poor surface quality.
3. Poor workpiece dimensional precision.
4. Risk of tool breakage.
5. Increased cutting temperatures.

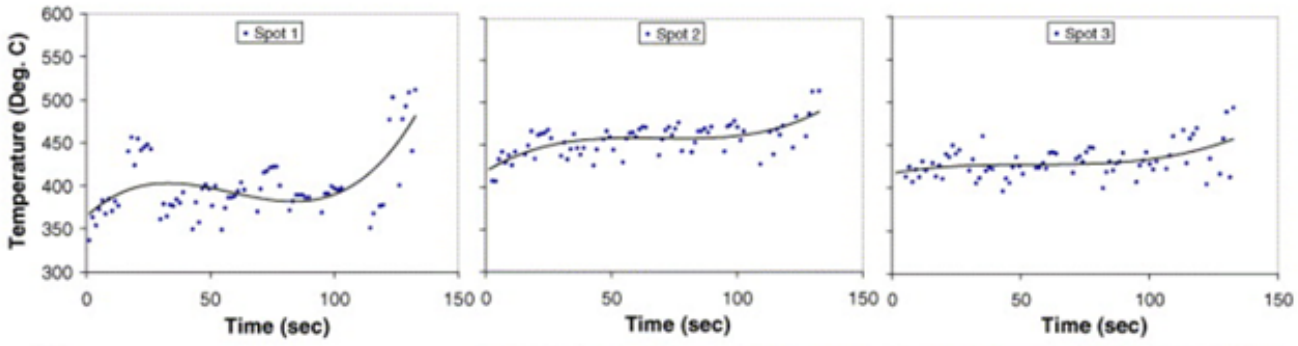

Figure 3.23: Tool temperature taken in three different locations on the tool for medium-carbon AISI 1045 turning [138].

As analysed in [138] the temperature taken in three different spots of a turning tool (spot1 shows the temperature at the tool nose, spot2 on the land and spot3 on the secondary face) does not reach a steady state value but keeps rising pushed by the wear of the tool.

6. Increased friction: this phenomenon is strictly correlated to the previous one. High temperatures favour the softening of the materials involved in cutting and softer

surfaces promote an increment of the friction coefficients. At the same time the heat generated by friction increases promoting temperature rising.

In order to quantify the level of wear that affects a tool some quantitative parameters must be defined:

- $V_{(B,max)}$ = maximum flank wear depth
- $V_{(B,mean)}$ = mean flank wear depth

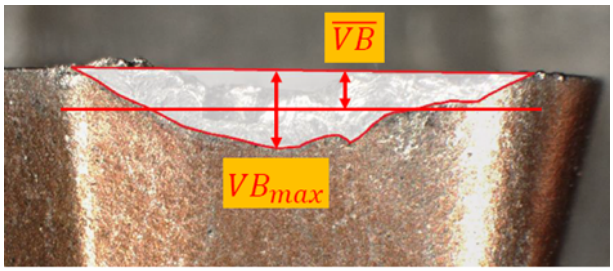

Figure 3.24: Average and maximum flank wear

- KT = crater depth
- KM = mean (centre) position of the crater with respect to ideal cutting edge
  These last two quantities are usually adopted in turning operations

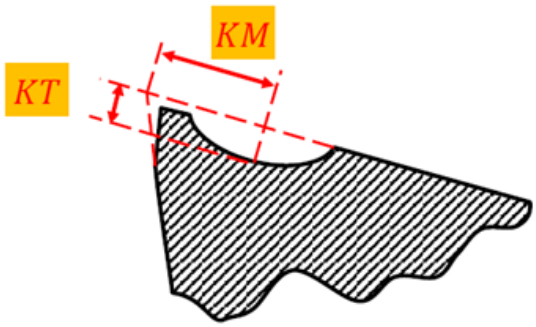

Figure 3.25: KT and KM representation.

3.2. Tools' Materials

For every industrial process based on chip removal the material of the tools plays a fundamental role and historically every sensible enhancement of the production rates is strictly related to the adoption of new materials for the cutters. Three main characteristics are

required:

- Toughness: capability of a material to absorb energy without breaking.
- Hot hardness.
- Wear resistance (hardness): it is the most important feature to contrast the abrasion.

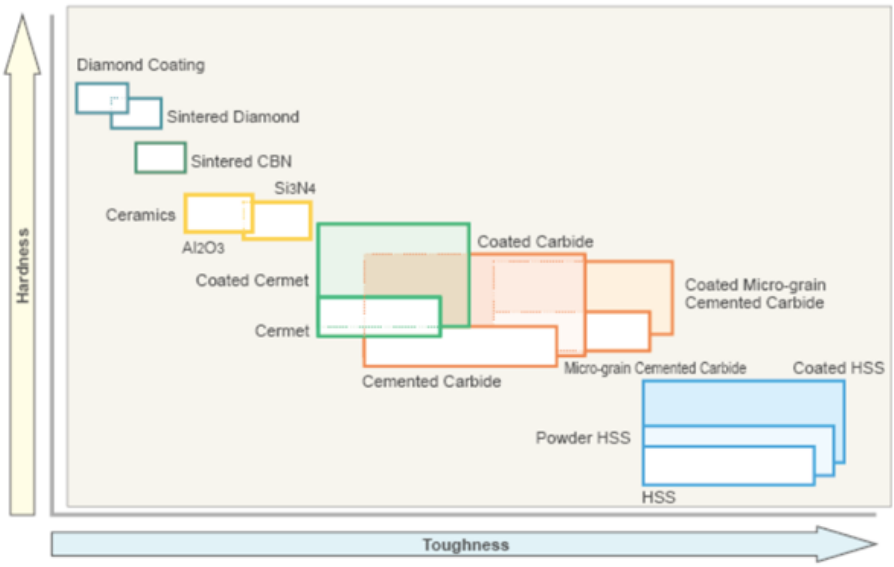

Figure 3.26: Qualitative classification of materials for tools from 'Mitsubishi Materials' website.

MATERIAL	HARDNESS	TRS=TRANSVERSE ROPTURE STRESS [MPa]
Carbon steel	60HRC	5200
HSS	65HRC	4100
Cobalt-alloys	65HRC	2250
Sintered tungsten carbides (WC) Low Co content High Co content	93HRA – 180HK 90HRA – 180HK	1300 – 2400
Cermet (TiC)	2400HK	1700
Alumina (Al_2O_3)	2100HK	400
cBN	5000HK	700
Polycrystalline diamond	6000HK	100
Natural diamond	8000HK	1500

Table 3.1: Hardness and TRS of materials for tools.

HSS: it is an high alloy steel capable of maintaining good hardness at high temperature, better than low alloy steels or steels with an high content of carbon. This family of materials can be subdivided in two categories. 1) HSS with tungsten, in which W is the main alloy element accompanied by chromium (Cr) and vanadium (V). It is indicated with quality T from the American Iron and Steel Institute (AISI). 2) HSS with molybdenum, where Mo is the main alloy element accompanied by chromium (Cr), Vanadium (V) and cobalt (Co). It is indicated with quality M. The HSS finds many applications in particular when the shape of the tool is complicated. The introduction of these materials on the market dates back to more than one hundred years ago, in the meanwhile many adjustments have been performed to their compositions keeping them competitive, especially for the excellent toughness (see figure above) that harder materials can not exhibit. With physical vapor deposition it is possible to deposit a coating of TiN capable of enhance the cutting performances[40].

Cobalt-alloys: the typical compositions are cobalt 35-45%, chromium 25-35% and tungsten 15-20%. These alloys are typically casted in graphite dies (casting guaranties good hardness) and then grinded. Their wear resistance and hot hardness is higher than the one of HSS but lower than the one of sintered carbides. Their toughness is higher than the one of carbides but lower than the one of HSS.

Sintered carbides: they are constituted by powder of WC with cobalt (Co) as binder element. Other carbides as TiC or TaC may be present in the mixture. In general they are featured by high compressive stress resistance, low tensile stress resistance, high hardness (90-95 HRA), good hot hardness, good wear resistance, high thermal conductivity and high Young Modulus (until 600'000 MPa). There are two families: 1) Sintered carbides for easy-to-cut metals, WC-Co. Their properties are mainly influenced by the grain size (0.5-5 μm) and the percentage of Co (3-12%). Bigger grains leads to high TRS but low hardness and hot hardness and vice versa. High contents of Co leads to high TRS but low hardness and hot hardness and vice versa. As consequence sintered carbides with high contents of Co are used for roughing operations and sintered carbides with low content of Co are used for finishing purposes. 2) Sintered carbides for steel cutting, WC-TiC-TaC-Co where a 10-25% of WC can be replaced with TiC/TaC. In case the grain size goes below 1 micron the TRS is not lowered and these materials guarantee high hardness/hot hardness and toughness.

Cermet: they are composed by ceramic and metallic materials, according to this definition also the sintered carbides are cermet, but commercially this denomination is used only for combinations of TiC, TiN and TiCN with Ni or Mo as binder elements. More complex compositions may be Ta_xNb_yC with Mo_2C as binder. They are used for steel cutting at higher cutting speeds with respect to sintered carbides for steel cutting.

Coated carbides: they are sintered carbides coated with one or more thin layers of wear resistant materials as TiC, TiN, TiCN, TiAlN and Al_2O_3. In case of multiple layers the first two must have good adhesion properties and a thermal expansion coefficient similar to WC-Co that is under them. These materials suffer the thermal shocks principally due to the different thermal expansion coefficients of the coating layers and base material and are not featured by high toughness values. Coated carbides find applications also for cutting of non-ferrous and non-metallic materials, in this case they are coated with CrC, ZrN and diamond [72].

Ceramics: the majority of them is formed by Al_2O_3 without binder elements. They are sintered at high temperature and pressures, a small grain size is fundamental. The main application is highspeed-turning, their low toughness limits the application in milling operations, at least for roughing purposes. The stiffness and the stability of the machines that use ceramics cutters must be high because they are not capable of absorbing dynamic loads caused by vibrations and impacts. After Al_2O_3 the most diffused ceramics are SiN,

Sialon ($SiN - Al_2O_3$), $TiC - Al_2O_3$ and aluminium oxide reinforced with crystals of SiC.

Sintered Diamond: first of all diamond is the hardest known material in nature. Sintered diamonds are composed by SPD = sintered polycrystalline diamond, produced with small grains of diamond pressed at high temperatures without binder elements. The random orientation of the crystals gives better performances with respect to monocrystal diamonds. Usually a layer of 0.5 mm of SPD is deposited over the surface of a sintered carbide. Their application (in order to avoid atomic diffusion) is directed at non-ferrous and non-Ni-based alloys because Fe and Ni have high chemical affinity with carbon (of which diamond is constituted).

cBN = cubic boron nitride: after diamond is the hardest material in nature, like SPD is used as coating for WC-Co. Its advantage is that it does not chemically reacts with Fe and Ni. I report also an important plot from [117] in which is reported the behaviour of hardness of the various materials as function of the operating temperature.

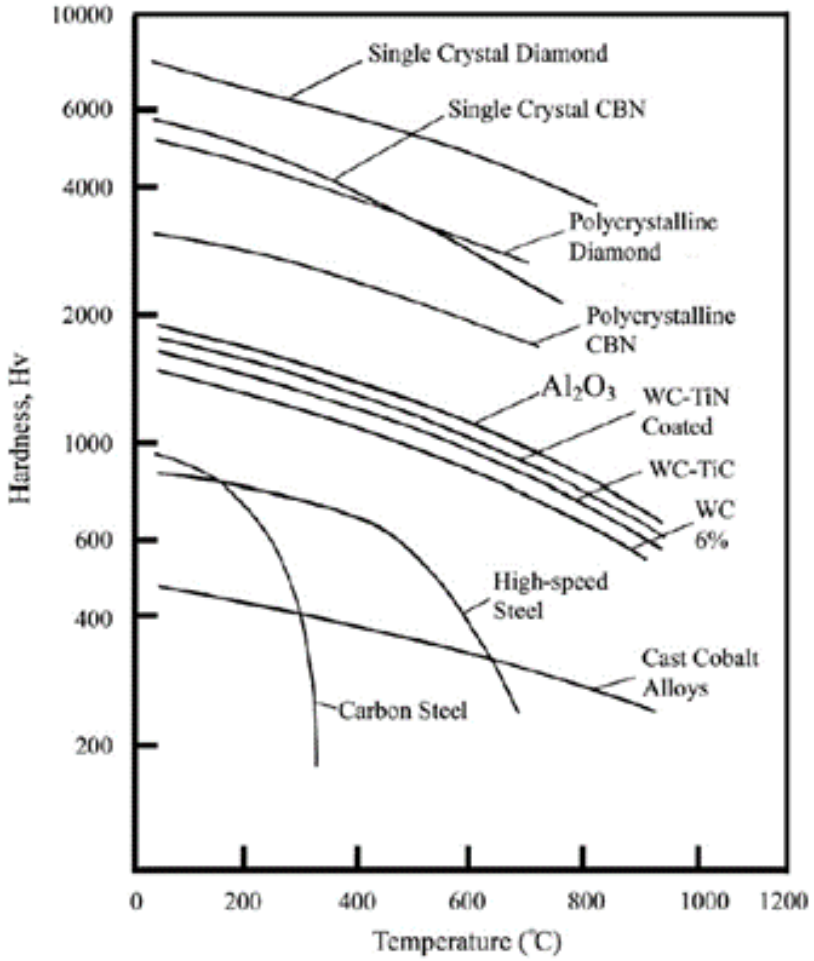

Figure 3.27: Tools' materials: hardness at different temperatures [117].

4 | Chip Morphology

Chip formation and morphology play an important role in determining machinability and tool wear during the machining of titanium alloys.
At low cutting speeds the chip is often discontinuous, while it becomes serrated as the cutting speeds are increased. In [55] it is investigated the chip formation and morphology in orthogonal cutting of Ti6Al4V, and it is pointed out that as the cutting speeds are increased the stress state near the tool tip changes, leading to the crack propagation shifting from the tool tip to the free surface of the deformed chip in the shear zone. This change in crack initiation and propagation is the primary reason for the chip changing from the discontinuous to a segregated continuous morphology.
Serious vibrations are often encountered due to typical chip segmentation of Ti6Al4V that limits the material removal rates. Chip morphology also influences the thermo-mechanical behaviour at the workpiece/tool interface having a direct impact on the tool life.
Using a high speed movie camera and an explosive quick stop device, Komanduri et al. [58] investigated chip morphology in Ti6Al4V machining and defined the serrated chip produced as "catastrophic shear chip". They attributed this chip serration primarily to plastic instability in the primary shear zone leading to catastrophic shear failure along a shear surface. Most of the segment is formed by an upsetting process undergoing small amounts of strain separated by a thin highly strained concentrated shear band, which acts as plastic hinge. They concluded that the catastrophic shear chip exists in all speed ranges and is independent of tool geometry. However, this theory can not be used to explain why the chip morphology is different under different cutting speeds.
According to the theory that the primary element of the mechanism of ductile fracture in metal working is crack initiation under shear deformation, fracture exists in all types of chip formation (even in continuous chip formation). Shaw et al. [113] after a complete work on hard steel also examined the titanium chips and found that:
1) As the cutting speed increases, the secondary deformation zone expands.
2) There is a severe deformation in secondary zone.
3) There is a subsurface deformation along the fracture surface (primary deformation zone).

In [55] experiments were conducted on a CNC turning center at cutting speeds of 60, 120 and 240 m/min, feeds of 0.127 and 0.35 mm/rev and a depth of cut of 2.54 mm. The workpiece was a Ti6Al4V annealed rod.

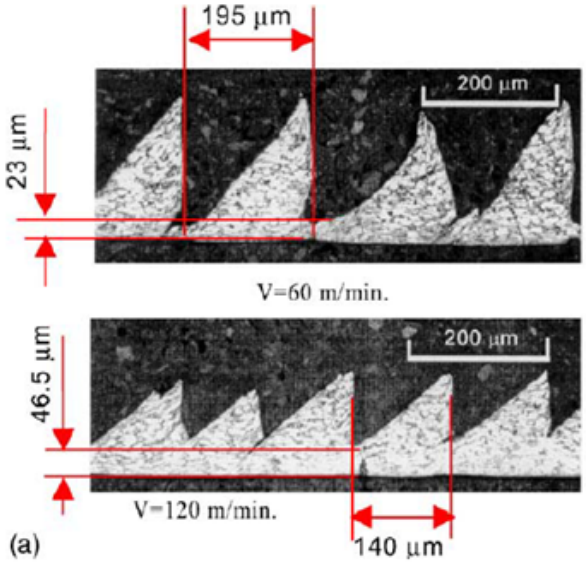

Figure 4.1: Chip morphology at different cutting speeds [55]

Analysing the results the authors assess that in case of orthogonal cut the crack which determines the serrated chip during cutting Ti6Al4V always occurs in the primary shear zone on the tool tip side. This is because this is the region where the maximum principal stress and shear stress are located. Shear stress in the shear plane and tensile stress facilitate the initiation of the crack. At low cutting speed, the crack that occurred during the cutting of Ti6Al4V propagates toward to tool tip due to high positive hydrostatic stress produced on this side, with negative stress on the free surface side of the workpiece, which tends to produce a discontinuous chip. At high cutting speed, the crack that occurred during the cutting process developed to the free surface side since the large negative hydrostatic stress is located on the tool tip side of the primary deformation zone, depressing the propagation of the crack in this direction, while the less compressive hydrostatic stress that exists on the free surface side promotes crack propagation in this direction. Due to the high temperature on the tool face side, and thus the thermal softening effect, no crack occurs in the tool tip side. The chip just formed during the cutting process connects to the workpiece, forming the serrated chip segment.

In industrial practice during the Ti6Al4V machining the presence of serrated chip also called saw-tooth chip is a constant, here is the reason explained in [143]: it exists a specific cutting speed at which chips change their morphology from continuous to segmented. For

Ti6Al4V this speed is 9 m/min, then increasing the cutting speed no further morphology variations will occur. Being the one of Ti6Al4V one of the lowest critical speed among metals of manufacturing interest, in real applications this threshold is always overpassed in order to reach acceptable MRR. Materials that tend to form this type of chip are characterized by poor thermal conductivity and diffusivity and/or limited ductility (i.e. materials with HCP crystal structure). Komanduri also suggests that an additional feature for the shear localization phenomenon may be the transaction from the low-temperature HCP crystal structure to the high-temperature BCC structure.
The β-phase of Ti6Al4V is formed by this second crystal structure, that has more slip planes than the α-phase that is formed by the first type of structure. This increment in the number of slip system would act to further localize the shear strain.
In [73] the whole chip formation process is divided in two stages and it is graphically explained. In the first stage the movement of the tool creates a wedge-shaped volume of material immediately ahead the tool tip. Once the critical shear strain in reached in the line marked as "5", the thermo-plastic instability happens, in this way the further shear strain is concentred in this zone. In this way, surface "5" separates in two different planes, marked as "2" and "3"(referred to previous segmentation).

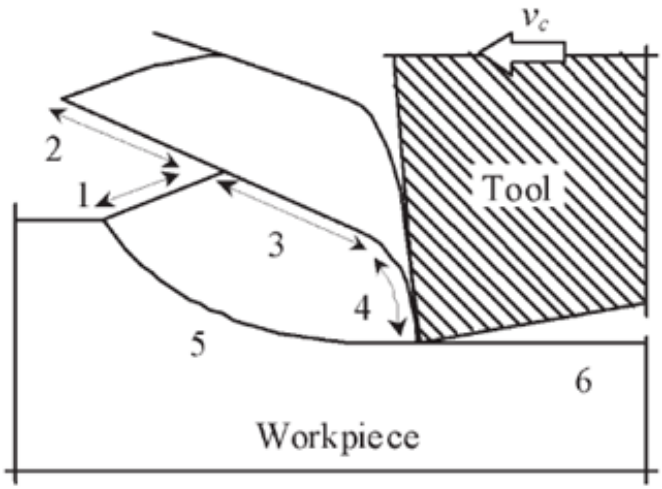

Figure 4.2: Formation mechanism of saw-tooth chip typical of Ti6Al4V [73].

Barry et colleagues in [11] point out that there is a short time window in which the relative motion between the chip and the tool is zero. This static condition in presence of high temperature favours micro-welding between workpiece and tool cutter. The entity of this process is proportionally related to the temperature (so to the adopted cutting speed) that promotes chemical reactions between the two materials. Furthermore, the fracture of these welds constitutes the dominant source of acoustic emission when cutting

titanium alloys above cutting speeds of 30 m/min. In presence of such a peculiar chip formation process and chip morphology, during the cutting operations, there is a strong oscillation of cutting forces values. In fact, to the static contributions of the cutting forces a cyclic dynamic contribution is added. Typical values of these forces can reach also the 25-30% of the static contribution, constituting a danger for tool integrity, surface quality, dynamic stability and delicate parts of the machine.
As pointed out in previous sections, the low Young Modulus of Ti6Al4V worsens significantly its machinability; if subject to the same cutting force, titanium deflects twice whit respect to steel, promoting a spring-back effect that favours the increment of cutting temperatures and flank wear.
Sun et al. [127] investigated the correlation between chip formation mechanism and forces in orthogonal cut.

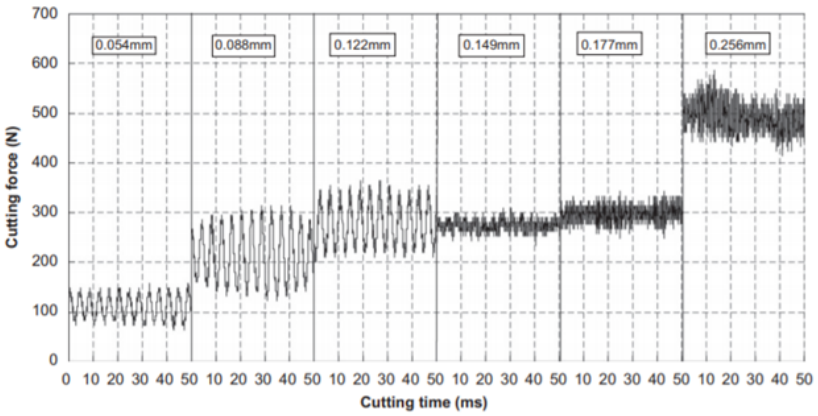

Figure 4.3: Effect of feed on amplitude variation of cutting force at a cutting speed of 75 m/min [127].

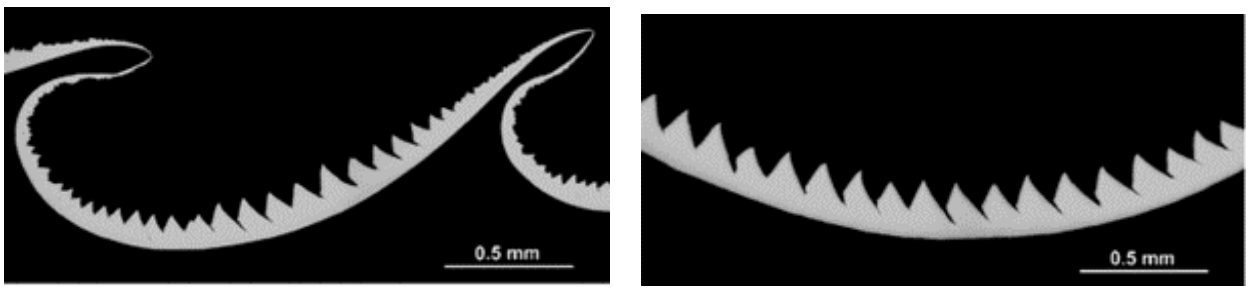

Figure 4.4: chip made at a feed of 0.054 mm/rev and 280 mm/rev [127].

It is important to notice that the saw-tooth cross-sectional area is the product of a non-periodic segmentation with a non-regular variation of thickness and sectors of continuous or segmented chip alternate. The surface quality left by the formation of this chip is low.

For a feed rate above 0.149 mm/rev with same cutting speed the low frequency oscillatory behaviour is not present anymore and the obtained chip is featured by a periodic segmentation. The authors also showed that the maximum feed rate at which low frequency oscillations occurs is function of the cutting speed. The change from non-periodic to periodic saw-tooth chip happens at higher feed rates in case of higher cutting speeds. In the first part of the plot (feed rate below 0.149 mm/rev) the vibration of the tool is constant at 260 Hz, passing to feed rates over 0.149 mm/rev the low frequency oscillation is replaced by an high frequency oscillation which frequency decreases linearly with a feed rate increment. This is due to the different chips' segments spacing at different feeds. The ratio between the maximum force value taking into the account the vibration component and the static force value and the chip segmentation spacing, does not depend on the depth of cut; the cutting speed, on the contrary, influences linearly the frequency of the cyclic force.
Defining the segmentation frequency as the ratio (Cutting speed)/(Chip segmentation spacing) it is possible to find a strong linear correlation (R=0.98) between this value and the cyclic force frequency.

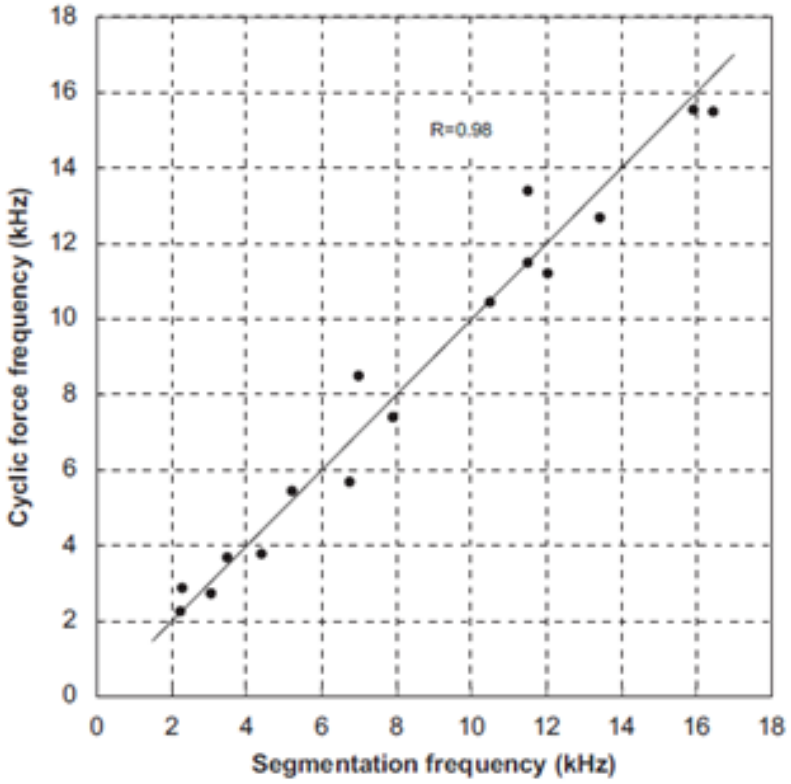

Figure 4.5: Linear correlation between cyclic force frequency and segmentation frequency[127].

This results clearly shows how the chip segmentation phenomenon is responsible of the cyclic variations of the cutting forces. In this discussion, precious observations are from Barry et al. [11]. In their work they look for a microscopic explanation to Ti-alloys chip formation mechanism. They focused on the formation of chips at the very beginning of an orthogonal cut experiment. In this phase, first of all the tool starts to engage the workpiece and goes into a position in which overcomes h_{min} = minimum undeformed chip thickness necessary to the actual formation of the chip. A chip formed in correspondence of h_{min} exhibits a lamellar structure on the external surface, the same structure that can be found in chips of materials featured by continuous chips like steel. When the thickness of the undeformed chip overcomes h_{min}+1.2 μm the lamellae are supressed and the structure is a fold type, similar to the one of the free surface of continuous chips obtained with hardened steels. According to these trials, continuous chip for Ti6Al4V can be formed only when the undeformed chip thickness is in the range of several microns and a key part of the transition from continuous to saw-tooth chip is the transition from lamellar type to fold type structure.

The chip segmentation, as discussed above, contributes to the hard machinability of Ti6Al4V, but also constitutes an advantage in the automation of manufacturing processes. The absence of long, continuous and hard to evacuate chips (especially in turning) represents a non-negligible advantage. The risks of shutdowns of the manufacturing process due to intervention for chip evacuations in case of Ti-alloys machining is really low.

In general, there is not a univocal theory on the chip formation for Ti6Al4V as for others Ti-alloys, many hypothesis find confirmation in experimental works, others not. The situation worsens if from orthogonal cut we pass to conventional turning and no complete works are allowable for chip formation in milling operations. As consequence a unique ad reliable material model to be used in FEM simulations is not present, but this topic will be discussed later in a dedicated chapter.

5 | Common Cutting Conditions

5.1. Dry Machining

Since the objective is to obtain a satisfactory material removal rate in Ti6Al4V machining, in industrial practice, dry machining (cutting operation without any cutting fluid delivery in the cutting zone) is not a competitive alternative. Jianxin et colleagues in [62] studied the effect of the atomic diffusion across the Ti6Al4V and WC-Co carbide tools at temperatures up to 800 °C. Dry turning tests on Ti6Al4V were carried out with WC-Co carbide tools. There is evidence of diffusion of W and Co elements of the carbide to Ti6Al4V, and Ti of Ti6Al4V to the carbide at 400 °C. W and Co diffused a long way into Ti6Al4V at 600 °C, and the penetrating depth reached 20 μm at 800 °C. The hardness values near the interface of the diffusion couples are lower than those far away from the interface owing to element diffusion. The diffusion of elements from the Ti6Al4V to WC-Co carbide tool (and vice versa) through the tool/chip interface in machining processes leads to a composition change of the tool substrate, which may accelerate the tool wear. Higher is the temperature in the cutting zone, the more severe is this effect.

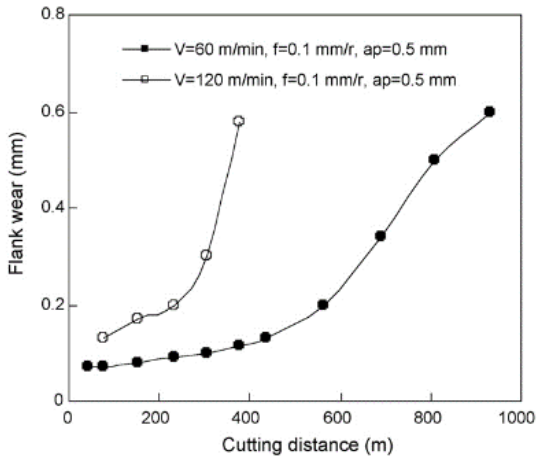

Figure 5.1: Flank wear of the WC-Co carbide tools in dry machining of Ti6Al4V at different cutting speeds [62].

From the figure above it is clear that with dry cutting, adopting high cutting speeds is detrimental for tool life, with an exponential behaviour of flank wear. In general, for the machining of titanium alloys the principal drawbacks of dry machining are: extremally high cutting temperatures, high frictional forces, no evacuation of the chips due to the absence of a medium able to flush them away, need for more advanced tools, low productivity rates, bad surface finishing and risk of ignition of chips due to high reactivity with oxygen.

5.2. Wet Machining

Substances used in machining for cooling and/or lubrication can be defined as cutting fluids, gas-based coolants/lubricants and solid lubricants. In industrial practice cutting fluids are exploited for several reasons:

- With their high heat capacity and overall heat transfer coefficient they are able to decrease the temperature in correspondence of the cutting zone and friction zones.
- They can reduce the friction coefficients between tool and chip, tool and workpiece. In this way the cutting forces (and cutting power) and heat generated by friction are lower.
- They reduce the temperature of machined surfaces, increasing safety of post-machining handling and set up operations.
- They prevent possible ignition of hot chips.
- They do not promote corrosion reactions both on workpiece and tool side.
- They help in the evacuation of the chips from the working zone.
- With addition of anti-welding additives they prevent micro-welding formation.
- They improve dimensional stability and surface finishing of the pieces.

It is possible to categorize the cutting fluids according to their main function: refrigeration or lubrication [40].
Refrigerants: they are used in order to dissipate the generated heat reducing the temperature of tool and workpiece. Their main features are high specific heat and thermal conductivity. Since these properties are typical of water it is used as base for refrigerant fluids.
Lubricants: they are used in order to reduce the friction between tool/workpiece and

tool/chips. The base substances are oils. If used at high pressures, thanks to the presence of sulphur, chlorine and phosphorus, they favour the formation of thin layers of solid salts on the hot machined metal surfaces. These layers enhance the reduction of the friction coefficient with respect to traditional lubricants. Lubricants are more effective at low cutting speeds, in facts over 100-150 m/min the movement of chips tends to make difficult the contact between oils and the friction zones between tool and chips. Moreover, the high temperatures leads to the evaporation of the oils, reducing at minimum their positive effect. The temperature reduction happens thanks to the reduction of friction but also thanks to the high specific heat and thermal conductivity. Another non negligible contribution is given by the fact that with lower friction coefficients the angle of friction is lower and according to Merchant equation a lower angle of friction makes the shear plane angle increse, reducing the amount of thermal energy generated in the cutting zone.

$$\phi = 45 + \frac{\gamma_0}{2} - \frac{\beta}{2}$$

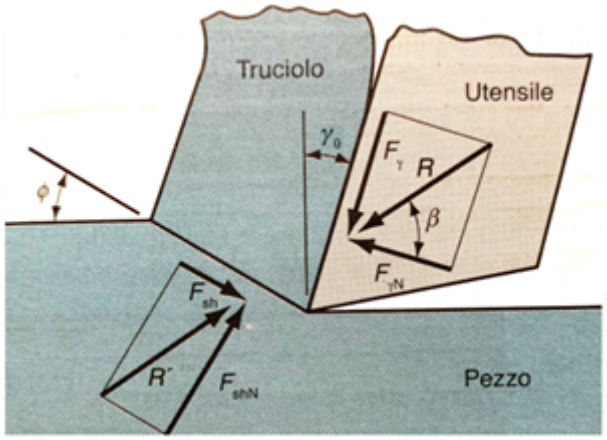

Figure 5.2: orthogonal cut with merchant's angles in evidence [40]

The tendency is to use fluids with both the lubricant and refrigerant properties to exploit the advantages of both the categories. According to the chemical composition it is possible to distinguish four main categories: cutting oils (best lubricant action), emulsions, semisynthetic fluids, synthetic fluids.

Cutting oils: their basis can be oil derived from petroleum, animal oil, marine oil or vegetal oil. Mineral oils (derived from petroleum, naphthenic mineral oils and paraffinic mineral oils) are the most used worldwide. It is possible to mix various kinds of oils and add chemical additives containing sulfur, chlorine and phosphorus to improve the lubricant properties.

Emulsions: they are formed by small suspended drops of oil in water. Water and mineral oils (30:1 proportionally) are mixed with the addition of an emulsifying agent. Additives containing sulfur, chlorine and phosphorus in order to exploit high pressure lubrication. The presence of both water and oil gives to the mixture good properties both under lubrication and refrigeration point of view.

Synthetic fluids: they are composed by chemical substances (composites of sulfur, chlorine and phosphorus) dissolved in water. They are featured by excellent refrigerant properties and moderate lubrication effect. In order to enhance the lubrication effect it is often added oil in emulsion and in this case they take the name of semisynthetic fluids, constituting an hybrid category between emulsions and synthetic fluids.

Based on the first law of metal cutting developed by Makarow, the highest machinability is achievable at a critical cutting temperature known as optimal cutting temperature θ_{opt} , it is the temperature at which the highest ratio of cutting tool hardness over workpiece hardness can be achieved. θ_{opt} is independent by the cutting parameters or machining condition and it is based on the material properties of the tool and the workpiece [117]. Increasing the cutting temperature close to θ_{opt} , machinability increases. Although, further increases in cutting temperature beyond θ_{opt} exacerbate the machining condition. Using cutting fluids is one of the most widely adopted techniques to maintain the cutting temperature below the optimal cutting temperature.
Despite the significant effects of cutting fluids in machining, the selection of the type and delivery system are usually based on the recommendations of cutting fluid suppliers and machine tool manufacturers which are not necessarily aware of the machining conditions. It is approximated that yearly consumption of cutting fluids in the United States is 100 million gallons while it was equal to 71 bn Japanese Yen in Japan where 42 bn Yen is the disposal cost. In 1994, the cutting fluids consumption in manufacturing industries in Germany was estimated to be 75,491 t where 28,415 t of it was water-miscible cutting fluids. It is estimated that the costs associated with cutting fluids are about 16% of the total manufacturing costs while in machining difficult-to-machine materials they reach 20–30%. This is much higher than the tooling costs which are about 2–4% of the total manufacturing cost [101]. The associated costs with cutting fluids are not only limited to their purchase and preparation but also include the maintenance and disposal costs. Disposal costs of the cutting fluids can be up to two or four times their purchase price in the United States and Europe, respectively. This is mainly due to the fact that most cutting fluids are not naturally bio-degradable and require expensive treatments prior to disposal. Cutting fluids also require regular maintenance to control their optimum characteristics.

According to a deep review proposed in [117], cutting fluids are a rich environment for growth of bacteria and fungi. Presence of bacteria in the fluids could split the emulsion and reduce the lubrication effect. They could also change the PH of the cutting fluid and increase the risk of corrosion on the machine tool and workpiece. In addition, they could be dangerous for the workers on the shop floor. To control the bacterial growth in cutting fluids different kinds of bactericides, humectants and germicides are currently in use in industrial scenario and even in the presence of bactericides it has been proved that some bacteria such as Pseudomonas could survive. The presence of the bacteria is not limited to the cutting fluids and microbial masses and particularly endotoxin have been evident at the shop floor atmosphere. This increases the importance of controlling the bacterial growth in metal working fluids. While chemical additives are necessary to control the bacterial growth in cutting fluids, they are accounted as hazardous substances for both the environment and workers' health. Discharge of cutting fluids containing biocides could affect the natural decomposition process and some municipalities prohibited the disposal of biocides into these wage systems. It has been argued that antimicrobials and biocides are used to maintain the cutting fluids functionality rather than protect the workers. Many of the available biocides release formaldehyde which is a potential carcinogen. Similarly, the International Agency for Research on Cancer reported that mineral oil used in metal workings is carcinogenic and exposure to it could result in skin cancer. On the other hand, non-formaldehyde releasing biocides are very dangerous for health and highly corrosive to the skin [47]. In addition to biocides, there are many other chemical substances in the cutting fluids which are considered hazardous to the environment and health. Chlorinated and sulphurised additives in extreme pressure cutting fluids chemically react with metallic surfaces leading to friction reduction. However, they are considered as toxic substances for the workers' health as well as the environment. Chlorinated paraffin in extreme pressure cutting fluids changes by heat and pressure to dioxin which is a toxic substance. The existence of chlorine in cutting fluids also increases the disposal costs by a factor of 7 due to restrictive environmental regulations. Cutting fluids in machining operations could be vaporised and atomised due to high pressure and temperature and form cutting fluids mist. As a result, the airborne particles of cutting fluids could be easily inhaled by workers causing different kinds of lung diseases ranging from mild respiratory problems to asthma and several types of cancers. The effect of aerosols of the cutting fluids on the workers' health is not limited to the lung disease and could also increase the risk of oesophagus, stomach, pancreas, prostate, colon and rectum cancers. Some manufacturers use cutting fluids in order to reduce the machining solid dust. However, it has been found that wet machining could produce 12–80 times more airborne particulate matter than dry cutting. In addition, airborne particles produced at wet machining are much smaller than that of

dry cutting. Smaller particles could remain suspended longer in the working area and are easier to inhale. They are also more likely to pass the larynx and penetrate into the conducting airways and bronchial part of the lungs. Skin exposure to the cutting fluids could also cause skin dermatitis. In [122] Simon et al. performed experiments when machining Titanium at low speed with demineralized water and used auger analysis to examine the cutting effect on a chlorinated fluid. It was observed that chlorine film is made on the surface of workpiece. It was also concluded that machining Titanium with chlorinated cutting fluid cannot be sustained and some very serious health and environment-related hazards are observed. It is important to notice that this last work is dated back in 1979, so it is more than forty years that the research world has a deep consciousness of risks and hazards related to the usage of conventional cutting fluids, but still this technology is the most diffused worldwide. It has been reported that, annually only in the USA, around 155 million gallons of cutting fluids are discharged and exposed to the environment [109]. A renowned work in medical field as [22] collects and reviews evidences and correlations between cancer risk and metal cutting fluids exposure, starting from the '40s. MWF (metal working fluid) exposure, primarily straight oil MWF exposure, has been associated with an increased risk of skin and scrotal cancer. Among six studies that defined occupational categories in sufficient detail to examine risk associated with exposure to MWF, and that controlled for smoking and alcohol, one found a significant risk of laryngeal cancer. It was also found an elevated laryngeal cancer risk among those with "ever employment as a machinist" and among those with "ever employment as a metal grinder". A population-based case-control study of incident cases of rectal cancer in Sweden found that male workers ever exposed to cutting fluids had an elevated risk of rectal cancer. A wide number of studies with statistically significant findings suggests that exposure to some MWFs may increase the risk of pancreatic cancer, even if the evidences on this correlation are less strong than for other diseases. Several case-control studies have also examined the risk of bladder cancer among those whose occupations may involve MWF exposure. Only those studies that controlled for smoking, a known risk factor for bladder cancer are included in this review [22]. In a large population-based case-control study from the United States, was found an elevated risk of bladder cancer among white men ever employed as machinists or drill press operators. Furthermore, among drill press operators, the risk increased with increasing duration of employment. Another study examined occupational risk factors for bladder cancer and reported an elevated risk for the summary category "Metal machinery". An hospital-based case-control study conducted in Germany found that individuals ever employed as turners had an increased risk of bladder cancer and the risk was consistently elevated with increasing duration of employment. Similar negative trends were found in Belgium, Italy and various states of the USA. Although the route of

exposure to MWFs is generally through dermal contact or through inhalation, the large size of many airborne MWF droplets can lead to gastrointestinal exposure. A significant proportion of airborne MWF particles is in the non-respirable range (i.e. particles with a mass mean diameter > 9.8 μm)

5.3. Disposal of cutting fluids

In the recent years regulations governing the discharge of industrial wastes, including spent MWFs, have become more stringent. These now require companies to take any and all measures necessary to ensure the safe collection and disposal of waste oils and must, as far as possible, give priority to the processing of waste streams. As a result, businesses need to treat spent MWFs before the wastewater component can be discharged to sewers. Italian legislation categorizes as special wastes almost all the exhausted oil-water emulsions, forbids their free dispersion in the environment and strictly regulates the disposal process. Mixtures with more than 15% (weight basis) of water are considered emulsions and manufacturers have to pay for their pick up, while mixtures with less than 15% of water are considered used-oils and the manufacturers are paid for their pick up. Similar legislations are present also in the European and American countries. After the pick up phase, specialized companies are in charge of the handling and final disposal of the fluids. In particular, after their lifecycle in industries, water-mix MWFs are the most difficult to treat under an environmental point of view. Treatment and disposal options applicable to water-mix MWFs depend on the type and volume of waste, their goal is to minimize:
COD = measure of contamination of water by MWFs, tramp oils and many other chemical compounds such as detergents, surfactants, biocides and anti-corrosion agents found in MWFs.
BOD = measure of how quickly micro-organisms use up the oxygen in water.
TSS = measure of suspended solids in water which include a wide variety of particles from the work pieces found in waste MWFs. There may also be solids from other stray objects which sometimes find their way into machine pumps. Treatments are divided in:

- Primary treatment: Pre-treatment options to remove separated oil (tramp oil) and particulates, these include gravitation, filtration, floatation and centrifugation. The equipment type (skimmers, oil absorbent pillows, settling tanks, magnetic separators, hydro cyclones, microfilters, chemical coalescing agents, air induced floatation and centrifuges) has a cost (fixed and operating) that ranges from low to medium.
- Secondary treatment: Treatment options to separate or “treat” the emulsified fluid

by:
Ultrafiltration = suitable for macro-emulsions and semi-synthetic fluids. MWF is passed through a membrane under pressure. Tiny pores in the membrane allow water through but oil and surfactants are retained.
Chemical separation = Suitable for macro-emulsions and semi-synthetic fluids. A chemical agent is used to split the emulsion into oil and water phases.
Evaporation = suitable for all types of water-mix MWFs. Spent MWF is heated in special evaporating vessels to drive off water, leaving a reduced volume for disposal as hazardous waste. Evaporation is unaffected by fluid variations and contaminants; however it is essential to consider carefully the energy cost.
Biological treatment = suitable for macro-emulsions and semi-synthetic fluids. Micro-organisms are added to a bioreactor containing spent MWFs to reduce organic and inorganic materials. Biological treatment can only be carried out as a continuous process and is slow compared to chemical treatment or filtration. It is most economical for large users.

- Tertiary treatment: Further polishing/cleaning of the recovered phases from secondary treatment, it reduces the COD to a very low level so that the recovered water could be re-used on-site for low grade use. It includes: Reverse osmosis: it occurs when pre-treated spent MWF is moved across the membrane against the concentration gradient, from lower concentration to higher concentration. It separates water from dissolved matter (including metal ions). The end stream (water phase) has high re-use potential. Nanofiltration: this process uses semi-porous membranes to remove metal ions and organics from wastewater. The end stream (water phase) has high re-use potential and the by-product is disposed of with used membranes. Pre-treatment of the feed stream, usually by ultrafiltration, is required to remove solids and macromolecules. The operation of nanofiltration is similar to that of reverse osmosis. The main difference is membranes used for nanofiltration are not as "tight" as the reverse osmosis membrane. Nanofiltration operates at a lower pressure and it does not remove monovalent ions (i.e. those with a single charge or valence of one) from the water as effectively as the RO membrane. Carbon Adsorption: Activated carbon is used to adsorb dissolved components of spent MWFs from the water phase following secondary treatment. The end stream has high feed re-use potential. The oily phase by-product is disposed of with waste adsorbent. Ion Exchange Resins: dissolved metal salts, acids and bases found in spent MWFs are removed by contact with functional chemicals attached to beads of resin. Organic material, oil or grease can foul the resin and therefore the technique is only suitable

for water phases where the COD is less than 150 mg/l [26].

Many new technologies are being investigated for the treatment of spent MWFs and other wastes. Most of these methods are based on combinations of filtration technologies coupled with a process of "oxidation" where the larger molecules of oil and solvents are broken down into smaller, water-soluble compounds. As the molecules are broken down into smaller fragments they become less toxic, eventually only releasing carbon dioxide as the main end by-product. It should be noted that these processes have a long way to go in development. They are: Ultrafiltration coupled with chemical oxidation, Ultrafiltration coupled with electrochemical oxidation and Mechanical vapour recompression (MVR) [26].

6 | Energy Consumption and Optimization

6.1. Energy Consumption

Energy consumption is considered as one of the most important parameters in machining processes as it not only contributes to a significant part of the total manufacturing cost, but also has a great impact on environment. There is a direct link between energy consumption in industry and CO2 emissions in atmosphere, researchers call this link Carbon Emission Signature (CES) [60]. Globally the annual carbon dioxide emission is rising worryingly and the trend is driven principally by countries that are facing fast growth and industrialization.

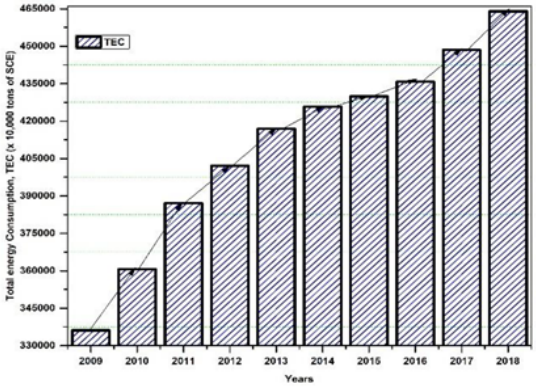

Figure 6.1: Energy consumption in China (National Bureau of statistics of China).

In the machining process the energy efficiency is typically very low, in modern milling most of the energy is consumed during non-cutting phases of the working cycles. Energy used in actual cutting process is about 15% of the total energy consumed [42]. While machining hard to cut materials a longer machining time is required and this percentage usually rises. The process efficiency is influenced by several factors linked to workpiece, cutting tool, machining conditions, cutting fluid and lubricating technique as synthetized

in the figure below.

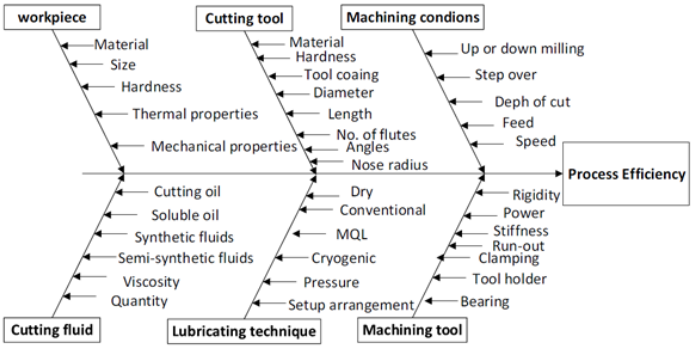

Figure 6.2: parameters influencing process efficiency in milling [69].

Energy efficiency has become an inevitable trend for sustainability in the manufacturing sector, it is necessary in facing contemporary challenges as climate change, global resources depletion and rising energy price. Historically, in manufacturing field, the largest effort of R&D and practitioners has always been directed to productivity enhancement and reduction of utilized resources. Recently, the reduction of energy consumption, workers' health and safety and disposal of harmful industrial wastes are becoming important focuses of many researchers. In this new scenario, sustainable machining of hard to cut materials is one of the most challenging topics. 30% of the global energy consumption is due to the manufacturing sector [69]. In the United States 31% of total electricity consumption is accounted for by the industrial sector and in the industrial sector 90% of the total energy consumption is accounted by the manufacturing process and 75% of manufacturing electricity consumption is occupied by machine tools (EIA 2013). In China, the industrial sector is responsible for 70% of primary energy utilization and 80% of CO2 emissions. It is reasonable to affirm that the energy consumption index for a machine tool will be a key evaluation index in the next years.

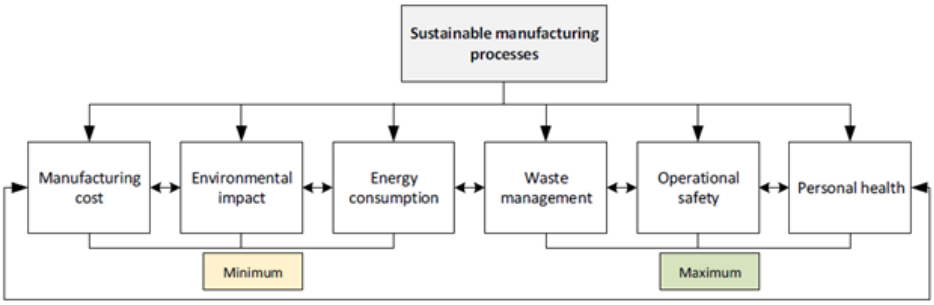

Figure 6.3: Factor affecting the machining process sustainability and their desired levels [69].

The energy assessment and characterization of a machine tool is not a trivial topic, many different phases can be defined during the cycle time.

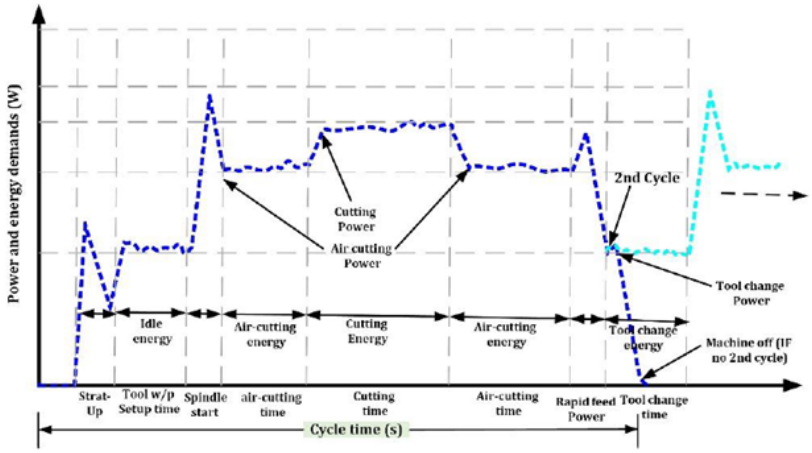

Figure 6.4: Cycle time, power, and energy consumption profiles of the machine tool during the machining process [69].

The power demands by different components of a machine tool vary and it is tough to determine the demand of each component. In general, total machining power consists of Pi = idle power, Pst = set up power, Pa = air cutting power, Pc = cutting power, Pcs = power during cutting stage (machine power), Ptc = power consumed during the cutting tool change and Pl = lubrication power (not applicable for dry machining). Initially, when the machine is switched on, start-up phase comes and power increases as different components of machine tool extract current. After the start-up phase, the programmable logic controller of machine tool and electrical motors are turned on. However, the spindle and feed axes are at rest, and this phase is called stand-by or idle stage. A fixed amount of power is consumed during the stand-by phase. A CNC machine tool consumes a constant amount of stand-by power during the idle stage and setup stage which includes workpiece/cutting tool setup and cutting tool changing stage. Normally, cooling and lubrication systems are built-in in the machine tool. However, old machines are not equipped with the cooling and lubrication mechanism. Hence, external cooling/lubrication also consumes power different from the machine tool's power and this quantity must be added into the analysis.

In general, nevertheless the specific analysed process, the absorbed energy in machining can be subdivided in two contributions. One is proportional to the volume of processed material, the other is linked to the energy absorbed by the machine modules during air

cutting.

$$E_p = p_{\text{ave}} * \Delta t = (p_{\text{cut}} + p_{\text{air}}) * \Delta t = e_{\text{cut}} * \text{Vol} + (p_{\text{edge}} + p_{\text{air}}) * \Delta t$$

Where p_{cut} is the power absorbed by the spindle and the axes (mainly the spindle) that is directly connected to the material removal. p_{air} is the power absorbed when the machine is not cutting, p_{edge} is the contribution of friction, e_{cut} is the specific cutting energy. The energy used for processing a unit of volume can be considered a performance indicator:

$$E_{\text{ave}} = (e_{\text{cut}} * MRR + p_{\text{air}}) * \Delta t$$
$$\frac{E_p}{Vol} = e_{cut} + p_{\text{air}} * \frac{\Delta t}{Vol} = e_{\text{cut}} + \frac{p_{\text{air}}}{MRR}$$

e_{cut} is given by two main contributions: one connected to the process, one connected to friction and other undirect aspects non connected to chip formation itself. Referring to a simple example of orthogonal cutting, it is possible to distinguish two force components:

$$F_t = \text{ tangential force } = F_{tc} + F_{te} = K_{tc} * b * h + K_{te} * b$$
$$F_f = \text{ feed force } = F_{fc} + F_{fe} = K_{fc} * b * h + K_{fe} * b$$

with b = depth of cut, h = chip thickness, K_{ij} specific cutting pressures with i = direction (tangential or feed), j=contribution (cut or edge). Considering only the tangential contribution (since it is the major) it is possible to write:

$$P_{cut} = K_{tc} * b * h * V_c + K_{te} b * V_c = K_{tc} * MRR + K_{te} * \frac{MRR}{h}$$

With V_c = cutting speed. Dividing for MRR:

$$e_{cut} = K_{tc} + \frac{K_{te}}{h}$$

so the process efficiency increases if the forces required are lower (for example using a sharper tool) and also an increment of chip thickness is useful. An equivalent conclusion ca be done looking at the force model proposed by Sandvik, where the specific cutting pressure is:

$$K_t = \frac{1 - 0.01 * \gamma_0}{h_m^{m_c}} * k_{c1.1}$$

with h_m = correction factor due to chip thickness, γ_0 = correction due to rake angle. This effect can be experienced with a wide range of materials.

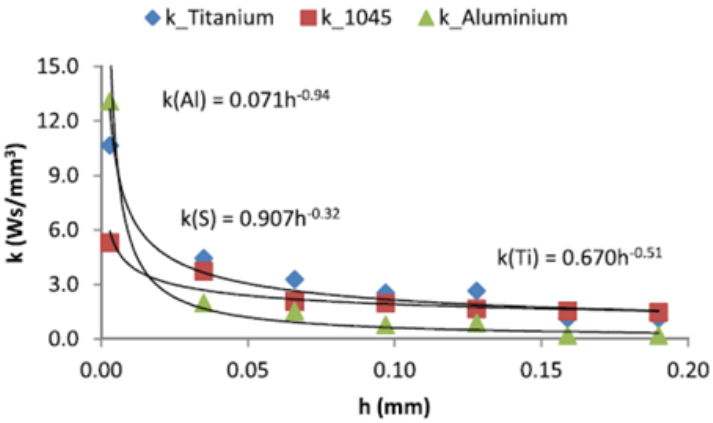

Figure 6.5: Specific energy comparison for aluminium AW6082-T6 alloy, AISI 1045 and Ti6Al4V [10].

Here a specific energy comparison for aluminium AW6082-T6 alloy, AISI 1045 and Ti6Al4V [10]. Recalling $\frac{E_p}{Vol} = e_{cut} + p_{air} * \frac{\Delta t}{Vol} = e_{cut} + \frac{p_{air}}{MRR}$ it is possible to notice that there are three main way to follow in order to increase the efficiency of the cutting operation:

- Increasing the feed rate (even at the same cutting speed), in fact e_{cut} decreases thanks to h increment and MRR increases too. The drawback is an increment of requested torque and the possible shortening of tool life. It is generally a suitable application for titanium pocket milling.

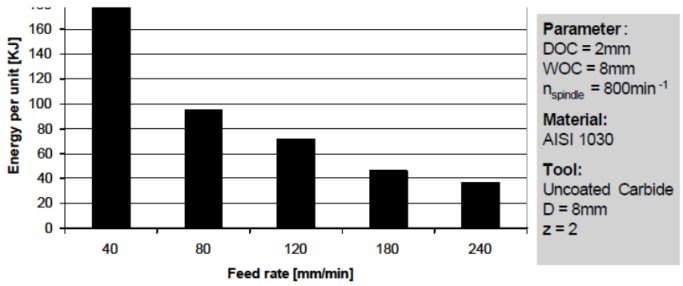

Figure 6.6: Effect of feed rate increment at constant cutting speed [44].

- Increasing the cutting speed keeping constant the feed rate f_z, because MRR increases. At the same time the requested cutting power and tool wear rise up.

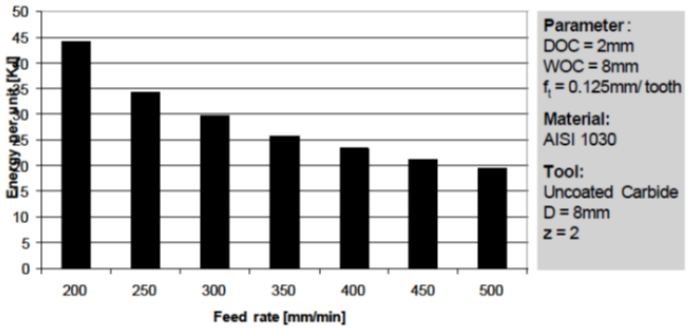

Figure 6.7: Cutting speed increment effect keeping constant f_z [44].

- Increasing the cutting area in order to increase once again the MRR. In this case, in addition to augmented forces and power, there is the possibility to experience strong vibration issues.

In order to avoid waste of time, energy and resources it is convenient to optimize the cutting conditions. Possible goals of an optimization procedure may be: production time or production cost minimization, profit rate maximization or (under an environmental point of view) the minimization of the overall energy consumption.

If the objective function is the production time:

$$t_p = t_0 + \frac{V}{Q} + \frac{V}{Q * T} * t_{cu} = t_0 + \frac{V}{Q} * \left(1 + \frac{t_{cu}}{T}\right)$$

with t_0 = fixed times (independent by process parameters) [min], T = tool life [min], t_{cu} = tool change duration [min], V = volume of material to cut away [mm^3], Q = material removal rate $\left[\frac{\text{mm}^3}{\text{min}}\right]$.

If the objective function is the production cost:

$$C_p = C_0 + C_m * \frac{V}{Q} * \left[1 + \frac{1}{T} * \left(t_{cu} + \frac{C_{ut}}{C_m}\right)\right]$$

with C_0 = fixed costs $[euro]$, C_m = hourly cost of the machine tool $\left[\frac{euro}{\text{min}}\right]$, C_{ut} = average cost of a cutter $\left[\frac{euro}{cutter}\right]$.
If the objective function is the profit rate:

$$P_r = \frac{R - C_p}{t_p} \left[\frac{euro}{time}\right]$$

with R = operating income, C_p = operating cost, t_p = production time.
In any case it is possible to write a general goal function: $F = F_0 + \frac{\alpha}{Q} * \left(1 + \frac{\varphi}{T}\right)$.
Coming from: $F = F_0 + \frac{\alpha}{s*V_c} * \left(1 + \frac{\varphi}{T(V_c)}\right)$ and if $\alpha' = \frac{\alpha}{s}$ it is possible to write
$F = F_0 + \frac{\alpha'}{V_c} * \left(1 + \frac{\varphi}{T(V_c)}\right)$ and imposing
$\frac{dF}{dV_c} = -\frac{\alpha'}{V_c^2} * \left(1 + \frac{\varphi}{T(V_c)}\right) + \frac{\alpha'}{V_c} * \left(-\frac{\varphi}{T(V_c)^2} * \frac{dT}{dV_c}\right) = 0$ grouping $\frac{1}{V_c^2}$:
$\frac{dF}{dV_c} = -\frac{\alpha'}{V_c^2} * \left(1 + \frac{\varphi}{T(V_c)} + \frac{\varphi * V_c}{T(V_c)^2} * \frac{dT}{dV_c}\right) = 0$ so it is true that
$\left(1 + \frac{\varphi}{T(V_c)} + \frac{\varphi * V_c}{T(V_c)^2} * \frac{dT}{dV_c}\right) = \left(1 + \frac{\varphi}{T(V_c)} + \frac{\varphi}{T(V_c)} * \frac{V_c * dT}{T(V_c) * dV_c}\right) =$

$$= \left(1 + \frac{\varphi}{T\,(V_c)} + \frac{\varphi}{T\,(V_c)} * \frac{d\ln T}{d\ln V_c}\right) = 0$$

and it exists an extremum if $\frac{d\ln T}{d\ln V_c} < -1$. In order to understand if the extremum is a maximum or a minimum it is necessary to study the second derivative
$\frac{d^2 \ln T}{d(\ln V_c)^2} < \frac{d(\ln T)}{d(\ln V_c)} * \left[1 + \frac{d\ln T}{d\ln V_c}\right] = \delta$
and since the condition was $\frac{d\ln T}{d\ln V_c} < -1 \rightarrow \delta > 1$ and the extremum is a minimum.
Cutting speed is bounded to tool life through the Taylor's Law: $V_c * T^n = C$, so $\frac{d\ln T}{d\ln V_c} = -\frac{1}{n}$
and substituting in the first derivative written above it is possible to obtain
$1 + \frac{\varphi}{T} * \left(1 - \frac{1}{n}\right) = 0$ and so $T_{opt} = \varphi * \left(\frac{1}{n} - 1\right)$ because $\frac{\varphi}{T} - \frac{\varphi}{T*n} = -1$ and $\frac{\varphi}{T} * \left(1 - \frac{1}{n}\right) = -1$.

In the end $\begin{cases} T_{opt} = \varphi * \left(\frac{1}{n} - 1\right) \\ V_{c,opt} = \frac{C}{T_{opt}^n} \end{cases}$

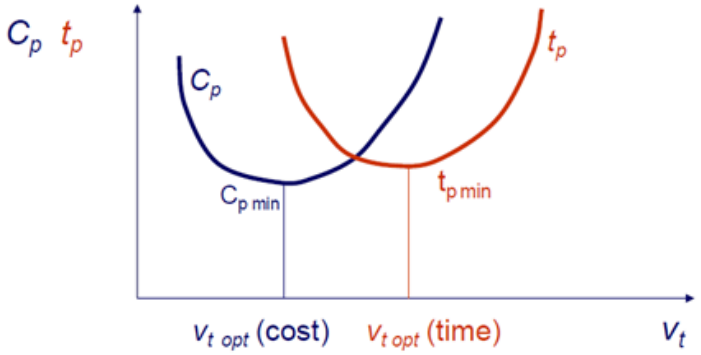

Figure 6.8: Production Cost and time functions of cutting speed.

The goal function: $F = F_0 + \frac{\alpha}{Q} * \left(1 + \frac{\varphi}{T}\right)$ takes different values in relation of the objective function we are considering:

	t_p	C_p
F_0	t_0	$C_0 + C_m * t_0$
α	V	$C_m * V$
φ	t_{cu}	$t_{cu} + C_{ut}/C_m$

Table 6.1: Different values inside the goal function depending on the objective function.

According to [84] the global energy consumption of a machine tool can be split in four different contributions:

$$E = E_1 + E_2 + E_3 + E_4$$

E_1 = energy consumed during machine tool set-up = $P_0 * t_1$,
E_2 = energy used to power the machine modules = $P_0 * t_2 + p_t * Z * t_2$,
E_3 = energy used during tool change = $P_0 * t_3 * \left(\frac{t_2}{T}\right)$,
E_4 = energy footprint linked to the tools = $y_E * \left(\frac{t_2}{T}\right)$, where t_1 = set up time, $t_2 = \frac{V}{z} = \frac{V}{V_t^* S} =$, time taken for cutting $t_3 = t_{cu}$ = time taken to change the tool, P_0 = power consumed by machine modules (stand-by power consumption), p_t = specific cutting force, T = tool life, y_E = energy for cutting edge.

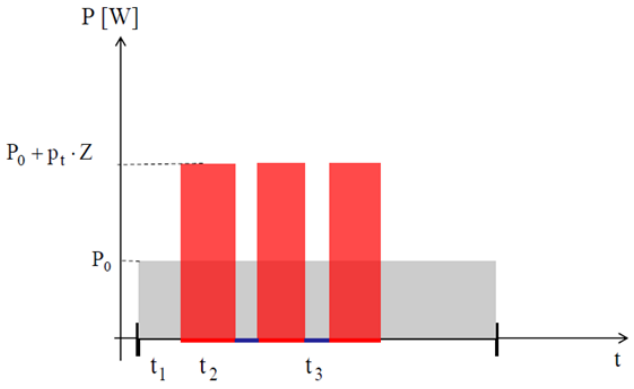

Figure 6.9: Machine Tool power consumption modelling [84]

So it is possible to write

$$E = P_0 * t_1 + P_0 * t_2 + p_t * Z * t_2 + P_0 * t_3 * \left(\frac{t_2}{T}\right) + y_E * \left(\frac{t_2}{T}\right) =$$
$$= P_0 * t_1 + P_0 * \frac{V}{Z} + p_t * Z * \frac{V}{Z} + P_0 * t_{cu} * \frac{V}{z} * \frac{1}{T} + y_E * \frac{V}{z} * \frac{1}{T} =$$
$$= P_0 * t_1 + P_0 * \frac{V}{z} + p_t * V + P_0 * t_{cu} * \frac{V}{z} * \frac{1}{T} + y_E * \frac{V}{z} * \frac{1}{T} =$$
$$= (P_0 * t_1 + p_t * V) + P_0 * \frac{V}{z} + P_0 * t_{cu} * \frac{V}{z} * \frac{1}{T} + y_E * \frac{V}{z} * \frac{1}{T} =$$
$$= (P_0 * t_1 + p_t * V) + P_0 * \frac{V}{z} * \left(1 + \frac{t_{cu}}{T} + \frac{y_E}{P_0} * \frac{1}{T}\right) =$$
$$= E_0 + P_0 * \frac{V}{z} * \left(1 + \frac{1}{T} * \left(t_{cu} + \frac{y_E}{P_0}\right)\right).$$

It is important to notice that $(P_0 * t_1 + p_t * V)$ is invariant with respect to cutting speed, $P_0 * \frac{V}{z}$ decreases by increasing cutting speed and $P_0 * t_{cu} * \frac{V}{z} * \frac{1}{T} + y_E * \frac{V}{z} * \frac{1}{T}$ increases by increasing cutting speed.
It is possible to write $F = F_0 + \frac{\alpha}{Q} * \left(1 + \frac{\varphi}{T}\right)$ With $F_0 = E_0 = (P_0 * t_1 + p_t * V), \alpha = = P_0 * V, \varphi = t_{cu} + \frac{y_E}{P_0}$.

And so also for energy consumption optimization it is possible to find
$$\begin{cases} T_{opt} = \varphi * \left(\frac{1}{n} - 1\right) \\ V_{c,opt} = \frac{c}{T_{opt}^n} \end{cases}$$

It is evident that cutting speed is a fundamental parameter in the optimization of cutting procedures, thus having a colling/lubricating medium that allows the adoption of different cutting speeds keeping high the tool life is very important.

7 | Sustainable Alternatives to Conventional Wet Machining

7.1. Minimum Quantity Lubricant

An alternative to conventional flood coolant is represented by MQL=Minimum Quantity Lubricant or near dry machining. It also provides an alternative for machining operations in which dry machining is not applicable especially where machining efficiency and/or high surface quality are of more interest [30]. MQL basically consists in the application of a small amount of cutting fluid (10–100 ml/h) mixed with compressed air to form an aerosol. This mixture is then penetrated to the cutting zone in order to lubricate the chip–tool contact area and reduce the temperature. Boundary lubrication on the contact surfaces results in a lower friction coefficient whilst heat transformation is mainly in the form vaporisation at the cutting zone and conduction through the flow of the air. Evaporation of the liquid at the cutting zone eliminates the requirements for maintenance, circulation and disposal of the cutting fluid and the associated costs [112]. Most of the commercial products available in the market consist of five main parts: air compressor, liquid container, tubings, flow control system and spray nozzles. Generally, in all MQL systems, the coolant and pressured air are mixed together and a controlled flow of the mixture is delivered through the tubings and nozzle into the cutting point. The nozzle could be external or internal which is also known as a through-the-tool cooling/lubricating system [117].

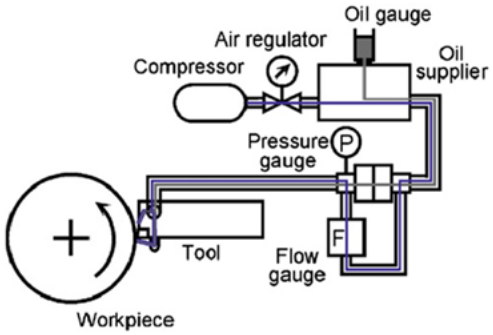

Figure 7.1: Example of MQL cooling system for turning operations [117].

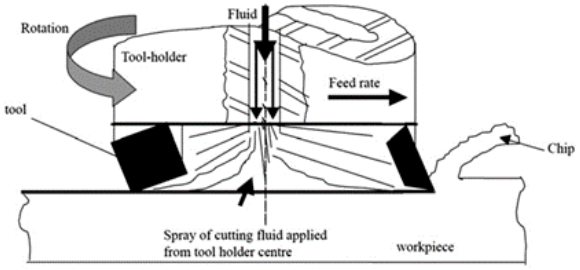

Figure 7.2: View of a through-the-tool MQL cooling system designed for face-milling [117].

MQL is introduced where dry cutting is not applicable and flood cooling is not desirable. Machining ductile materials is one of these cases where high cutting temperature increases the tendency of adhesion between the cutting tool and workpiece materials. The high cutting temperature in the case of ductile materials is mainly due to large plastic deformation at the primary cutting zone and high friction coefficient at the second shear zone between the chips and rake face. This high temperature increases the adhesion of the chip material to the cutting tool resulting in the formation of BUE. The presence of BUE on the cutting tool in most cases not only reduces the tool life but also worsens the machined surface quality. For instance dry machining of aluminium alloy parts is specifically critical. Heat generated during machining transforms into the workpiece due to its high thermal conductivity. Changes in the workpiece temperature during machining could cause thermal deformation and/or geometrical deviations. Aluminium alloys also tend to adhere to the cutting tool and form BUE. This affects the surface finish of the machined part as well as tool life, cutting forces and power consumption. Studies on the application of MQL in drilling aluminium alloys showed that it could drastically increase the tool life up to 8 times [70]. A complete work by Sharma et al. [111] collects results

from MQL applications in turning, drillingn, grinding and milling. First of all, very interesting results in terms of forces reduction, friction reduction, surface roughness and energy saving have been experiemced through years. The best results in particular come from MQL applications on soft materials, while in case of harder materials the results on tool life are not univoque and the advantages on dry cut are way thinner. Applications of MQL on Ti6Al4V are rare and this lack is also wider in the specific case of milling. Till today very few researches have studied the optimization of MQL operating parameters, such as flow rate, spray distance, spray nozzle orientation angle and air pressure and their effects on machining. The optimization of the above parameters can be attained in various other machining processes as well. Further investigation can also be focussed on the application of MQL with hybrid nanofluids. Infact the addition of metallic nanoparticles into conventional cutting fluid enhances its thermal conductivity (cooling capabilities) significantly [110]. Being expansive, the nanofluid is not advisable to use as cutting fluid in wet machining. However, its application with MQL technique makes it as a viable alternative to the wet machining.

7.2. Cryiogenics

The science and technology of producing low temperature environments is generally referred to as cryogenics. There are inconsistencies in identifying at what point on the temperature scale refrigeration ends and cryogenics begins. However, most researchers and standards organizations assume that it starts at or below -150 °C (123 K or -238 °F). Cryogenically assisted manufacturing processes are emerging as environmentally-benign, toxic-free, hazardless operations, producing functionally superior products [59]. The earliest use of liquefied gases as coolant in machining operations is reported by Reitz in Germany in 1919 [105], where carbon dioxide (CO2) was used as a coolant in machining. Generally in chips removal operations, liquid gases such as nitrogen, carbon dioxide and helium are used as alternative coolants to traditional oil and water-based coolants/lubricants. The most diffused cryogenic fluid is LN2. Nitrogen is an inert, non-hazardous, non-toxic, non-flammable, colorless and odorless gas and constitutes 79% of air. It is lighter than air and disperses into it after application, thus reducing the requirements for maintenance, post-machining cleaning and disposal.

Cryogenic fluxes are fed to workpieces in order to vary their mechanical properties and/or to cool down the cutting zone. The first method is adopted for soft materials such as aluminium or polymers, to enhance compactness and brittleness of the workpiece. The second approach is used to control the cutting region temperature of hard to cut materials such as Ti-alloys, Ni-alloys. Fe-Ni-Cr-alloys, Co-alloys, high strength steels and

so on. Cryogenic techniques are also applied in machining of ceramics and composites, exotic metals such as tantalum and porous tungsten for electrodes. In composites low temperatures allow better delamination control, for ceramics they enhance the tool life, for porous materials they stabilize the structure. In case of magnesium alloys, the lower temperature avoids reactant chips burning. Low temperatures can modify the metallurgical structure of the machined surface, promoting hard phases, compressive residual stresses, grain refinement and thinner deformed layers.

	Effects of the cooling and lubricating strategy	Flood (emulsion/oil)	Dry (compressed air)	MQL (oil)	Cryogenic (LN_2)	Hybrid (LN_2 + MQL)
Primary	Cooling	Good	Poor	Marginal	Excellent	Excellent
	Lubrication	Excellent	Poor	Excellent	Marginal	Excellent
	Chip Removal	Good	Good	Marginal	good	Good
Secondary	Machine Cooling	Good	Poor	Poor	Marginal	Marginal
	Workpiece Cooling	Good	Poor	Poor	Good	Good
	Dust/Particle Control	Good	Poor	Marginal	Marginal	Good
	Product Quality (Surface Integrity)	Good	Poor	Marginal	Excellent	Excellent
	Sustainability Concerns	Water pollution, microbial infestation, and high cost	Poor surface integrity due to thermal damage	Harmful oil vapor	Initial cost	Initial cost, oil vapor

Figure 7.3: Effectiveness and application of various cooling and lubricating strategies [59].

The effect of cryogenic machining on tool-life has been investigated extensively for decades. In general, the application of cryogenic fluids, mainly LN2, often leads to a significant decrease in tool-wear. However, it is not clear if this fluid can increase the tool resistance by a macroscopic cooling of all the components (cutting tool, chip, work material) [71], or if the cryogenic fluid modifies the local tribological conditions, especially the friction at the tool-workpiece material interface [48]. The potentialities of cryogenic machining are wide and regard:

- Increased tool life
- Increased productivity
- Increased surface and subsurface hardness of the machined piece (better product quality)
- Increased surface finish
- No needs of pumps and filtration
- Clean chips and workpiece

- Shorter and more controllable chips
- Negligible inviromental impact and reduced health issues

7.3. Cooling strategies

Having a cryogenic flux in liquid phase and being capable of bringing it to the desired spot is really important because it allows to expolit the latent heat of evaporation of the substance, giving a boost to the cooling capability of the flux. This feature strongly depends on the interaction mode between cryogenic fluxes and the bodies to be cooled down, in particular are important: the state of the fluxes (liquid only, liquid and vapor, vapor only), pressure, nozzle position and orientation.
In several scientific works it is shown as at very high speeds of cut the heat tranfser is lowered. According to Yildiz in [141] this happens because the higher flow of chips leads to the obstruction of the cutting area that becomes not accessible to the cooling media. At the same time, at elevated speeds the heat generation increases and it may be not balanced by the flow rate or by the pressure of the fluid. In fact the calibration of cryogenic systems is not trivial at all and jet speed, spot size, fluid quality, mass flow rate, nozzles' distance and orientation should balance the heat generation rates of the cutting process. A non-sufficient adduction of the cryo-flux induces a condition o of near dry cutting, on the other hand excessive adduction of cryo-flux is responsible for overhardening of the workpiece and reduces the tool life. Another problem pointed out by Shokrani [118] is that the nitrogen once in contact with the hot materials promotes the formation of a vapor cushions. On one side it has a beneficial effect because it insulates the cutting zone from gases present in the atmosphere and potentially able to react with tool or workpiece, but on the other side it significantly reduces the cooling effect of the cryogenic flux. The heat extraction and generation rates must be compared and flow properties or nozzle design adjusted so to promote a balance. A proper design involves multidisciplinary knowledges including thermo-fluid dynamics, technical physics, machining processes and material science. There are mainly three techniques used to cool down the cutting zone:

1. **Workpiece Cooling:** it is suitable for materials that does not exhibit excessive hardening at low temperatures. Materials as aluminium or polymers at ambient temperature can melt or lead to burr formation, so this kind of cooling strategy can be particularly effective [15]. The same holds for materials subjected to delamination that require compactness such as composites or material that shows difficult flow of the chips like magnesium. In order to lower the temperature of the workpiece

it is possible to perform:

Cooling bath: high energy and quantity of fluid are necessary, time demanding, generally the piece is overhardened. Abrasion and cutting forces are higher and dimensional deviation must be considered.

Flood cooling: less quantity of coolant and less time are necessary, it is more localized, shearing stress of the material is enhanced, dimensional deviation may occur.

Jet cooling: less energy consuming and more localized, but cooling effect can be insufficient. It is a viable option in case the desired effects are embrittlement, chip breakability, burning avoidance and at the same time excessive hardening must be avoided. Overhardening of the piece, dimensional deviation and forces/energy/power increments are typical phenomena of workpiece cooling.

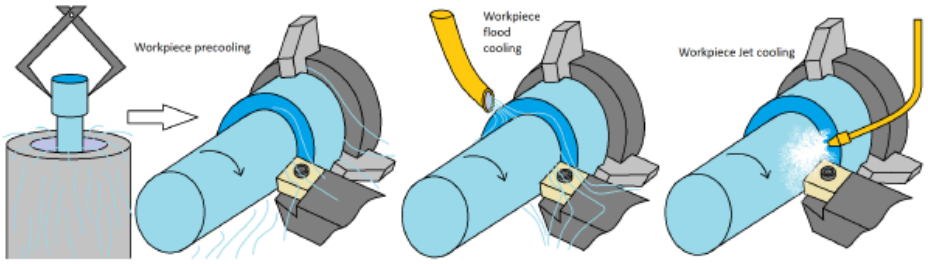

Figure 7.4: Different strategies for Workpiece Cooling: workpiece pre-cooling, workpiece flood-cooling, workpiece jet-cooling. (credit to L.Losa)

2. **Indirect Cooling:** in this case the only cooled object is the insert, it is also addressed as tool back cooling or conductive remote cooling [141]. The thermal conductivity of the workpiece material becomes a key parameter, as consequence ceramic materials will benefit less from its application due to their lower ability to conduct heat. Similarly, the effectiveness is higher if liquid N2 or CO2 are used thanks to their high heat transfer capacity. Usually the cryogenic fluid is supplied to the rake and rear face of the tools by means of external covers, with the tool set in a sort of sandwich of cryogenic flux. The benefits of this method come from the material properties at low temperature and not from the possible lubricant effect of cryogenic fluxes over which there are incoherent results in scientific literature. Logically, the most evident advantage of indirect cooling is the lack of overhardening of the workpiece [137].

3. **Pressure jet cooling:** it is the alternative with the highest potentialities. The jet can be controlled and delivered where it is necessary, for example on the rake, on the flank or on the bending chip. Having a controlled and localized delivery of the cryogenic fluid it is important to avoid waste of fluid and alteration of the workpiece material [118]. An important option in the design phase is to place micro-nozzles that minimize the cryogenic flow rate and maximize the cooling effect with a precise and localized delivery on the cooling target [141]. Heat transfer properties are strictly correlated to the dynamics of the cryogenic flow. In case of localized flow (directed at the rake-chip interface or at the bending chip) we talk about confined flow. Differently it is possible to talk about free flow when it is directed to the flank or impinging on the insert [59].

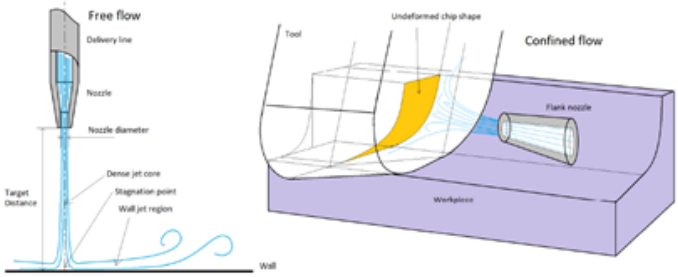

Figure 7.5: Free and confined flow (credit to L.Losa).

Free and confined flow: considering LN2, in case of free flow the jet impinging on the surface is featured by a dense jet core. When it collides with the surface to be cooled down, there is the formation of a stagnation point, on its sides the flow forms the so called wall jet region, it is deflected and spans radially with speed parallel to the surface itself. The formation of the liquid wall jet region, featured by vortices, deeply influences the heat transfer properties of the jet. After a distance form the nozzle equal to ten times the diameter, it is unlikely to have the jet still in liquid phase, for this reason the cooling target must be close to the nozzle. At forty diameters from the nozzle, the 50% of LN2 is in gas phase. Gaseous N2 occupies a volume 694 times larger than LN2, this expansion can favour chips evacuation but decreases the heat transfer coefficient of the jet [59]. The value of heat transfer coefficient is up to $50\frac{kW}{m^2K}$ in the core of the jet of LN2 while in the wall region it decreases drastically until $1.5\frac{kW}{m^2K}$.
In practical situations the cooling flow is confined in the crevice between the tool rake or flank and the chip (confined flow). In this condition heat transfer mechanisms are governed by strong mixing momentum transfer. Heat transfer capacity is influenced by geometry and by surface overheat temperature.

7.4. Material Properties at Cryogenic Temperatures

As underlined in [59], generally for a metallic material at cryogenic temperatures, hardness, yield strength, tensile strength, wear resistance and fatigue strength increase. The material results to be stronger. At the same time residual stresses at low temperature tend to be lower and dimensional stability increases. FCC cell structures show a slight decrease in ductility and toughness, whereas BCC and HCP become brittle. For alloys like Ti and Ni toughness and ductility decrease at a much lower rate than the increase in strength properties [49]. Cooling the tool will result in a harder and stronger cutter, more wear resistant, with reduced chemical activity, as the workpiece, with less sticky rake and flank faces leading to lower wear rates and BUE suppression in many cases [140]. In [49] Hong at al. began their study in the field of cryogenic machining by examining material properties at low temperature. In general, on the workpiece side, at the very low temperatures achieved with cryogenic cooling, hardness, wear resistance and strength rise, while chemical affinity and toughness decrease. For what concerns the tool side, indentation, three-point bending, impact strength and microstructural observations tests were done on several carbide grades, all of them capable of maintaining their strength and toughness at low temperature, rising hardness and wear resistance. However, other tool materials (more attractive for hard to cut materials working) were not considered, for example more expensive CBN, B-CBN, PCD, ceramics, or cheaper HSS.

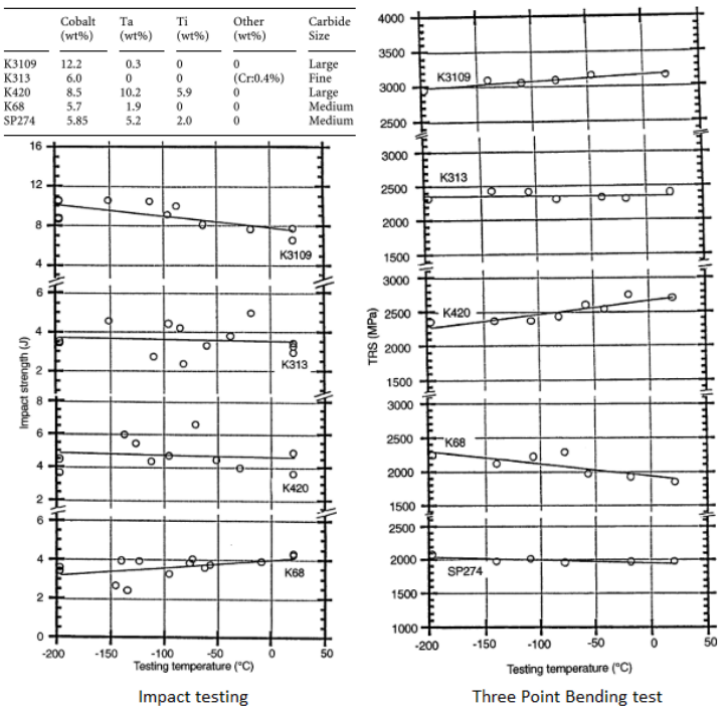

Figure 7.6: Different Carbide grades properties at low temperatures [49].

Passing from the tool to the workpiece side the study suggests that:
Mild-low carbon steels, AISI 1010, 1070 at low temperature have lower toughness and ductility, reduced elongation, reduction in area and impact strength, higher hardness and yield strength.
High strength steels AISI E52100, Al A390 increase their hardness and strength promoting higher tool wear, in this case a smart solution would be to cool the tool only if this operation enhances its wear resistance.
Ti6Al4V does not markedly loose its toughness, elongation impact strength and ductility while increasing hardness and yield.

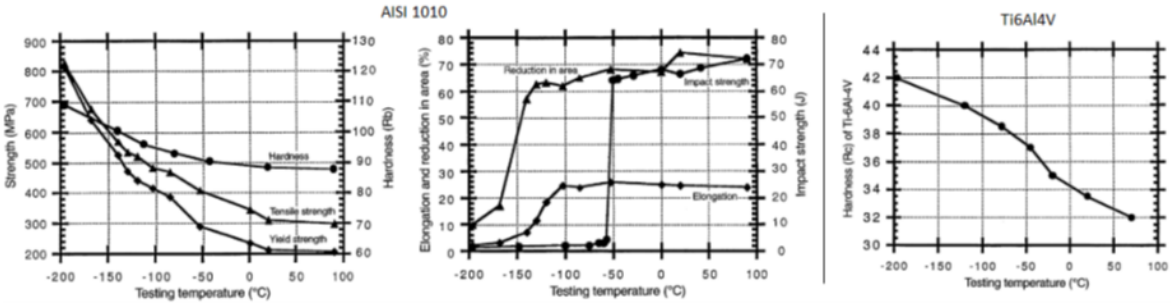

Figure 7.7: Different material's properties at low temperatures [49].

Cooling the workpiece is not the smartest idea for alloys that retain toughness and ductility at low temperatures, raising the shearing stress limits [118]. The position of nozzles for cryogenic cooling fluxes must be carefully tuned to avoid overhardening of the workpiece material. It would lead to higher forces and power, increased energy consumption (the more the consumption if production of cryo-fluids is considered), increased wear rate of the tool. A trade off must be achieved. For ductile, soft and low strength materials, cooling the work material would reduce the fracture strain, having better control in chip formation. These materials have generally a precise temperature of ductile to brittle transition (like glass temperature for polymers). Welding tendency and BUE formation can be suppressed by cryogenic cooling, [118]. However, cooling the piece in the wrong way will lead also to higher strength, therefore a "soft to cut material" such as aluminium would be unreasonably hardened. A smart approach is freezing locally the chip, to promote chip breakability without altering too much the properties of the workpiece. [59] suggests that among all possible benefits coming from the application of cryogenic machining, one of the most relevant is the enhancement of surface properties. With respect to dry conditions, deterioration of the tool (tool wear rate) was decreased for the majority of performed tests in the literature, resulting in better surface finishing for longer cutting time. This proved to be wrong for large grained workpieces overhardened by the coolant. Researchers

pointed out as well the reduction in chemical activity of piece and tool. Cryogenics can induce beneficial phase transformation, promote severe plastic deformation layers (SPD), high dislocation density and grain refinement, enhanced microhardness. Furthermore, it has been showed how the effect of low temperatures on the machined surface can induce improved compressive residual stresses, heightening fatigue life, stress corrosion resistance and pitting corrosion resistance. Performance characteristics include surface oxidation resistance and chemical reactivity, surface polarization and biological parameters such as cell attachment and proliferation. By the way literature gaps are evident in these particular topics, and taking into the account that in aerospace field the surface quality is regulated by strict and severe standards, these are fields to be better investigated and characterized to make cryogenic machining attractive for aerospace industry.

7.5. Applications of cryogenic machining

The adoption of cryogenic cooling strategies is simpler in case of turning operations, while it is much more delicate in case of milling. Lathes have the advantage of the presence of a fixed tool on which it is possible to deliver, through nozzles, the cryogenic fluid. This adduction may also happen with more sophisticated set-ups, for instance through small holes in the tool holder/on the cutting insert itself or also with properly shaped chip brakers and insert holders. On the contrary, the development of a delivery system on a rotating mill is more complicated [141][118]. To simplify this aspect many researchers have adopted external delivery systems.
One weakness of cryogenic milling is the interrupted nature of cutting. If coupled with a phase of heating of the inserts (cutting phase) and a sudden freezing (idle phase) it can lead to the brittle failures of the cutters under the thermo-mechanical stress. This problem could have been enhanced by the use of external nozzles which allow for low precision in targeting the heat generating zones, cooling too much the workpiece and the inserts, but unable to reach the rake and flank face during cutting. In other cases researchers used internal nozzles, carved into the spindle and holders, exiting directly at the inserts. As consequence, at industrial level the most diffused application is cryogenic turning and the most adopted cryogenic fluid is LN2 [118].

It is important to note that every effort in the delivery system design could be irrelevant if on the other side (tool geometry / material) there is not a comparable research work. The tool life achieved in turning experimental campaign, by now, have never been replicated in milling. Turning tools are bulky. Flank angles can be small as the roundness of the workpiece can avoid the flank face to rub the workpiece surface. In Milling, higher

flank angles are needed. Especially for solid mills, the reduced space and tolerances push in designing light geometries with sharper angles. At MUSP lab, Piacenza, Politecnico di Milano, has been formulated the hypothesis (after experimental findings) that largely positive rake angles are detrimental for cryogenic milling, the tool should be strengthened. Probably an excessive overhardening of the workpiece occurs, leading to higher forces. And also an excessive cooling of the tool is present, raising its hardness but lowering too much its toughness. The combination of milling strategy and insert shape also plays its role. For example, square shoulder inserts with small or null recline angles in wall milling are subjected to intense hammering action when approaching the cut. The whole insert edge is engaged at once, the engagement is sudden and not gradual. Moreover the square shoulder concentrates the load on a thin rake area. This rapid and cyclic mechanical load could be the explanation of the poor results obtained with square shoulder mills, under cryogenic cooling [131]. In [106] and [107] Sadik, adopting round shaped high feed inserts, obtained excellent results with LCO2 cooling, justifying it mainly thanks to the gradual engagement between the cutting profile and the material to remove.

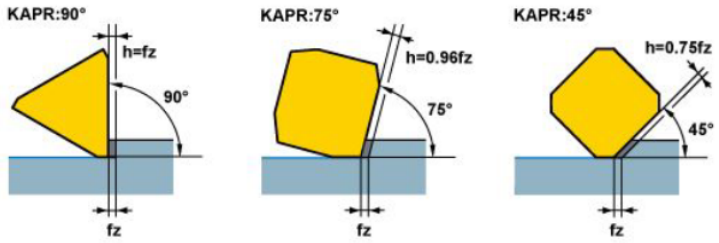

Figure 7.8: Shoulder angle variation in Milling.

The milling strategy can influence the thermal and mechanical load seen by the insert. In dry cutting, thermal loading is steeper for up milling, while it is more gradual for down milling [108]. On the other side, up milling generates smoother mechanical loads, due to the gradual increase of chip thickness from zero, while down milling generates impacts when the cut is engaged. For a deeper comprehension of the thermomechanical cycles on the inserts a comprehensive analysis of different strategies with different cooling strategies and different cutting parameters would be helpful, but it is not available in literature by now. The strategy should also be tuned on the material of interest, remember that up milling is not recommended for Ti6Al4V as the alloy has a strong tendency to refuse the cut, due to its strength coupled with a low elastic modulus.

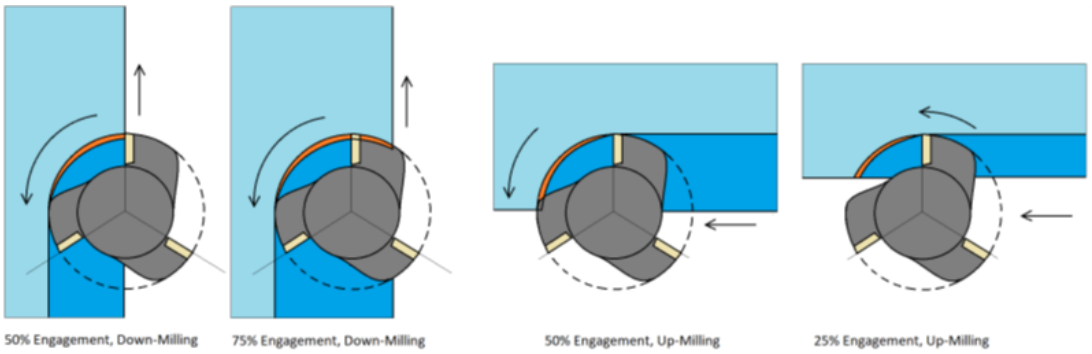

Figure 7.9: Milling engagement, Up and Down milling strategies (credit to L.Losa)

Even more complicated is the delivery of cryogenic fluid in case of drilling, where small holes able to bring the jet at liquid phase in the cutting zone should be performed inside the tool (EDM on tools' material is required).

7.6. Cryogenic parameters

One of the biggest problems affecting the available scientific literature about cryogenic machining is the absence of a detailed information about the strategy and parameters (pressure and mass flow rate) adopted in the adduction of the cryogenic fluid. In [83] for LN2 are reported 0.5÷3.5 [Kg/min] at a pressure ranging in between 1.4 and 24 [bar] and the most common combination is reported to be 1 [kg/min] at around 7.5÷15 [bar]. No relation with materials and nozzle apparatus is given. Slightly higher values are applied in milling with 4.5 [kg/min]. In [136] authors justify qualitatively the applied flow rate of Nitrogen by achieving stable flow and avoiding OH of the workpiece. For LCO2 the data are even more confusing. Fluid-dynamics flow properties such as pressure and flow rate are fundamental parameters in cryogenic machining. The absence of reliable data of that nature in many experimental trials, puts in doubt the reliability of entire works. For instance, cryogenic flow pressure determines the value of the jet speed while approaching the target, that is an indicator of the capacity in breaking the vapour cushion formed in the contact with the hot target. The flow rate primarily influences the fluid consumption which has a great impact on the sustainability of the cryogenic approach.
Regarding Liquid Nitrogen, measuring the flow quality at the nozzle is crucial. It is necessary to prefer having full fluid title at the exit of the final nozzle [102] as its conductivity is much higher than the one of the vapour phase and it is possible to exploit the latent heat of vaporization. Gaseous layers, if not broken by the liquid jet, are considered of insulating nature for the hot cutting zones. All the parameters inside the delivery circuit must be set with two goals: the first is to deliver a stable liquid jet, the second is to avoid

unnecessary waste of cryogenic fluid; thus a compromise should be found. Properties of Liquid and Gaseous Nitrogen are reported below [102].

Nitrogen Phase Properties					
	$T - [°C]$	$\rho - [kg/m^3]$	$c_p - [kJ/kg°K]$	$\mu - [Pa \cdot s]$	$\lambda - [W/m^2K]$
LN2	$-196°C$	803.6	2.046	$1.463 \cdot 10^{-4}$	0.132
GN2	$-196°C$	4.979	1.351	$0.05331 \cdot 10^{-4}$	0.0077

Table 7.1: Properties of Liquid and Gaseous Nitrogen

Liquid Nitrogen is purchased and delivered inside vacuum/insulated stainless steel tanks called dewars, containing up to 500 kg of liquid, kept at constant pressure with a valve that releases the evaporated fraction in the ambient air. The full content of a dewar, due to heat leaks of the tank, can evaporate in three days; for this reason it can not be stored in the shop floor and it must be used instantly.

The majority of LN2 is produced by "cryogenic distillation", in practice Nitrogen is taken from air and liquified. With the same process also medical liquid Oxygen is obtained. An alternative is the use of selective membranes to insulate only Nitrogen and the subsequent liquefaction. Liquid Carbon Dioxide is purchased in pressurized bottles, also grouped in pallets as the single bottle can hardly contain more than 50 kg of liquid. This also raises the importance of a smart and low consumption of the substance. Generally, high purity CO2 is available at high pressure in the liquid state for the food and beverage industries. Its cost is in most of the cases prohibitive for machining operations with the actual flow rates.

7.7. Cryogenic delivery systems

After the dewar, in order to deliver the LN2 toward the cutting zone at the liquid state, it is necessary to adopt a vacuum jacket tube. It is characterized by an inner flow of high pressure liquid nitrogen, an outer flow of low pressure evaporated nitrogen coming from a gas separator, an insulating vacuum tube and a reflecting material outside [83]. It is difficult to achieve low flow rates coupled with a stable flow. The evaporation of nitrogen in not only determined by heat leaks but also by the cavitation phenomena that may occur in presence of valves and bends present in the tubing system [129]. Reaching a stable flow is also time demanding, all the circuit has to reach a certain temperature

before the proper delivery of the fluid in a liquid state. During this time the flowing nitrogen is inevitably lost. It is also possible to install dedicated sub-coolers to reach rapidly the steady state flow, but they increase both the cost and the energy consumption of the equipment. It is important to optimize all the production routine and part programs of the machine tool before applying cryogenic cutting, to avoid expensive waste of LN2. The delivery system of LCO2 is less critical, it is basically composed by high pressure pipes that do not thermally affect the machine tool organs.

Indirect cooling, practical applications: in [137] Wang and colleagues develope a recirculating system made of copper, to cool down (internally) a tool for turning operations. The LN2 enters inside the tool from one tube near the tool tip, then with another tube is recirculated outside. Then with the addition of thermocouples they measure the temperature at a certain distance from the cutting zone (anyway representative of the peak temperature there) and compare it with dry cutting and wet cutting. Among the tested material there are also hard to cut materials as Ti and Ni alloys. In every tested case a significative temperature reduction is measured by the thermocouples in case of cryogenic cutting. The authors demonstrate a significant improvement in tool life with the cooling of the insert only.

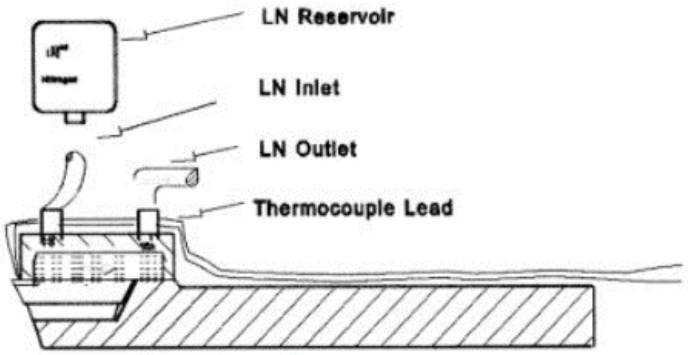

Figure 7.10: Indirect cooling of turning insert [137]

In [97] and [126] the authors develope an internal cooling system for milling tool, tested in wall operations at high depth of and small engagements. The results suggest that this strategy has not a beneficial effect on milling cutters' life if applied alone. On the contrary an evident tool life enhancement is reachable if coupled with minimum quantity lubrication (MQL) outside.

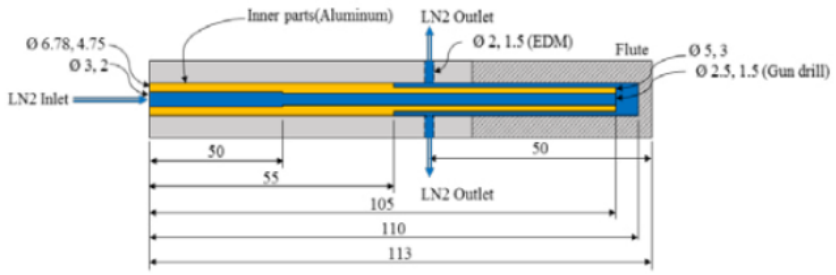

Figure 7.11: Internal cooled mill [97], [126]

Direct cooling, practical applications: this technique finds many more applications in literature. In [145] is presented a technique of double phase nitrogen spraying through external nozzles on the tool rake face. Compared to the conventional wet approach, the cryogenic one is able to improve the tool life and surface hardness for all the tested materials in these conditions, while the surface roughness is improved only in case of PM steels. No comparison between forces is provided in the above cited work.

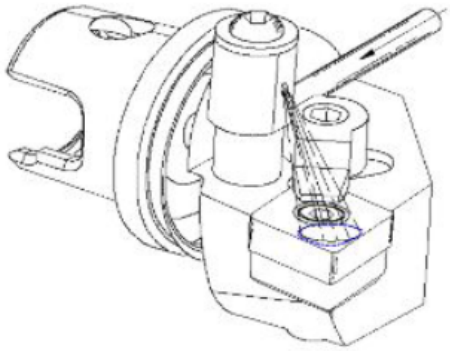

Figure 7.12: External nozzle delivery system [145].

In [31] the authors, using external nozzles, could not increase the tool life or reach an improved surface roughness while milling an hard to cut material as Inconel 718. In [12] the authors applied LN2 to rake and flank by a system of tool cap and copper nozzles.

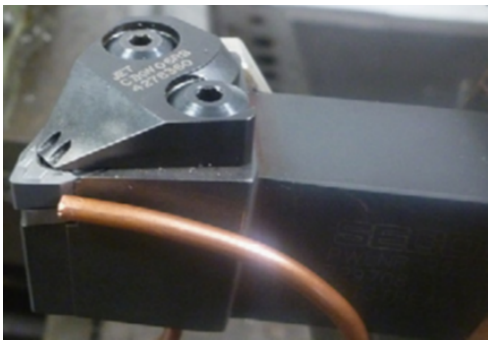

Figure 7.13: External delivery system adopted in [12].

Very interesting is the comparison between high pressure emulsion and LN2 with different nozzles' layouts made always by Bermingham in [13]. Their results underline that the most effective parameter on the tool life is not the cooling approach but the nozzle position. Best performances where achieved with design 3 for cryogenic cut and with designs 3/4 for high pressure emulsion. In those cases the nozzles orientation are parallel and opposite to chip flow on insert rake and nose. These findings underline that nozzles' positions and orientations must be carefully optimized looking at chip flow, and works in which these information are missing loose inevitably a part of their reliability.

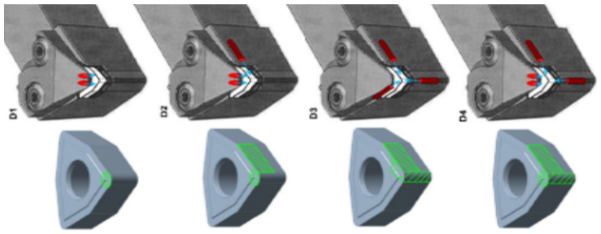

Figure 7.14: Nozzles' configurations adopted in [13].

Other alternatives are proposed in [125] with a modified holder designed to reach both the rake and the flank with LN2, and then also in [68] the liquid is sprayed in both the zones but with a different configuration (two copper nozzles).

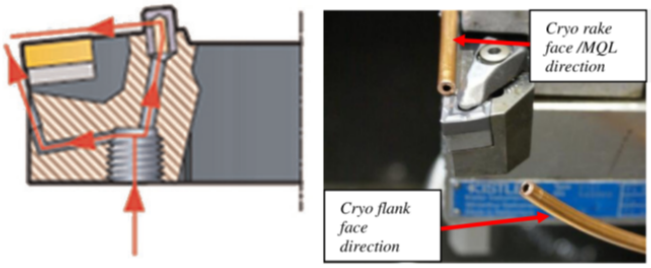

Figure 7.15: Flank/rake delivery [125], [68].

In [120] and [119] a static ring-nozzle for the LN2 delivery for milling operations is presented and tested on Ti6Al4V. Due to its bulkiness it is possible to adopt this system only for face milling applications, anyway in the tests reported it increases the tool life.

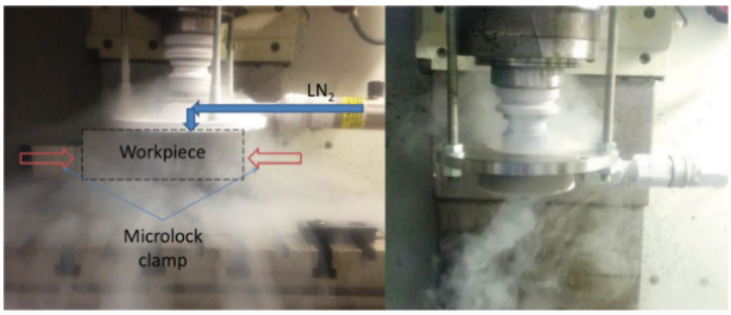

Figure 7.16: Ring-nozzle system for cryogenic milling [120], [119].

Direct localized delivery: in [48] and [52] Hong and colleagues show a patented project, that is one of the most advanced and sophisticated LN2 delivery systems available in literature. The cryogenic fluid passes through a particular chip breaker thanks to small channels obtained by EBM. LN2 exits in correspondence of the rake face. The same system can be designed also for the flank. Different configurations can be obtained playing on the number of holes in the breaker, micro grooves on the rake, flank delivery switching (on-off) and nozzles' orientation on the rake face.

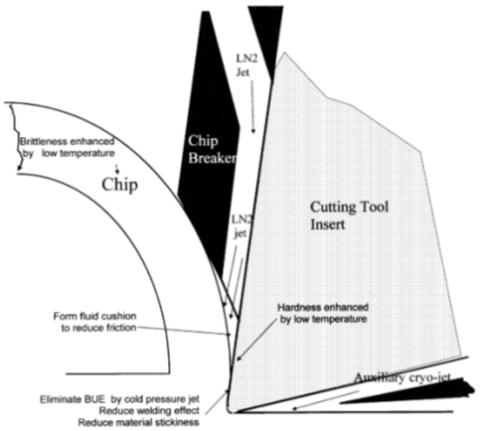

Figure 7.17: Chip breaker and micro-nozzles system [48], [52].

The aim is to cool down the zone affected by the highest temperature, because it is proven that in that specific zone of the rake face the crater wear is generated, approximately at a distance from the tip equal to the undeformed chip thickness. The chip breaker is able to lift up the chip helping the cryogenic flux to reach the most thermally stressed area.

The nitrogen in contact with the hot material evaporates, the expansion ratio from liquid to gas phase probably is the main help in reducing the friction, wear and heat build-up. After the optimization of the position of the chip-breaker for Ti6Al4V machining, the tool life is proved to be double in case of flank and rake jet activation. This configuration is so successful because it avoids the overhardening of the workpiece and reduces the thermal peak on the tool, without embrittle it. Many successive studies, primary with external fluid delivery characterized by poor or negative tool life enhancement, do not consider these important findings dated many years ago. Obviously, also this setup has its own weaknesses, firstly it is not flexible, in the sense that is not applicable with very different depth of cut. The tool's mounting and dismounting time and its production costs are not negligible.
In [47] it is illustrated the delivery of LN2 through an aluminium cap (by means of two grooves sealed with the insert), used to machine AISI 304 stainless steel and with the goal of minimizing the LN2 consumption. This kind of nozzles showed promising results both in terms of tool life and cryogenic fluid consumption. In particular in these articles, even if old with respect to the majority of literature regarding cryogenic machining, many crucial aspects are pointed out:

- Nozzle direction must be opposite to chip flow.
- Nozzles must be positioned as near as possible to their targets to achieve their maximum effectiveness.

In many works during the following decades these aspects are not taken into the account leading to poor results.

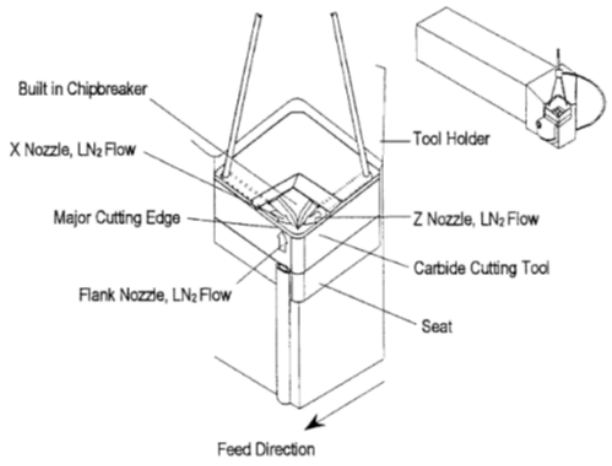

Figure 7.18: Nozzle cap delivery system [47].

In [29], thanks to EBM, little holes are made on the rake, primary and secondary flank

in order to deliver LN2 precisely in heat affected zones avoiding the overhardening of the material. The pressure level able to provide stable flow is 3 bar. The majority of the fluid is directed on the rake face, the remaining part goes on the flank. The system is proved to be good for cooling the insert and the cutting zone, avoiding overhardening of the workpiece at all speed thus achieving lower forces, decreasing flank and rake wear. Note that is an hybrid technique between direct and indirect colling of insert and cutting zone. It can benefit at the same time of cutting tool thermal evacuation and cutting zone temperature control.

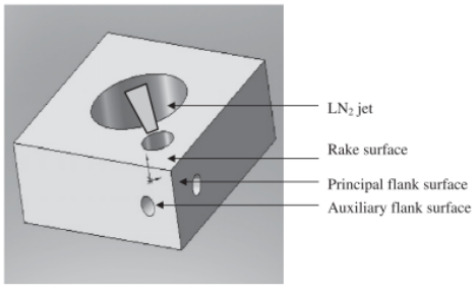

Figure 7.19: Hybrid direct/indirect cooling [29].

In [97] an internal LN2 delivery system for end-milling of Ti6Al4V is presented. The fluid is fed through the tool holder and ejected by small holes toward the tool-chip interface. The results are positive with indexable mill and low axial depth of cut. On the contrary they are poor in case of wall milling with high axial depth of cut and small radial engagement, due to the long tool-chip contact area which is hardly reachable by LN2. In these conditions, the mill exhibits severe adhesion. This phenomenon can be avoided with MQL.

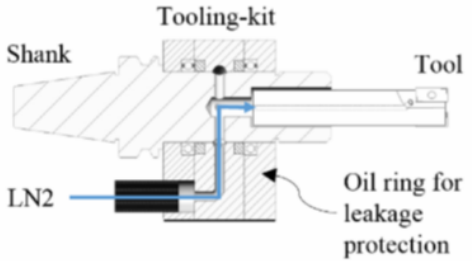

Figure 7.20: through tool holder delivery system [97].

In [107] is presented the delivery of LCO2 through channels in a tool holder provided by Sandvik (CoroMill 600-040Q16-12H) with four spherical inserts at a pressure of 50 bar

and variable flow rate of 0.15÷0.19÷0.64 kg/min, excellent results are obtained in this way.

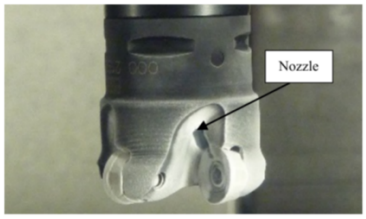

Figure 7.21: LCO2 through holder delivery [107].

In [37] is presented an internal CO2 delivering system for local spraying on milling inserts, during cutting of hard to cut materials. The only part that is modified is the tool holder without interfering with the interior of the spindle system. The cryogenic fluid is delivered at 50 bar.

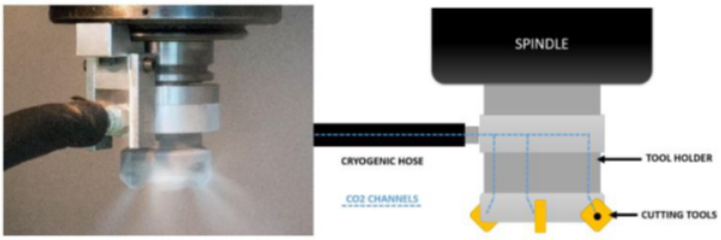

Figure 7.22: Internal CO2 delivery system [37].

8 | Energy Consumption Comparison

The adoption of a cryogenic cooling system in a machine tool allows the user to rid of all the pumps and auxiliaries connected to the conventional cutting fluid suction, recirculation, handling, adduction and so on. The energetic / power advantages of this choice must be evident in order to promote the cryogenic cutting as a strong alternative to conventional wet machining and to promote its diffusion in the industrial scenario pushed by an environmental conscious perspective. Anyway the theoretical advantages must be assessed in real applications and with different materials. In these sense a precious work performed by P.Albertelli [2] analyses in a rigorous way the energy consumption during Ti6Al4V milling, making a comparison (at different perspective levels) between operations with different cooling strategies. The results of the tests reported in the article shows that the cooling strategy strongly affects the cutting forces values, suggesting a possible energy saving at cutting process level adopting cryogenic milling since (as reported in the figure below) in cryogenic conditions the forces are the lowest registered.

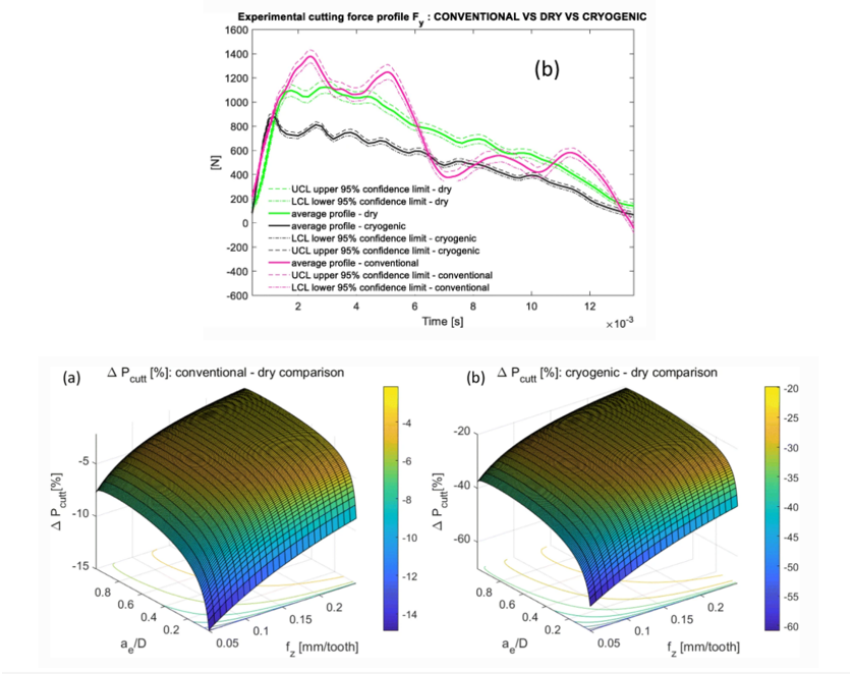

Figure 8.1: Cryogenic-dry-conventional cutting force comparison and cutting power assessment.

The expected cutting power saving (with respect to dry cutting) ranges from -20% to -60% depending on cutting parameters. The higher saving is in cryogenic cutting with low radial immersion and lower feed-rates (finishing operations). The minimum saving on the contrary is experienced with full engagement and high values of feed. In these conditions the tangential cutting force is dominated by the shear contribution linked to K_{tc} (refer to mechanistic force model). While reducing the feed and the radial depth of cut the friction contribution linked to K_{te} plays the main role, drastically decreasing the cutting power in comparison to dry cutting.

Passing to conventional-dry comparison, for rough milling the cutting power is comparable, while for finishing operations (lower feed and radial engagement), the conventional cutting is less energy demanding than dry cutting mainly thanks to lubrication effect (and lower K_{te}). From these results, focusing on power associated to cutting, cryogenic cutting seems the most sustainable cooling/lubricant solution. Looking at the same problem, but from the spindle point of view, the absorbed power is: $P_{\text{Spindle}} = P_{\text{mechanical,spindle}} + P_{\text{loss,spindle}}$

Where

$$P_{\text{mech,spindle}} = (\mu_s * \text{sign}(\omega_{\text{spindle}}) + \mu_v * \omega_{\text{spindle}} + J_{\text{spindle}} * \dot{\omega}_{\text{spindle}} + \text{Torque}_{\text{cut}}) * \omega_{\text{spindle}} =$$
$$= k_{t,\text{ spindle}} * i_{q-rms,\text{ spindle}} * \omega_{\text{spindle}}$$
$$P_{\text{loss,spindle}} = R_{\text{spindle}} * i_{q,\text{ spindle}}{}^2$$

And underlining the main process parameters

$$P_{\text{spindle},\,j}\left(v_c, \frac{a_e}{D}, f_z\right) =$$
$$= \omega_{\text{spindle}} * \left(\mu_s * \text{sign}(\omega_{\text{spindle}}) + \mu_v * \omega_{\text{spindle}} + \frac{P_{\text{cut},j}}{\omega_{\text{spindle}}}\right) + R_{\text{spindle}} *$$
$$* \left(\frac{\sqrt{2}}{K_{t,\text{ spindle}}} * \left(\mu_s * \text{sign}(\omega_{\text{spindle}}) + \mu_v * \omega_{\text{spindle}} + \frac{P_{\text{cut},j}}{\omega_{\text{spindle}}}\right)\right)^2$$

with μ_s = static friction [Nm], μ_v = viscous friction [Nm* s/rad], J_{spindle} = inertia [kg* m^2], $k_{t,\text{ spindle}}$ = torque constant [Nm/A$_{\text{rms}}$], R_{spindle} = phase resistance [Ω].
Then both cryogenic and conventional cooling strategies are compared to dry cutting in this way:

$$\Delta P_{\text{spindle,cryo/dry}}\,[\%]\left(v_c, \frac{a_e}{D}, f_z\right) = 100 * \left(\frac{P_{\text{spindle,cryo}}\left(v_c, \frac{a_e}{D}, f_z\right) - P_{\text{spindle,dry}}\left(v_c, \frac{a_e}{D}, f_z\right)}{P_{\text{spindle,dry}}\left(v_c, \frac{a_e}{D}, f_z\right)}\right)$$
$$\Delta P_{\text{spindle, conv /}dry}[\%]\left(v_c, \frac{a_e}{D}, f_z\right) = 100 * \left(\frac{P_{\text{spindle, conv}}\left(v_c, \frac{a_e}{D}, f_z\right) - P_{\text{spindle,dry}}\left(v_c, \frac{a_e}{D}, f_z\right)}{P_{\text{spindle,dry}}\left(v_c, \frac{a_e}{D}, f_z\right)}\right)$$

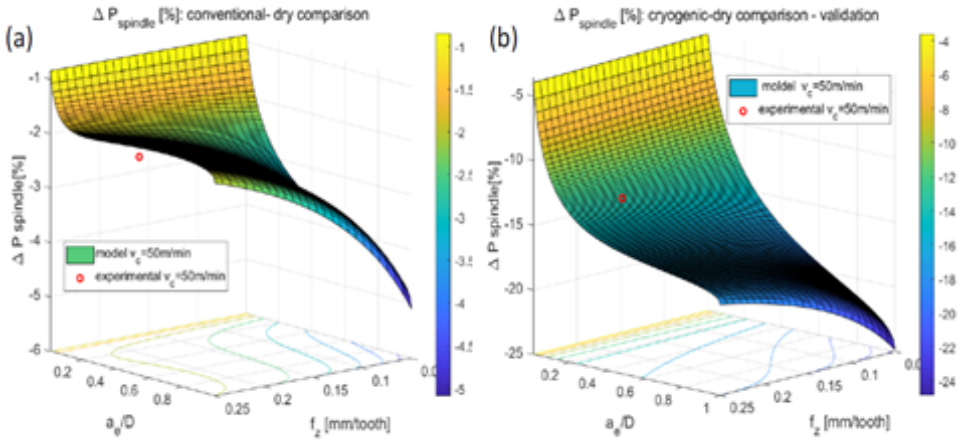

Figure 8.2: Conventional-dry comparison and cryogenic-dry comparison

Conventional cutting shows that spindle power consumption is similar to the one observed in dry cutting. Indeed, only slight differences in the order of -6% can be observed. On the other hand, cryogenic cutting remains particularly convenient especially for operations in which the tool is rather engaged in the workpiece. This matches the typical needs of applications like aerospace industry, where up to 90% of the material is removed from the blank workpiece by machining operations. For finishing operations, the energy savings with respect to conventional cooling are rather limited (less than 5%). Passing now to the Machine Level, as previously mentioned, some energy demanding auxiliary devices (like high pressure pumps or suction pumps) are removed in case of cryogenic (or dry) cutting. The power absorbed from the suction pump in conventional cutting is strictly bounded to the flow rate of lubricant delivered [l/min]. The average Power is:

$P_{\text{suct-av,conventional}}\ (Q_{\text{lube}}) = \frac{P_{\text{suct-on}} * \Delta t_{\text{on}}}{\Delta t_{\text{on}} + \Delta t_{\text{off}}}$[W],

$P_{\text{feed-suct,dry}} = P_{\text{feed-suct,cryo}} = 0$

where: $\Delta t_{on} = \frac{-V_{\text{tank,max}}}{Q_{lub} - Q_{\text{suct}}}$ and $\Delta t_{off} = \frac{V_{\text{tank,max}}}{Q_{lub}}$

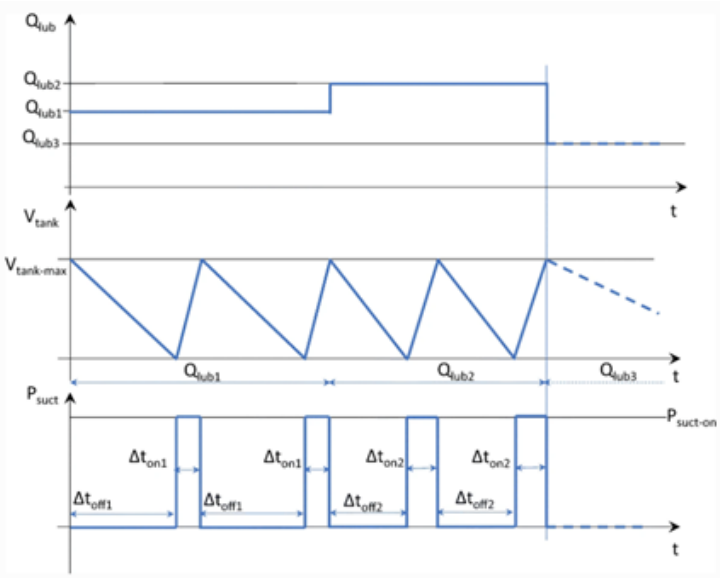

Figure 8.3: Suction pump behaviour.

$$\Delta P_{\text{feed, } j-dry}[\%] = 100 * \frac{(P_{\text{feed, } j} + P_{\text{spindle, } j}) - (P_{\text{spindle,dry }})}{P_{\text{spindle,dry}}}$$

$$\Delta P_{\text{feed,conv-dry }}[\%]\left(Q_{\text{lube }}, \bar{v}_c, \frac{a_e}{D}, f_z\right) =$$

$$= 100 * \frac{\left(P_{\text{feed,conv }}(Q_{\text{lub }}) + P_{\text{spindle,conv }}\left(\bar{v}_c, \frac{a_e}{D}, f_z\right)\right) - \left(P_{\text{spindle,dry }}\left(\bar{v}_c, \frac{a_e}{D}, f_z\right)\right)}{P_{\text{spindle,dry }}\left(\bar{v}_c, \frac{a_e}{D}, f_z\right)} \tag{8.1}$$

$$\Delta P_{\text{feed -suct,cryo-dry }}[\%]\left(\bar{v}_c, \frac{a_e}{D}, f_z\right) \equiv \Delta P_{\text{spindle,cryo-dry }}[\%]$$

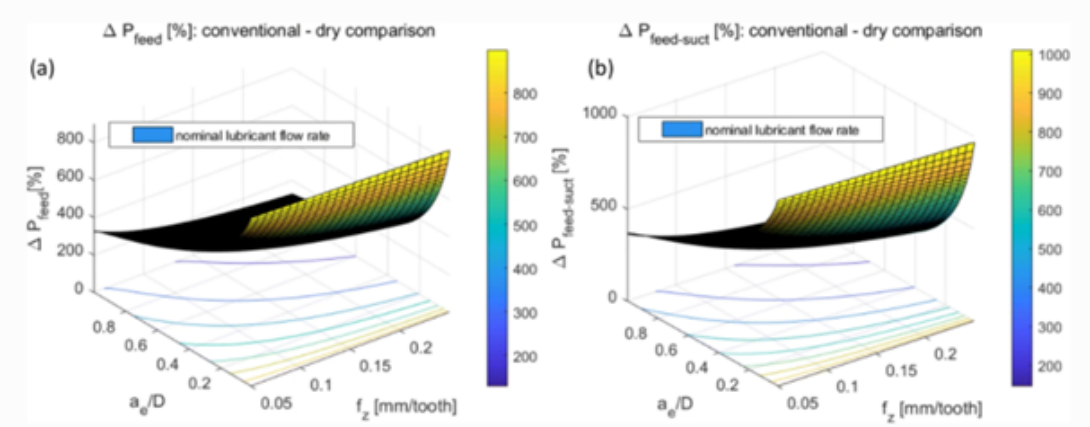

Figure 8.4: Power at the machine level (conventional-dry comparison), high-pressure pump and high-pressure and suction pumps (considering the nominal flow rate $\bar{Q}_{lub}$ and the nominal $\bar{v}_c$).

The high-pressure pump has a huge weight on the power consumption of the machine, (about 1312 W in nominal condition), while the power absorbed by the suction pump is quite limited (average of about 163 W). Even for roughing operations, the power percentage increment with respect to dry cutting is considerable (145%). Moreover, reducing $\bar{Q}_{lub}$ makes the conventional cutting even more power demanding (200% for roughing operations and 1387% for finishing operations). This result is really important if we consider the perspective of a manufacturing plant, indeed the energy saving with the adoption of cryogenic machining ranges from three times (in case of roughing operation) until peaks above eleven times (in case of finishing operation). So from this perspective the advantage would be double, on one side the absence of dangerous/unhealthy/pollutant fluids, and on the other side a considerable electrical energy saving.

The analysis can also be moved to an higher "global" level, taking into the account also

the energy required for the production of the lubricants in case of conventional cutting and of liquid nitrogen in case of cryogenic cutting. From this point of view it is necessary to add a new parameter called CED=cumulative energy demand, thus: $P_{\text{global}} = P_{\text{spindle}} + P_{\text{feed}} + P_{\text{suct}} + P_{CED}$ and the comparison is

$$\Delta \mathrm{P}_{\text{global. } j-dry}[\%] = 100 * \frac{(P_{\text{spindle, } j} + P_{\text{feed, } j} + P_{\text{suct },j} + P_{CED,j}) - (P_{\text{spindle,dry }})}{(P_{\text{spindle,dry }})}$$

In case of conventional-dry :

$$\Delta \mathrm{P}_{\text{global.conv-dry }}[\%]\left(V_{\text{lub }}, \bar{Q}_{\text{lub }}, \bar{v}_c, \frac{a_e}{D}, f_z\right) =$$
$$= 100*$$
$$* \frac{\left(P_{\text{spindle,conv }}\left(\bar{v}_c, \frac{a_e}{D}, f_z\right) + P_{feed-\text{ suct,conv }}\left(\bar{Q}_{lub}\right) + P_{CED,\text{ conv }}\left(V_{lub}\right)\right) - \left(P_{\text{spindle,dry }}\left(\bar{v}_c, \frac{a_e}{D}, f_z\right)\right)}{\left(P_{\text{spindle,dry }}\left(\bar{v}_c, \frac{a_e}{D}, f_z\right)\right)}$$

(8.2)

$$P_{CED,\text{ conv }}\left(V_{lub}\right) = \frac{\left(V_{H_2O*\rho_{H_2}O*CED_{H_2}O} + V_{\text{oil }} * \rho_{\text{oil }} * CED_{\text{oil }}\right)}{N_{\text{days / year }} * N_{\text{hours / day }} * 3600} \tag{8.3}$$

$V_{\mathrm{H_2O}}$ = consumption of water per year [l/ year], assumed equal to 7000l/ year in the analysis, $V_{\text{lub }} = V_{\mathrm{H_2O}} + V_{\mathrm{H_2O}}*$ conc and conc= concentration of oil in the lubricant, assumed equal to 12%, $\rho_{\text{oil }}$ = oil density = 0.82[kg/l].
$CED_{H_2O} = 0.00355$[MJ/kg], $CED_{\text{oil }} = 31.74$[MJ/kg].
In case of cryo-dry:

$$\Delta \mathrm{P}_{\text{global.cryo-dry }}[\%]\left(\dot{m}_{LN}, \bar{v}_c, \frac{a_e}{D}, f_z\right) =$$
$$=100 * \frac{\left(P_{\text{spindle,cryo }}\left(\bar{v}_c, \frac{a_e}{D}, f_z\right) + P_{CED,\text{ cryo }}\left(\dot{m}_{LN}\right)\right) - \left(P_{\text{spindle,dry }}\left(\bar{v}_c, \frac{a_e}{D}, f_z\right)\right)}{\left(P_{\text{spindle,dry }}\left(\bar{v}_c, \frac{a_e}{D}, f_z\right)\right)}$$

$$\text{With } P_{CED,cryo} = P_{CED,cryo}\left(\dot{m}_{LN}\right) = \frac{\dot{m}_{LN*CED_{LN}}}{3600}$$

$\overline{\dot{m}_{LN}} = 45$[kg/h] is the liquid nitrogen mass flow rate measured in the nominal condition of pressure (press = 3.5 bar). The energy required for the production of the liquid nitrogen was set equal to $CED_{LN} = 6.49$[MJ].
Note: the formulation does not consider the energy required for the lubricant disposal and the energy contribution linked to the production of the inserts that need to be substituted

when worn. It was assumed that the cutting performance, in terms of wear rate, are comparable in all the cases although a worse performance is expected for dry cutting. According to the literature, the comparison between conventional and cryogenic cutting in milling is often not in agreement.

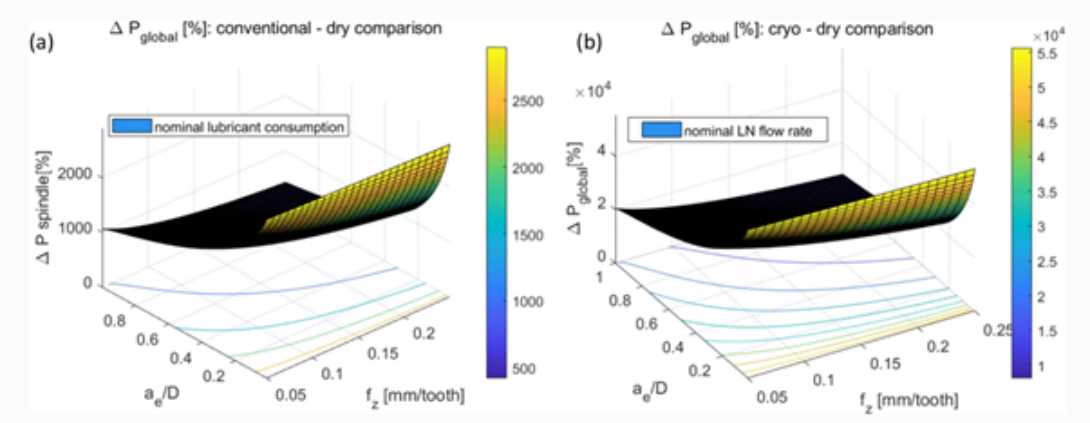

Figure 8.5: Global power assessment, conventional-dry and cryo-dry.

When the liquid nitrogen exits from the nozzles and touches the hot cutting region rapidly evaporates, obviously its recirculation and reutilization is not possible, increasing so its consumption. As consequence, for cryogenic cutting the involved global power, considering also the cumulative energy demand, is much higher than dry or conventional cutting (about 19 times greater than conventional cutting for finishing and up to 16 times in case of rough milling).

Note: this analysis takes into consideration the primary power consumption, but it is not focused on other environmental aspects like global warming, acidification, water usage, solid wasted nor energy used in the floods' disposal neither features linked to the quality of the processed parts.

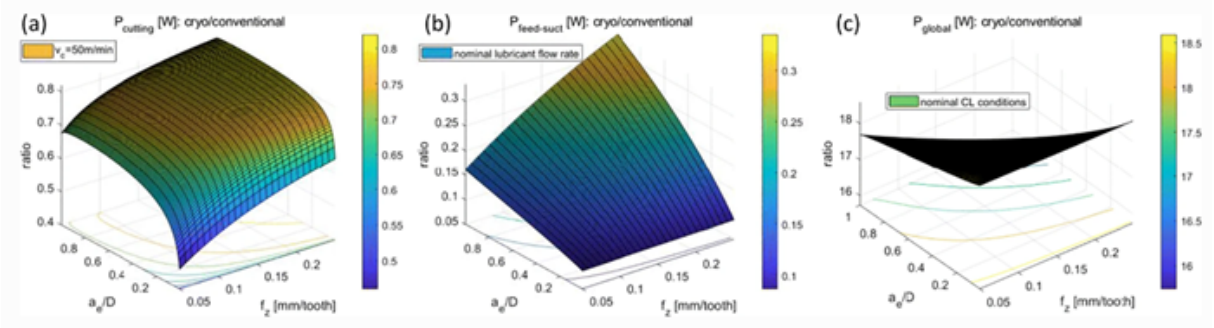

Figure 8.6: cryogenic cooling – conventional cooling comparison at different levels: (a) cutting power, (b) machine level, (c) primary power.

Since, as analysed in previous sections, dry cutting should not be considered as a valid alternative in case of Ti6Al4V machining, this last picture compares the two valid alternatives, cryogenic and conventional, summing up the considerations done before.

Concluding: the liquefaction of nitrogen is an energy demanding process; its advantages are consistent until machine level, while globally requested energy in cryogenic cutting is close to be from 16 to 19 times higher than in conventional cutting. In order to make cryogenic LN2 even more environmental compliant, research efforts should be addressed to improve the efficiency of the feeding system that should assure a stable flow even with low LN2 rates. A more localized action of the jets needs to be pursued to avoid any waste of nitrogen and to enhance the cutting performance in terms of tool life and MRR. At the same time the liquefaction process should be optimized, reducing its environmental impact.

9 | Cutting Force Models

9.1. Mechanistic model

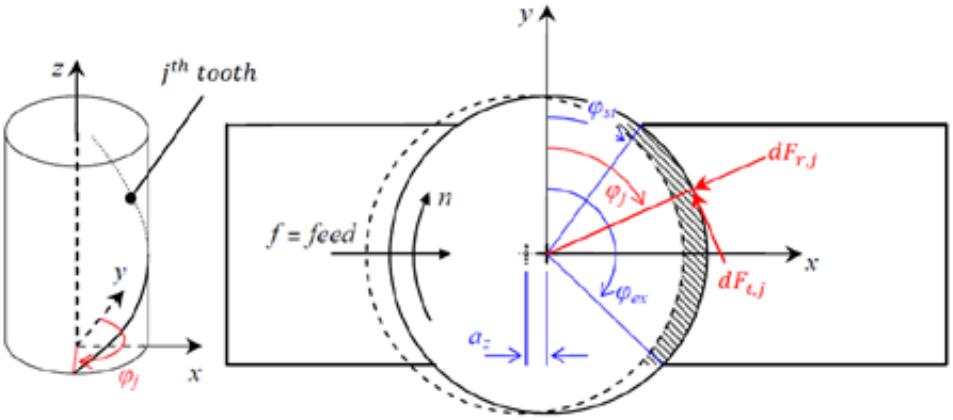

Figure 9.1: Geometric model of a milling operation.

Where:

φ_j = instantaneous angle of immersion of the j^{th} tooth [rad]$(j = 1, ..., Z)$, $\varphi_j(t) = \varphi_0 + \frac{2\pi}{N} \cdot (j-1) + \int_{t_0}^{t} 2\pi \cdot n\,(t')\,dt'$, φ_{st} = cutting entry angle [rad], φ_{ex} = cutting exit angle [rad], Z = number of teeth of the tool, f = feed [mm/ round], n = rotational speed of the spindle [rpm] = $\frac{\omega_T}{z} * 60$, ω_T = tooth passing frequency [Hz], $a_z = f_z$ = feed rate $\left[\frac{mm}{\text{tooth} * \text{round}}\right]$.

It is possible to distinguish three (tangential, radial and axial) different contributions to the cutting forces:

$$\begin{cases} dF_{t,j} = dF_{t,j}(\varphi) = [K_{tc} * h_j(\varphi) + K_{te}] * dz \\ dF_{r,j} = dF_{r,j}(\varphi) = [K_{rc} * h_j(\varphi) + K_{re}] * dz \\ dF_{a,j} = dF_{a,j}(\varphi) = [K_{ac} * h_j(\varphi) + K_{ae}] * dz \end{cases}$$

(e stands for "edge contribution, c for "cut contribution") so: K_{tc} = cutting coefficient in tangential direction K_{rc} = cutting coefficient in radial direction, K_{ac} = cutting coefficient in axial direction, K_{te} = edge coefficient in tangential direction, K_{re} = edge coefficient in radial direction, K_{ae} = edge coefficient in axial direction.
The force components are function of the chip section $A(t) = a_p * h_j(t)$ through the uncut chip thickness $h_j(t)$ that is not a constant value. It depends on $\varphi_j(t)$ function of time.

$$h_j(t) = a_z * \sin\varphi_j(t) \rightarrow h_j(t) = h_j(\varphi(t))$$

So it is possible to express the chip section as $A(t) = a_p*(a_z * \sin\varphi_j(t)) = a_p*a_z*\sin\varphi_j(t)$. Following the mathematical steps explained by Y.Altintas in "Manufacturing Automation: Metal Cutting Mechanics, Machine Tool Vibrations, and CNC Design" [60] the cutting forces in X,Y,Z directions will be:

$$\begin{aligned}
\bar{F}_x &= \left\{ \begin{array}{c} \frac{N*a_p*a_z}{8\pi}\left[K_{tc}*\cos(2\varphi) - K_{rc}*(2\varphi - \sin(2\varphi))\right] + \\ +\frac{N*a_p}{2\pi} * \left[-K_{te}*\sin(\varphi) + K_{re}*\cos(2\varphi)\right] \end{array} \right\}_{\varphi_{st}}^{\varphi_{ex}} \\
\bar{F}_y &= \left\{ \begin{array}{c} \frac{N*a_p*a_z}{8\pi}\left[K_{tc}*(2\varphi - \sin(2\varphi)) + K_{rc}*\cos(2\varphi)\right] - \\ +\frac{N*a_p}{2\pi} * \left[+K_{te}*\cos(\varphi) + K_{re}*\sin(2\varphi)\right] \end{array} \right\}_{\varphi_{st}} \\
\bar{F}_z &= \left\{ \frac{N*a_p}{2\pi} * \left[-K_{ac}*a_z*\cos(\varphi) + K_{ae}*\varphi\right] \right\}_{\varphi_{st}}^{\varphi_{ex}}
\end{aligned} \tag{9.1}$$

While instantaneously holds:

$$\left\{ \begin{array}{l} F_x(t) = \sum_{j=1}^{N} g_j(t)\left[-F_{t,j}(t) * \cos\left(\varphi_j(t)\right) - F_{r,j}(t) * \sin\left(\varphi_j(t)\right)\right] \\ F_y(t) = \sum_{j=1}^{N} g_j(t)\left[F_{t,j}(t) * \sin\left(\varphi_j(t)\right) - F_{r,j}(t) * \cos\left(\varphi_j(t)\right)\right] \end{array} \right.$$

9.2. Square Shoulder Mills vs High-Feed Mills

Figure 9.2: square shoulder mill example

As pointed out in the figure above, square shoulder mills are characterized by a lead angle of 90°. With this configuration, in order to achieve high material removal rates the key parameter is the axial depth of cut since the feed is limited to a few tenths of a millimeter per tooth at every rotation.

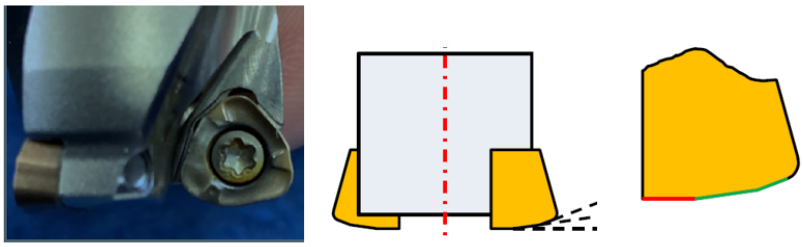

Figure 9.3: Example of high-feed mill and details on the cutter.

The high feed mills are characterized by two different values of lead angle in the cutting edge, resulting in a minor edge (red line) and a double phased cutting edge (green line). The maximum depth of cut is limited, but in order to achieve considerable material removal rates it is possible to increase the feed per tooth at every rotation. The peculiar geometrical configuration modifies the force profiles during the cut. The chip thickness and the maximum chip thickness are reduced, the high radial force typical of square shoulder mills is split in a radial part plus an axial part. The axial contribution is not critical for the process because the system in that direction is way stiffer than in other directions. The main cutting forces act in the lower part of the cutting edge. For this reason, the angle of cutting forces at a large radius is closer to the spindle axis. This distance is smaller than for the tools that have a small shape radius.

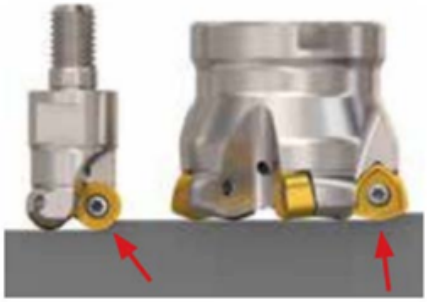

Figure 9.4: Comparison between forces' direction.

Referring to the figure representative of the mechanistic force model, in reality the trajectory followed by the insert is a cycloid, but in case of small feed per tooth its approximation with a series of consequent circumferences is correct.

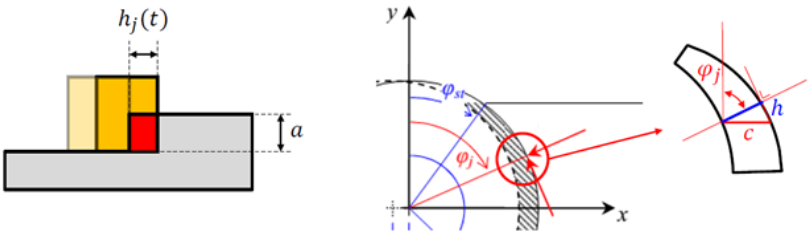

Figure 9.5: Chip section approximation in case of square shoulder milling.

Another approximation that holds in square shoulder milling is that the chip thickness is proportional to the feed per tooth through the sine of the angular position of the tooth. The mechanistic force model is based on these assumptions and it is not applicable in case of high feed mills since the chip section is completely different.

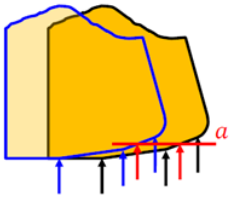

Figure 9.6: Two subsequent teeth marked with different colours (blue lines=previous insert, black lines=actual insert, red lines=intersections of axial depth of cut with two inserts).

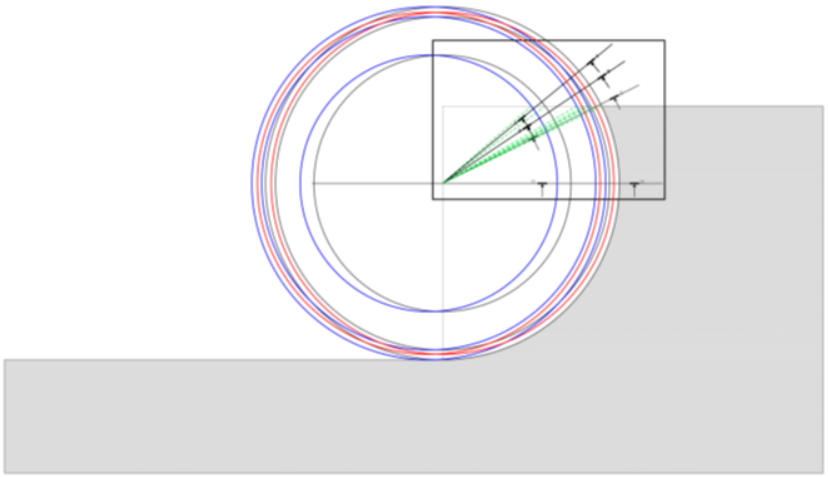

Figure 9.7: Evolution in time of the positions of the points evidenced by black, blue and red arrows in figure 9.6

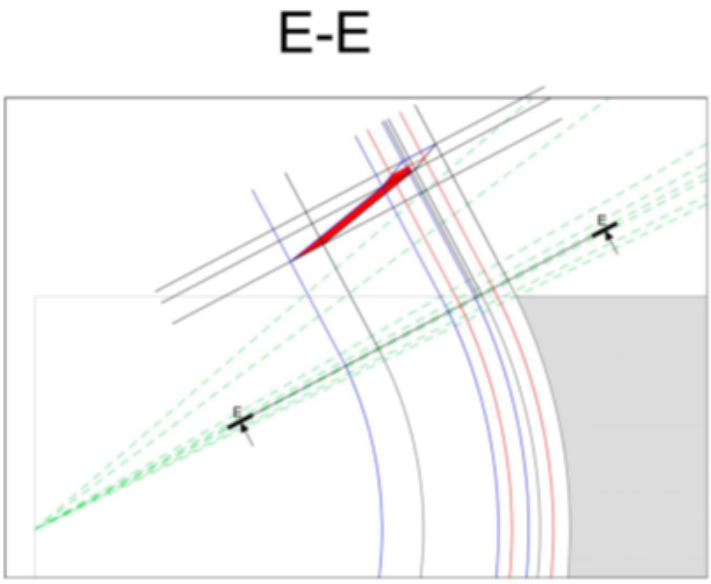

Figure 9.8: Chip section with high feed milling.

It is possible to integrate along the cutting edge the infinitesimal contributions of the forces in radial and tangential directions.

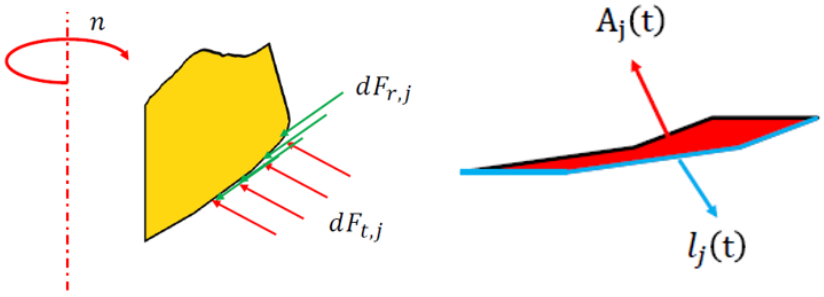

Figure 9.9: Infinitesimal forces acting on the cutting edge and chip area.

The infinitesimal forces in radial and tangential directions are functions of the z coordinates and they depend on the chip thickness at the selected coordinate and on the chip height at the selected coordinate, adding also the friction contributions the integration follows, the steps are reported below:

$$dF_{t,j}(\varphi_j, z) = K_{t,c} * h(\varphi_j, z) * dz + K_{t,e} * dl_j * (\varphi_j, z)$$
$$dF_{r,j}(\varphi_j, z) = K_{r,c} * h(\varphi_j, z) * dz + K_{r,e} * dl_j * (\varphi_j, z)$$

Integrating:

$$F_{t,j}(t) = \int_0^a K_{t,c} * h(\varphi_j, z) * dz + \int_0^a K_{t,e} * dl_j * (\varphi_j, z) =$$
$$= K_{t,c} * A_j(t) + K_{t,e} * l_j(t)$$
$$F_{r,j}(t) = \int_0^a K_{r,c} * h(\varphi_j, z) * dz + \int_0^a K_{r,e} * dl_j * (\varphi_j, z) =$$
$$= K_{r,c} * A_j(t) + K_{r,e} * l_j(t)$$

Referring to the section E-E highlighted above, one example can be:

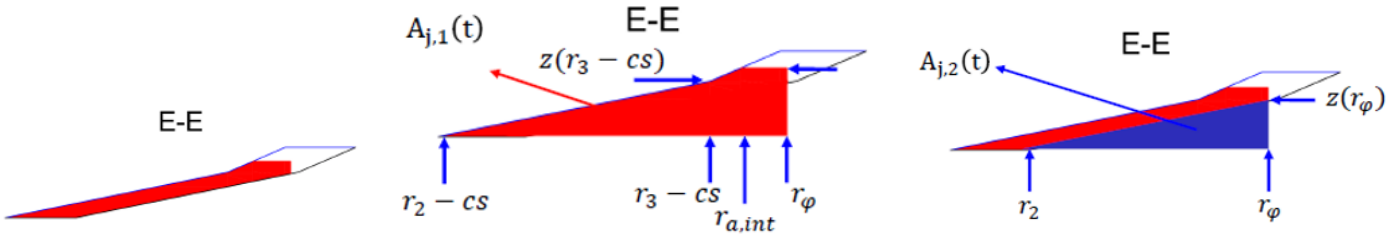

Figure 9.10: Example of high feed chip section calculation.

$$
\begin{aligned}
&A_j(t) = A_{j,1}(t) - A_{j,2}(t) \\
&A_{j,1}(t) = \frac{1}{2} * z\,(r_3 - cs) * (r_3 - r_2) + \\
&+ \frac{1}{2} * (z\,(r_3 - cs) + a) * (r_{a,int} - (r_3 - cs)) + \\
&+ a\,(r_\varphi - r_{a,int}) \\
&A_{j,2}(t) = \frac{1}{2} * z\,(r_\varphi) * (r_\varphi - r_2)
\end{aligned}
\tag{9.2}
$$

In milling machines / machining centres of recent production, with the suitable tools, it is possible to work in high feed conditions, in which small depths of cut are allowed in conjunction with high feed per tooth [32]. The maximum depth of cut rarely overcomes 2 mm, while the feed per tooth may also reach values in the order of 4 mm/tooth [33] (obviously depending on the machined material).

The basic advantages of high feed machining are:

- No requirement of high spindle speed
- Axial direction of cutting forces to the spindle
- Reduction of vibrations
- Enhanced stability of the working process
- Improved tool life
- Creation of clear shapes that do not require the semi-clear machining

9.3. High feed and cryogenic milling

Scientific literature about cryogenic cutting presents many gaps that must be covered if the aim is the promotion of this technology among the industrial scenarios. One of these gaps is represented by the lack of statistically reliable studies regarding the performances of cryogenic milling operations and the comparison between cryogenic and conventional (wet) milling. The work [3] by Albertelli et al. tries to cover this gap proposing the results of an experimental campaign that compares the life of an high feed mill at different cutting speeds, in cryogenic and wet conditions taking as tool life indicator the value (mean or maximum) of the flank wear VB. The adopted tool is characterized by nominal diameter D=20 [mm], number of inserts Z=3 (carbide substrate and PVD coating characterized

by an Al-rich (Al,Ti)N single layer). The operation is characterized by fixed axial engagement a_p=0.4 [mm], fixed radial engagement a_e=13 [mm], fixed feed per tooth f_z=0.7 [mm/rev*tooth] and variable cutting speed V_c= 50÷70÷125 [m/min]. The mass flow rate of cryogenic fluid (LN2) is measured $\dot{m}_{LN} = 45[$ kg, while the lubricant (obtained mixing water with a synthetic metalworking fluid with a volume ratio of 12%) has a mass flow rate of $\dot{m}_{lub} = 2770[$ kg/h].

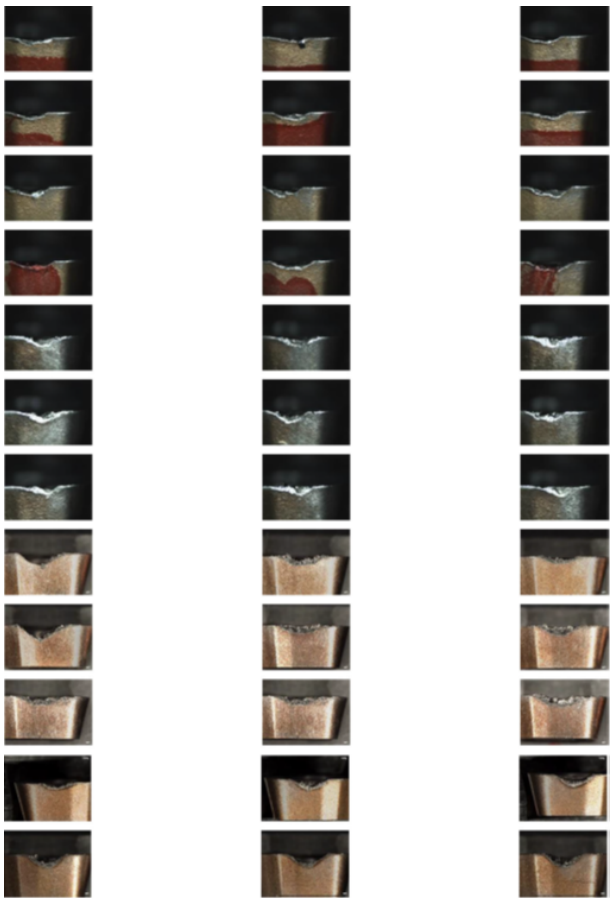

Figure 9.11: Worn out inserts.

Thirty-six inserts are taken to end of life and after the evaluation of Taylor's coefficients and statistical considerations the findings are: at low cutting speeds, for cryogenic milling, an adhesion phenomenon is clearly visible (assimilable to the built-up edge that typically occurs when the set cutting speed is too low). This phenomenology tends to decrease at higher velocity. It can be concluded that cryogenic cooling seems very promising, with respect to conventional cooling, in highspeed Ti6Al4V cutting. This cooling technology would assure an enhancement of the cutting performance (increasing the material removal rate through cutting velocity increment) without a detrimental effect on the life of the tool. At 125 [m/min], the tool averagely lasted more than 15 minutes that is reasonable

even from the industrial perspective. At lower speeds, adhesion-like phenomenon can be observed. This probably causes a chipping effect especially at low cutting velocity. Conventional cooling assures higher tool duration at low cutting speeds. The flank wear is regular in this case. At high cutting velocity, the tool durations are more similar. Moreover, the identified models show that at higher velocities it is expected better performance for the cryogenic cooling approach. This duration can even be feasible for the shop floor scenario (time to change the tool). These findings suggest also that high feed milling is suitable for cryogenic refrigeration. The same can not be stated for square shoulder milling, in facts different studies show that this approach, in cryogenic condition, can also shorten the life of the tool making it not attractive in large scale applications.

10 | Machining Simulations

In the last two decades the availability of computational tools for engineering applications has grown exponentially. The machine tools' field has been revolutionized under many points of view, mainly thanks to the boost given by new software solutions. Nowadays, for instance, machine tools manufacturers rely on software able to simulate simultaneously all the components' and fields' behaviour before the production of the machines themselves, reducing at the minimum the time and economical impact of design issues. With the creation of digital twins of the machines it is possible to reach the virtual commissioning of such complex mechatronic systems, maximizing the customization level, the reliability of the product and the satisfaction of the customers. New machines are equipped with a rising number of sensors, from their outputs it is possible to monitor online the health of the components of the machine (and its auxiliaries) and the quality of the manufactured pieces, and also to enhance the safety of the machines. Nowadays machine tools' users can exploit advanced Computer Aided Design and Computer Aided Manufacturing systems (CAD/CAM) to design and manufacture their products, simulating the production routine from the raw material to the finished workpieces, reducing at the minimum time and costs of the production cycle.

Digitalization, Industry 4.0, Internet of Things (IT) have become key words for every industry involved in the machine tools' world, from the machine builder to the final user. Every player involved in this chain must follow this revolution to stay competitive on the market today and in the future.

It is then reasonable to assess that the new-coming industrial revolution will be the environmentally conscious one, adding complexity and need of new competences in the industrial scenario. Following this trend, it is important to find new and less impacting manufacturing techniques compared to the one used today. The cryogenic machining is one of the most promising in this sense.

Is it possible to implement a reliable simulation of it ? Dealing with cryogenic processes an high number of process variables must be calibrated/optimized. Added to the classic process parameters of feed, speed, depth of cut, cutting angles, number of teeth, strategy and so on. In cryogenic processes are also needed the flow rates, pressure, nozzles' position,

orientation, diameter, number, cooling flux nature, cooling strategy. Dealing with hard to cut materials and super alloys like Ti, Ni, Co, Mg, Al alloys, stainless steels, tool-steels modelling becomes fundamental because it can reduce the number of necessary cutting trials and also helps in understanding the critical issues of the process with the aim of finding a solution.
In literature it is possible to find Regression Modelling, Response Surface Methodology, Artificial Neural Networks and Genetic Algorithms applied to cryogenic machining for evaluating principally tool life and surface finish. Finite element simulations in this filed have been applied manly for the calculation of stresses and strains in the cutting zone or on the cutting tool, temperatures, forces and powers. In general this method is the most promising for the estimation of:

1. Cutting forces (useful also to calculate torques, powers, energy consumption and to make predictions on the dynamic response of the machines).
2. Chip morphology (useful in a preliminary phase to assess the goodness of material and contact models, then useful to understand stresses-strains, strain rates, tool-chip interactions. All elements needed for predictions on wear phenomena).
3. Tool wear (through values of the thermal and mechanical stresses it is possible to understand where the wear phenomenon is likely to appear and how severe it will be).
4. Surface quality (grain size, hardness, phase changes, roughness, deformation layers, residual stresses are quantities that can already be forecasted by tuning the models with experimental data and by the modification of material constitutive models).

In order to obtain reliable results, materials' properties, contact and thermal interaction properties are needed. It is important to underline the necessity of a good material model, able to represent with accuracy the strain, strain rate and thermal effect on the stress flow. To deeply understand the cryogenic cutting topic, a multidisciplinary knowledge is mandatory. A crucial role is played by the thermodynamics of the process, in this field once again simulation tools are precious. For example, through Computational Fluid Dynamics (CFD) it is possible to analyse the problem and find optimal solutions for the nozzle design, hybrid thermodynamic-CFD simulations are needed to forecast heat transfer coefficients of fluxes so to predict characteristics of the flow to be delivered at the cutting zone. These data are fundamental for a correct calibration of the FEM models.

10.1. Tribology

With this term it is possible to indicate the science and engineering that study interacting surfaces in relative motion. It includes the study and application of the principles of friction, lubrication and wear. If the material model influences cutting forces and chip morphology, the contact properties influence the temperature build up and tool wear. Material model and contact model represent a source of uncertainty, they are strictly bounded in a FEM simulation in the sense that it is not possible to definitively separate their contributions. Only in presence of an accurate material model with all possible strains and strain rates, it would be possible to isolate the contribution of the contact model alone. In the last decades friction was modelled as a simple slide/stick model, then most sophisticated contact formulations have been developed but they did not provide the hoped results, mainly due to the fact discussed above.

10.2. Contact Models

$F_f = \mu * F_n$ is the formula to compute the friction force in case of Coulomb friction. It is the most common formulation used for solid friction. Between the two bodies in contact is present a force proportional to the normal reaction between them. However it is completely neglected the possible modification of the actual force in case of deformation of the bodies. In this case the Tresca friction model is used: $\tau_f = m * \tau_{lim}$, where m is a coefficient and τ_{lim} is the shear stress limit. FEM software usually combine the two models, implementing a slide/stick contact model where:

$$\tau_f = \begin{cases} \mu * \sigma_n \text{ if } \mu * \sigma_n < m * \tau_{\text{lim}} \\ m * \tau_{\text{lim}} \text{ if } \mu * \sigma_n > m * \tau_{\text{lim}} \end{cases}$$

limiting the possibility of the coulomb friction to overcome the shear stress limit of the material.

In [88] it is possible to find an example of contact behaviour modelled as temperature dependent. Friction depends by the average temperature of the contact interface $\mu = \mu\left(\bar{T}_{int}\right)$, so pressure and sliding speed can modify (indirectly) the friction behaviour as they modify the temperature. The interface temperature is obtained analytically, through an approximated model. The coefficient μ is obtained by fitting experimental data. The final data tell that apart from a little shift at high feed, the model can accurately estimate feed and cutting forces. The authors, after the validation of the model,

studied the speed-feed sensitivity. Higher values of feed and speed lead to an increment of temperature and a reduction of friction. Positive rake angles lead to lower temperatures and higher friction coefficients, lower forces and contact lengths.

In [92] Ozel and colleagues analysed the influence of friction models on the results of cutting simulations (orthogonal cutting of low carbon steel). The best way to describe the contact behaviour of tool and chip is directly measuring the stresses, for example by split-tool techniques. The best situation would be to consider the actual shear stress limit as dependent on the material flow stress $\bar{\tau} = \frac{\bar{\sigma}}{\sqrt{3}}$. In order to overcome the problem of sharp variations between Shirakashi's friction model and Dirikolu's friction model

$$\tau_f = k\left(1 - e^{-\frac{\mu\sigma_n}{k}}\right)$$

with k=material's limit shear stress (Shirakashi)

$$\tau_f = m * k * \left(1 - e^{-\left(\frac{\mu\sigma_n}{m*k}\right)^n}\right)^{1/n}$$

with n coefficients, 0<m<1(Dirikolu)

other models are developed: 1) constant shear friction, 2) constant shear and friction regions (Coulomb-Tresca), 3) variable shear friction as Dirikolu, 4) variable friction depending on normal stress from split tool techniques, 5) variable shear plus variable friction with given predetermined lengths. The results of orthogonal cutting simulations adopting different models are compared. Model 3) and 4) gives the best prediction of feed force, temperature and shear plane angle at 50,150,250 m/min. However, cutting force is clearly overestimated, probably due to the low accuracy in the material model in case of thermal softening of the material.

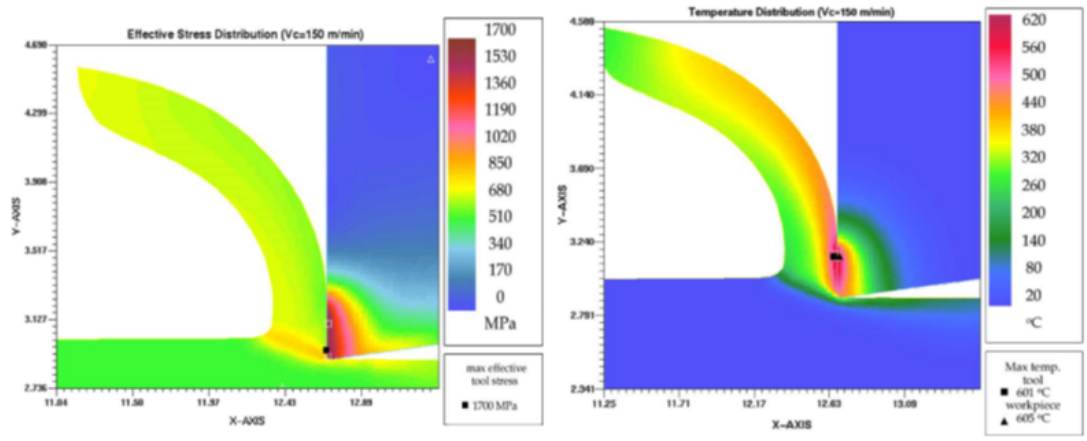

Figure 10.1: Simulation of model number3, effective stress and temperature visualization [92].

In [38], during cutting simulations, different friction models are tested:
Constant shear friction, constant Coulomb friction, Coulomb-Tresca mixed model with constant coefficients (with and without predefined sticking length) and Dirikolu's model. In general feed force and chip thickness are underestimated, while shear angle is overestimated and there is no friction model that influences much the results. The conductance value is iteratively adjusted comparing the temperature filed on the tool with experimental data, with this method for some friction model it is possible to reach a convergence of T, with others not. Probably a new friction and conductance model is needed, but the most important factor is the material model, fundamental in order to fit a good friction model.
In [43] there is another comparison between friction models, for AISI 4140. They underline how previous studies found the friction stress to be almost constant for half of the tool-chip contact length, then decreasing to zero and the shear friction limit depends on the material flow stress. The simulations consist in a predefined chip free to evolve to the final shape. Constant Coulomb model, two zone constant Coulomb friction, shear limit and Coulomb friction and three new temperature dependent friction models are tested:

- Temperature dependent friction model: $\mu(T) = \begin{cases} 1 & T < T_1 = 625°C \\ 1 - \frac{T-T_1}{T_m-T_1} & T_1 < T < T_m \end{cases}$

- Temperature dependent shear stress limit, depending on yield, plus constant friction coefficient: $\tau_{lim}(T) = \sigma_y(T), \quad \tau_f = \begin{cases} \mu\sigma_n & \mu\sigma_n < \tau_{lim}(T) \\ \tau_{lim}(T) & \mu\sigma_n > \tau_{lim}(T) \end{cases}$

- Temperature dependent friction coefficient plus constant shear limit: $\mu(T) = f(T)$,

$$\tau_f = \begin{cases} \mu(T)\sigma_n & \mu(T)\sigma_n < \tau_{lim} \\ \tau_{lim} & \mu(T)\sigma_n > \tau_{lim} \end{cases}$$

Cutting forces and feed forces are well estimated by the double Coulomb model, and note that the Chip thickness is guessed by all models. This confirms the findings of [38], that the chip thickness depends more on the material model than the friction conditions. In [114], contact phenomena between tool and chip are analysed, considering both friction and thermal aspects. The interface conductance is set to non-physical large values (as commonly done in cutting simulations) in order to reach thermal convergence in the cutting zone during the cutting time (few milliseconds). But the conductance depends on the contact nature and influences the thermal profile of the interface. A complex micro-mechanical friction model is implemented to predict he interface conductance. For the friction coefficient a normal pressure distribution and the Shirakashi model is adopted. Unless the deep effort spent in the elaboration of the model, the results are almost the same of a simple constant Tresca Model with m=0.9. This article underlines that the effect of the friction models is marginal, and it is worth spending more effort in the material model definition than in the contact/friction one.
In [5], the performance of different friction models in orthogonal cutting simulations is analysed (material = AISI 4340). The authors vary the shear limit stress of the Tresca shear friction model from 200 to 700 MPa. For the sliding region μ=0.48 is used, then when the shear stress reaches the limit it becomes constant, being illogically for it to go beyond the strength of the material. Better force predictions are obtained larger shear limit factors. All the models predict the pressure on the rake in the same way. The authors suggest that the limit shear stress can also be calculated with the material model, depending on temperature, strain and strain rates. A shear flow limit of 400 MPa, in agreement with the limit flow stress for good prediction of forces, is obtained with T=1000°C, $\varepsilon = 4, \dot{\varepsilon} = 10^5$. In conclusion, stick and slip models are more accurate, but the shear limit must depend on the material model.

In [86] and [87] Molinari and colleagues analyse the contact characteristics for orthogonal cutting. These works are an example on how to combine analytic and numeric methods to understand complex phenomena. The authors, with simulations and analytical models show how the friction becomes gradually sticking while increasing the cutting speed due to the decrease of the material flow stress at higher temperatures. The mean friction coefficient on the rake decreases evidently only if sticking is present because the temperature decreases the flow stress. Sticking contact is favoured by larger friction coefficients, for low friction coefficients the shear stress is not higher than the shear flow stress of the material, so sticking is not activated. Temperature rises in the sticking region, it reaches a

peak in the transition region and gets lower in the sliding region, as a result of the mutual effect of deformation heat, friction heat and chip drag. One issue with these works is that they comprehend speeds mainly out of the industrial practice (until 3000 m/min!!!).
An extensive analysis of contact behaviour between tool, chip and workpiece is presented in [132]. This article is an example of synergy between analytic and FEM models. The adopted insert is featured by rounded edges (also flank wear and change of the geometry of the tool are taken into account), the focus is on the flank wear and complete stress analytic evolutions along tool interface are built.

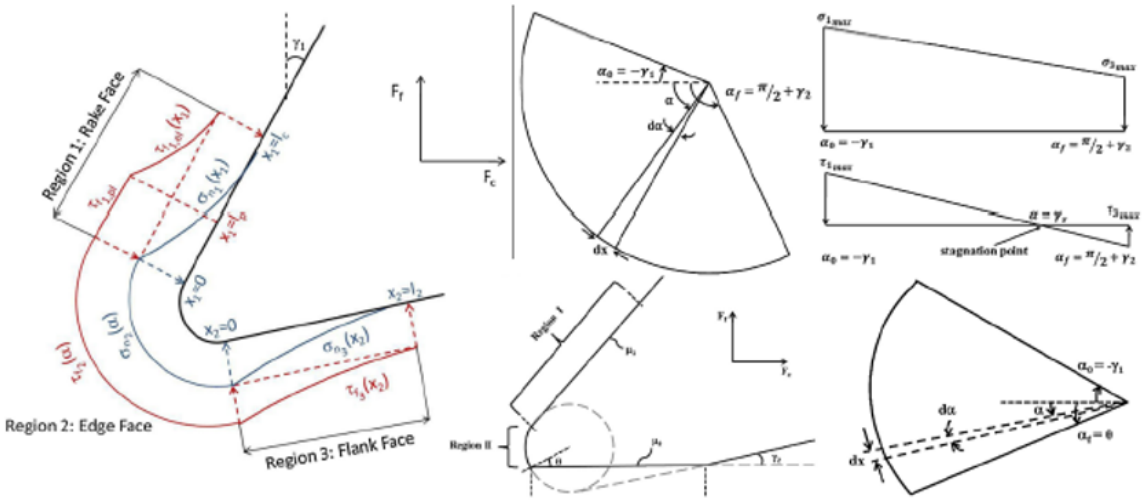

Figure 10.2: Scheme of the model [132]

- Along the rake face: $0 < x < l_{\text{rake}}$

$$\sigma(x) = \sigma_{\text{max,rake}} \left(1 - \frac{x}{l_{\text{rake}}}\right)^n, \quad \tau(x) = \begin{cases} \mu_{\text{rake}} \cdot \sigma(x) & \mu_{\text{rake}} \cdot \sigma(x) < m \cdot \tau_{\text{lim}} \\ m \cdot \tau_{\text{lim}} & \mu_{\text{rake}} \cdot \sigma(x) > m \cdot \tau_{\text{lim}} \end{cases}$$

- For the tool tip: $-\gamma_{\text{rake}} < \alpha < \pi/2 + \gamma_{\text{flank}}$

$$\sigma(\alpha) = \frac{(\sigma_{\text{max, flank}} - \sigma_{\text{max, rake}})\,\alpha + [\gamma_{\text{rake}} \cdot \sigma_{\text{max, flank}} + (\pi/2 + \gamma_{\text{flank}})\,\sigma_{\text{max, rake}}]}{\pi/2 + \gamma_{\text{rake}} + \gamma_{\text{flank}}}$$

$$\tau(x) = -\frac{(\tau_{\text{max, flank}} - \tau_{\text{max, rake}})\,\alpha + [\gamma_{\text{rake}} \cdot \tau_{\text{max, flank}} + (\pi/2 + \gamma_{\text{flank}})\,\tau_{\text{max, rake}}]}{\pi/2 + \gamma_{\text{rake}} + \gamma_{\text{flank}}}$$

The stagnation angle given by: $\alpha_s = \frac{(\pi/2+\gamma_{\text{flank}})\tau_{\text{max, rake}} - \gamma_{\text{rake}} - \tau_{\text{max, flank}}}{\tau_{\text{max, rake}} - \tau_{\text{max, flank}}}$. When tool wear

is present the final angle changes, and so the stresses at the border:

$$\theta = \gamma_{\text{flank}} + \arcsin\left(1 - \frac{VB\sin\gamma_{\text{flank}}}{r_{\text{edge}}}\right), \quad \alpha_s = \frac{\theta\tau_{\text{max, flank}} - \gamma_{\text{rake}}\,\tau_{\text{edge}}}{\tau_{\text{max, flank}} - \tau_{\text{edge}}}$$

$$\overrightarrow{\sigma_{\text{edge}}} + \overrightarrow{\tau_{\text{edge}}} = \overrightarrow{\sigma_{\text{max, flank}}} + \overrightarrow{\tau_{\text{max},flank}} \Longrightarrow \begin{cases} \sigma_{\text{edge}} = \sigma_{\text{max},f\,\text{lank}}\,(\mu_{\text{flank}}\,\sin\theta - \cos\theta) \\ \tau_{\text{edge}} = \tau_{\text{max},f\,\text{lank}}\,(\mu_{\text{flank}}\,\cos\theta - \sin\theta) \end{cases}$$

$\sigma(\alpha) = \left(\frac{\sigma_{edge} - \sigma_{\text{max},rake}}{\gamma_{rake}+\theta}\right)(\alpha + \gamma_{rake}) - \sigma_{\text{max},rake}$,
$\tau(\alpha) = \left(\frac{\tau_{edge} - \tau_{\text{max},rake}}{\gamma_{rake}+\theta}\right)(\alpha + \gamma_{rake}) - \tau_{\text{max},rake}$
with the constraints: $2\sin(\gamma_{\text{flank}}) < \frac{VB}{r_{\text{edge}}} < 1 + \frac{1}{\sin(\gamma_{flank})}$ to be able to calculate θ, and $\mu_{flank} < \frac{1}{\text{tg}\,\theta}$ for the stagnation point to be on the edge;
- For the flank face, spring back is neglected, the contact length is equal to the flank wear: $0 < x < VB$

$$\sigma(x) = \sigma_{\text{max},f\,\text{lan}\,k}\left(1 - \frac{x}{VB}\right)^m, \quad \tau(x) = \begin{cases} \mu_{flank}\cdot\sigma(x) & \mu_{flank}\cdot\sigma(x) < m\cdot\tau_{lim} \\ m\cdot\tau_{lim} & \mu_{flank}\cdot\sigma(x) > m\cdot\tau_{lim} \end{cases}$$

All the geometrical quantities are known exception made for the tool-chip contact length on the rake l_{rake} , the normal pressure distribution must be guessed $\sigma_{\text{max},i}$, n, m, the friction coefficients μ_{rake} , μ_{flank} must be determined. Forces and wear are deduced by experiments, then l_{rake} , $\sigma_{\text{max, flank}}$, $\sigma_{\text{max, rake}}$, μ_{rake} , μ_{flank} , n, m are guessed and iteratively updated to obtain the cutting forces. This is the first step of a large iteration cycle in which the friction coefficients are fed to a FEM simulation, stress distributions are extracted and $\sigma_{\text{max, flank}}$, $\sigma_{\text{max, rake}}$, n, m are used for the following iteration to find μ_{rake} , μ_{flank} .
A Calamaz-modified JC model is adopted for Inconel 100 and Ti6Al4V. The tool was considered rigid until chip formation and then it changes to deformable until internal stresses convergence. Two edge radii, rake angles and variable speeds are simulated. Finally a fitting formula for the friction coefficient as a function of speed, uncut chip thickness and edge radii is provided. Rake maximum stress is higher at higher speeds, feed, edge radii and rake angle. For the flank normal stress the speed is almost insignificant, while higher feeds increase the stress but both increments in the rake angle and edge radius reduce tool solicitation.

10.3. Determination of Friction Coefficients

The friction forces are often deduced starting from the whole cutting forces' profile, but how it has been underlined before, this practice would give exact results only in the ideal

case in which it is available a material model able to work exacly with all possible strains and strain rates. Trying to overcome the introduction of approximations with this method, researchers prefer using tribometers that are devices able to reproduce contact conditions between sliding bodies. Reproducing the same conditions of average pressure (more than one GPa), temperature (much above 500°C) and sliding velocity (until speed of cut) of a real cutting operation, in a controlled experimental environment, is not a trivial task. It is also difficult to reproduce the same adduction of lubricant of a real machining operation, and it is impossible to avoid the deformation of the bodies. Thus the deduced friction coefficients are the result of sticking, sliding and material deformation. In conclusion, with tribometers it is possible to reliably determine macroscopic friction coefficients only.

S.Y. Hong with a series of studies [51], [50], [53], [45], [46] gave to this topic an important contribution. In [50] is reported a 3D force decomposition model for determination of friction coefficients during turning of Ti-alloy. Cutting, feed and thrust forces are projected over the chip flow direction. The flow chip inclination angle β is projected and measured looking at the insert wear after machining (it depends on the influence of nose radius). It is possible to determine the friction coefficient by a ratio between normal and tangential force on the rake surface. This model neglects frank friction, the authors say that this simplification is possible in case of unworn inserts.

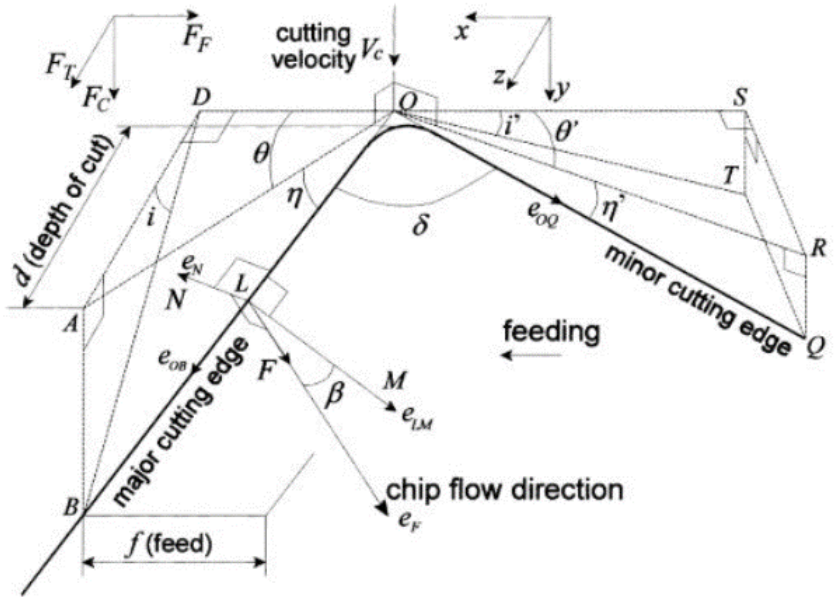

Figure 10.3: Geometrical representation of the model described in [50].

In [53] it is underlined that, in case of cryogenic colling, the friction coefficient decreases also due to vapour expansion phenomena that take place in the gaps between the bodies.

The authors describe a tribometer (mounted on a lathe) able to provide the same average contact pressure of the cutting process. Using AISI 1018 the authors note that the average friction coefficient can be lowered at low normal load with an high pressure (24 bar) liquid nitrogen jet, but at high load the behaviour is similar to dry cutting. Also using Ti6Al4V the LN2 high pressure jet lowers the friction coefficients, but its effectiveness decreases at higher loads. Anyway, it performs better than emulsion and dry cutting, because it removes heat and reduces adhesion/built up edge. Reducing the pressure of the liquid jet to 6.5 bar, the performances are the same of dry cutting.

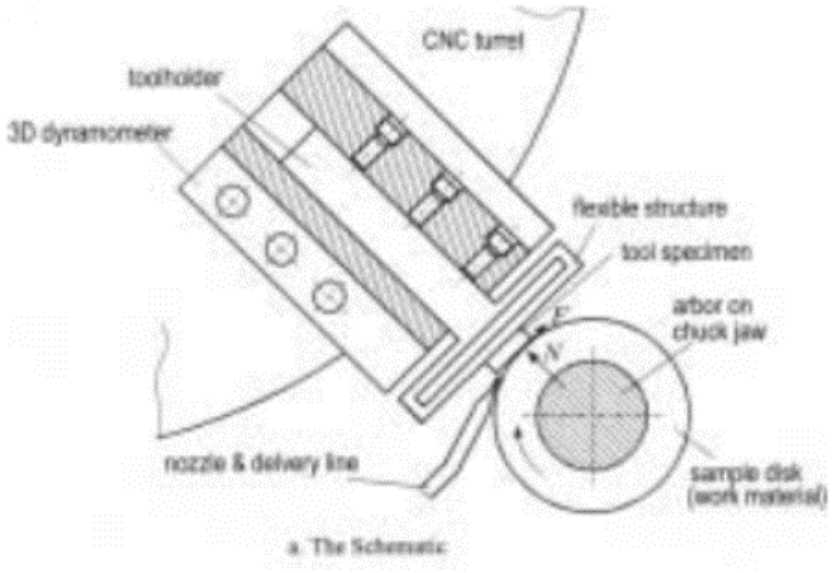

Figure 10.4: Tribometer mounted on the lathe [53].

This set up underlines some practical limitations of adopting a tribometer to determine the friction coefficients for cutting operations. In a real cutting operation one of the biggest challenges is to deliver the cryogenic fluid at the liquid state in the cutting zone. With the above illustrated design this is an easy task since the position of the nozzle and the rotation of the disk favour the direct adduction of liquid in the interested zone, the tribometer acts always on the same surface (easy to cool down). In real applications the cutters always see a new surface, hard to cool down. Moreover, the geometrical and dynamic resistance developed in the crevices between rake/chip and workpiece/flank are not so favourable to the spreading of LN2 in the zones of interest. In [63] through vector manipulation, force projection and geometrical relations is proved that friction coefficient in case of cryogenic cooling with rake/flank delivery is lower than in case of common emulsion or dry cutting. Using macroscopic cutting forces it is not possible to separate clearly the material property variation and the friction variation. Anyway once understood that with cryogenic cooling there is a clear friction reduction it is necessary to know why

this happens. Since the cryogenic liquid, once in contact with the hot working surfaces instantaneously evaporates, it is difficult to imagine a real lubricating action of the liquid itself, for example with the formation of a lubricating film. It is more likely that the friction reduction comes from an alteration of the properties of the material themselves. In [45] and [46] Hong and colleagues focalize their attention on the friction reduction in case of cryogenic cooling. The goal is to better understand if there is a lubricating action or, as suggested before, a meaningful alteration of the properties of the material. Unfortunately, once again the jet is positioned in a position able to ease the penetration in the friction zone thanks to the rotation of the disk. Since the normal forces and the rotational speed are low in this case, what is investigated is the low load friction coefficient in case of hydrodynamic induced lubrication of LN2, which clearly does not take place in real cutting. Anyway, it is underlined that coated tools may exhibit worse behaviours with LN2. This affirmation must be taken as clearly dependent on the limitations of the experimental setup.

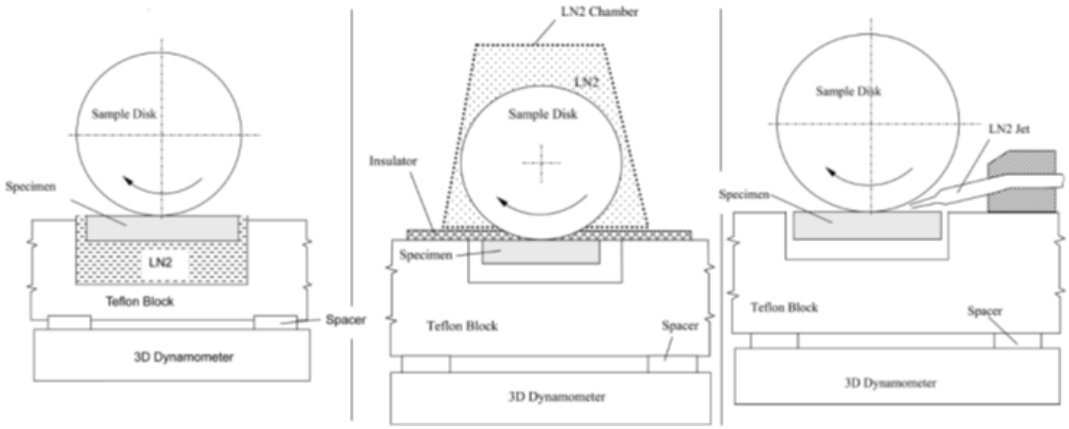

Figure 10.5: experimental set up, different tribometers [46].

In [35] it is possible to find an exhaustive evaluation of the friction coefficient for two titanium alloys: Ti6Al4V and Ti5Al4V against WC in both dry and cryogenic conditions. The friction coefficient is studied as function of speed, load and sliding time $\mu = f(v,N,t)$, also their mutual effects are investigated. The aim of the study (the determination of the friction coefficient based on local normal pressure, temperature and sliding velocity) is rather interesting, but the results can not be taken as reference for cryogenic cutting since: the loads are too low, cutting speeds are limited to less than 60 m/min, the sliding surface is not refreshed on the work material side. Once again, the cryogenic fluid is dragged by the favourable rotation of the disk.
In [6] the authors look for a new approach for the determination of average friction

coefficient through orthogonal cutting test. The relation proposed by Merchant for the calculation of the friction coefficient is: $\mu = \text{tg}\left[\text{tg}^{-1}\left(\frac{F_f}{F_t}\right) + \gamma\right]$ with γ = rake angle.

Another relation proposed by Albrecht considers the linear portion of the feed and cutting force graph (with variable undeformed chip thickness):

$$\mu = \text{tg}\left[\text{tg}^{-1}\left(\left.\frac{dF_f}{dF_t}\right|_{\text{linear zone}}\right) + \gamma\right]$$

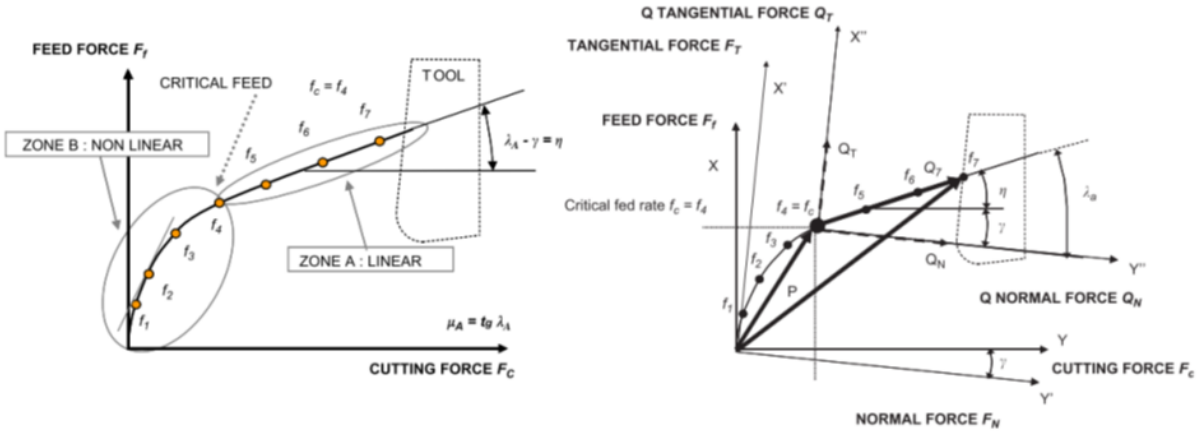

Figure 10.6: Decomposition of forces for friction determination [6].

The friction coefficient is experimentally obtained for AISI 4140. The simulations are carried out with variable feed and cutting speed. Feed forces, cutting forces and chip thickness are evaluated. The last two are very well predicted, feed forces on the contrary are much lower. So the authors have evaluated other two friction models, one considering variable friction coefficient until the linear zone, obtained deriving the expression also for the non-linear zone. For the rest of the contact length, depending on the start of the linear zone, a constant friction coefficient obtained with the first method is adopted. The second model considers a variable friction coefficient calculated over the whole contact length. The feed forces estimated by the simulations, adopting these two models, are better than in previous cases. The article suggests that (always starting with a proper material model) it is possible to improve the results of cutting simulations with an experimentally based friction model, accounting for the friction variability along the nose and the rake face.
Another interesting approach is the one proposed in [16] where friction behaviour between AISI 316L and carbide tools is studied with a "pin on rod" tribometer. Important FEM simulations are carried out to separate the adhesive friction coefficient from the plastic one, because the pin on rod experiment gives the macroscopic sum of the two effects:

$\mu_{app} = \mu_{adh} + \mu_{plast}$ with $\tau_{\text{friction}} = \mu_{adh} * \sigma_n$. The plastic deformation generates a portion of heat that remains almost entirely in the workpiece land it is one order of magnitude smaller than the heat produced by friction. The friction power toward the pin is measured and the experimental heat partition coefficient α is calculated $P_{\text{pin}} = \tau_{\text{friction}} * v_{sl} * \alpha$. The experimental heat partition coefficient is largely different from the theoretical one $\alpha_{\text{theo}} = \frac{\sqrt{\rho_{pin} * c_{pin} * k_{pin}}}{\sqrt{\rho_{wp} * c_{wp} * k_{wp}} + \sqrt{\rho_{pin} * c_{pin} * k_{pin}}}$.

Then adhesive friction and heat partition coefficients are plotted as function of the average local sliding speed obtained in the FEM simulation. In [17] always Bonnet and colleagues evaluate the performance of a sliding speed dependent friction coefficient in machining simulation of the same material (AISI 316L). In practice the friction coefficient is modified by the sliding speed. $\mu = \mu_{\max} + r * v_{sl}$ with $\mu_{\max} = 0.4$ and $r = -2 * 10^{-3}$.

In [34] an interesting characterization of friction and heat partition coefficients during Ti6Al4V machining is performed. The authors criticize the common choice of measuring the friction coefficient through cutting tests because they approximate the rake as flat, the tool as ideally sharp and no contact on the flank. In addition, the variation of the friction coefficient does not influence much cutting forces, so it makes no sense to calculate it from cutting forces. Once fixed the materials pair and lubrication type, contact properties depend on: sliding speed, temperature (dependent on shear zone and sliding velocity) and pressure. A proper tribometer should be able to reproduce a wide range of speeds and pressures. Roughness influences the problem, the sliding pair must be highly polished. In this work a pin on rod technique is used, in order to provide a fresh surface to the friction region, with average pressures (0.75÷1.5 GPa) and temperatures similar to cutting processes. Considering the heat produced in the process as the total dissipated power ($Q = F_f * v$) it is possible to calculate the partition coefficient toward the tool. From the results the evidences are: with high pressures the average friction coefficient decreases, while heat partition coefficient increases. Higher speed corresponds to lower average friction and heat partition, for pressure high enough, while at low speed the coefficients are almost similar for every pressure. The authors indicate a threshold pressure and speed beyond which adhesion begins to be important. The low-pressure friction is representative mainly of sliding, the high-pressure friction includes also sticking phenomena. With these data it is possible to implement a variable average friction coefficient as a function of pressure and speed for FEM simulations.

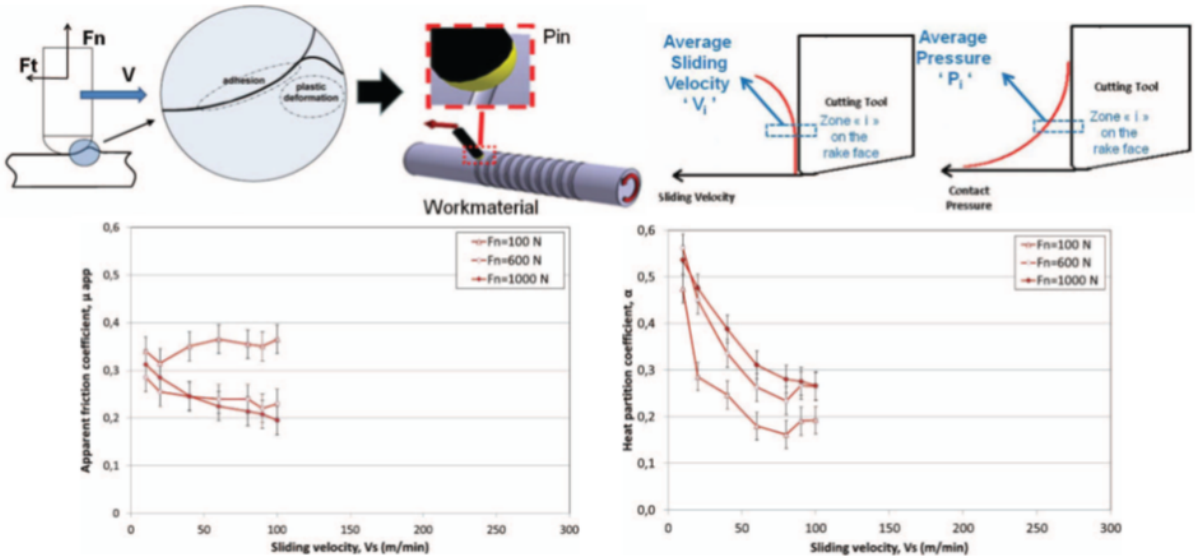

Figure 10.7: Dry friction and heat partition coeff of Ti6Al4V [34].

In [100] is presented a new model of tribometer easy to reproduce on a lathe machine. It is interesting because it provides fresh surface to the friction zone, proper pressure, speed and temperature similar to the ones experienced during real cutting of hard to cut materials. It is composed by a grooving tool against a rotating disk. The weakness of this setup is that high-speed tests need a quick positioning and retracting devices, and no thermal steady state can be achieved. The forces are measured with a dynamometer on the tool side, the temperature is measured with a two-colours pyrometer, the friction coefficient is then calculated. At low speed the adopted material (AISI 1045) shows intense sticking phenomenon. Despite forces have a variable behaviour, temperature and friction coefficient remain almost constant.

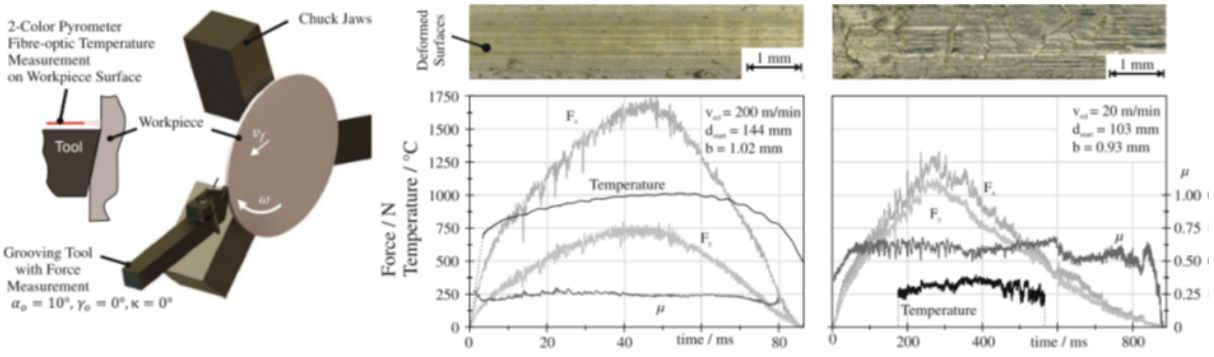

Figure 10.8: Results of new tribometer tested in [100].

In [27] hard to cut materials are studied, in particular the behaviour of friction and heat partition coefficient as function of speed is monitored in both dry and cryogenic

conditions. From the results it is possible to assess that Inconel 718 significantly reduces its average friction coefficient and heat transmitted toward the tool passing from dry to cryogenic conditions. Ti6Al4V does not significantly change its friction coefficient, while heat partition is lowered in cryogenic environment.
In [104] an open pin on rod tribometer is exploited to study the friction and heat partition coefficient of different hard to cut materials. The two coefficients are fitted in cutting speed. Two different models are implemented (one speed-invariant, one speed-variable) for 2D orthogonal cutting simulations dedicated to AISI 1045. The variable model shows very good results, in particular for prediction of the amount of heat exchanged.

Work material against TiN coated carbide	Friction model	Heat partition model
AISI 1045 ferrito-perlitic – dry	$\mu_{loc} = 3.75(V_s)^{-0.538}$	$\alpha = 1.27(V_s)^{-0.458}$
AISI 304L austenitic – dry	$\mu_{loc} = 3.91(V_s)^{-0.559}$	$\alpha = 0.55(V_s)^{-0.283}$
Ti6Al4V – dry	$\mu_{loc} = 0.31(V_s)^{-0.163}$	$\alpha = 1.78(V_s)^{-0.346}$
CFRP – dry	$\mu_{loc} = 3.91(V_s)^{-0.559}$	$\alpha = 1.27(V_s)^{-0.458}$
Inconel718 – dry	$\mu_{loc} = 1.01(V_s)^{-0.385}$	$\alpha = 1.17(V_s)^{-0.293}$
AISI 4142 martensitic – dry	$\mu_{loc} = 2.2(V_s)^{-0.469}$	$\alpha = 1.27(V_s)^{-0.485}$
AISI 4142 martensitic – straight oil	$\mu_{loc} = 0.09$	$\alpha = 1.27(V_s)^{-0.485}$
AISI 4142 martensitic – emulsion	$\mu_{loc} = 0.19$	$\alpha = 0.99(V_s)^{-0.617}$

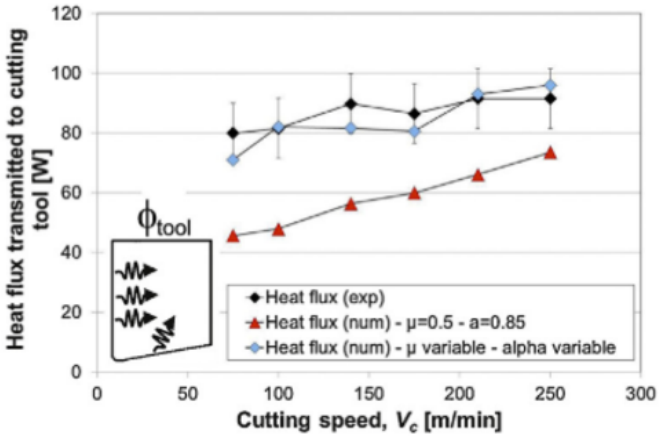

Figure 10.9: Results of the model presented in [104].

In [142] the average friction coefficient of Ti6Al4V against a carbide pin CrN-Coated is experimentally determined, both in dry and cryogenic conditions. The same trial is reproduced in a FEM simulation to calculate the influence of adhesion phenomena on the friction coefficient, by inverse methodology. The authors in this work underline how the rugosity is the most influent factor in determining the average friction coefficient.
In [124] it is possible to find the comparison between a closed and an open tribometer. The contact area is situated between the flat part of a cutting insert (WCCo) and the side

of the workpiece (Ti6Al4V and 42CrMo4). This setup is easily replicable on a common lathe, the only component to be modified is the tool holder. Using 42CRMo4, the average friction calculated on the pin on disk tribometer is lower for lubrication through emulsion, and much lower if LCO2 is used, compared to the value calculated with the open device. In case of dry cutting there is not a substantial difference between the two setups. Using Ti6Al4V the closed tribometer needs some sliding distance to give stable measured values. According to the results, this system shows lower average friction coefficient, but if in case of 42CRMo4 the emulsion is able of lowering the friction coefficient, with Ti-alloy nor emulsion nor CO2 are able to replicate this trend. The authors underline how the results of the closed tribometer can be inaccurate, especially in case of cryogenic cooling due to the presence of ice on the workpiece.

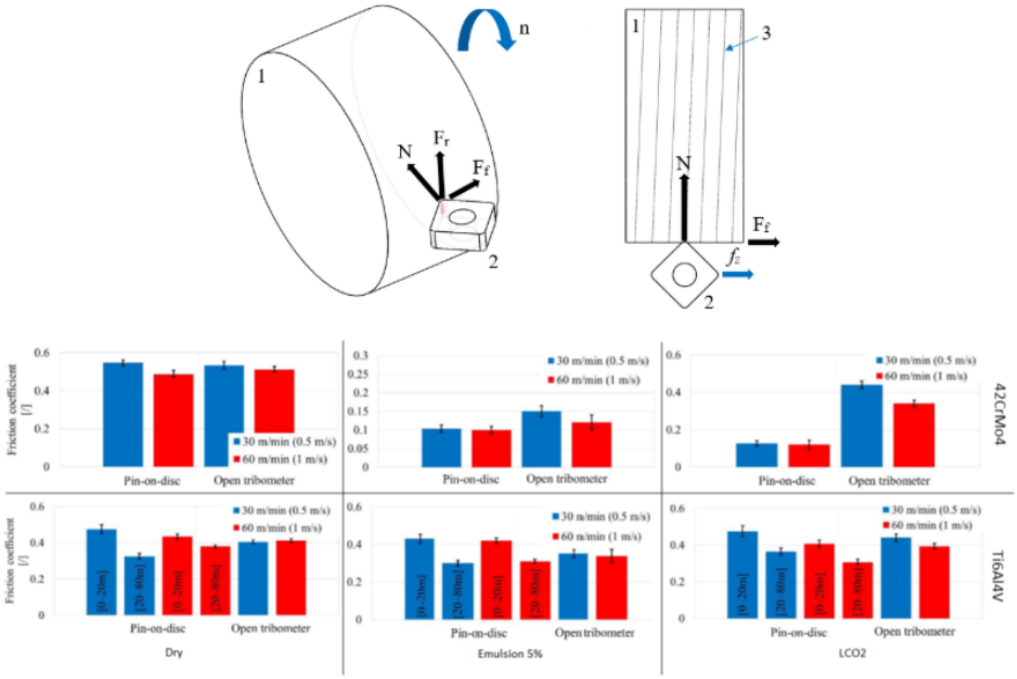

Figure 10.10: Experimental setup and average friction coefficients of 42CrMo4 and Ti6Al4V [124].

10.4. Material Models

The bases of a finite element simulation are the geometry of all the involved parts, the load applied, the boundary conditions and the material models that describe the behaviour of the materials. It is possible to define a material model as an equation that associates to a given applied force, or stress, a certain resulting deformation, or strain. A simple list of material parameters is not sufficient to describe the behaviour of a material in a FE

analysis. In this field the definition of a proper material model is a crucial aspect, in which researchers spend their efforts from decades. One of the most diffused material models is the Johnson-Cook, it is characterized by a small number of parameters available on catalogues for a wide range of materials. Other famous models are the Zerilli-Armstrong, the Power Law, the Baumann-Chiesa-Johnsons (even if its parameters are available only for a tight range of materials).

Johnson-Cook:

it is based on reduced number of coefficients that can be determined with a small number of tests. It is easy to be implemented on the majority of the FE software available on the market. It separates the effect of strain, strain rate and temperature on the flow stress, without considering the possible mutual effects:

$$\sigma = \left(A + B\varepsilon_p^n\right)\left(1 + C\ln\dot{\varepsilon}_p^*\right)\left(1 - T^{*m}\right) = JC(\varepsilon) * JC(\dot{\varepsilon}) * JC(T)$$

where n, m, A, B, C = material constants, A = yield strength sensitivity of the material, B = strain sensitivity of the material, C = strain rate sensitivity of the material, $\dot{\varepsilon}_p^*$ = normalized strain rate = $\frac{\dot{\varepsilon}_p}{\dot{\varepsilon}_{p0}} = \frac{\text{effective platic strain rate}}{\text{reference plastic strain rate}}$, T^* = normalized temperature = $\frac{T-T_0}{T_m-T_0}$, T_m = melting temperature of the material, T_0 = reference temperature of the quasi static test used to determine the material constants.
$JC(\varepsilon)$ accounts for strain hardening, $JC(\dot{\varepsilon})$ accounts for strain rate, $JC(T)$ accounts for thermal softening. n, m, A, B, C are often determined through pressure bar tests for a range of strains up to 0.6, strain rates up to 10^4[1/s] and temperatures until 1000°C. During cutting processes strains can reach values between 3 and 10 in the secondary deformation zone and strain rates are between $10^5 \div 10^6$ depending on the cutting speed.

10.5. Damage Models

Damage models are needed to numerically reproduce the fractures that occur in chip removal processes. Elements of the material are progressively labelled with a certain damage factor. When it reaches a threshold value, the corresponding element is deleted to simulate the fracture. Dealing with it Ti6Al4V is not trivial since (as previously explained), this material is featured by the shear bending effect, if subject to important strain rates. The chip morphology is an important feature, often used as a validation factor of the whole FE model. It is possible to find many scientific works in which authors try adapting the material behaviour in order to reproduce the shear banding phenomenon.

The two main strategies are:

1. Addition of damage models to the stress flow rheological models.
2. Modification of rheological models without the description of a dedicated damage model.

The most diffused damage models are the Latham-Cockcroft and the Johnson-Cook, then depending on the software adopted, it is possible to access to different predefined libraries of models or also modify the default rheological models.

Latham-Cockcroft damage model:

This model is widely used in FE simulations, especially for its compactness.
Basically, when the higher tensile component of the stress tensor along the effective strain path reaches a critical value, depending mostly on temperature and microstructure of the interested material, the material element is considered as damaged and a crack is initiated:

$$\int_0^{\varepsilon_f} \sigma_1 * d\varepsilon = D$$

A common practice in numerical simulations is to iteratively update the value of D, until the chips are featured by a morphology satisfactory similar to the one obtained in experimental tests. Also the normalized version of this formula is widely applied, addressed as Normalized LC:

$$\int_0^{\varepsilon_f} \frac{\sigma_1}{\bar{\sigma}} * d\varepsilon = D_n$$

Where the higher tensile component of the stress tensor along the effective strain path is divided by the effective stress, forcing D_n to take values between 0 and 1.
The principal drawback of this model is the absence of any lack of strength by the material, until the sudden failure when the threshold is reached.

Johnson-Cook damage model:

It is the most diffused damage model, it is frequently coupled with the Johnson-Cook material model, the coefficients are available in literature for a wide range of materials, for new materials their determination is standardized. The model is based on the formulation of an equivalent strain to fracture. It depends on the actual stress, strain rate, temperature and pressure.

$$\varepsilon_{d,i} = \left[D_1 + D_2 e^{D_3 \eta}\right] \cdot \left[1 + D_4 \ln\left(\frac{\dot{\varepsilon}}{\dot{\varepsilon_0}}\right)\right] \cdot \left[1 - D_5 \left(\frac{T - T_r}{T_m - T_r}\right)^m\right], \quad \eta = \frac{\sigma_1 + \sigma_2 + \sigma_3}{3 \cdot \sigma_{VM}}$$

With D_i = five constants fitted with experimental tests.

A cumulative damage variable is representative of the level of damage of each element

$$D = \sum \frac{\Delta\varepsilon}{\varepsilon_{d,i}}, \quad D_i = \int \frac{1}{\varepsilon_{d,i}(\eta, \dot{\varepsilon}, T)} d\varepsilon = 1$$

Where $\Delta\varepsilon$ is the strain cumulated in one integration cycle. The fracture occurs when the damage variable D reaches the value of 1.

10.6. Application on Titanium and Shear Banding Reproduction

In this section I report some examples available in literature of material models applied to Titanium (and similar hard to cut materials) cutting.
In [93] the coefficients for Johnson-Cook and friction coefficients are evaluated through orthogonal cutting tests (Oxley model for describing stresses and strains). For several materials, including Ti6Al4V, the friction model is formulated combining Oxley model and integrating the stresses over the rake to find the feed and cutting forces. At the same time the JC constants are determined by non-linear regression (Gauss-Newton and Levenberg-Marquardt modification). The main obstacle is the fact that Oxel model considers a continuous chip, while Ti6Al4V exhibits chip segmentation which would lead to alteration of results in case of high cutting speed.
In [41] it is possible to find the application of Baumann-Chiesa-Johnson material model on AISI 52100 bearing steel. The model is powerful, it is dislocation based, it can describe complex loading histories, recovery and microscopic effects. The main limitation is the high number of coefficients (20) required, which are difficult to be determined. The coefficients in this case are obtained with quasistatic and isothermal tests, in the simulations a cumulative damage criterion is also added for chip separation purposes. The chip morphology is well predicted for maximum and minimum saw heights, but saw pitch prediction is clearly overestimated. The limit of this model is that the big efforts spent in the determination of the coefficients is not justified by the final result, which are good but not excellent as reported in this paper.

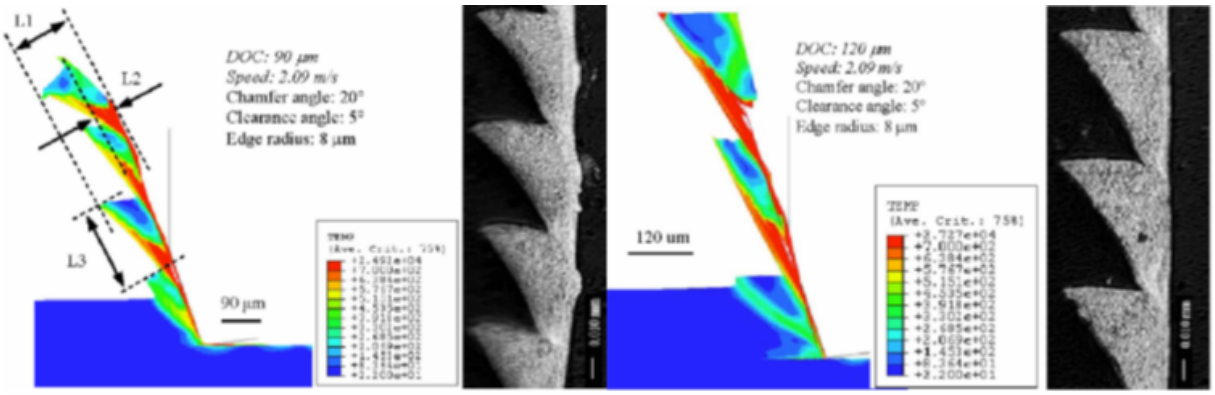

Figure 10.11: Results of Baumann-Chiesa-Johnson material model [41]

In [4] the authors present a review of some important material models and a model developed by themselves. One example is the Andrade-Meyers where T_c=recrystallization/recovery starting temperature, so a variation of the thermal softening function of a normal JC is present:

$$\bar{\sigma} = [A + B\varepsilon^n]\left[1 + C\ln\frac{\dot{\varepsilon}}{\dot{\varepsilon}_0}\right] \cdot \left[\frac{1}{1-\left\{1-\left[\frac{(\sigma_f)_{\text{rec}}}{(\sigma_f)_{\text{def}}}\right]\right\}\cdot u(T)}\right], \quad u(T)\begin{cases}0 & T < T_c\\ 1 & T > T_c\end{cases}$$

The second model they analyse is the Usui-Shrakashi, that is based on a modification of the power law model. Inside the term related to the strain rate, there is an integral part accounting for the strain rate history:

$$\sigma = \left[\frac{A}{1000}\dot{\bar{\varepsilon}}\right]^M \cdot \left[\frac{e^{KT}}{1000}\dot{\bar{\varepsilon}}\right] \cdot \left[\int_{[T,\dot{\varepsilon}=h(\varepsilon)} e^{\frac{KT}{n}}\dot{\varepsilon}^{-\frac{m}{n}}d\varepsilon\right]^n \quad A, k, n, m \text{ constants}$$

The authors present also their own model that is defined as a dislocation based thermo-mechanical model. On one hand an increment of temperature promotes the dislocation movement, on the other hand an high strain rate increases the pinning effect of atoms in the solution, easing the entanglement of dislocations. The flow stress is divided in a thermal and a-thermal part accounting for long range dislocation barriers such as GBs, dislocation forests and precipitates. The thermal part accounts for resistance of dislocation due to short range barriers as point defects, vacancies, interstitials, alloying elements, interacting dislocations and slipping planes:

$$\sigma = \sigma_a + \sigma^*, \quad \sigma_a = a_0 + a_1 \cdot \varepsilon^n$$
$$\sigma^* = \hat{\sigma}^* \cdot \left[1 - \left(-\frac{kT}{G_0} \cdot \ln\left(\frac{\dot{\varepsilon}}{\dot{\varepsilon}_0}\right)\right)^{1/q}\right]^{1/p}$$
$$\Delta G = G_0 \left[1 - \left(\frac{\sigma^*}{\hat{\sigma}^*}\right)^p\right]^q, \quad \dot{\varepsilon} = \dot{\varepsilon}_0 e^{\left(-\frac{\Delta G}{kT}\right)}, \quad \dot{\varepsilon}_0 = \rho_m b \bar{v}$$

With ΔG = energy barrier a dislocation has to overcome, G_0 = energy needed for the dislocation movement in case of null thermal stress, $\hat{\sigma}^*$ = stress needed to the dislocation to overcome the barrier at 0 K, ρ_m = average dislocation density, b = burger vector, $\bar{v}$ = average dislocation speed, k = Boltzmann constant = $1.38^{*}10^{-23}$[J/K]. The material constants are found through SHPB compression tests.
Unfortunately, an application of this model in cutting simulations is not available in literature.
In [19] Calamaz and colleagues propose a modification of JC in order to reproduce shear bending phenomenon in case of Ti6Al4V 2D cutting simulations. The new model is called Tanh, it introduces the effect of strain softening. The equation for the flow stress of the material is:

$$\bar{\sigma} = \left[A + B\varepsilon^n \cdot \left(\frac{1}{e^{a^a}}\right)\right] \cdot \left[1 + C \ln \frac{\dot{\varepsilon}}{\dot{\varepsilon}_0}\right] \cdot \left[1 - \left(\frac{T - T_r}{T_m - T_r}\right)^m\right] \cdot \left[D + (1 - D) \cdot \tanh \frac{1}{(\varepsilon + s)^c}\right]$$
$$D = 1 - \left(\frac{T}{T_m}\right)^d, \quad s = \left(\frac{T}{T_m}\right)^b$$

a, b, c, d are additional material constants. The parameter d controls the softening degree, at the level of the stress strain curve at high strains while c at low strains after the peak stress, which magnitude is set by b. The tool during the simulation is considered as rigid, the tool-chip interface conductance is set to 20 kW/m^2 K. The contact model is a Coulomb-Tresca:

$$\tau_f = \begin{cases} \mu \cdot \sigma_n & \mu\sigma_n < m \cdot \frac{\sigma_0}{\sqrt{3}} \\ m \cdot \frac{\sigma_0}{\sqrt{3}} & \mu\sigma_n > m \cdot \frac{\sigma_0}{\sqrt{3}} \end{cases}$$

d varies between $1 \div 1.5$, m varies between $0.5 \div 1, \mu$ varies between $0.05 \div 0.3$. The Tanh model correctly predicts the shear bands at low cutting speeds (60 m/min), on the contrary the unmodified JC leads to the formation of a continuous chip. The best estimation of forces is with m = 1, d = $1.5, \mu = 0.3$. However, for a value of d = 1.5 the shear band frequency is underestimated. In order to perfectionate the shear bands' prediction, a Latham-Cockroft damage criterion with $D = 2400$ is added. In conclusion, the proposed Tanh model is an efficient modification of the simple JC model, but the

presence of a damage model is still necessary.

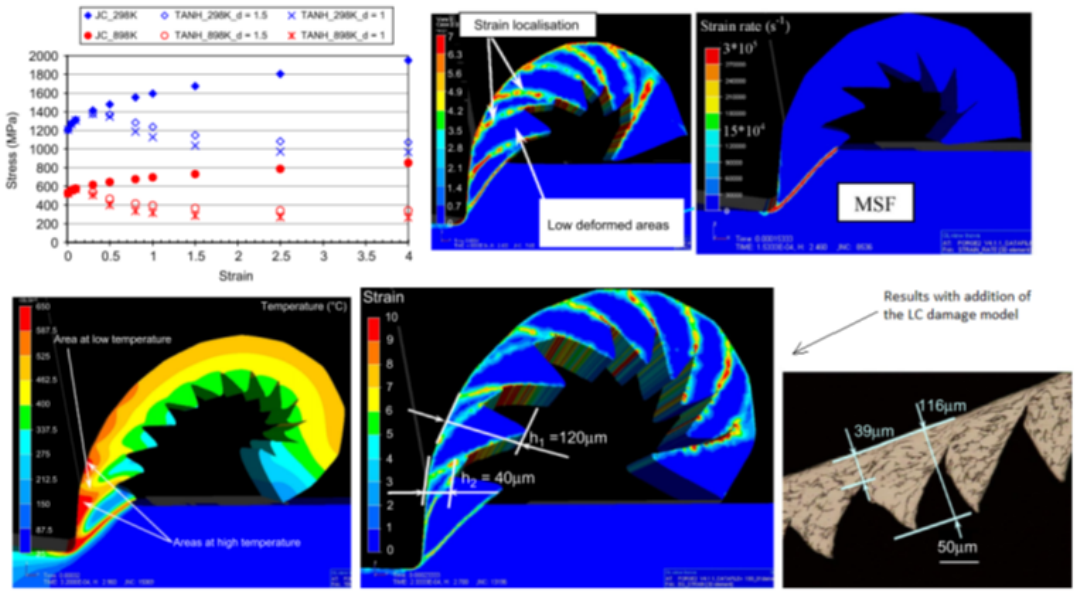

Figure 10.12: Tanh model results [19]

This model also is tested, with good results, in a 3D turning simulation on Inconel 718 [95].

An important work is [133] by Umbrello and colleagues. Performing cutting simulations on Ti6Al4V they underline the importance of an accurate knowledge of the material behaviour in FE modelling, the material model is the fundamental basis of every simulation. Then damage models can be updated by iterations looking at the chip morphology, friction coefficients can be updated with iterations looking at cutting forces. In the work, different material flow stress models are compared at a speed of 120 m/min and at ultra-high speeds like 1200 and 4800 m/min. The best JC coefficients are the ones obtained by Lee and Lin, they guarantee good results if coupled with adjusted damage model and friction coefficient.

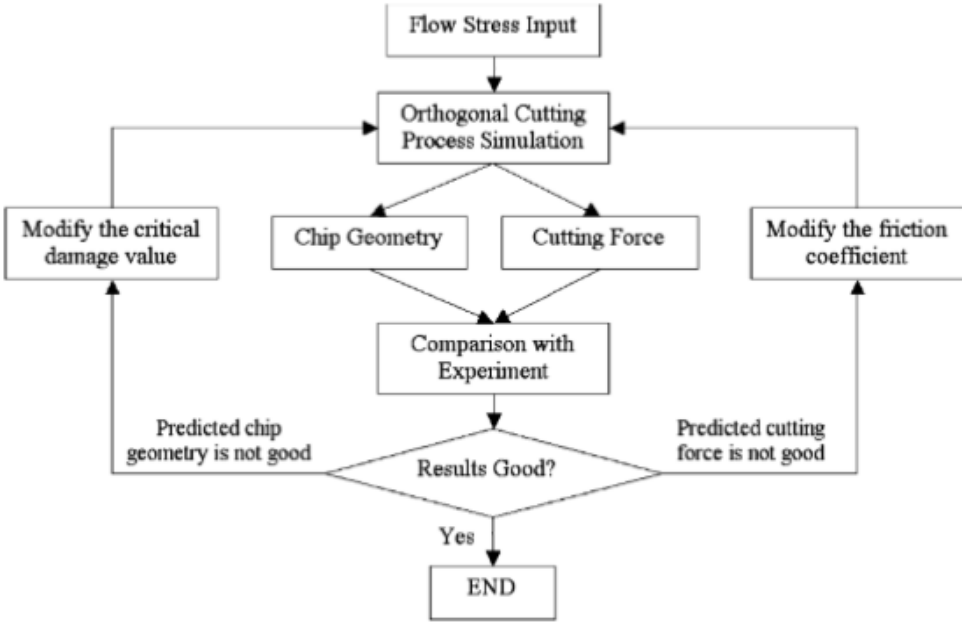

Figure 10.13: D and μ iterative calibration procedure [133]

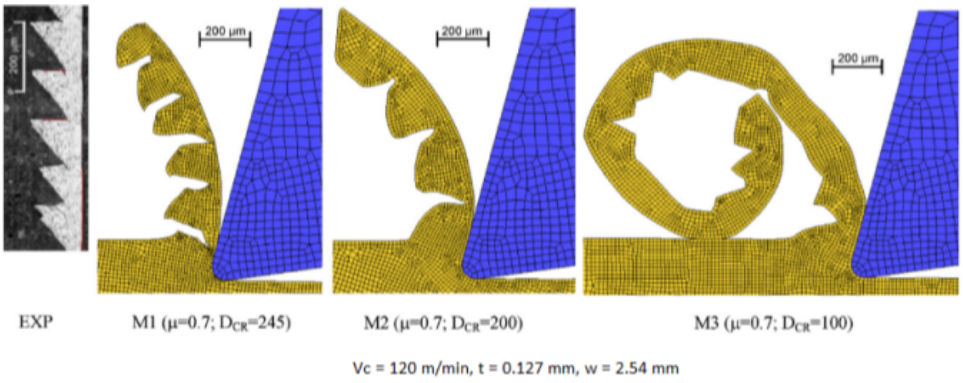

Figure 10.14: Chip morphology for different models [133]

In [94] different JC coefficients are tested for Ti6Al4V, with LC damage criterion. Different coefficients of the material model influence chip morphology, cutting forces and temperatures. From the results, Lee and Lin, Mayer and Kelponis models are addressed as the most accurate.

In [121] the authors analyse the performance of the Tanh model in case of Ti6Al4V cutting simulations. They evaluate three different models: Tanh, Andrade-Mayers modified JC, Nemat-Nasser micromechanical model (following formula):

$$\bar{\sigma} = \sigma_a + \sigma*, \quad \left\{ \begin{array}{l} \sigma_a = \sigma_0 \varepsilon^m \\ \sigma* = f(T, \dot{\varepsilon}) = \hat{\sigma} = \left\{ 1 - \left[-\frac{K}{G_0} T \cdot \ln \frac{\dot{\epsilon}}{\dot{\varepsilon}_0} \right]^{1/p} \right. \end{array} \right\}^{1/q}$$

The main goal of Nemat-Nasser model is a more accurate description of the dynamic strain aging of the material. K=Boltzmann constant, G_0=total energy barrier, p=constant between 0 and 1, q=constant between 1 and 2. The material flow stress depends on three variables and it is not easy to separate the contribution of each of them alone. Some considerations can be done by looking at the strain rate sensitivity and temperature sensitivity: the first one decreases in presence of higher strains, the second is almost constant.

$$S_{\dot{\varepsilon}} = \frac{\sigma_2 - \sigma_1}{\ln(\dot{\varepsilon}_2/\dot{\varepsilon}_1)}, \quad S_T = \frac{\ln(\sigma_2 - \sigma_1)}{\ln(T_2/T_1)}$$

The authors simulate orthogonal cutting with three different versions of the Tanh model:

1. Tanh-1: temperature independent parameters

$$\bar{\sigma} = [A + B\varepsilon^n] \left[1 + C \ln \frac{\dot{\varepsilon}}{\dot{\varepsilon}_0} \right] \cdot \left[1 - \left(\frac{T - T_r}{T_m - T_r} \right)^m \right] \cdot \left[M + (1 - M) \cdot \tanh \left(\frac{1}{(\varepsilon + p)^r} \right)^s \right]$$

M = strain threshold over which softening begins, however the softening effect is applied at all temperatures.

2. Tanh-2: temperature dependent parameters

$$\bar{\sigma} = [A + B\varepsilon^n] \left[1 + C \ln \frac{\dot{\varepsilon}}{\dot{\varepsilon}_0} \right] \cdot \left[1 - \left(\frac{T - T_r}{T_m - T_r} \right)^m \right] \cdot \left[D + (1 - D) \cdot \tanh \left(\frac{1}{(\varepsilon + p)^r} \right)^s \right]$$
$$D = 1 - \left(\frac{T}{T_m} \right)^d, \quad p = \left(\frac{T}{T_m} \right)^b$$

d and b controls the softening effect 3.

Tanh-3: strain softening effect

$$\bar{\sigma} = \left[A + B\varepsilon^n \cdot \left(\frac{1}{e^{\varepsilon^a}} \right) \right] \left[1 + C \ln \frac{\dot{\varepsilon}}{\dot{\varepsilon}_0} \right] \cdot \left[1 - \left(\frac{T - T_r}{T_m - T_r} \right)^m \right] \cdot \left[D + (1 - D) \cdot \tanh \left(\frac{1}{(\varepsilon + p)^r} \right)^s \right]$$
$$D = 1 - \left(\frac{T}{T_m} \right)^d, \quad p = \left(\frac{T}{T_m} \right)^b$$

a controls the strain at which strain softening starts, b controls the position of the stress

peak value, d the stress level at high strains, S the strain level at which softening starts.

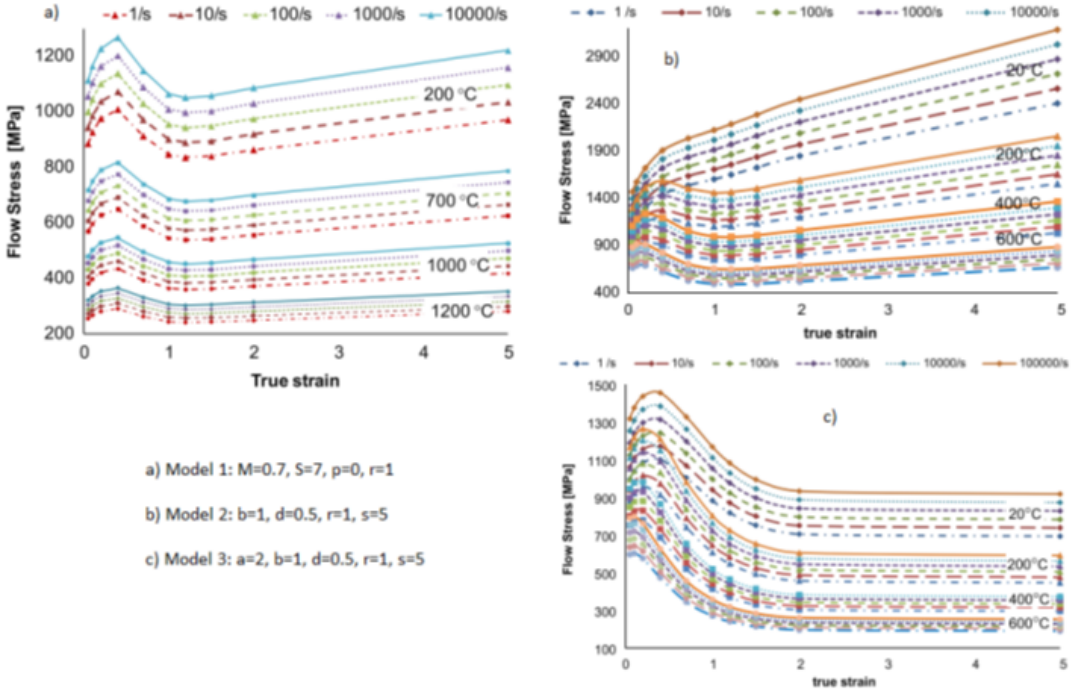

Figure 10.15: Flow stress/true strain plots for Tanh model 1-2-3 [121]

The results say that with first model the softening effect is constant for all the temperatures, while for the second the softening effect is higher for higher temperatures, with the third the presence of strain softening contributes to flatter the flow stress curve at high strains. The friction region is divided into three parts: sticking part around the tool nose (Tresca factor m=1), rake sticking region (m=0.9) and Coulombian sliding region (μ=0.5). The combination of values [a,b,d,r,S]=[2,5,1,1,0.05] is the one that gives better results.

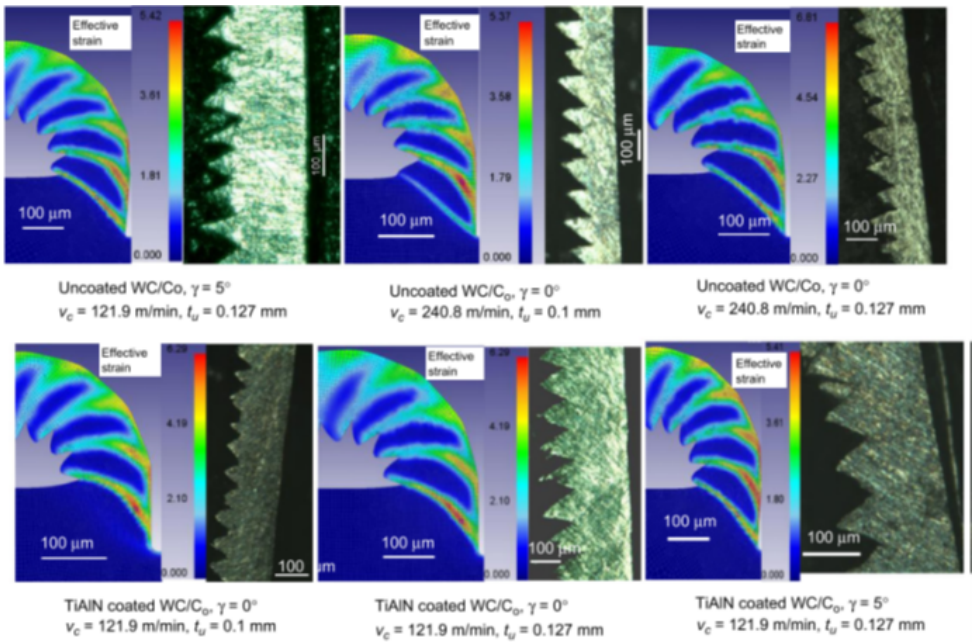

Figure 10.16: Tanh-3 model results [121]

One open problem is the extrapolation of material models' parameters from experimental data. It is difficult to simulate and monitor processes with strains and strain rates typical of real machining operations, so the parameters must updated iteratively but the question is always the same: Where is the border between influences of material model and contact model?

In [20] Calamaz and colleagues modify their previous model [95] to better capture the strain softening effect of Ti6Al4V.

$$\bar{\sigma} = [A + B\varepsilon^n]\left[1 + C\ln\frac{\dot{\varepsilon}}{\dot{\varepsilon}_0}\right]\cdot\left[1 - \left(\frac{T - T_r}{T_m - T_r}\right)^m\right]\cdot\left[D + (1 - D)\cdot\tanh\left(\frac{1}{(\varepsilon + \varepsilon_0)}\right)\right]$$

$$D = 1 - \left[\frac{p\cdot\varepsilon}{1 + p\cdot\varepsilon}\cdot\tanh\left(\frac{T - T_r}{T_{\text{soft}} - T_r}\right)^q\right]$$

where ε_0 regulates the strain corresponding to the peak and stress and the start of softening. D function of T and ε describes the range of temperatures for the softening phenomenon and the shape of the curve during the softening. FORGE 2005 is used to set up the new model, the friction coefficient μ is assumed constant for all the simulations. The results are excellent in predicting shear bands and chip morphology, but a strong divergence of forces is present in correspondence of high cutting speeds.
In [65] Karpat and colleagues develop present model which goal is to better capture the thermal softening of Ti6Al4V. The authors take into the account effect of dynamic re-

crystallization, occurring between 0.4 and 0.5 times the melting temperature T_m. The generation of slip bands is favoured by the phase transformation from α to β and GBs sliding. Their model is:

$$\sigma(\varepsilon, \dot{\varepsilon}, T) = \left[ae^{n^*} + b\right] \cdot \left[cT^{*2} + dT^* + e\right] \cdot \left[1 - \left(1 - \left(\frac{\ln \dot{\varepsilon}_0}{\ln \dot{\varepsilon}}\right)^q\right)\left(\frac{1}{l \cdot \tanh(\varepsilon + p)}\right)\right], \quad T^* = \frac{T}{T_r}$$

After a certain ε_{cr} the softening phenomenon starts. Multiplying the stress at the critical strain and multiplying it by the term S (< 1 if softening is in progress), it is possible to find the steady state softened stress. For the softening region the stress is reduced by a Tanh function influenced by the distance from the critical strain, which in his turn must be defined as function of strain rate and temperature.

$$\sigma_s = S \cdot \sigma\left(\varepsilon_{cr}, \dot{\varepsilon}, T\right), \quad S < 1$$

$$\sigma(\varepsilon, \dot{\varepsilon}, T) = \sigma - (\sigma - \sigma_s)\left(\tanh\left(k \cdot \varepsilon^*\right)^r\right), \quad \varepsilon^* = \frac{\varepsilon - \varepsilon_{cr}}{\varepsilon_{cr}} u(\varepsilon), \quad u(\varepsilon) = \begin{cases} 0 & \varepsilon < \varepsilon_{cr} \\ 1 & \varepsilon \geq \varepsilon_{cr} \end{cases}$$

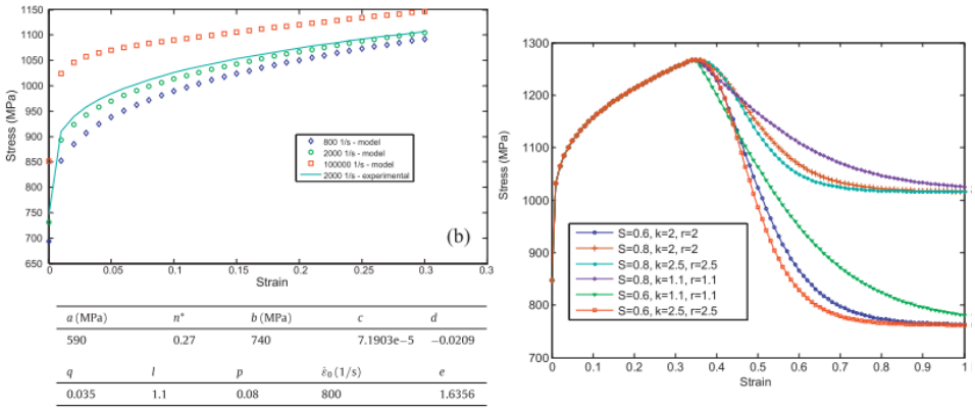

a (MPa)	n^*	b (MPa)	c	d
590	0.27	740	7.1903e−5	−0.0209

q	l	p	$\dot{\varepsilon}_0$ (1/s)	e
0.035	1.1	0.08	800	1.6356

Figure 10.17: Stress/strain for different strain rates, table of parameters, strain/stresses for different combinations of S-k-r [65]

The cutting simulations are featured by different starting temperatures of softening. As friction model a Coulomb-Tresca with $\mu = 1.2^* \mu_{\text{sperimental}}$ is selected, material properties are variable with temperature. Very good results come from S = 0.6, starting temperature of softening = 350° and strain hardening from ambient T, r = k = $2, \varepsilon_{cr} = 0.35$. The authors underlines how the shear band formation is influenced by the mesh size of the shearing zone: larger the mesh size, larger the shear band and smaller the serration degree.

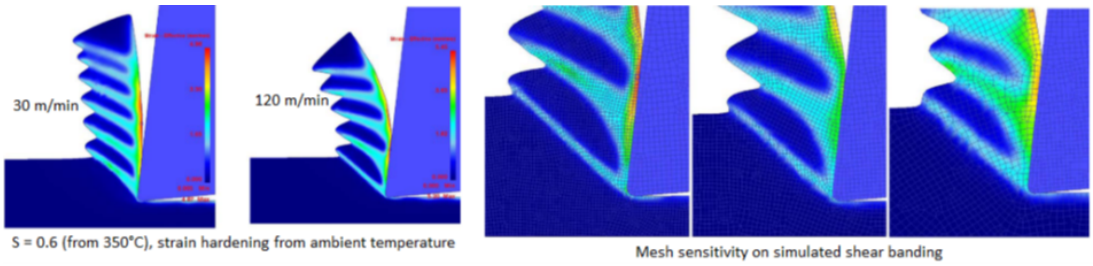

Figure 10.18: Model results for different cutting speed and different mesh size in the shearing zone [65].

In [24] it is possible to find the simulations of high-speed machining (170÷250 m/min) of Ti6Al4V with JC material model and JC damage evolution. Then, also a shear damage criterion to facilitate chip separation from the piece is implemented on a narrow band of the workpiece at a depth equal to the uncut chip thickness. This procedure needs also to avoid remeshing algorithms. From the results both cutting forces and chip morphology agree with the experimental data, anyway the setup showed in this article is difficult to reproduce with more complicated geometries and kinematics.
Calamaz and colleagues in [21] propose another modification of their material model for Ti, abandoning the Tanh function and the thermal softening, substituting them with a more sophisticated strain and strain rate dependency. The aim is to better capture shear banding phenomenon.

$$\bar{\sigma} = \left[A + B\left(\frac{1}{\dot{\varepsilon}}\right) \cdot \varepsilon^{[n-0.12(\varepsilon\cdot\dot{\varepsilon})^a}\right]\right]\left[1 + C\ln\frac{\dot{\varepsilon}}{\dot{\varepsilon}_0}\right] \cdot \left[1 - \left(\frac{T - T_r}{T_m - T_r}\right)^m\right]$$

Both the cutting forces and chip segmentation frequency are well reproduced by the simulation for a wide range of speed and feeds for $a = 0.11, \mu = 2$. However, this friction coefficient does not find a physical justification. The authors say that it is necessary in order to represent sticking with a coulomb friction law. Adopting such an high value leads inevitably to an increment of temperatures in the secondary deformation zone and possible material softening. Moreover, no analysis on heights and pitches of the segmentation is reported, but from the images reported in the article they do not seem in agree with the results of the simulation.

In [79] the authors start from the Zerilli-Armstrong model that accounts for the stress saturation at high strains:

$$\sigma = \sigma_a + B \cdot e^{-(\beta_0 - \beta_1 \ln\dot{\varepsilon})\cdot T} + B_0 \cdot \sqrt{\varepsilon_r\left(1 - e^{-\frac{\varepsilon}{\varepsilon_r}}\right)} \cdot e^{-(\alpha_o - \alpha_1 \ln\dot{\varepsilon})\cdot T}$$

and they modify it in order to consider the void nucleation and crack initiation during shear banding typical of Ti6Al4V. Shear bands are believed to be caused by both thermal softening effects (dynamic recrystallization and recovery) and void coalescence forming a crack. The model modification proposed is:

$$\sigma = \left[\sigma_a + B \cdot e^{-(\beta_0 - \beta_1 \ln \dot{\varepsilon}) \cdot T} + B_0 \cdot \sqrt{\varepsilon_r \left(1 - e^{-\frac{\varepsilon}{\varepsilon_r}}\right)} \cdot e^{-(\alpha_o - \alpha_1 \ln \dot{\varepsilon}) \cdot T}\right] \cdot \left[H + (1 - H)\left(\tanh \frac{a}{\varepsilon}\right)^k\right]$$

where H is the asymptotic stress factor that controls the softening at high strains. Under that strain rate, heat conduction compete with temperature localization hindering shear banding.

$$H = \begin{cases} 1 & \dot{\varepsilon} < \dot{\varepsilon}_0 \\ \left[\frac{1}{\log_{10}(\varepsilon)}\right]^{h_0} & \dot{\varepsilon} \geq \dot{\varepsilon}_0 \end{cases}, \quad \dot{\varepsilon}_0 = 10\frac{1}{s}$$

a = critical strain at which softening starts $= a_1 * [\log_{10} \dot{\varepsilon} - a_2]^2 + a_3$ and $[\log_{10} \dot{\varepsilon}]^{k_0}$. In the end to the classical seven constants of Zerilli-Armstrong, other seven constant parameters are needed $[h_0, a_1, a_2, a_3, k_0]$.

Cutting forces are predicted in an accurate way, the chip morphology is not properly analysed, the only parameter regarding it that the author present is the serration frequency (slightly overestimated at high feed).
In [25] the authors modify the JC material model for Ti6Al4V introducing the concept of stress triaxiality:

$$\bar{\sigma} = \left[A + m\varepsilon_p^n\right] \cdot \left[B + C \ln\left(E + \frac{\dot{\varepsilon}}{\dot{\varepsilon}_0}\right)\right] \cdot \left[1 - \zeta\left(\eta - \eta_0\right)\right] \quad \eta = \frac{\sigma_m}{\bar{\sigma}}$$

There is no influence of thermal softening, justified by two reasons principally: 1) The heat generation due to inelastic heat fraction during the experimental tests, unto which models are based, already account for heat generation in the small time scale, in practice the workpiece is not preheated. 2) Temperature in the primary deformation is moderate (hardly reaches 400°C) thanks to chip transport. Doing so the contact between insert and workpiece and the wear behaviour will be distorted since for the secondary deformation zone the strong assumption above does not hold anymore. In addition to the material model a JC damage evolution is added

$$\bar{\varepsilon}_i^p = \left[D_1 + D_2 e^{D_3 \eta}\right] \cdot \left[1 + D_4 \ln\left(\frac{\dot{\varepsilon}}{\dot{\varepsilon}_0}\right)\right] \quad \bar{\sigma} = (1 - D)\tilde{\sigma}, \quad D = \int_{\bar{\varepsilon}_i^p}^{\bar{\varepsilon}^p} \frac{\bar{\sigma}}{G_f} \cdot d\bar{\varepsilon}^p, \quad G_f = \int_{\bar{\varepsilon}_i^p}^{\bar{\sigma}_f^p} \bar{\sigma} \cdot d\bar{\varepsilon}_p$$

D_i = damage model constants, D = damage variable, G_f = fracture energy. Once deter-

mined all the parameters of the model through experiments on three different specimens, the model is tested in a FE simulation, the consequent prediction of chip morphology is satisfactory.

	Experiment	Simulation
Peak (µm)	226.7 ± 12.1	139.5
Valley (µm)	116.6 ± 13.1	81.9
Pitch (µm)	161.3 ± 24.3	100.5
CCR	1.51 ± 0.08	0.93

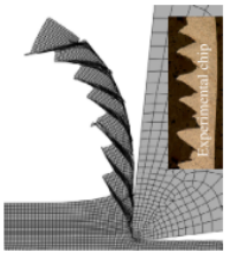

Figure 10.19: Chip morphology comparison [25].

In [14] the authors characterize the material flow stress behaviour (Ti6Al4V) at low temperature for cutting simulations. Split Hopkinson Tension Bar tests are performed after a cryogenic bath for 1 mm sheets of Ti6Al4V. As we know the goal in cryogenic machining is delivering an highly localized liquid jet of LN2 in a localized area so to avoid excessive heat build up on the tool side, but at the same time no overhardening of the workpiece should be ensured. Ideally the plastic work around the shearing zone should not increase the temperature of the workpiece much above the ambient temperature. Nevertheless, the work material is observed to freeze after cryohenic milling trials.

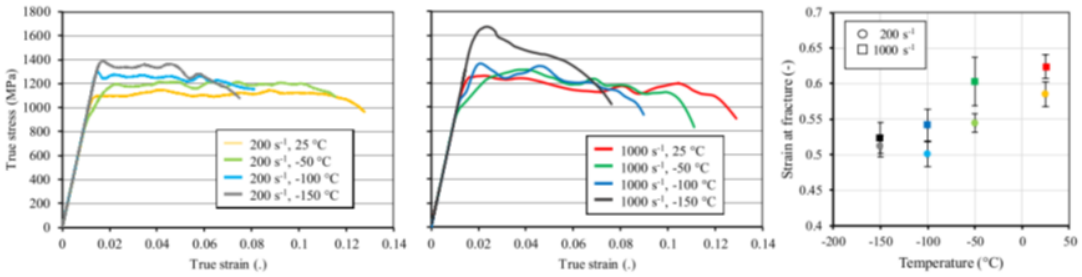

Figure 10.20: Split Hopkinson Tension Bar results for different strain rates and T on Ti6Al4V [14].

10.7. Computational fluid dynamics

CFD analyses play a fundamental role in the development of efficient cryogenic cutting setups. They allow to reduce the costs of experiments that would be need for the optimization of the process and permit to understand micro and macroscopic phenomena governing the interaction between the cryogenic fluid and the other actors of the process.

The goal is to maximize the heat transfer coefficient of the impinging jets minimizing the mass flow rate of fluid, reaching at the same time energetic, economic and manufacturing objectives. For example, with the help of CFD analysis it is possible to calibrate the velocity and pressure of the liquid jet that must be able to brake the vapour layer in contact with the hot surfaces of the cutting zone, limiting the insulating nature of it. At the same time too high velocities and pressures lead to high discharge coefficient in the delivery circuit, lowering the amount of fluid phase at the exit of the nozzle.

Properties of liquid nitrogen [102]:
N_2 liquid $(-196°C)$: $\rho = 803.6$ kg/m^3, $c_p = 2.046$ kJ/kgK, $\mu = 1.463 \times 10^{-4}$ Pa s, $\lambda = 1.320 \cdot 10^{-1}$w/mK
Properties of gaseous nitrogen: N_2 gas $(-196°C) : \rho = 4.979$ kg/m^3, $c_p = 1.351$ kJ/kgK, $\mu = 0.05331 \times 10^{-4}$ Pa s, $\lambda = 0.07658 \times 10^{-1}$ W/mK

The liquid phase is characterized by a higher specific heat, viscosity and thermal conductivity. This practically means that:

- A larger amount of energy is required to raise the temperature of a given mass of liquid by 1 °C compared to the same mass of gas.
- Some of the small end volumes would not be reachable in the liquid phase due to significantly higher viscosity (by a factor of 30), and the cooling and lubrication properties will differ from those of the gas phase.
- The thermal conductivity, comparing gaseous and liquid phases, differs by a factor larger than 10. This means that in the case of the liquid nitrogen phase, the heat transfer across the liquid occurs at a higher rate and does not depend on the work material that is machined.

When correlating these comparisons with the cooling capacity/capability of different nitrogen phases, it has to be taken into account that when nitrogen is delivered to the cutting zone in the liquid phase, a larger amount of heat is used due to its more favourable physical properties. Additionally, with the boiling mechanism (latent heat of vaporization for nitrogen is $Q_L = 199$ kJ/kg), a much higher cooling capability is expected with the liquid phase delivery. The major heat transfer mechanism involved during the application of LN is boiling heat transfer due to the fact that the applied LN is typically under super-critical status when pumped from a pressurized Dewar.
In the determination of heat transfer coefficient of a LN2 impinging jet, scientific literature is not univocal. In different works it is possible to find very different values.

Article	S.Y. Hong aug2001	S.Y. Hong oct2001	Jin 2009	Rotella 2014
$HTC_{LN2} W/m^2K$	$23270 \div 46750$	$48270 \div 74950$	$0 - 3500$	20000

Table 10.1: Heat transfer coefficient of LN2 in different articles.

But this variability is largely justified since there is not a standard equipment for the delivery of cryogenic fluid in the cutting zone and there are no standard values of pressure and velocity of the jet to be followed in the experimental campaigns/industrial practice. Between different works distance of the nozzle, spot size, incidence angle and other parameters may vary. Moreover, it is not easy to have a total control of the phase of the cryogenic flux that encounters the hot surfaces around the cutting zone. Always in [102] it is possible to find a newly developed optical nitrogen phase sensor with experimental verification of its robustness and response time in order to sense and control the delivered phase. From the results it is possible to assess that, with an optimized setup, a stable flow with almost only liquid phase is reachable only 100 s after the start of the delivery.

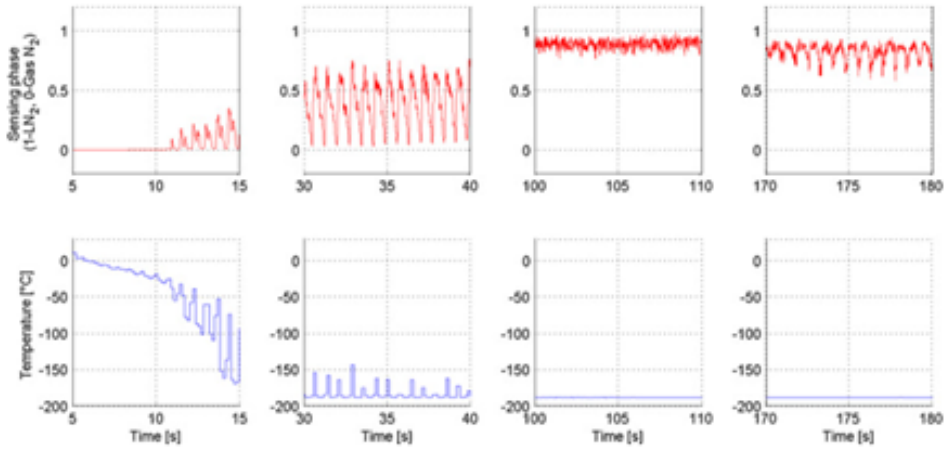

Figure 10.21: Flow phase monitoring [102]

The authors also want to determine an acceptable value of heat transfer coefficient for the impinging jet (jet speed=4.5÷7.4,m/s, pressure 1 bar). By inverse heat transfer determination on an overheated specimen (simulating the hot flank face of a tool on a workpiece) cooled down with a LN2 flux, they are able to extrapolate heat transfer coefficient values as a function of wall overheat temperature. It should be noted that after a certain overheating temperature $T_{\text{overheating}} > 200°C$, the HTC can be assumed constant around 20000 W/m^2K. Being the temperature of the chips or the tool faces

usually higher than 0°C it means that a constant value for the HTC of 20 kW/m^2K is a trustful approximation.

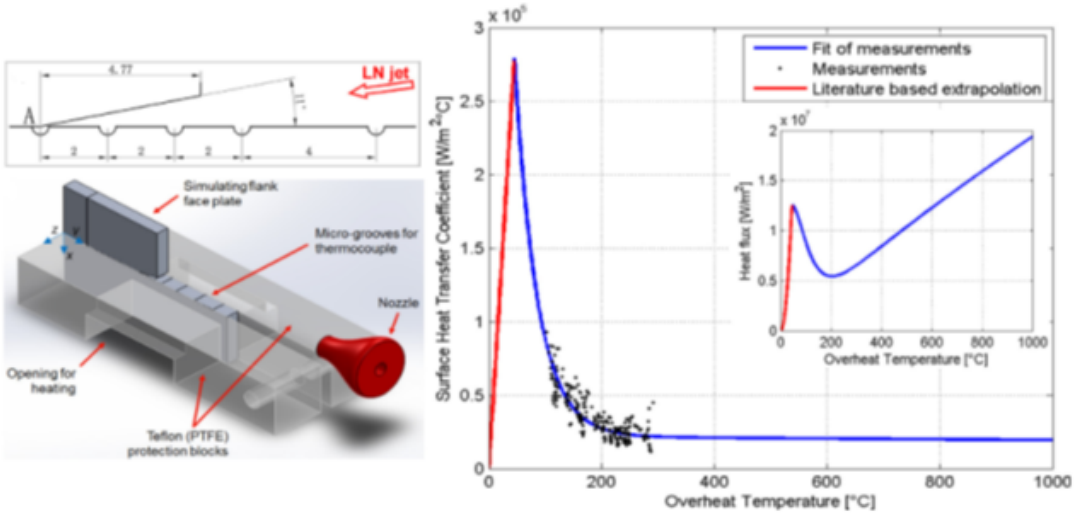

Figure 10.22: Heat transfer coefficient determination of impinging jet [102].

In [54] the authors present an experimental and simulated model to determine, by inverse methodology, the heat transfer coefficient of a normal impinging LN2 jet on an Inconel 718 plate. The trend of their results is very similar to the one presented before in [102]. The highest value of heat transfer coefficient of 75 kW/m^2K is reachable for a wall temperature which keeps Nitrogen (at least a part of it) at the liquid state. Above ΔT>160°C the heat transfer coefficient drops down at a value around 15 kW/m^2K.
In [130] the authors investigate the behaviour of LN2 inside the delivery circuit. The cooling effectiveness depends on pressure, velocity, temperature, gas/fluid fraction and pipe geometry. An optimized design of this last component of the chain is mandatory from the sustainability point of view. During the experimental campaign pressure varies (2, 4 and 6 bar), percentage of gas phase varies (10, 30 and 50 %) and also the bending angle of the final is variable. No influence of tube wall roughness or cavitation effect are taken into the account. Results show that a rectilinear pipe assures the higher liquid quality and the lower temperature increment, with no particular relevance of the pressure value. The final delivery sector must be rectilinear, or at least low angles for the final delivery sector to the nozzle are preferable.
In [77] the authors present an analysis on the heat transfer coefficient of impinging LN2 jet on a plate as function of incidence angle, nozzle diameter, distance from the plate and pressure of the jet. They studied the problem with CFD simulations with an iterative adjustment of the liquid quality and the assumption of a Gaussian normal distribution of

the heat flow. Higher heat transfer coefficients (around 15 kW/m^2K) are obtained with higher pressures, larger diameter, lower distance and perpendicular jet.
In [129] Tahmasebi and colleagues propose an evaluation of the behaviour of liquid nitrogen inside and outside the tubes of the delivery circuit. Differently from the previous works, in this case the cavitation boiling effect inside the tubes is taken into the account. In fact, it is responsible of the degradation of the liquid quality and clogs the tubes (with vapour bubbles) leading to unstable flow and non-negligible heat transfer phenomena with the tube walls. Then, outside the tube, the interaction of LN2 with the air and the inserts is studied. The figure below is explicative of the behaviour of the fluid inside a tube. Initially the flow is composed by a single liquid phase, then small vapour bubbles are generated due to the evaporation of the liquid subjected to heat exchange, the bubbles increase their number and size. At a certain point the amount of vapour is enough to occupy an entire section generating slug flow and clogging of the tube section. Also annular flow with liquid on the walls is a possible configuration.

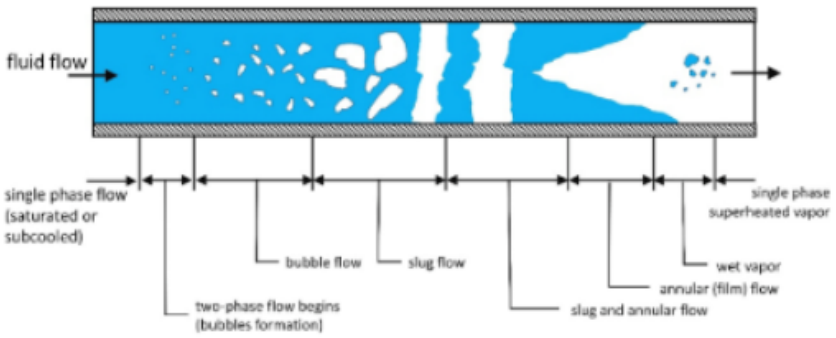

Figure 10.23: Behaviour of the LN2 inside a tube [129].

The analysis of the internal flow also comprehends the collector and tool holder channels of a cryogenic milling system. Even if the delivery line is adiabatic hydrodynamic cavitation is able to introduce important losses. Cavitation is modelled with HEM=homogeneous equilibrium model. The discharge coefficients are calculated assuming non-slip conditions with the tube walls and pressures of 2, 4, 6, 8 bar. The result show that higher pressures increase the losses due to cavitation.

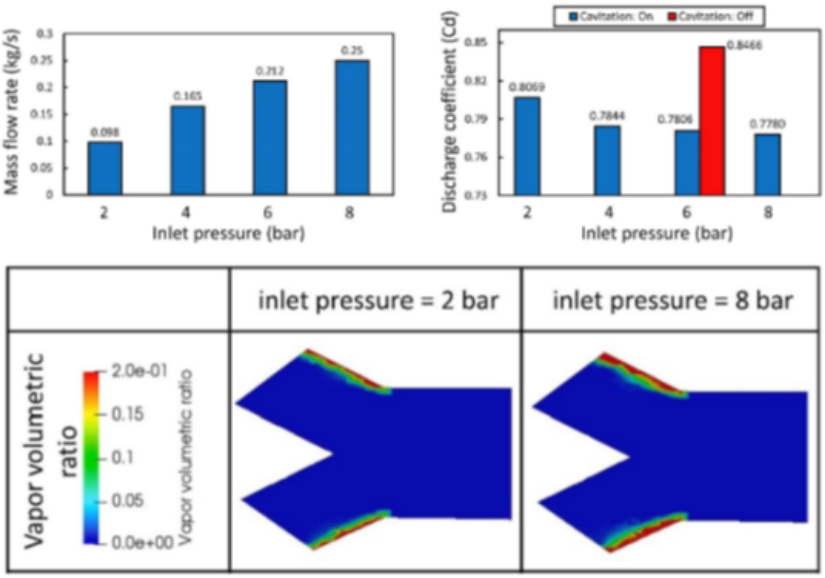

Figure 10.24: Mass flow rate and discharge coefficient as function of pressure and cavitation zones [129].

Accentuate tube bends cause pressure drops and subsequent vaporization of nitrogen. From this point of view the spindle collector is a risky part, also because it offers to the fluid a large non insulated steel area. A Nitrogen supply system should be designed with the minimal amount of surfaces for the liquid to exchange heat with. In this zone experimental observations and CFD simulations give different results, suggesting that the hypothesis of full liquid state at the entrance of the ring is not acceptable. Interesting findings come also from the analysis of the external flow (tested from 2 to 10 bar). The highest pressure do not lead to best results since the liquid leaves too rapidly the hot surfaces and it is partially deflected back from the insert faces. The cutting zone is proved to be surrounded by an higher amount of liquid nitrogen if the pressure is kept low. Experimental test confirms the finding of the CFD analysis. If liquid nitrogen is used at high pressures the performances are similar to the one of dry cutting, while at low pressure the cutting forces are reduced. The authors suggest a pressure range between 2 and 4 bar. With such low pressures the delivery system must be designed carefully avoiding accentuate bends to stay far from cavitation phenomena, and also limit the heat exchange area. These constraints bring efficiency both on the manufacturing and the economical point of views.

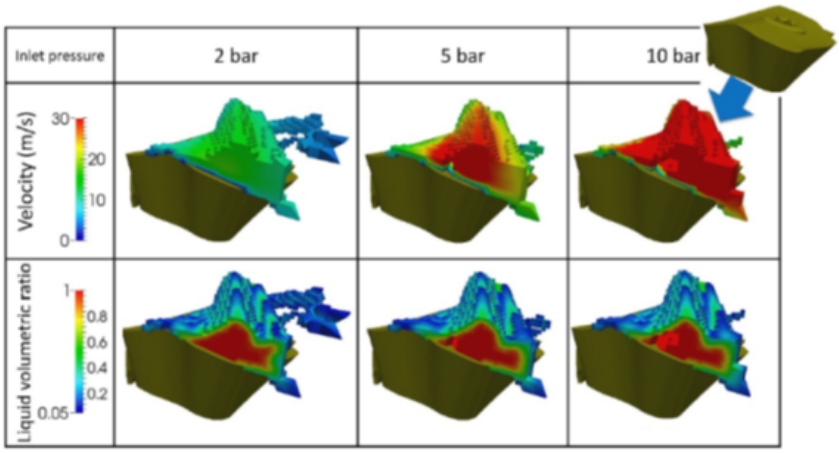

Figure 10.25: distribution of Nitrogen jet on the insert [129].

In [39] the authors concentrate their attention on the gaseous layer formed by nitrogen when in contact with an hot surface. In this circumstance the evaporation of the fluid is so fast that the contact time of the liquid phase with the hot spots is almost negligible if compared to the permanence time of the gaseous layer in this zone. They modelled the evolution of a gas layer formed on a jet parallel to the surface, the heat transfer is evaluated in the vertical direction. The experimental evidence is that the dimension of the gaseous layer grows proportionally to the distance from the nozzle. At lower speed of the jet corresponds a larger growth of the gaseous layer, the same behaviour is replicable adopting lower pressures. A larger gaseous layer brings to a reduction of the heat transfer coefficient. All these factors suggest that the heat transfer coefficient of a cryogenic jet sliding on a tool can be much lower than the ones proposed in the majority of the dedicated studies. According to the authors' findings, its order of magnitude is around 1 kW/m^2K. It is also important to notice that at the end of the crevice between the tool and the workpiece, the cryogenic jet is forced to stop its sliding. In this zone it is likely to find a portion of liquid able to break the gaseous layer, enhancing the heat transfer coefficient.

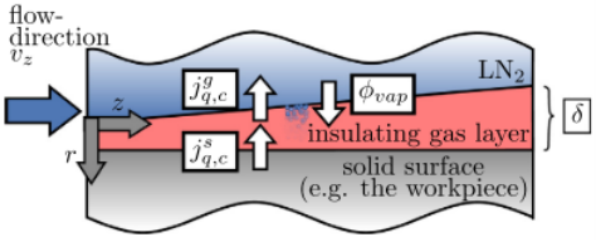

Figure 10.26: Insulating gaseous layer between workpiece and liquid flow [39]:

10.8. Cryogenic cutting simulations

It is not easy to find in literature examples of cryogenic machining simulations and the majority of them refers to simple operations (orthogonal cutting) way distant from the industrial practice. Anyway it is a fundamental starting point for further developments of this kind of simulations. In [18] it is possible to find the finite element simulation of a semi-finishing turning on Ti6Al4V, both in dry and cryogenic conditions. The authors here adopt a full Calamaz modification material model:

$$\bar{\sigma} = [A + B\varepsilon^n]\left[1 + C\ln\frac{\dot{\varepsilon}}{\dot{\varepsilon}_0}\right]\cdot\left[1 - \left(\frac{T - T_r}{T_m - T_r}\right)^m\right]\cdot\left[D + (1-D)\cdot\tanh\left(\frac{1}{(\varepsilon + p)^r}\right)^s\right]$$

$$D = 1 - \frac{T}{T_m}, \quad p = \left(\frac{T}{T_m}\right)^s$$

As friction model Coulomb-Tresca is adopted, with m $= 0.4, \mu = 0.3$ in cryogenic conditions and m $= 0.3, \mu = 0.2$ in dry conditions. A cryogenic window is defined and its heat transfer coefficient is set to $h_{\text{cryo}} = 20$ kW/m^2 K. Feed forces and temperatures of the simulation do not match accurately the experimental outputs, while the cutting force is well predicted by the finite element simulation.

In [28] the authors reproduce the chip formation during orthogonal cutting of Ti6Al4V, both in dry and cryogenic conditions. Unfortunately, no detailed information about the material model are provided. The friction model is a simple Coulomb one with μ=0.55 in dry conditions and μ=0.62 in cryogenic conditions. The heat transfer coefficient of the optimized jet zone, in cryogenic simulations, is set to 2000 kW/m^2 K that is larger than common values available in literature, but the authors justify it with the necessity of fast convergence of the thermal field. On the chip side, the morphology is well predicted by the model but low attention is given to the comparison of the segmentation of experimental and simulated chips. Both the cutting forces and feed ones are satisfactory predicted by the FE model.

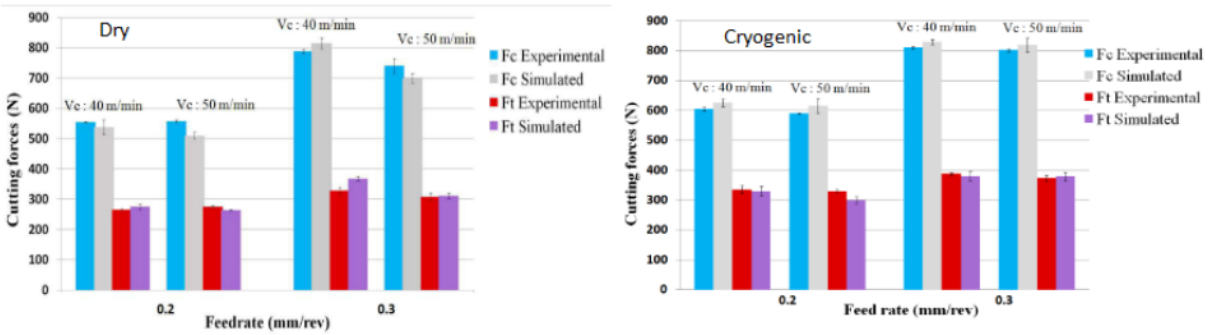

Figure 10.27: force prediction of FE model [28]

In [56] there is another turning simulation, always on Ti6Al4V both in dry and cryogenic conditions. Once again the material model is a full Calamaz modification and the coefficients A,B,C,n,m are the ones proposed by Lee and Lin, while a,b,c,d are taken from [121]. The friction model is a Coulomb-Tresca with m=0.95, μ=0.8 in dry simulations and m=0.6, μ=0.5 in cryogenic simulations. The heat transfer coefficient for the cryogenic jet is set to 20 kW/m^2 K, a value commonly reported in cryogenic machining studies. This set up gives very good results in the prediction of cutting forces, feed forces and chip temperature if compared with experimental results. Particular importance is also given to the prediction of the deformed layer left on the workpiece, which once again is well predicted by the FE model.

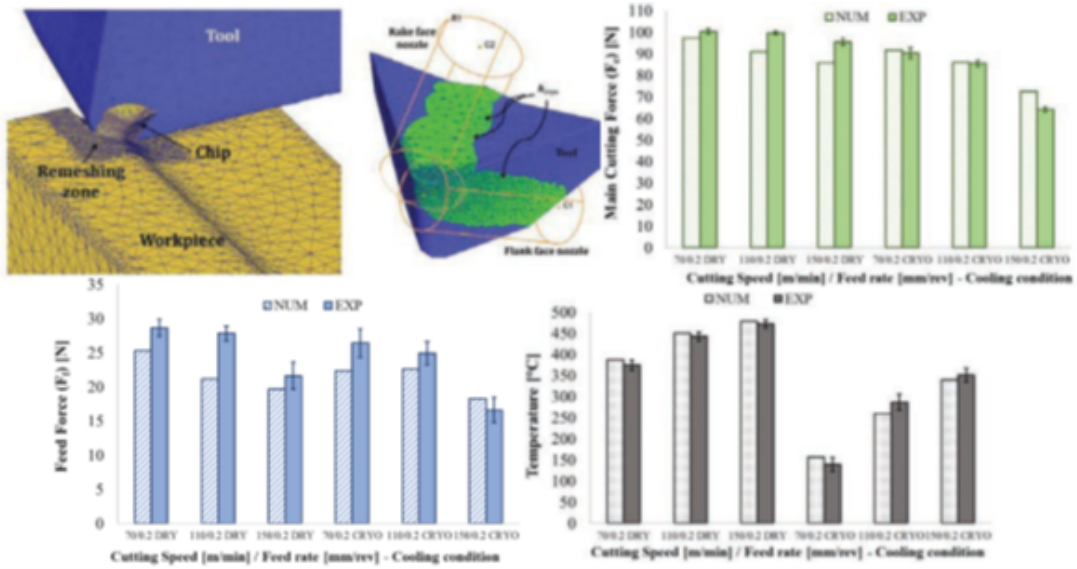

Figure 10.28: results of FE simulations [56]

Differently from previous works, in [123] finite element simulations are exploited in order to test different configurations of fluxes in cryogenic machining. Internal and external delivery of the jets are tested. The internal jet configuration was based on a micro hole in the insert at variable position and of variable diameter. The heat transfer coefficient is defined as function of the surface temperature, it increases for higher temperatures. This trend is not commonly adopted in other works and it is not confirmed by the dedicated literature. In parallel the heat capacity of the tool is strongly reduced to reach thermal steady state within the short time of the simulation. The system is surrounded by air which is characterized by an heat transfer coefficient of 100 W/m^2 K, a value higher than usual, justified by the authors due to the presence of cold nitrogen vapours in the surrounding of the cutting zone. Among the different configurations, the one with lowest tool temperature in FE simulations is composed by an internal channel at 1.5 mm from the

flank face and one external jet with 1.5 mm of contact length over the tool. In addition, the most effective internal channel is the one with the largest distance from the flank face, that is also the one that assures the higher robustness of the tool.

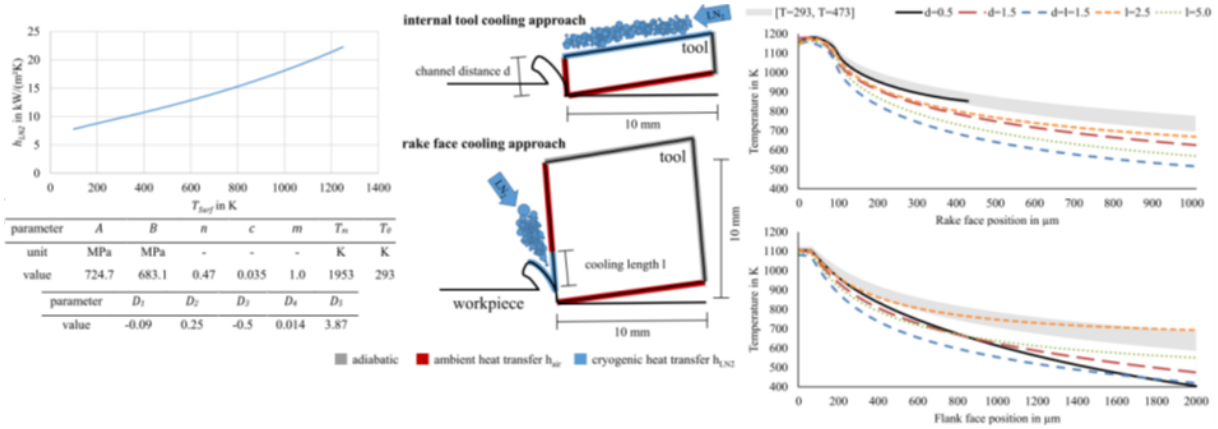

parameter	A	B	n	c	m	T_m	T_0
unit	MPa	MPa	-	-	-	K	K
value	724.7	683.1	0.47	0.035	1.0	1953	293

parameter	D_1	D_2	D_3	D_4	D_5
value	-0.09	0.25	-0.5	0.014	3.87

Figure 10.29: Parameter of the FE model, nozzle configurations and results [123].

An important review in the filed of cutting simulation is [85], the aim of the work is to analyse data, models and experimental techniques to describe the material constitutive properties, tool-workpiece friction, thermal and microstructure properties needed to model and simulate metal machining. The suggestion of the authors is to use a material model depending on strain, strain rates, temperature, stress state (triaxiality) and microstructure. They assess that due to the complexity of these models, generally phenomenological models are adopted, like JC and its modifications, Power Law, strain path models. After the first pass of the tool it is reasonable to have a microstructure transformation around the cutting zone, with a non-negligible effect on the properties of the material in correspondence of the new uncut chip thickness. Phenomena as recovery, recrystallization, grain growth, twinning, solid state transformations should (ideally) modify iteratively the material flow stress.

Analysing the complex problem regarding the friction models, they underline the influence also of motion, pressure, temperature, stiffness and vibrations. Friction is the most important parameter governing the temperature distribution on the tool face. The ideal procedure would be model the friction coefficient as $\tau_f = \tau_f(\sigma_n, \sigma_{flow}, V_{sliding}, T_{interface})$ but a precise temperature measurement at the tool interface is not an easy task, the risk is to invest a lot of effort in the friction model definition with moderate/low incidence on the results, considered also the fundamental bound between material model and friction model. Moreover, friction increases with the progressive wear of the tool. For a thermal analysis, in the review, the authors suggest the implementation of a variable heat transfer coefficient, that is preferable with respect to an average value. The other fundamental

factor influencing the thermal distribution of the analysis is the conductance at tool-chip interface. In the very last years also works combining both CFD and FE simulations have been published. Their detailed description goes far away from the aim of this work, but it is significant to briefly present some information taken from them. For example, in [115] the authors implement a hybrid model for the simulation of Ti6Al4 V cryogenic machining. RANS with Turbulence Kinetic Energy model are adopted, added by Multiple Cavitation Model approach to properly treat the double phase flow of nitrogen.
The heat transfer coefficient follows the equation $h_{\text{cryo}} = \frac{q}{\Delta T}$ with
$\Delta T = T_{\text{surface}} - T_{\text{fluid}}, q = k\frac{\partial T}{\partial x}$ where k = thermal conductivity of the hot target and $\frac{\partial T}{\partial x}$ = temperature gradient in the hot target.
On the CFD side the authors simulated a jet-on-plate configuration, the jet flows with a constant volumetric flow rate of 1 l/min and speed of 20 m/s, inside a nozzle of diameter d = 1 mm placed at 20 mm from the hot (700 K) target. The computed heat transfer coefficient varies between 20 and 50 kW/m^2 K. The finite element model is fed with $h_{\text{cryo}} = 32$ kW/m^2 K, $\mu = 0.28$ and Voce Power Law:

$$\bar{\sigma} = [a - be^{c\bar{\varepsilon}}] \cdot \left[\left(\frac{\dot{\bar{\varepsilon}}}{\dot{\bar{\varepsilon}}_0}\right)^d\right] \cdot \left[\left(\frac{T}{T_0}\right)^v\right], \quad [a, b, c, d, v] = [1705.2, 837.6, -1.92, 0.0048, -0.86]$$

The resulting forces predict very well the experimental measurements. Passing to the thermal side of the problem, the authors decide to simplify the cutting model into a 2D orthogonal one, considering the thermal convergence in a 3D simulation too time demanding. Once estimated the temperature at the tool-chip interface, the values are used to make an evaluation of the tool wear exploiting Usui's Law:

$$\frac{\partial w}{\partial t} = A \cdot \sigma_n \cdot V_s \cdot e^{Q/T}, \quad A = 7.8 \cdot 10^4 \frac{1}{MPa}, Q = 2500°\text{K}$$

Here the adhesive wear rate is related to the normal pressure, normal velocity and temperature. In particular Temperature has a huge weight, since wear rate is an increasing exponential function of it.

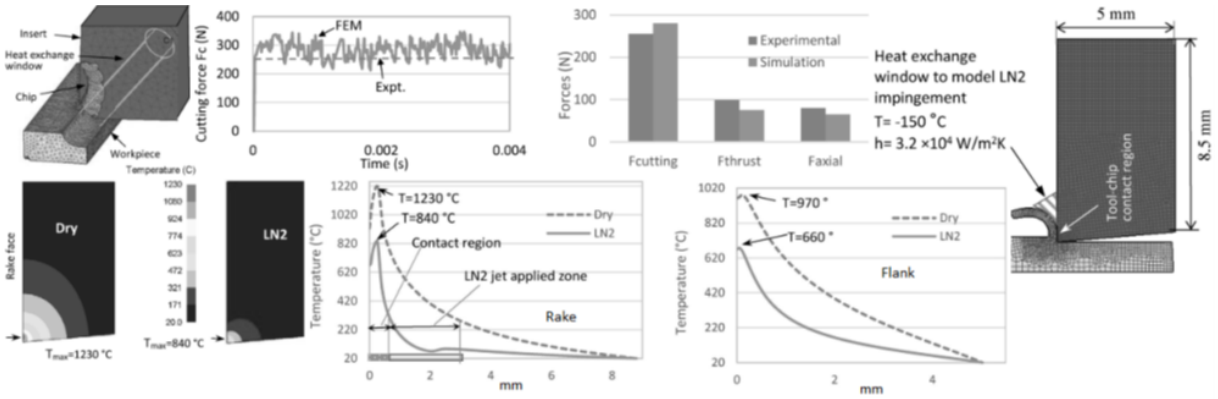

Figure 10.30: 3D model, forces results, 2D model and thermal field results [115].

10.9. Thermal analysis in a chip removal simulation

One of the clearest limitations of FEA in the machining filed is the huge duration of a single simulation, in which just few milliseconds or cents of second are actually simulated. The motivations are multiple, first of all the mesh size must be really small both on the workpiece and on the tool side, and the gradient of refinement should be smooth and gradual in the surrounding of the cutting zone in order to have reliable results. So large zones of really fine mesh (also under 0.05 mm as characteristic dimension) must be adopted and in a 3D problem the number of nodes becomes huge. Obviously the problem is not static at all, the cut is generated by the relative motion of cutter and workpiece. Displacements and deformations are huge if compared to the scale of the mesh, thus multiple and frequent remeshings are mandatory to avoid excessive distortion of the elements, increasing exponentially the time required for the simulations. Moreover the contact conditions must be updated with minimal time steps; the thermal problem is strictly bounded to the mechanical one, the temperature build up influences the mechanical properties of the components involved in the simulation, so once again small mesh size, remeshing and short time steps are required. Also with powerful resources of calculus the simulation of more than one revolution of a milling insert is hard for time and storage space required. In a turning procedure, the temperature of the cutter needs a certain amount of time in order to reach a steady state value, once kept constants all the working parameters.
In this case it is necessary to play on the conductance coefficients of the tool-chip interface, increasing them (above 10 kW/m^2 K), it is possible to reach steady state values (similar to the ones measurable in experimental trials) within the limited time of a simulation covering just a portion of a cutting revolution. This approach has obviously some limits, it is like depositing a super conductive layer between tool and chip, which is clearly unphysical and it would require perfect contact (which in reality is not present) but it is a

necessary compromise.
Anyway a significative number of studies cover this topic in case of orthogonal cutting or simple turning operations, it is not the same in case of milling where the exact calibration of interface conductance is still an open question due to unsteady nature of the process itself.
From the studies of Umbrello and colleagues [134], that compare the temperature developed in a short FE 3D thermal simulation with the data coming from tool-embedded thermocouples, through iterative update of the conductance at the tool chip interface, an agreement between simulated data and experimental one is reached around 1000 kW/m^2 K, clearly an unphysical quantity. The operation is orthogonal cutting of AISI/SAE 1045 with cemented carbide ISO P20. This study confirms that short simulations with modified conductance and 3D pure thermal calculations are able to reproduce the thermal field in the insert at steady state.

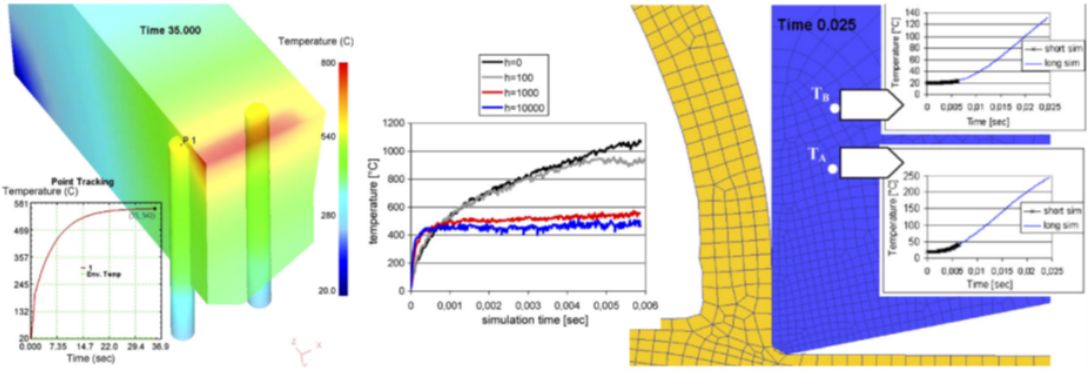

Figure 10.31: Experimental and FE set up, experimental and FE temperatures comparison [134].

Also in [23] it is possible to find an analysis of conductance values at the tool-chip interface. The authors study the material couple of AISI 1045 and both coated and uncoated carbide inserts. The friction phenomenon is treated with a Coulomb-Tresca model and the heat transferred to the tool is divided into two contributions. The first one accounts for the heat generated by shear friction $Q_1 = \tau_f * v_s * J * \lambda$, where J = energy conversion factor, τ_f = shear stress at the interface, v_s = sliding velocity, λ = heat partition factor. The second one accounts for the heat transferred due to a difference of temperature between the tool and the chip $Q_2 = h\,(T_w - T_t)$, where h =heat transfer coefficient, T_w = workpiece contact temperature, T_t = tool contact temperature. They test different cutting parameters in the 3D finite element analysis and every time they update the interface conductance until convergence with experimental data from thermocouples. The results of these procedure show that with higher cutting speeds higher temperatures and pressures on the rake

face arise, the cutting forces slightly decrease but the contact length decreases more, thus conductance increases. With higher feed rates higher temperatures arise, forces increase but not as much as the contact length leading to lower average pressures, thus the conductance plot will show a minimum.

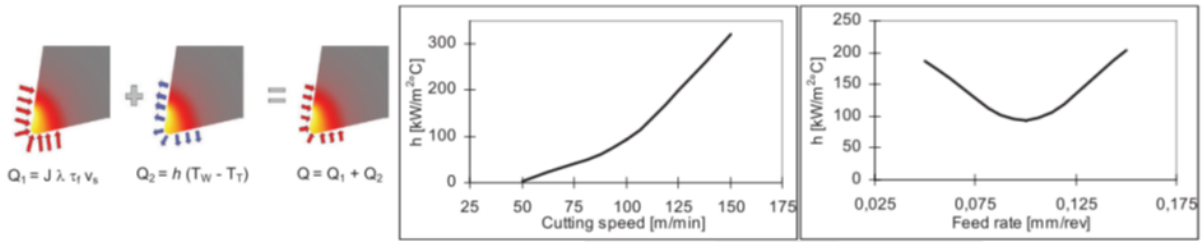

Figure 10.32: Heat transfer model and h variation with cutting parameters [23].

Development of the high feed milling FE model

11 | Simulation set up and model validation

This section describes the design of a finite element model for high feed milling of Ti6Al4V both in wet and cryogenic conditions and the results of the simulations are discussed.

Other students (A.Elefanti and L.Losa), in the past years, developed FE models of square shoulder milling of Ti6Al4V.
Experimental studies demonstrated how the application of cryogenic cooling in case of square shoulder milling can reduce the tool life with respect to the application of wet lubro/cooling strategies. Successive studies [3] demonstrated how the application of cryogenic cooling in case of high feed milling (keeping the same delivery system for the cryogenic fluid) can enhance the tool life with respect to the application of wet lubro/cooling strategies. Thanks to FEA it is possible to better investigate mechanical and thermal stresses acting on tool and workpiece during the cutting phase. This will possibly help in understanding the reason of such a different behaviour on tool life basis of the two milling strategies, and if the reason is inside a particular combination of pressure and relative speed on the tool skin or if it is inside the different thermo-mechanical solicitation history seen by the tool.
Once chosen the material model, many iterations are necessary to properly calibrate the FE model comparing the computed results with experimental results (where available) and following literature indications / reasonable results where experimental ones are not available. The variables to be adjusted are many: mesh size, kinematics, friction coefficients, damage model, heat transfer coefficients and so on, facing also the lack of reliable experimental data in some fields (as thermal field).
It is fundamental to find a set up able to provide reliable results in relatively short time in order to accelerate al the calibration procedure. Moreover, no data on high feed milling in dry conditions were available that would have been the simplest condition to calibrate thanks to the absence of an external cooling media if not hot air.

In the thesis work by L.Losa [81] there is a deep literature review on cryogenic machining and machining simulations on Ti6Al4V, a finite element model for sqaure shoulder milling has been validated both in dry and cryogenic machining. It is interesting to understand if a similar model is adaptable to high feed machining. In particular the material model and the damage models are the same, because also in this case they demonstrate their effectiveness and in cryogenic conditions the heat transfer coefficients with ambient media and tool-wp conductance at the interface are the same. In this way also a comparison of the results is possible between the two models. The main differences between them are the friction coefficients adopted, choice driven by the comparison with experimental results and some boundary conditions as initial temperature of the worpiece and tool skin's temperature profile.
No similar works on wet machining were available, so all the choosen quantities are calibrated in order to get closer to experimental results.

The finite element sftware used in this work is Forge Nx T 3.0. It is basically conceived for forging and more in general for metal deformation procedures. So, it easily deals with important deformations and phenomena bounded to friction or heat exchange. All the bodies in the simulations are addressed as dies and they can be rigid or deformable. According to the available license, the software allows the computation on multiple cores. The simulations were run with 16 cores on a 60 core – 4 processors workstation with 2.5 GHz base clock speed and 356 GB DDR3 RAM.

11.1. Geometry Generation

A good result in the finite element simulation largely depends on the precision of the involved geometries. In particular for complicated shapes, it is necessary to create a CAD model, convert it into an .stl file and import it in the FE software to complete the set up and perform the simulations.
The CAD file represents a portion of the Ti6Al4V workpiece and a portion of the cutting tool. More in detail, the tool is the one descripted in [3], thus a 20 mm diameter tool with Z=3 inserts from Mitsubishi (Tool body: AJX06R203SA20S and isnert: JOMT06T216ZZER-JL MP9140).
The cutting inserts are formed by a carbide substrate and PVD coating characterized by an Al-rich (Al,Ti)N single layer. On the Mitsubishi website it is possible to find DXF, STP and STL files representing the tool holder and the cutting inserts.

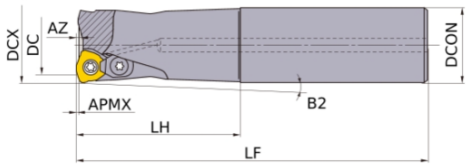

AZ	0.3
DC	12.9
DCX	20
DCON	20
B2	1°18'
RMPX	1.5
LF	130
LH	50
APMX	1
GAMP	+4°
GAMF	-6°
Cutting item count: CICT	3
Peripheral effective cutting edge count: ZEFP	3

Figure 11.1: Tool body AJX06R203SA20S from Mitsubishi website.

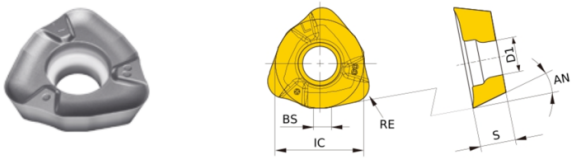

D1	2.95
IC	6.35
AN	13°
BS	1.2
S	2.78
RE	1.6

Figure 11.2: Insert JOMT06T216ZZER-JL MP9140 from Mitsubishi website.

Looking at the centre of the cutting insert (attached through a screw to the tool holder) during the cutting operation it follows a cycloid trajectory that is the combination of linear feed and rotation of the mill. Its position is described by the equation:

$$\bar{x}(t) = \begin{bmatrix} x(t) \\ y(t) \end{bmatrix} = \begin{bmatrix} -Re\left\{d \cdot e^{j\vartheta}\right\} + S_f - S_t \\ -\operatorname{Im}\left\{d \cdot e^{j\vartheta}\right\} \end{bmatrix}, \quad \begin{cases} \vartheta = \left(\frac{\pi}{2} - \theta\right) + \omega \cdot t - S_\theta \\ S_f = v_f \cdot t \end{cases}$$

In which: d = radius of the trajectory = distance from tool holder centre and insert fixing screw centre, $S\theta$ = engagement shift (along the arc), St = translation shift of the tool centre (along the holder feed direction), v_f = linelar feed in mm/s,
ω = rotational speed in rad/s.
Using Excel, it is possible to plot the trajectory followed by the tool centre of different teeth one after the other.

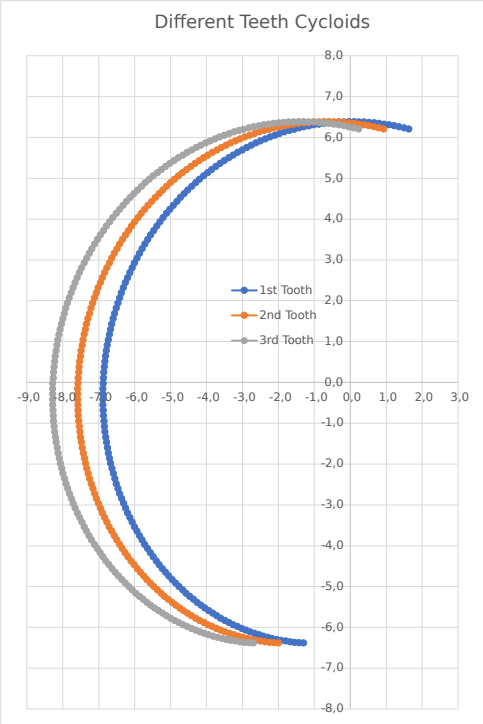

Figure 11.3: Arc of cycloid for three teeth with fz = 0.7 mm/rev*tooth (axes are reported in mm).

For the generation of the CAD file, Autodesk Inventor 2021 has been used. First of all a point has been selected as centre of the entire project and the trajectories of two subsequent teeth from Excel as CVS splines have been imported, taking as reference (centre of cycloids) the previously selected point. Then a parallelepiped has been extruded below these trajectories, calculating a final radial engagement = ae = 13 mm = 65% on the tool (nominal) diameter.

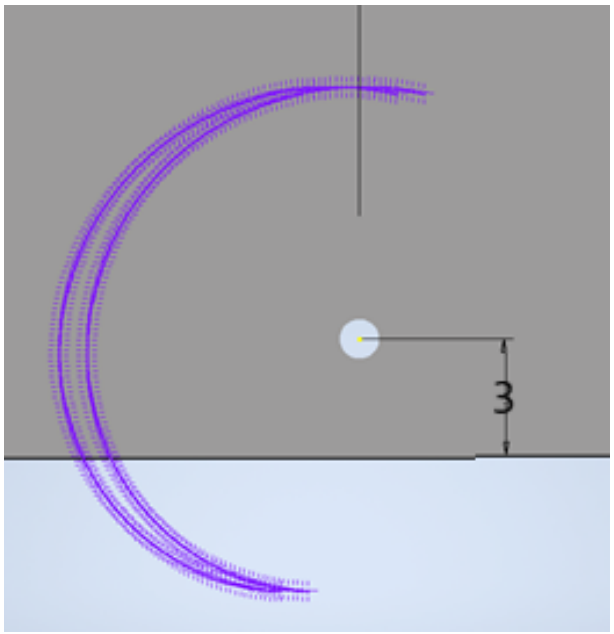

Figure 11.4: Workpiece positioned to guarantee ae = 13 mm.

Then the tool has been imported, fixing its vertical axis perpendicularly to the upper face of the workpiece and passing through the centre point. After that the vertical position of the workpiece was adjusted in order to guarantee an axial depth of cut = ap = 0.4 mm. The tool has been positioned to have the centre of a cutter exactly on one of the points of the spline of the first tooth, a z-y plane tangent to the lower edge of the cutting insert has been created and the external profile of the cutter has been projected on it. Then a swipe cut of this geometry was imposed following the spline of the first tooth. The projection introduces a little approximation into the model because it limits the influence of radial and tilting angles of the cutter. Anyway on CAD software it is not possible to perform a swipe cut with a 3D object on another 3D object so the only option is to perform the cut with this 2D profile accepting the small approximation introduced that is smaller in the first part of the cutting arc and larger in the final part of the cutting arc.

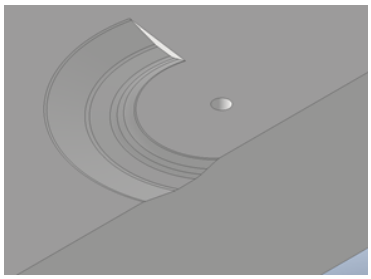

Figure 11.5: Track of one tooth on the workpiece.

Now, considering that the second tooth performs the same trajectory as the first one just shifted along the negative X direction of 0.7 mm (being fz = 0.7 mm/rev*tooth) the tool has been shifted of 0.7 mm in that direction. This prepares the passage of the second tooth, positioning it in a known position and avoiding the introduction of further approximations. Once positioned the tool for the upcoming cutting passage it is possible to cut the model maintaining only the strictly necessary parts for the finite element analysis, in order to reduce the volume of the model thus the number of necessary nodes thus the computational burden.
The necessary pats are a portion of the workpiece and a portion of the cutting insert. The dimension of the final workpiece are such that the temperature increment at the external boundaries due to conduction never goes much above the initial temperature (+/- 50°C). Finally it is possible to convert the file in an .stl file and import it on FORGE.

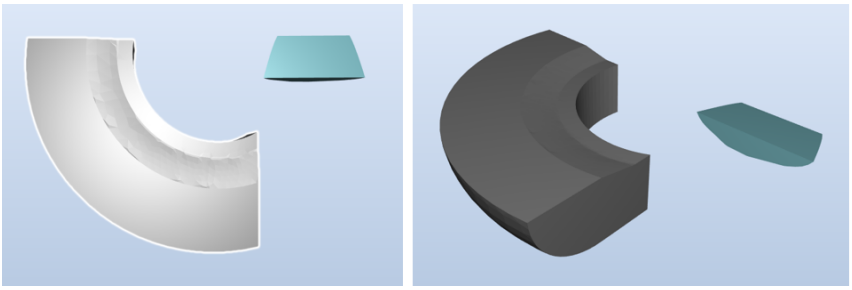

Figure 11.6: Workpiece and tool imported on Forge.

11.2. Motions

The workpiece is maintained fixed thanks to a 3D manipulator, that is defined as a portion of volume and all the nodes inside it can be moved or kept fixed. In this way, the adoption of any other rigid fixed die it is not necessary to keep in the correct position the workpiece, thus no other nodes of mesh are added.
Moreover, the 3D manipulator does not influence the thermal exchange between workpiece and external environment.

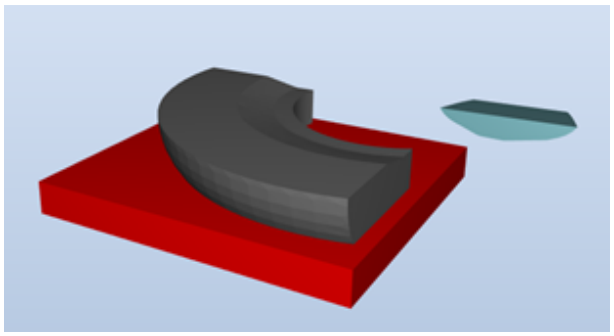

Figure 11.7: Application of the 3D manipulator.

Acting on the cutter, the kinematics of the arc of cut was imposed.
On Forge it is possible to apply complex motions to the involved parts, selecting for example "Generic Press" in the library. Here it is possible to define the speed of revolution of the tool in rpm:

$$n = \frac{V_c * 1000}{\pi * D}$$

where V_c = cutting speed [m/min], D = nominal diameter of the tool [mm]. And the linear feed [mm/s] in one of the three directions (-X in this case) equal to:

$$V_f = \frac{n}{60} * f_z * Z$$

where n = number of revolutions per minute [rpm], fz = feed per tooth [mm/rev*$tooth$], Z = number of teeth.
It is important to define the axis of rotation of the tool, recalling the procedure adopted in the geometry generation phase, the cutter is shifted 0.7 mm towards −X so the centre of rotation is initially located at the coordinates $[-0.7, 0.0, 0.0]$.

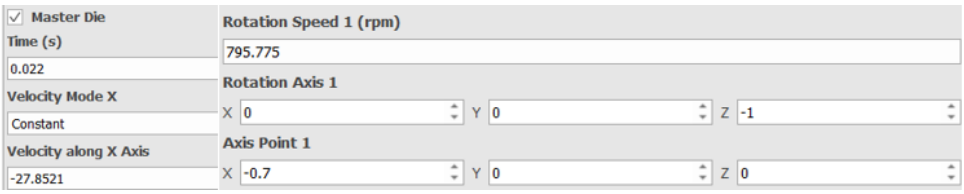

Figure 11.8: Values given at the generic press with Vc=50m/min and fz=0.7 mm/rev*tooth

The software allows a preview of the kinematics, useful for every needed adjustment in this preliminary phase.

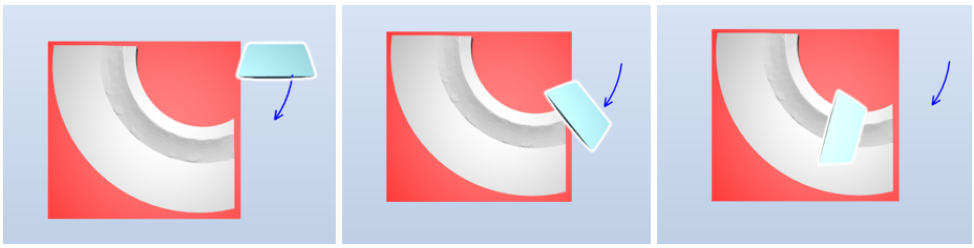

Figure 11.9: Animation of the cutting process.

11.3. Mesh Generation

The quality and the size of the mesh are crucial aspects in finite element analyses. Forge uses a Lagrangian formulation and a built-in remesher. The geometry of the mesh can be directly defined on the software interfaces in case of simple geometries as boxes or cylinders. Alternatively, it is possible to define volumes as off-sets of existing parts or design a particular volume in a CAD environment and import it. The geometry of the mesh as well its characteristic dimension must be calibrated after some trials. A reliable and repeatable result must be achieved in a reasonably short time.
The software provider suggests that the characteristic dimensions of two neighbouring mesh regions should not overcome a multiplication factor of 4. If this constraint is not satisfied the possibility to encounter errors during the simulation considerably grows up. After some trials I decided to mesh firstly the entire workpiece with elements of 1.4 mm as characteristic dimension. Then I passed to 0.4 mm in a zone around the trajectory of cut with a fixed box. I defined two boxes attached to the tool's centre of gravity, one smaller with characteristic dimension of 0.05 mm, one bigger with a characteristic dimension of 0.1 mm. This is done because a different configuration (really fine mesh permanently attached to the workpiece) requires a longer time of computation (mainly due to remeshing). Doing so, the tool always finds a fine mesh of 0.05 mm on its way, and the chip is free to evolve in a fine mesh region without strong changes of characteristic dimensions able to stop the simulations.

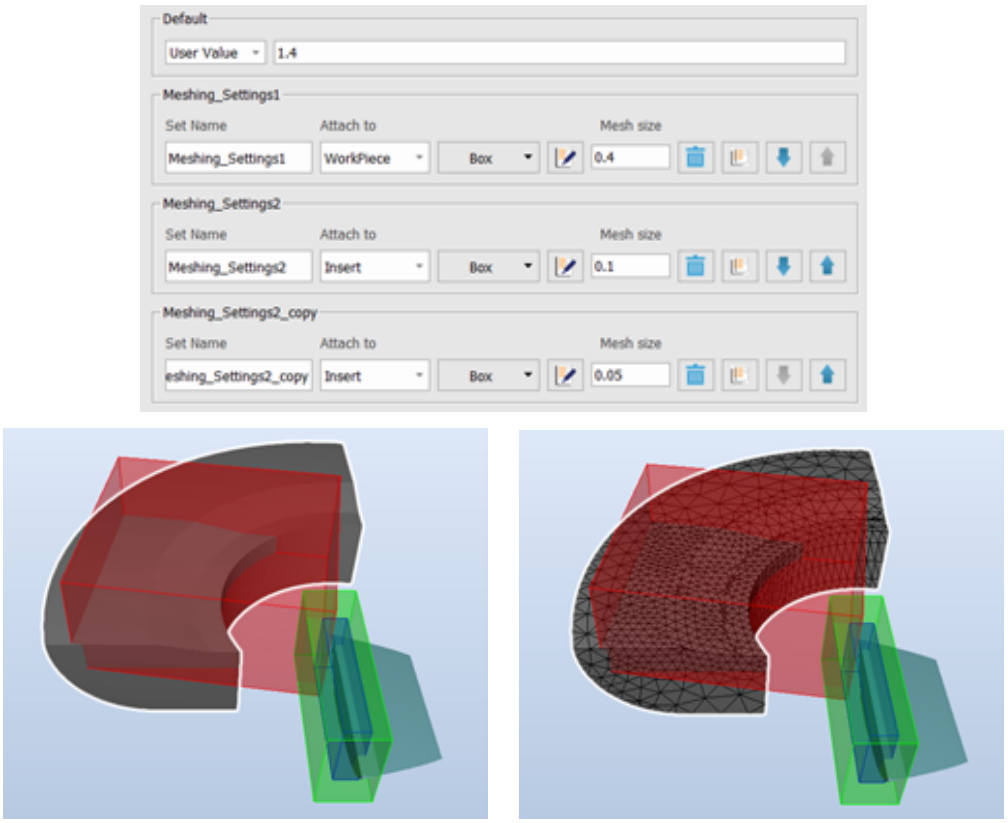

Figure 11.10: Meshing parameters and meshing boxes on the workpiece.

On the tool side I meshed with a series of boxes starting from 0.075 mm in the front and progressively enlarging until the back side of the cutter.

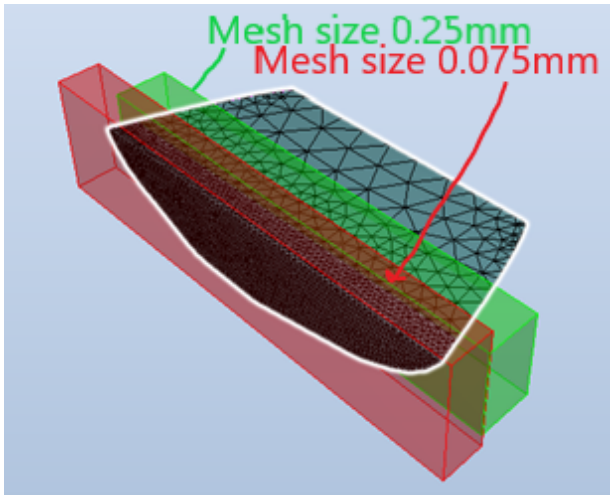

Figure 11.11: Mesh boxes on the tool.

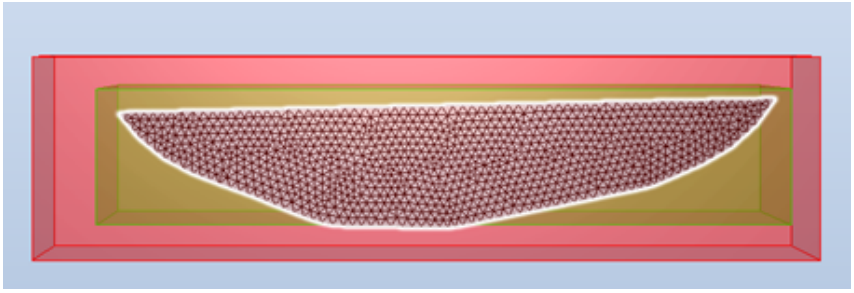

Figure 11.12: Front view of the cutter.

In case of large strains and distorsions with respect to the characteristic dimension of the elements, the mesh must be often updated and this is done thanks to the remeshing algorithm of the software. Frequent remeshing are mandatory considering a chip removal operation as high feed milling and they hugely influence the duration of the simulations. In this case the software remeshes the workpiece both on deformation basis (factor 1 m/m) and on period basis (factor 20).

11.4. Thermal interaction between tool and workpiece

When the contact behaviour between two bodies is defined on Forge, the software needs information both on the friction model, both on the thermal exchange between the bodies involved.
For the thermal part two quantities are needed the thermal conductivity between the two bodies and the thermal effusivity (when one of the two bodies is rigid). In the case of the carbide tool the effusivity is:

$$e = \sqrt{\rho * K * c_p} = 1111\frac{W}{K} * \sqrt{\frac{s}{m}} \quad \text{with } \rho = 15250 \text{ kg/m}^3, K = 44.03\frac{W}{m * K} \text{ and } c_p = 188\frac{J}{kg * K}$$

The thermal distribution of the rigid body (tool) is not computed by the software and only a series of values (representative of the average tool skin temperature during the cut) are taken as inputs. On these values no experimental data are available.
The effusivity is used to calculate the portion of shared heat through friction:

$$q_{\text{tool}} = \frac{\sqrt{K_t \rho_t c_t}}{\sqrt{K_t \rho_t c_t} + \sqrt{K_w \rho_w c_w}} \cdot q_f = \frac{eff_{\text{tool}}}{eff_{\text{tool}} + eff_{wp}} q_f = \beta \cdot q_f$$

where the heat generated by friction is:

$$q_f = \tau_f \cdot v_{sl}$$

and $q_{wp} = q_f - q_{\text{tool}} = q_f * (1 - \beta)$ is the heat that flows into the workpiece due to friction. β is called heat partition coefficient, the properties of the tool (rigid body) are not modified during the simulation while the properties of the workpiece (deformable body) are function of the temperature (see next section) so the heat partition coefficient is not constant and varies with T_{wp}.

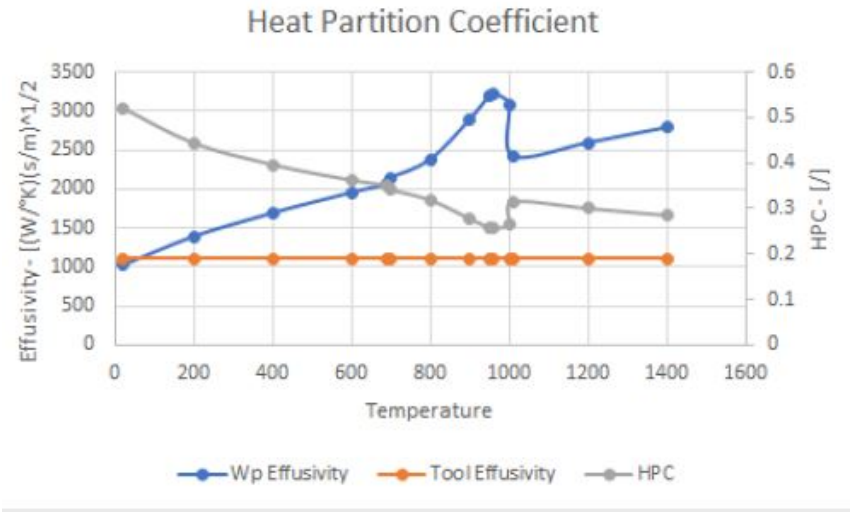

Figure 11.13: heat partition coefficient as function of T.

The heat shared through conduction between tool and workpiece is
$q_{\text{tool}} = K * (T_{wp} - T_{\text{tool}})$ where T_{wp} = skin temperature of the workpiece in the contact zone with the tool, T_{tool} = skin temperature of the tool, K is the tool-workpiece interface conductance.

11.5. Friction behaviour modelling

As underlined in the dedicated chapters, the friction behaviour plays a fundamental role in the thermal problem. At the same time strong efforts in the characterization of contact models, looking at the available literature, do not significantly improve the final results

with respects to more common and simple models. For this reason, a standard Coulomb-Tresca model has been adopted.
$F_f = \mu * F_n$ is the formula to compute the friction force in case of Coulomb friction. It is the most common formulation used for solid friction. Between the two bodies in contact is present a force proportional to the normal reaction between them.
However, it is completely neglected the possible modification of the actual force in case of deformation of the bodies. In this case the Tresca friction model is used: $\tau_f = m * \tau_{lim}$, where m is a coefficient and τ_{lim} is the shear stress limit. Combining the two models, it is possible to implement a slide/stick contact model where:

$$\tau_f = \begin{cases} \mu * \sigma_n \text{ if } \mu * \sigma_n < m * \tau_{lim} \\ m * \tau_{lim} \text{ if } \mu * \sigma_n > m * \tau_{lim} \end{cases}$$

limiting the possibility of the coulomb friction to overcome the shear stress limit of the material.

11.6. Material model

The previous works on this topic have been developed on two different material models. A.Elefanti used Pittala and Monno [99] material model, while L.Losa used JC with coefficients from Lee and Lin [76] reached superior results. Since this work wants to find the motivation of different behaviours on tool life basis between square shoulder (Losa's Model) and high feed milling in case of cryogenic machining, it is convenient to adopt the same material model of the work of L.Losa to have reliable data on which propose speculations.
Johnson Cook model in this case [76] takes the coefficients
$[A, B, C, n, m, \dot{\varepsilon_0}] = [782.7, 498.4, 0.028, 1.0, 10^{-5}]$. The authors in the article investigated the high-temperature deformation behaviour of Ti6Al4 V alloy using the split Hopkinson bar. The specimens were deformed under a constant strain-rate of 2×10^3 s^{-1} at an initial temperature varying from $700 - 1100°C$ at intervals of 100°C. They demonstrated that temperature has a significant effect on the flow behaviour of the material. The strength of the material and the work-hardening coefficient decrease rapidly with an increase in temperature.

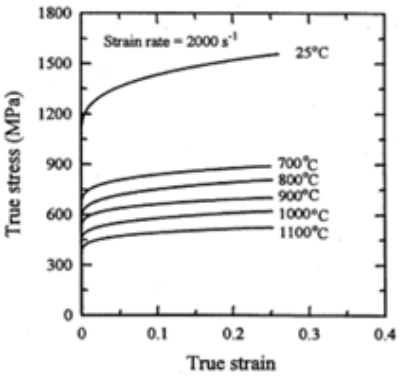

Figure 11.14: Typical true stress–strain curves of Ti6Al4V alloy deformed at different temperatures at the high strain-rate of 2×10^3 s^{-1} [76].

This can be explained by the increasing temperature decreasing the density and multiplication rate of dislocations, and consequently, resulting in a loss of resistance to plastic flow, therefore, the material becomes softer and more ductile. When a material deforms under both high temperature and high strain-rate conditions, its flow behaviour is predominated by a competition process between the rate of work hardening and the rate of thermal softening. Generally, high-rate deformation can cause the enhancement of a material's strength due to the high rate of work hardening. By contrast, an increase of temperature will lead to a rapid reduction in the rate of work hardening. When thermal softening becomes dominant, the plastic flow is controlled completely by the temperature effect which results in a rapid drop of flow stress. the variation of flow stress with temperature shows a linear relationship with a sharp gradient, which implies that there is a large change both in the density and the distribution characteristics of dislocations.

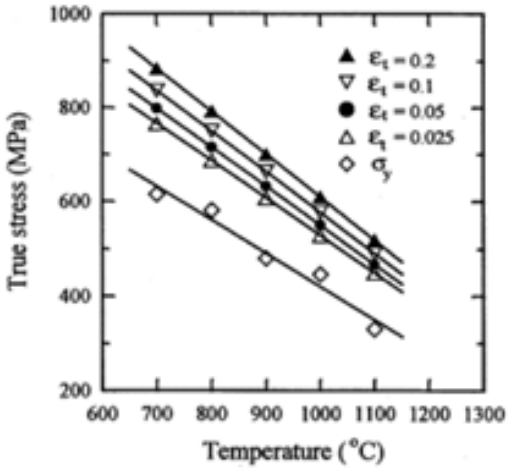

Figure 11.15: Variations of flow stress and yield stress as a function of temperature [76].

The Johnson-Cook model assumes that the dependence of the stress on the strain, strain rate and temperature can be multiplicatively decomposed into three separate functions:

$$\sigma = (\mathrm{A} + \mathrm{B}\varepsilon^{\mathrm{n}})\,(1 + \mathrm{C}\ln\dot{\varepsilon}^{*})\,(1 - \mathrm{T}^{*m})$$

A = yield strength sensitivity of the material, B = strain sensitivity of the material, C = strain rate sensitivity of the material, $\dot{\varepsilon}^{*}$ = normalized strain rate = $\frac{\dot{\varepsilon}}{\dot{\varepsilon}_0}$ = $\frac{\text{effective platic strain rate}}{\text{reference plastic strain rate}}$, T^{*} = normalized temperature = $\frac{T-T_0}{T_m-T_0}$, T_m = melting temperature of the material, T_0 = reference temperature of the quasi static test used to determine the material constants.

Then the authors, basing on experimental data and performing regression analysis were able to extract the value of $[A, B, C, n, m, \dot{\varepsilon_0}]$ as listed above.

Other properties of the material are given from the software in tabular form and they are Young's modulus, thermal conductivity, Poisson's ratio, density, specific heat and linear expansion. The values are plotted until a temperature of 1500°C while no data are available at cryogenic temperatures. In order to speed up the calculations it is useful to summarize these data with a reduced number of datapoints and include them in the same file of the rheological model.

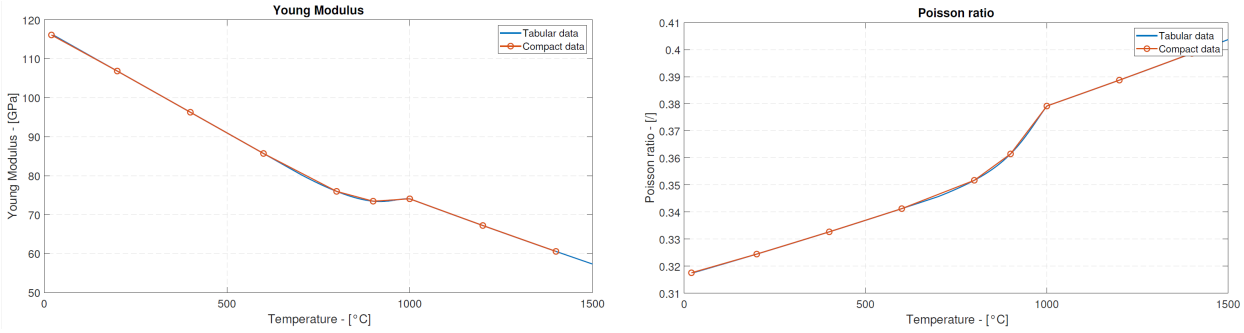

Figure 11.16: Young Modulus and Poisson Ratio of Ti6Al4V as function of temperature.

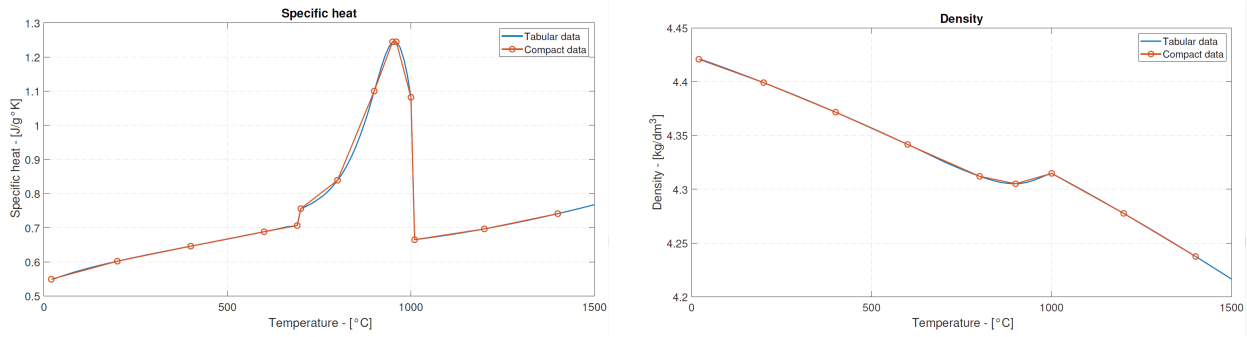

Figure 11.17: Specific heat and density of Ti6Al4V as function of temperature.

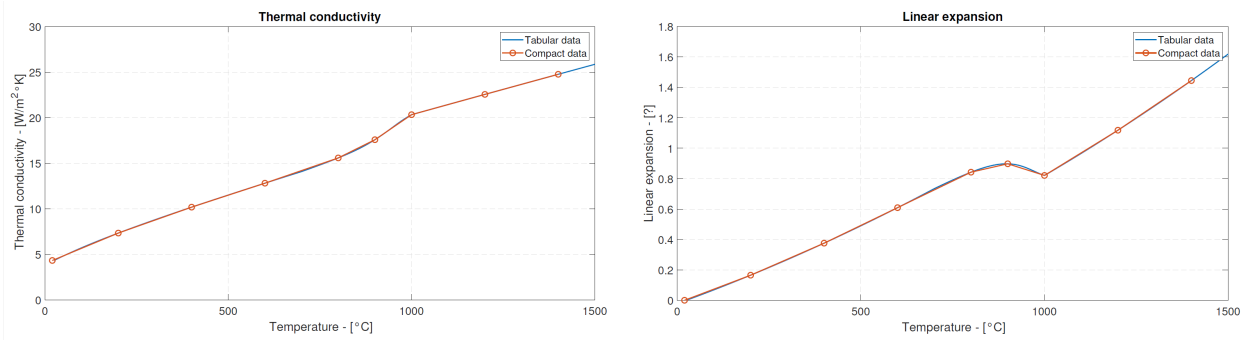

Figure 11.18: Thermal conductivity and linear expansion of Ti6Al4V as function of temperature.

11.7. Damage Model

In this work the main use of the damage model is directed to the prediction of the chip morphology, in particular its level of fracture. The used model is a simple Latham-Cockcroft which is decoupled from the stress flow of the material which means that an element keeps its full strength until it fractures and it is eliminated from the calculations. In literature, LC or JC damage models are always used. JC modifies the strength of the element from the first application of the stress to the failure of the element, providing a realistic and gradual fracture evolution, but the calibration of such a model is way longer than the one of Latham-Cockcroft.

Every simulation lasts several days so a model with an easier calibration is more useful. On Forge there are several other damage models: Oyane, Lemaitre, Rice and Tracey and Transvalor self-modified LC. The coefficients needed in their calibrations are not easy to be found in literature and to avoid other uncertainties inside the model the choice was the simple Latham-Cockcroft:

$$\int_0^{\varepsilon_f} \sigma_1 * d\varepsilon = D$$

11.8. Experimental set up

A cryogenic setup was conceived and developed. It was installed and tested on a 5-axes machine tool (Flexi model by Sigma, FFG group). A flexigas (pressurized liquid nitrogen reservoir) was placed on the back of the machine. The associated piloting electro-valve, a vacuum jacket flexible pipe, and a phase separator that is used to purge the evaporated nitrogen in the feeding line due to both heat transfer and cavitation phenomena are also visible.

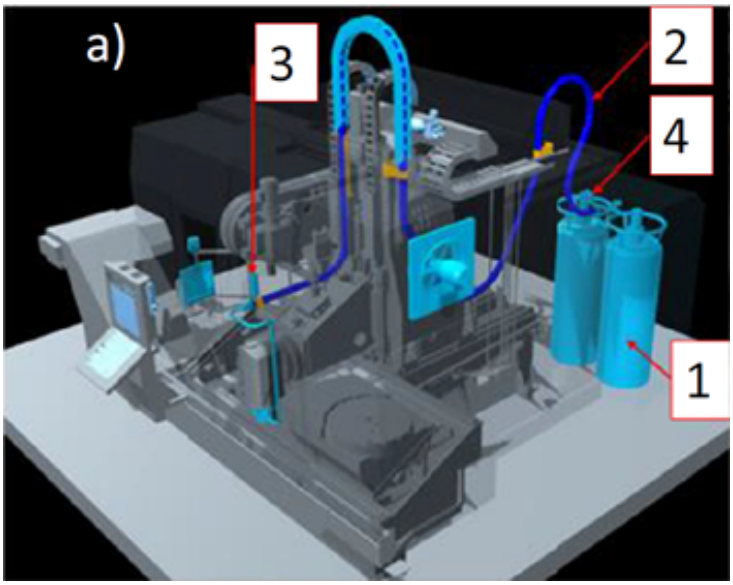

Figure 11.19: Representation of the machine tool equipped with cryogenic system [3]

where the main parts of the feeding line are. 1 = flexigas liquid nitrogen reservoir, 2 = insulated pipe, 3 = phase separator, 4 = electro valve.

Figure 11.20: Liquid nitrogen reservoir [3]

The developed solution allows the spindle head tilting. The workpiece held on a dynamometer fixed on the machine table.

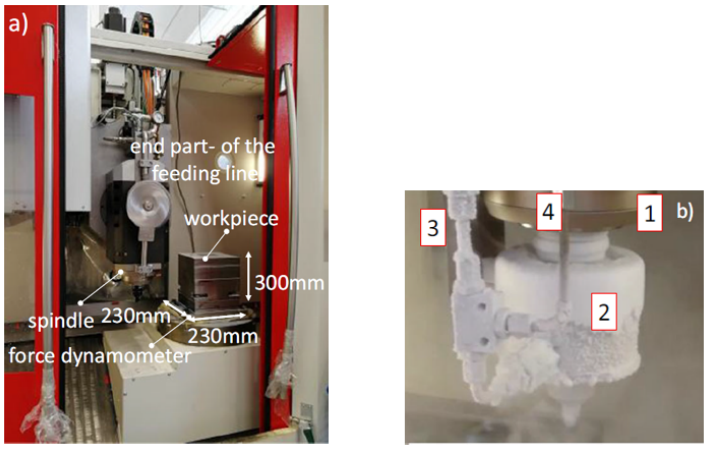

Figure 11.21: End part of the feeding line, workpiece, and force dynamometer + Cryogenic head.

Where 1 = spindle, 2 = cryogenic head, 3 = end part of the cryogenic feeding line, 4 = pressure sensor.
The described cryogenic setup was even equipped with some sensors: a pressure sensor installed at the output of the cryogenic reservoir, a pressure sensor placed close to cryogenic head and a dynamometer that was used to hold the cryogenic reservoir and to measure its weight variation during the experiments. The pressure sensor closer to the head was used

to measure the delivery pressure of the liquid nitrogen and to monitor the continuity of the liquid nitrogen flow during the cutting tests. The mass flow rate in cryogenic cutting was estimated exploiting subsequent weight measurements of the flexigas. It was observed that averagely the mass flow rate, at a pressure of 3.2 bar was about $\dot{m}_{LN} = 45$ kg/h. For the tests performed with the conventional coolant, a pressure of 40 bar was set for the pump and the observed flow rate was equal to $\dot{m}_{\text{coolant}} = 2770$ kg/h (measured using a flow sensor). A Kistler force dynamometer (9255B) with the corresponding amplifier (5070A) were used for acquiring and real-time monitoring the tool and the process conditions during the tests.
In the table below is reported the sequence of test.

No. of test	Cutting speed v_c (m/min)	Cooling condition	Pressure (bar)
1	50	Lubricant	40
2	50	Lubricant	40
3	70	Lubricant	40
4	70	Lubricant	40
5	50	Cryogenic	3.2
6	70	Cryogenic	3.2
7	70	Cryogenic	3.2
8	125	Cryogenic	3.2
9	125	Cryogenic	3.2
10	125	Cryogenic	3.2
11	125	Lubricant	40
12	125	Lubricant	40

Table 11.1: Sequence of experimental tests.

11.9. Results of experimental tests

In all the conditions the experimental cutting forces were stored, also some chips were collected and these two elements are at the basis of the comparison between Finite Element simulations and experimental results.
The force signals in the three directions (x,y,z) are affected mainly by noise and possible run out of the inserts. To limit their influence and to obtain reliable data under a statistical point of view, it is necessary to isolate the force signal of every tooth, superimpose a series

of them and perform an average on Matlab:

$$N_{\text{samples}} = \Delta t_{cut} \cdot F_s$$

$$F_{\text{average },j}(t) = \frac{\sum_{i=1}^{N_{\text{pass}}} F_{i,j}(t)}{N_{\text{pass}}}, \quad 0 < t < \Delta t_{\text{cut}} , \quad j = x, y, z$$

$$S = \sqrt{\frac{\sum_{i=1}^{N_{\text{pass}}} |F_j(t) - F_{\text{average },j}(t)|^2}{N-1}}, \quad (1-\alpha) = 95\%, \quad j = x, y, z$$

$$F_{\text{sup/inf },j}(t) = F_{\text{average },j}(t) \pm p \cdot \frac{S}{\sqrt{N_{\text{pass}}}}, \quad j = x, y, z$$

With N_{pass} = number of tool passes, F_s = sampling frequency = 5kHz, N_{samples} = number of samples in one cutting arc that lasts Δt_{cut}, S = standard deviation, p = Normal distribution quantile for 95% confidence interval.

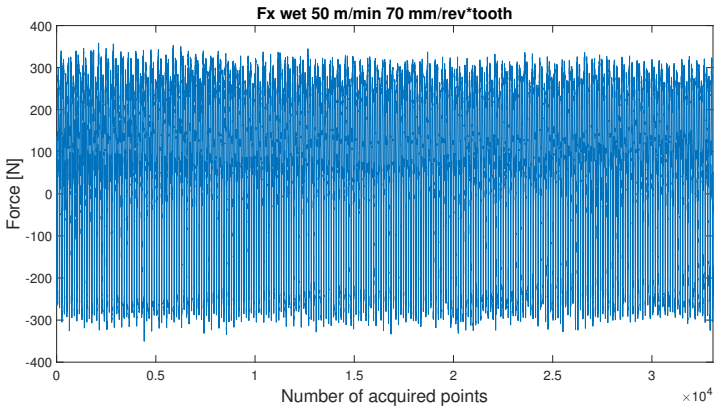

Figure 11.22: Example of force profiles for Fx at 50 m/min – 0.7 mm/rev*tooth.

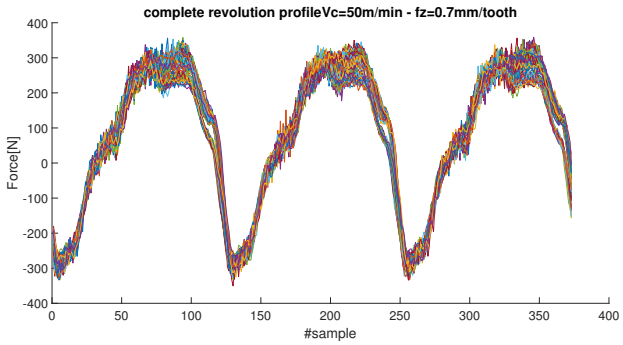

Figure 11.23: Superimposed profiles of a single revolution (3 teeth).

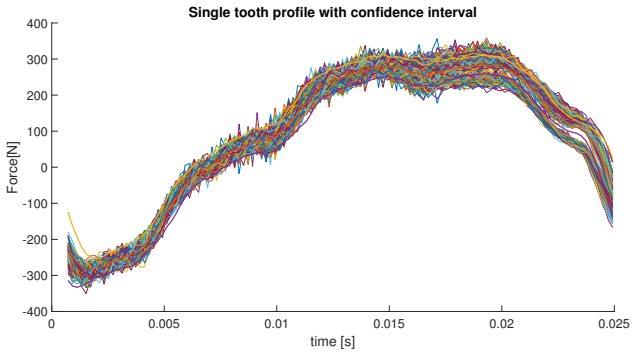

Figure 11.24: Superimposition of each single profile, mean value and confidence interval.

Here I report the averagig results for all the available ecperimental (forces) data:

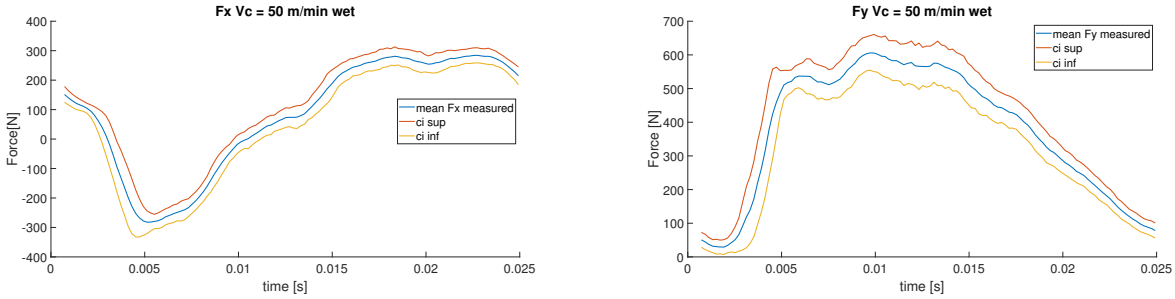

Figure 11.25: Fx and Fy for wet machining: Vc = 50 m/min, fz = 0.7 mm/rev*tooth

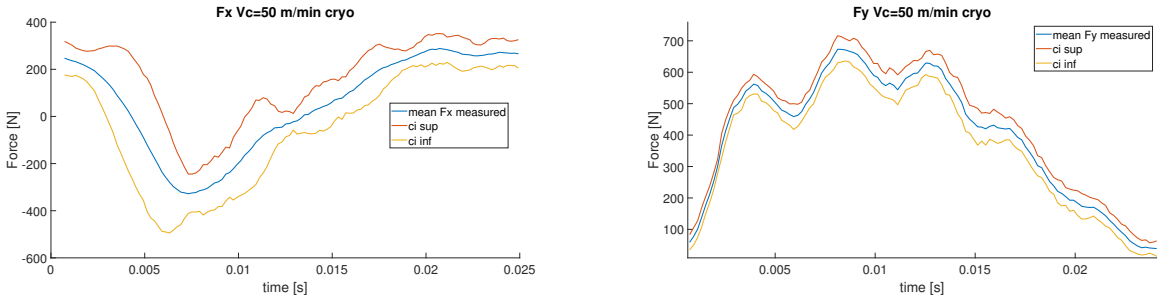

Figure 11.26: Fx and Fy for cryogenic machining: Vc = 50 m/min, fz = 0.7 mm/rev*tooth

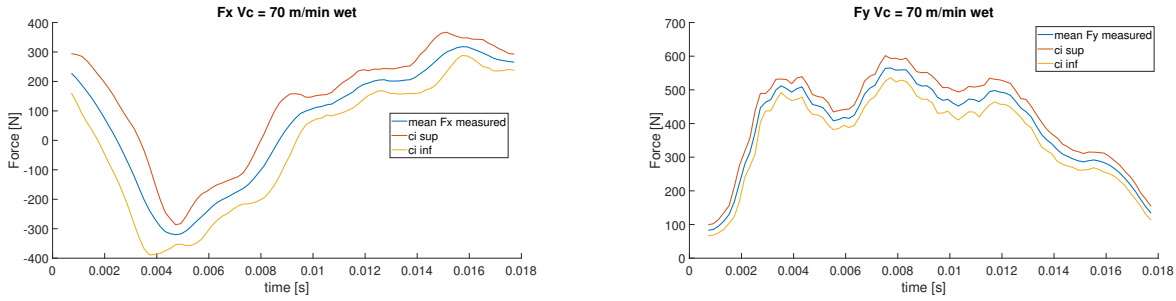

Figure 11.27: Fx and Fy for wet machining: Vc = 70 m/min, fz = 0.7 mm/rev*tooth

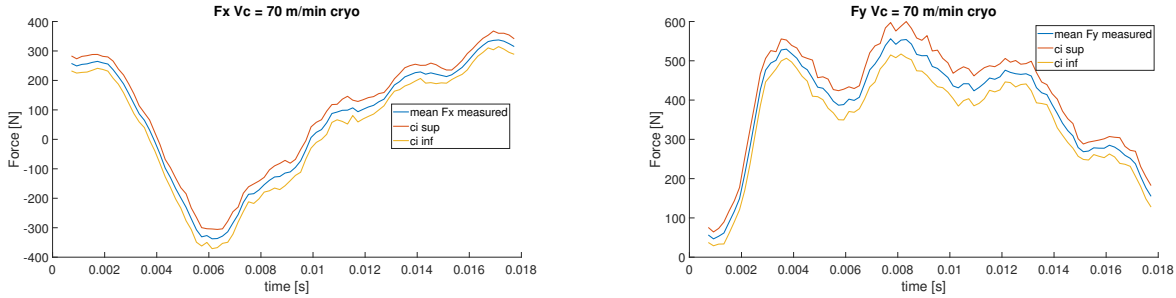

Figure 11.28: Fx and Fy for cryogenic machining: Vc = 70 m/min, fz = 0.7 mm/rev*tooth

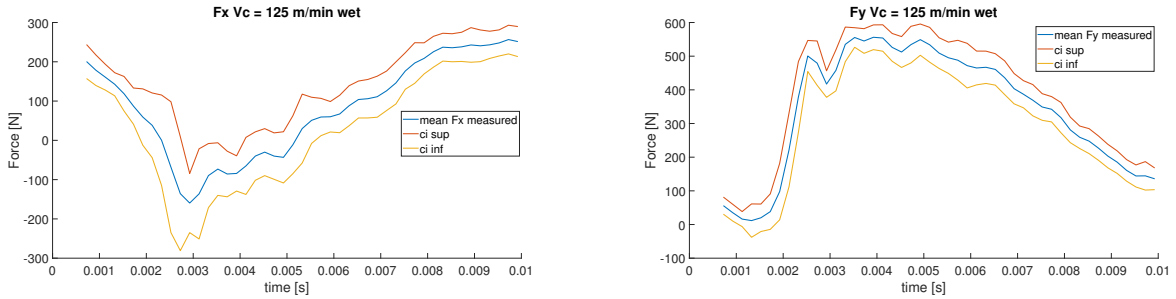

Figure 11.29: Fx and Fy for wet machining: Vc = 125 m/min, fz = 0.7 mm/rev*tooth

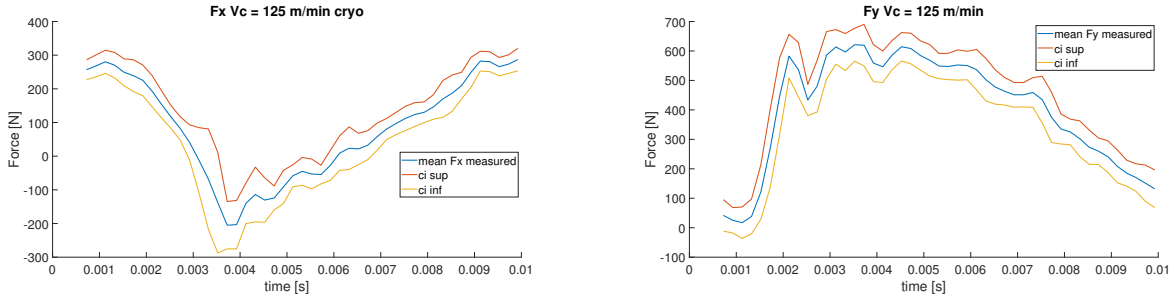

Figure 11.30: Fx and Fy for cryogenic machining: Vc = 125 m/min, fz = 0.7 mm/rev*tooth

In literature it is common to find lower cutting forces in case of cryogenic cutting if compared to wet or dry machining, the reasons are multiple and generally the main contribution for this reduction is given by a reduction of friction at the tool-workpiece interface. In this sense it is useful to verify if also in these tests the trend is the same. A fast approximation would consist in a comparison of the peaks of every force profile, but they can be influenced by the dynamics of the table, of the machine or of the tool tip, so this kind of comparison risks to be unreliable. Instead of considering the peaks, an average on time can better characterize the variation of the force with respect to the machining environment. Making the average or the approximated (mean point) normalized integral on time, is the same:

$$F_{j,\text{ average}} = \frac{\sum_{t=0}^{t=\Delta t_{cut}} F_j[t]}{N_{\text{samples}}} = \frac{\sum_{t=0}^{t=\Delta t_{cut}} F_j[t]}{\Delta t_{cut} \cdot F_s} = \frac{\sum_{t=0}^{t=\Delta t_{cut}} F_j[t] \cdot 1/F_s}{\Delta t_{cut}} \simeq \frac{I}{\Delta t_{cut}}$$

As it is the same to compare average forces and mean point integrals in time so to look at overall differences during the cutting arc:

$$\Delta F_{\%,j} = \frac{\sum_{t=0}^{t=\Delta t_{cut}} \left(F_j^{Cryo}[t] - F_j^{Wet}[t] \right)}{\sum_{t=0}^{t=\Delta t_{cut}} F_j^{Wet}[t]} = \frac{\frac{\sum_{t=0}^{t=\Delta t_{cut}} \left(F_j^{Cryo}[t] - F_j^{Wet}[t] \right)}{N_{samples}}}{\frac{\sum_{t=0}^{t=\Delta t_{cut}} F_j^{Wet}[t]}{N_{samples}}} = \frac{F_{j,av}^{Cryo} - F_{j,av}^{Wet}}{F_{j,av}^{Wet}}$$

In this table I report the result of the comparison, with the Fx_i values taken in absolute value due to the change of sign:

Cutting Speed	$\Delta F_{\%,x}$	$\Delta F_{\%,y}$
50 m/min	+0.88%	+3.922%
70 m/min	+0.18%	−1.8%
125 m/min	+14.68%	+18.36%

Table 11.2: Comparison of experimental forces on wet basis.

For sake of completeness the comparison between the peak of the mean forces (in absolute value) is reported below, along x are reported two values since there are two peaks (one positive and one negative) during the arc of cut.

For the negative peak of Fx : $\frac{|\min(Fx_{cryo})|-|\min(Fx_{wet})|}{|\min(Fx_{wet})|}$

For the positive peak of Fx: $\frac{|\max(Fx_{cryo})|-|\max(Fx_{wet})|}{|\max(Fx_{wet})|}$

For the peak of Fy: $\frac{|\max(Fy_{cryo})|-|\max(Fy_{wet})|}{|\max(Fy_{wet})|}$

Cutting Speed	$\Delta F_{\%,peak,x}$	$\Delta F_{\%,peak,y}$
50 m/min	+16.17% and + 1.41%	+11.09%
70 m/min	+5.45% and + 6.14%	−1.53%
125 m/min	+28.40% and 11.90%	+11.69%

Table 11.3: Comparison of peak values of forces on wet basis.

From these comparisons it seems that the cryogenic approach does not decrease the force values, on the contrary at high cutting speeds it increases the force values, and locally (on the peaks) this trend is visible in every condition. These data anyway do not constitute an absolute law since the tool wear state at which the forces have been acquired may be different and the dynamic behaviour of the machine + workpiece + dynamometric table may have its influence. The forces in y direction are all affected by strong oscillations and this factor may play an important role in this comparison. The detailed comparison between experimental results and finite element results will be discussed later on.

11.10. Cryogenic set-up on Forge

In this section I resume the parameters used on Forge to set up the cryogenic simulations.

Workpiece: The workpiece is defined as a deformable die and the generation of the geometry has been already discussed in previous sections. The material model selected is the Johnson Cook that in this case takes the coefficients $[A, B, C, n, m, \dot{\varepsilon_0}] = [782.7, 498.4, 0.028, 1.0, 10^{-5}]$ and the other properties of the material are reported above and summarized in the rheological model file. The damage model is the Latham and Cockcroft with damage value $D = 400MPa$.

Fold detection and self-contact are activated in order to promote the correct chip formation

in case of curled shape. The smoothing mode is set to low, in this way the shape of the chips is not modified when formed, as drawback the machined surface results damaged but since the surface quality is not a variable of interest for this work it is an acceptable compromise. Meshing zones and remeshing technique have been already presented.

Tool: the cutting insert is defined as a non-deformable die, its geometry and meshing technique have been already discussed. Its temperature is set to -100°C, the liquid nitrogen exits from the cooling channels and cools down the cutter. The liquid nitrogen is at -195°C and during the non cutting phase it is able to cool down the cutter, it is reasonable to assume a temperature below zero but at the same time it is unlikely that the skin of the tool reaches a thermal equilibrium with the liquid nitrogen. So I adopted a value between zero and -195°C.
-100 is just the skin temperature at the starting point of the engagement, obviously this temperature is not constant during the arc of cut so an increasing temperature profile in [°C] must be defined arbitrarly as shown in the figure below.

	Time	Variable Values
1	0	-100
2	0.00925	-100
3	0.011	100
4	0.014	350
5	0.016	500
6	0.018	600
7	0.02	680
8	0.022	700
9	0.025	720

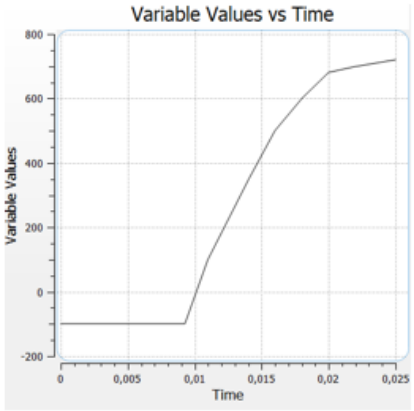

Figure 11.31: Imposed tool's skin temperature dependent on time in cryogenic conditions at 50 m/min – 0.7 mm/rev*tooth.

Ambient and interactions: The ambient temperature is set to -150°C.
The friction coefficients selected are m=0.25 and $\mu = 0.2$, since according to different experimental works, i.e. [2] the specific cutting pressure terms bounded to edge (friction) effects in case of cryogenic milling are lower than in case of wet machining, thus it is necessary to adopt low friction coeffcients in the simulation.
The thermal exchange modelling needs the input of three parameters: the interface conductance at the tool-workpiece interface = 10000 W/m^2 K, the effusivity of the tool

$$e_{\text{tool}} = \sqrt{\rho_{\text{tool}} * K_{\text{tool}} * c_{p_{\text{tool}}}} = 1111 \frac{W}{K} * \sqrt{\frac{s}{m}}$$

and the heat transfer coefficient with the ambient medium (in this case gaseous N_2) = 1500 W/m^2 K.

Then it is necessary to define a particular window in which the heat exchange with the ambient medium is enhanced due to the presence of the liquid nitrogen (following the example of Pusavec [102]). In practice the heat transfer coefficient of liquid nitrogen consistently changes with the temperature of the surface that it is impinging. For example, at −150°C it exhibits huge cooling potential with an estimated value of heat transfer coefficient equal to 280000 W/m^2 K. This value rapidly goes down until 20000 W/m^2 K at 0°C and then remains constant with the temperature. Inside this window the ambient temperature is set to −195°C (temperature of liquid nitrogen).

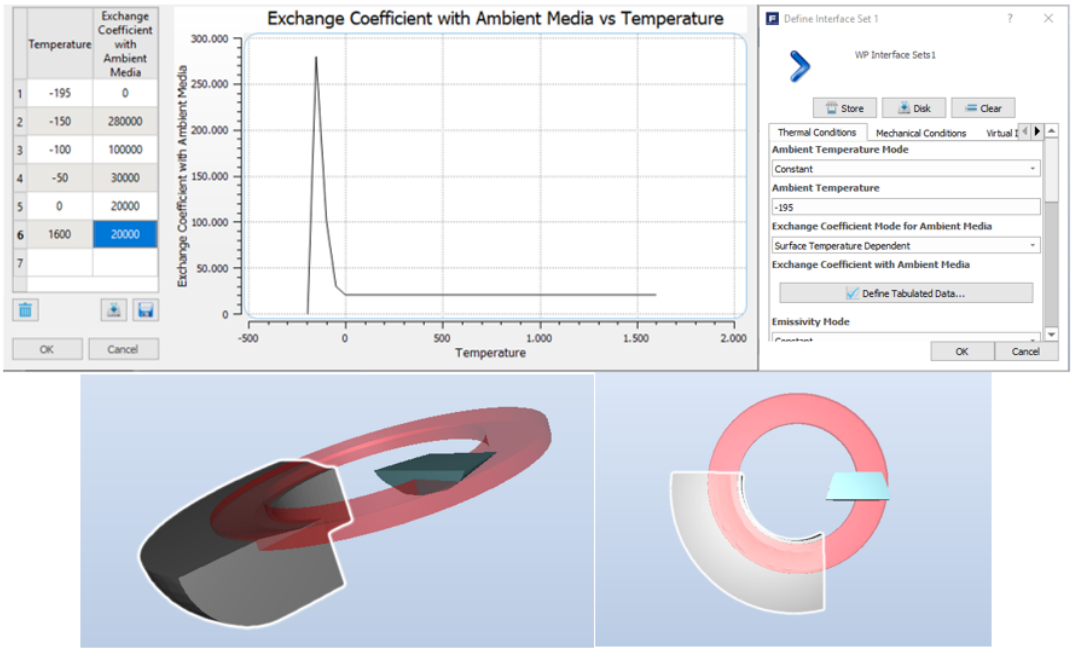

Figure 11.32: Window of enhanced heat transfer coefficient on Forge, Note: exchange coefficient with ambient media is evaluated in W/m^2 K.

11.11. Wet set-up on Forge

Wokrkpiece: for the workpiece the procedure and values presented for the cryogenic setup are unchanged.

Tool: The skin temperature of the tool at the beginning of the cut is 150°C, also in this case there are no experimental data available and also in literature no clear indication are given, so a reasonable value must be arbitrary guessed. Then this temperature evolves

in time with higher values with respect to the case of cryogenic milling due to the lower cooling capability of the emulsion flood. (Once again this temperature profile in [°C] is set arbitrarly).

	Time	Variable Values
1	0	150
2	0.00925	150
3	0.011	300
4	0.014	550
5	0.016	700
6	0.018	800
7	0.02	880
8	0.022	900
9	0.025	920

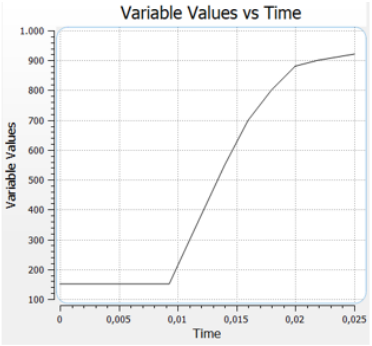

Figure 11.33: Tool skin temperature dependent on time in wet conditions at 50 m/min – 0.7 mm/rev*tooth.

Ambient and interactions: The ambient temperature is set to 30°C and also in this case no experimental data are available, so it is a guessed value.
After some trials to evaluate which friction coefficient is useful to better estimate the cutting force, the selected coefficients are $m = 0.5$ and $\mu = 0.2$. For the thermal interaction the tool effusivity is the same, so the heat partition coefficient β is modified only as function of the properties of the workpiece which are function of the temperature. The interface conductance at the tool-workpiece interface has the same value of the cryogenic case = 10000 W/m^2 K.
In the wet case the heat transfer coefficient with ambient media is set equal to 5000 W/m^2 K. Water in general has a variable heat transfer coefficient between 500 and 10000 W/m^2 K depending mainly on the turbulence of the medium. In this case it is not pure water due to the presence of oil in the emulsion that lowers the heat transfer coefficient. Not all the workpiece and not all the cutting zone is hit by the jet, at the same time the turbulence is strong and enhances the thermal exchange so, in absence of reliable data, I decided to input this value of 5000 W/m^2 K that is half the maximum possible value reachable by water. This approximation is confimerd by many studies, an example can be [82].

The choice of avoiding any more complicated model for the thermal exchange comes from the necessity of having a simple model to start its calibration comparing the finite element results with the experimental ones. Then calibrating the friction coefficients, the results were satisfactory so no other time consuming adjustments were added to the model.

11.12. Model Validation

The first data available for the validation of the finite element models were the cutting forces in the three directions x,y,z measured thanks to the dynamometric table shown before. The force in z direction is of low interest, its measured values are not reliable due to the weight force acting on the table so it is discarded from the analysis of the results. The force in y direction is highly affected by the dynamics of the system. At least four periods of oscillations are visible in the profile of one tooth's pass, the frequency is high (around 200 Hz) suggesting that the vibrating part is a light component (tool holder, spindle case or dynamometric table for example).
A first qualitative analysis of the forces in x directions suggests that the first part of these forces is not affected by evident dynamic oscillations, while in the second part small oscillations in the Fx values are present too. Obviously with the setup implemented on Forge it is not possible to reproduce the dynamic behaviour of the machine tool's components or of the external equipment (dynamometric table). As consequence the most interesting part for the validation of the finite element results is the first part of the forces along x (feed) direction.
In the plot below the force oscillation is evident in all the F_y profile and in the second part of the F_x profile.

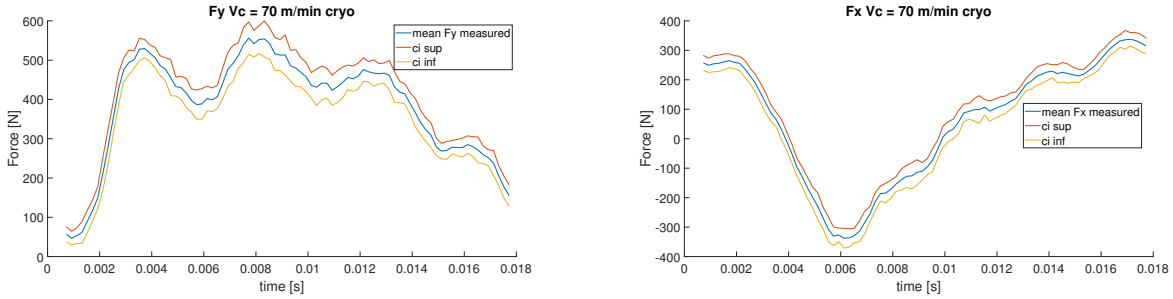

Figure 11.34: Fy and Fx with confidence interval at 70 m/min and 0.7 mm/rev*tooth and cryogenic conditions.

Another source of uncertainty is introduced by the big mass of the workpiece. It was a block of 230 mm x 230 mm x 300 mm and with a density of 4.43g/cm^3 its starting weight was over 70 kg. Such a big mass is able to modify the dynamics of the table introducing mainly low frequency oscillations.
Another source of uncertainty is introduced during the generation of the geometry on the CAD software. In particular, projecting the tooth profile on a vertical plane in order to allow the cut to follow the spline trajectory, minimizes the real effects of the rake angles

(axial and radial). So the cutter on Forge faces an uncut chip thickness that is not exactly the one faced by the real insert.
Here are reported all the comparisons between experimental and simulated F_x.

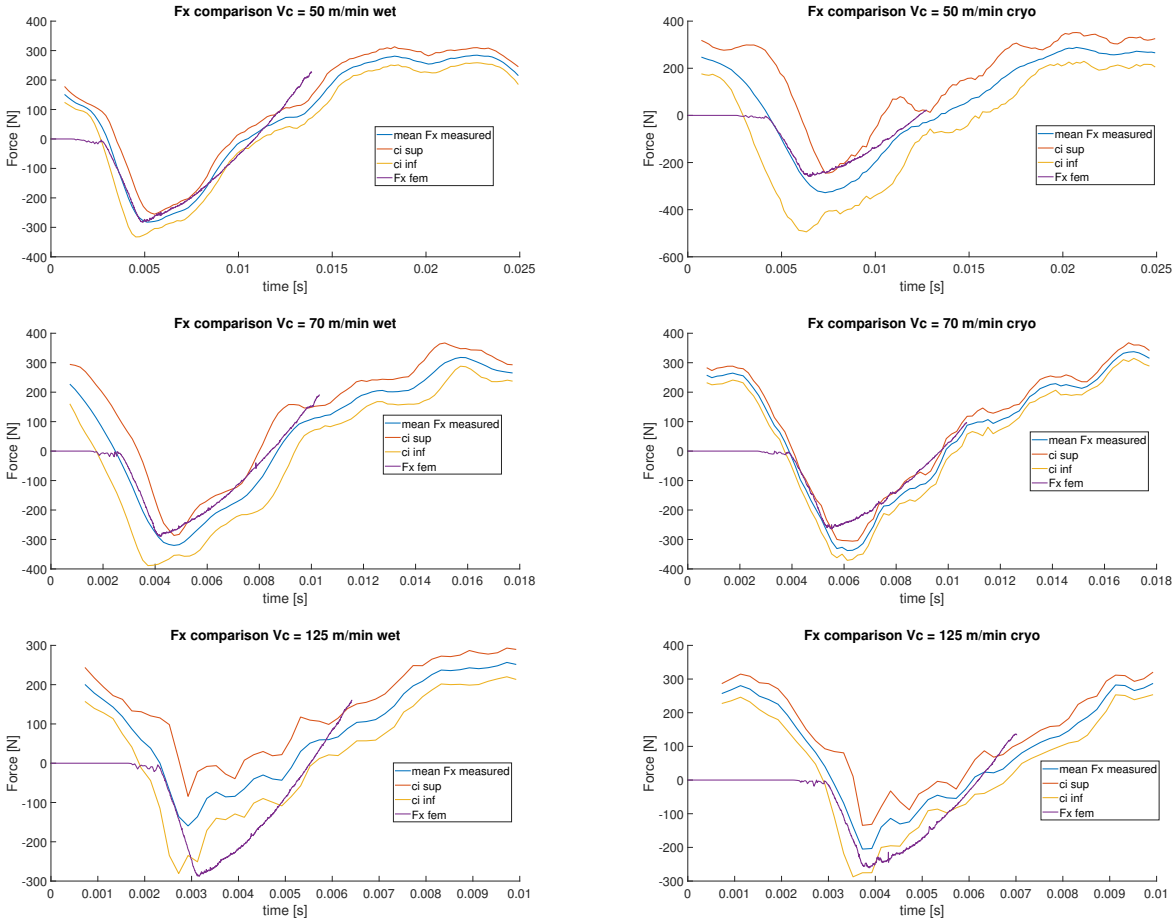

Figure 11.35: Comparison between experimental F_x forces (with confidence interval) and FE results, left side for wer environment at 50,70,125 m/min and right side for cryogenic environment at 50,70,125 m/min.

The peaks of the mean forces are well estimated (see next section for computation of peak erros), exception made for the wet case at 125 m/min and the cryo case at 70 m/min, but also here the simulated peaks are not far from the limits of the confidence intervals. And in general the FE forces lay inside the confidence interval of the experimental forces, giving reliability to the model, so the results presented in the next section acquire likelihood.
The errors has been minimized by calibrating the friction coefficients m and μ of the two different environments: wet and cryogenic. The best estimation is the one for wet environment at 50 m/min and this is not a case, since at low cutting speed the oscillations of

the experimental values seem lower and the strain rate is closer to the one at which the material model has been determined.

Chip morphology reproduction:

The comparison between simulated chips and experimental ones is only partial. The chips have been collected only for the tests at 125 m/min in both wet and cryogenic conditions. These are the most difficult conditions to be reproduced since the strain and strain rates developed are very far from the ones at which the material model has been determined. Moreover, the mesh size necessary for a correct reproduction of the chip morphology is way smaller than the one requested for a reliable reproduction of the cutting forces and very frequent remeshings are necessary. As consequence, the simulation time for an optimal chip morphology reproduction is very high. With the availabe resources a compromise must be found.
The first simulations (Vc=50 m/min) have been carried out without references for the chip morphology and a damage threshold of D=400 MPa for the damage model has been selected since it was able to reproduce shear banded chips typical of Ti6Al4V. For successive simulations, increasing the cutting speed the chips were more damaged but having no real chips for comparisons it was not possible to further calibrate the damage value. At 125 m/min the simulated chips showed a tendency to fractures and this behaviour is in line with literature indications. Only at the very end of the work the chips for Vc=125 m/min were available and the the majority of them were continous and curled, so quite different from the simulated ones. In the simulations at high speed the segmentations given by shear bands phenomenon were able to evolve into fractures, in order to avoid this the damage threshold D was increased with a pace of 30 MPa, from 400 until 610 MPa. Doing so the chips were progressively less damaged and the shear bands' formation and following evolution in fractures was limited promoting continous and curled shapes. Anyway this modification of D did not modify significantly the value of simulated forces, suggesting that a modification of all the previous models was not a convinient choice.

The chips produced during cryogenic cutting are brighter than the ones formed during wet cutting, meaning that they undergo a different thermal cycle (which is confirmed in the analysis of results later on). At the same time the use of LN2 leads to more damaged chips, fact that finds confirmation in the results of FE simulations, where the material in cryogenic condition can bear lower strains without damaging. Here below are reported some images of the collected chips.

Figure 11.36: Chips formed at Vc=125 m/min, fz=0.7 mm/rev*tooth, ae=13 mm ap=0.4 mm during wet machining.

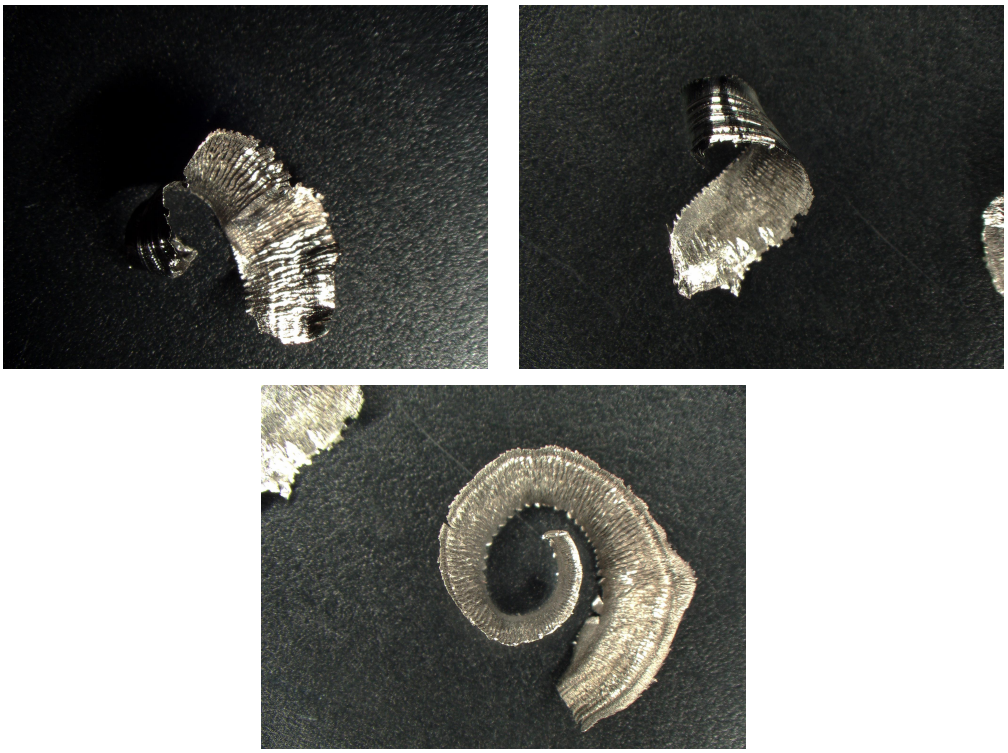

Figure 11.37: Chips formed at Vc=125 m/min, fz=0.7 mm/rev*tooth, ae=13 mm ap=0.4 mm during cryogenic machining.

Making a comparison between real and simulated chips it is possible to notice that the overall shape is well reproduced, the fragmentation on the external edge in quite similar, while the shear bands are not well reproduced. From measurements their pace is around 0.2 mm and 0.18 mm in wet and cryogenic conditions respectively, the meshing box used for promoting the chip formation has a characteristic dimension of 0.05 mm which results to be too large. Further decreasing this value the computational time increases significantly, abundantly over one week.
Looking at the pictures of the simulated chips it is possible to appreciate a more damaged chip in case of cryogenic environment if compared to the wet one.

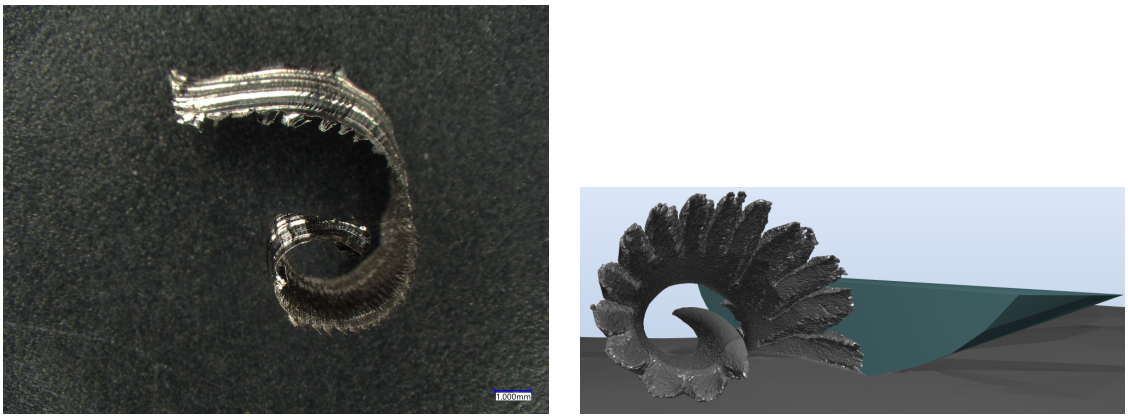

Figure 11.38: Comparison between real chip and simulated one in wet conditions, D=580MPa.

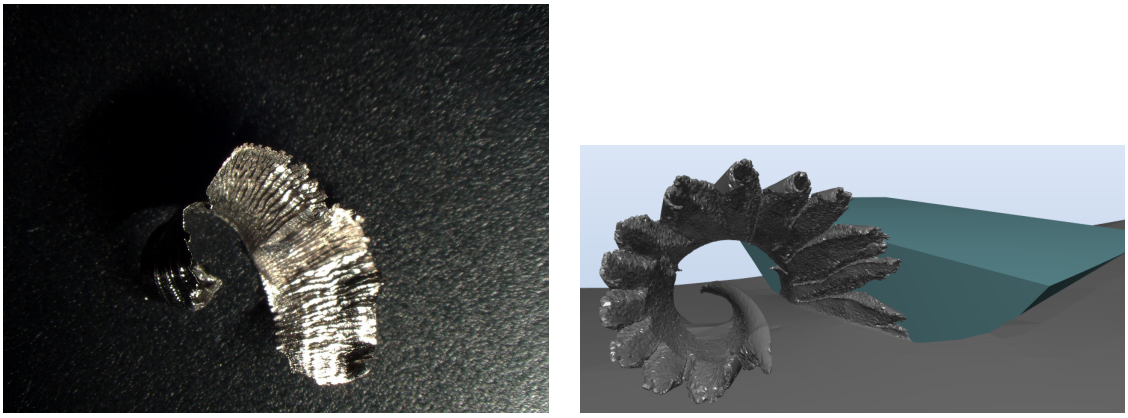

Figure 11.39: Comparison between real chip and simulated one in cryogenic conditions, D=580MPa.

In conclusions the obtained results suggest that the material model (and damage model) selected can reproduce the chip morphology only in a macroscopic way, for a more detailed investigation on this topic more powerful computational tools are necessary in order to carry out multiple simulations with smaller mesh sizes in a reasonable time.

12 | Results of FEA

Wet with Vc=50 m/min, fz=0.7 mm/rev*tooth, ap=0.4 mm, ae=13 mm:
The most important comparison is between experimental and simulated forces. It is straightforward to notice that the simulated forces copy well the force in x direction (feed direction) while in y direction (perpendicular to feed) a divergence is evident.
Defining the percentage peak error on F_x as:

$$\mathrm{Err}_{\mathrm{peak}}\ \% = \frac{|\min(\text{ FE force })| - |\min(\text{ experimental force })|}{|\min(\text{ experimental force })|} * 100$$

it takes the outstanding value of $+2.14\%$, that is a fundamental result in the validation of the model and gives reliability to the work.
It is possible to reduce the gap on F_y by reducing the friction coefficients until clearly unphysical values with a big influence on temperature evolution and chip formation, also with the disadvantage of modifying too much the force in feed direction. These evidences coupled with the considerations about the dynamics of the system (machine tool + workpiece + dynamometric table) suggest that a validation of the finite element model is possible taking as reference the first part of the Fx profile only.

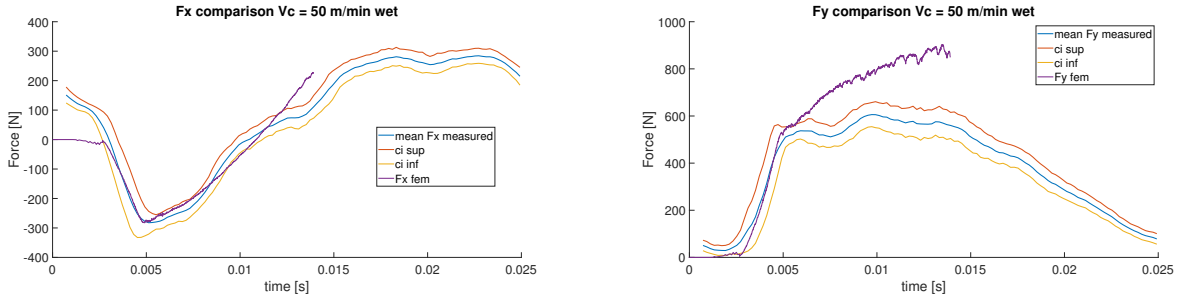

Figure 12.1: Comparison between experimental and FEM forces in x and y direction.

Looking at the temperature distribution on the workpiece it is evident that the hottest zone is the contact zone between tool and chip (secondary deformation zone), where the relative movement of the two bodies favours the temperature build up through friction

phenomenon. The maximum temperature on the workpiece firstly overcomes 1000°C and then slightly oscillates around 1020°C for the rest of the cutting arc. This quantity also suggests which can be the magnitude of the maximum temperature reached by the tool. In this model the tool is a "rigid die" that on Forge implies no stress and thermal computation on it. This is done because a calculation on the tool would double the time of each simulation compromising the investigation of different cutting conditions.

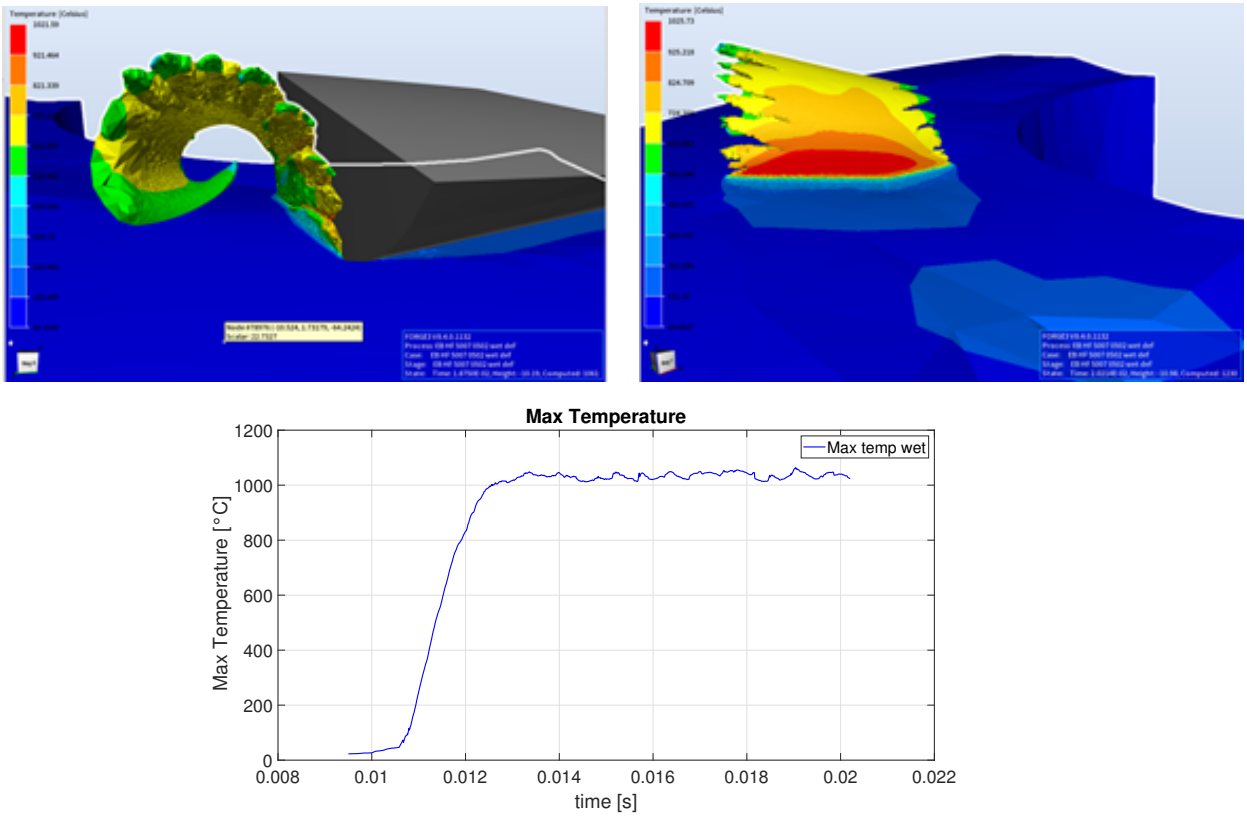

Figure 12.2: Temperature distribution on the chip, maximum temperature zone (removing the insert), maximum temperature profile.

As underlined before, a simple LC damage model has been implemented in order to avoid the introduction of undesired complexity in the finite element model. With two indicators as Element Deletion Areas and LATANDCO it is possible to verify the effect of this choice. It is evident that the areas in which the majority of the elements are delated from the computations are the ones where shear bands are formed. Looking at LATANDCO, the same areas are the ones where the damage value D reaches its maxima, so it can be said that the Damage model regulates the deletion of elements favouring the shear bands formation. Surely a deeper investigation of this phenomenon, a more sophisticated damage model and a finer mesh would be able to improve the formation of shear bands

but it would require a dedicated work. Anyway the use of a simple LC damage model for the reproduction of shear bands is, according to these results, an efficient and time saving choice.
Note: LATANDCO is simply the value of D in the damage model

$$\int_0^{\varepsilon_f} \sigma_1 * d\varepsilon = D$$

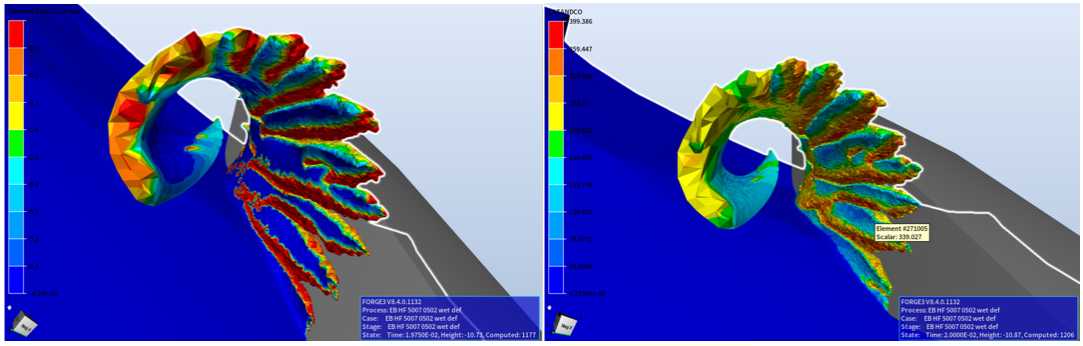

Figure 12.3: Element deletion areas and LATANDCO.

It is interesting to analyse the heat exchange during the cut. On the workpiece side it is possible to distinguish four contributions: 1) Heat exchange (through conduction) between dies, 2) Heat exchange due to radiation, 3) Heat exchange due to friction, 4) Heat exchange with ambient media.

1) It is almost negligible due to the small amount of time in which the tool and the workpiece are in contact. It is strongly influenced by the interface conductance between dies and by the contact model.
2) It is negligible.
3) It represents the main component of the heat exchanged, strongly influencing the temperature build up in the friction zone between tool and chip.
4) It has a negative trend because it is directly proportional to $(T_{\text{ambient}} - T_{\text{workpiece}})$, so while the temperature of the workpiece rises up, its magnitude does the same (in absolute value). In the end its value is similar to the one of friction exchange, but it is necessary to consider that this last contribution is localized in a small area between tool and workpiece while the heat exchanged with the ambient media is calculated on an increasing surface that takes into the account also the hot face of the workpiece left after the passage of the tool. Its temperature is higher than the one of the ambient media so the heat exchange takes place and it is accounted in this plot, but it is not entirely acting on the zone where the maximum temperature is developed.

In the legends of the plots the nomenclature given by Forge is maintained, so considering a unit of area
"Die Exch" = $K(T_{tool} - T_{wp})$ = thermal power exchanged through conduction between tool and workpiece, "Friction Exch" = $q_{wp} = q_f - q_{\text{tool}} = q_f * (1 - \beta)$ = thermal power generated through friction and flowing into the workpiece, "Media Exch" = $K(T_{tool} - T_{wp})$ = thermal power exchanged between workpiece and ambient media, "Radiation Exch" = thermal power exchanged between tool and workpiece through radiation.

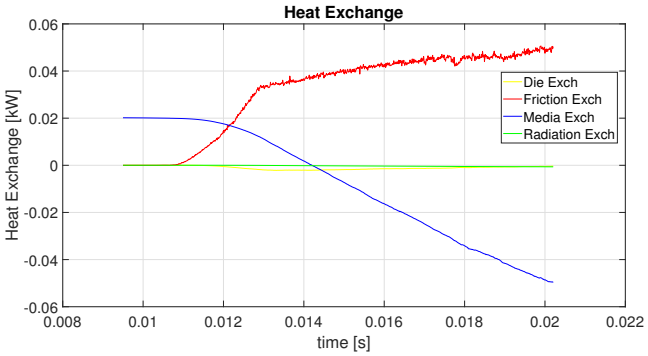

Figure 12.4: heat exchange during the simulation.

Here it is possible to evaluate which are the contributions of the mechanical power: 1) Elastic Power 2) Friction Power 3) Plastic power.

1) It can be considered as negligible
2) It has a small but non negligible contribution, it is not the dominant factor anymore as it was for friction in the heat exchange mechanism.
3) It is the most important contribution as expected for every chip removal process.

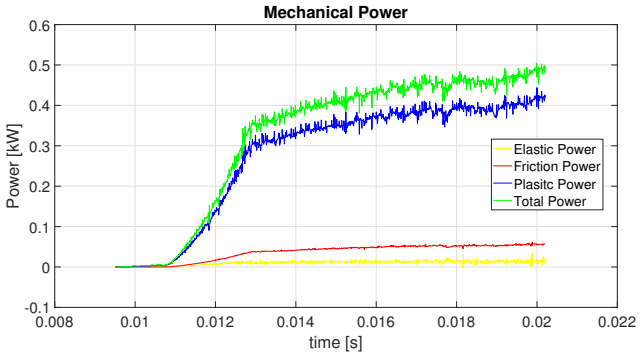

Figure 12.5: Mechanical Power.

The last two plots underline once again what is common to find in literature: the material

model strongly influences the cutting forces, in fact the properties of the material influences the plastic power (higher contribution in the mechanical power computation). On the other hand, the friction model is the major responsible of the temperature build up and of the thermal distribution, in fact the role of heat exchanged by friction is dominant in the plot of the heat exchange mechanisms.

The maximum effective strain has a peak of 8.5 but in general during the cut is between 7 and 8. The external part of the chip (free surface of the uncut chip thickness) is slightly affected by strain, while the inner part of the chip (part in contact with the tool) is the location where maximum stains rise up.

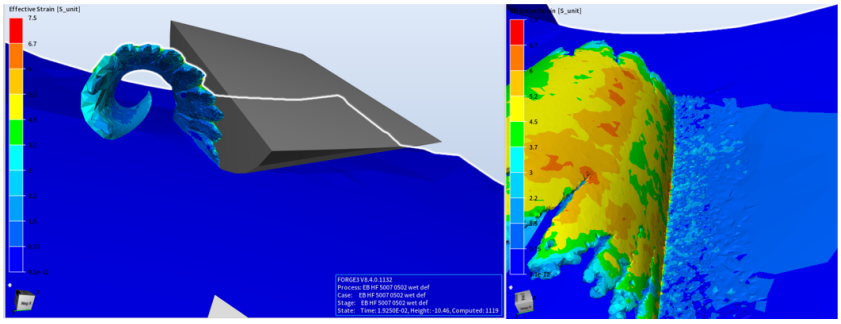

Figure 12.6: Effective strain.

For the visualization of the strain rate it is necessary to display the results in a logarithmic scale. Its maximum value oscillates between 150000 and 300000 s^{-1} and it is located in the primary and secondary deformation zone. It is important to notice that the Lee and Lin material model has been determined with tests at 2×10^3 s^{-1} that is two orders of magnitude lower than the strain rate experienced with this finite element simulation at Vc=50 m/min.

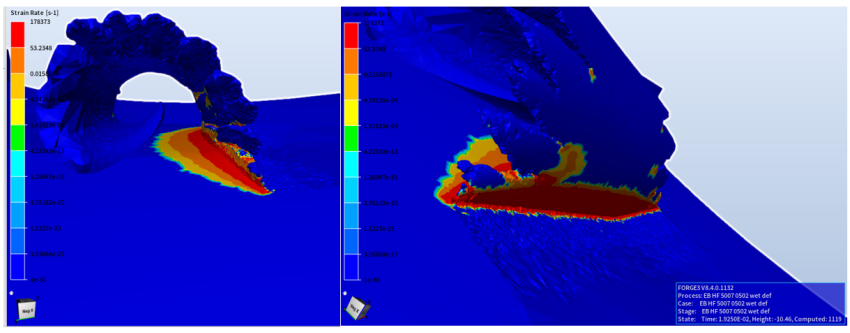

Figure 12.7: Strain rate visualization.

Cryo with Vc=50 m/min, fz=0.7 mm/rev*tooth, ap=0.4 mm, ae=13 mm:
Passing to the cryogenic cutting these are the results of the force comparisons. The force in feed direction is well estimated since it always lies inside the confidence interval of the experimental forces, even if the peak is slightly underestimated (in absolute value). The estimation of the force perpendicular to feed direction is way better than the one experienced with wet machining. In this case it is evident how dynamic phenomena are able to influence the force profile, promoting its oscillating behaviour and keeping it distant from the simulated results. The adoption of higher friction coefficients would help in a better estimation of the force in feed direction but would also increase the value of the force in y direction, so it is possible to consider the adopted values as a good compromise. Percentage peak error on F_x = $\mathrm{Err}_{\mathrm{peak}}$ % = -20.96% if referred to the mean value of the measured force, it becomes $+5.96\%$ if referred to the superior confidence interval.

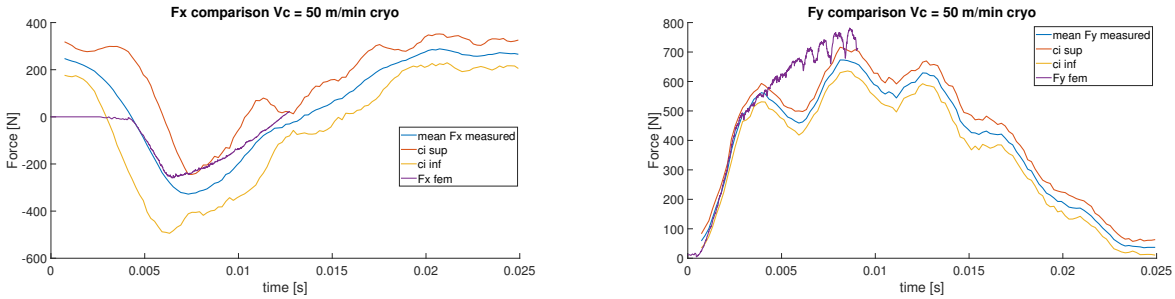

Figure 12.8: comparison between experimental and FEM forces in x and y direction.

The zone where the maximum temperature arises is more localized than in the case of wet machining. It is always located in the secondary deformation zone and it is always shifted toward left where relative speed between tool and workpiece is higher. Even in absence of detailed CFD studies it is reasonable to think that in this spot more heat is generated by friction and the liquid nitrogen can not reach and cool down the zone due to the inaccessibility given by the contact between chip and tool. So it is the zone more exposed to temperature build up and less exposed to the cryogenic jet.
The entire temperature profile is plotted below, and it is compared to the one in wet conditions. The temperature build up is less sudden and reaches lower values, also above 900°C but never approaching 1000°C. This temperature difference between the two approaches is given by the joint contribution of lower friction coefficients and higher heat transfer coefficients around the cutting zone in case of cryogenic machining.

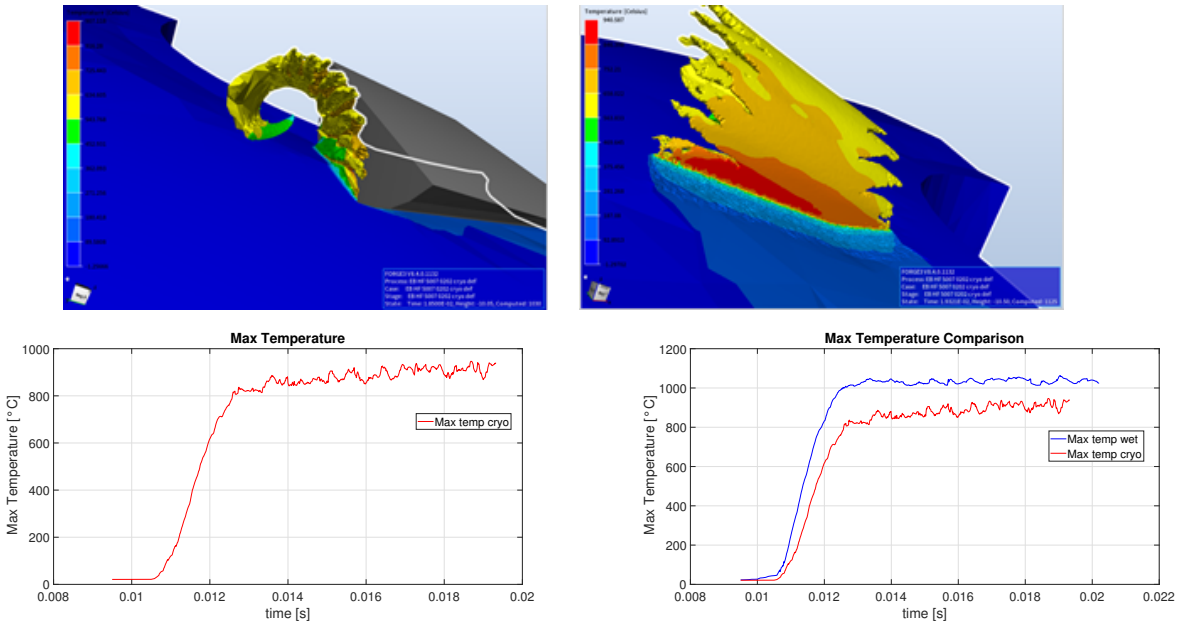

Figure 12.9: Temperature distribution on the chip, maximum temperature zone (removing insert), maximum temperature profile in cryogenic conditions, comparison with wet condition.

Analysing the heat exchange mechanism once again it is visible that the heat exchanged between dies (workpiece and tool) and heat exchanged throug radiation are marginal in the total computation (see plot on the left in the figure below). Looking at the comparative plot, thermal power generated through friction and entering in the workpiece in case of cryogenic cooling is largely decreased thanks to lower friction coeffcients while the heat exchanged with ambient media in absolute value is largely incresed. This last curve is less steep but its mean value is way larger than in the case of wet machining, keeping lower the maximum temperature.

(Note: in the plots regarding thermal power exchange the reference is the workpiece, so positive values are powers entering in the workpiece and negative values are powers exiting from the workpiece.)

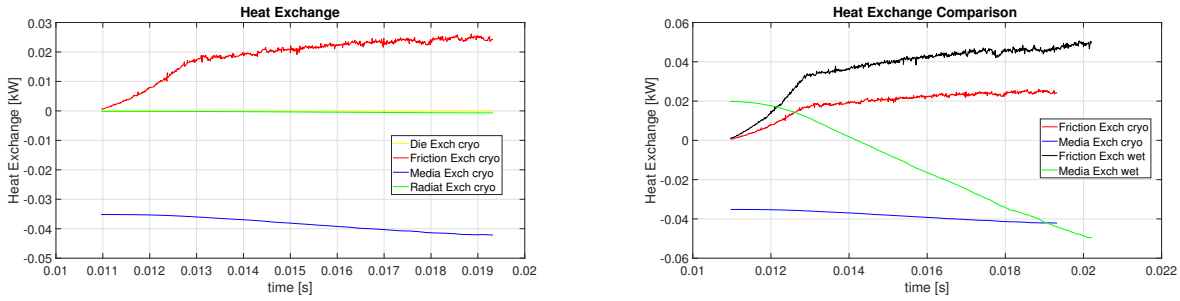

Figure 12.10: Heat exchange on workpiece side.

As expected the dominant contribution in the mechanical power computation is the plastic power also in case of cryogenic machining. One important finding, comparing the plastic power with the one of wet machining, is that using liquid nitrogen it is possible to reduce the plastic power. This because the material at lower temperatures is not able to exploit all its ductility and the shear action requires less energy.

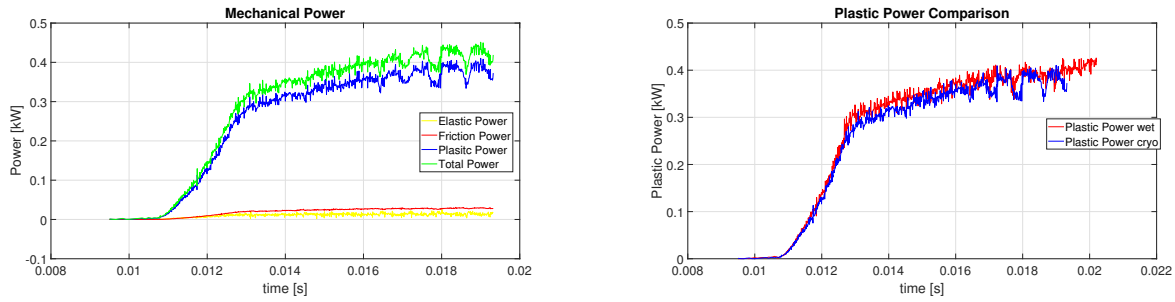

Figure 12.11: Contributions of mechanical power.

Another important results that confirms this finding is the maximum effective strain that in case of cryogenic milling is lower. As said before in case of wet machining this value oscillates between 7 and 8 with a peak of 8.5. Now with the set up that simulates the use of liquid nitrogen, the maximum effective strain oscillates between 6 and 7 with a peak of 7.4. So also this result suggests that for the shearing of the material in cryogenic conditions less energy is spent, thus lower mechanical power. Loking at the strain rate it is not possible to find remarcable differences with respect to the wet machining case, and the values once again oscillates between 150000 and 300000 s^{-1} (as aspected since the kinematics is the same) so two order of magnitudes higher than the one used for the determination of the material model.

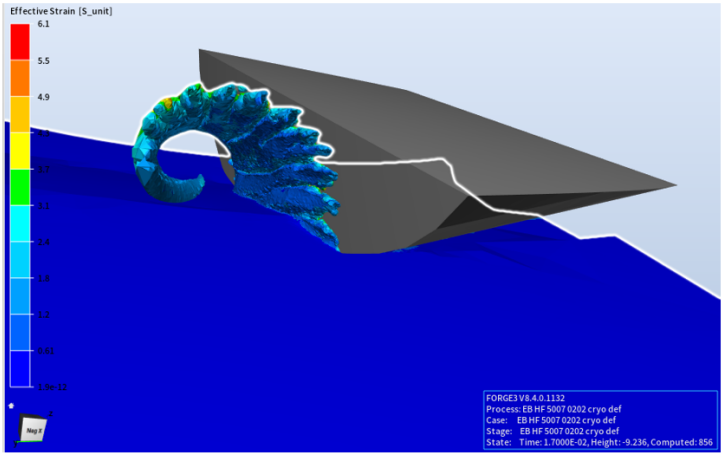

Figure 12.12: Effective Strain.

Also in this case comparing the elemet deletion areas and LATANDCO it is possible to see that the zones where the element are delated by the computation are the same where LATANDCO exhibits its peaks, so the use of a simple LC damage model as a first approximation for the formation of shear bands is a reasonable choice.

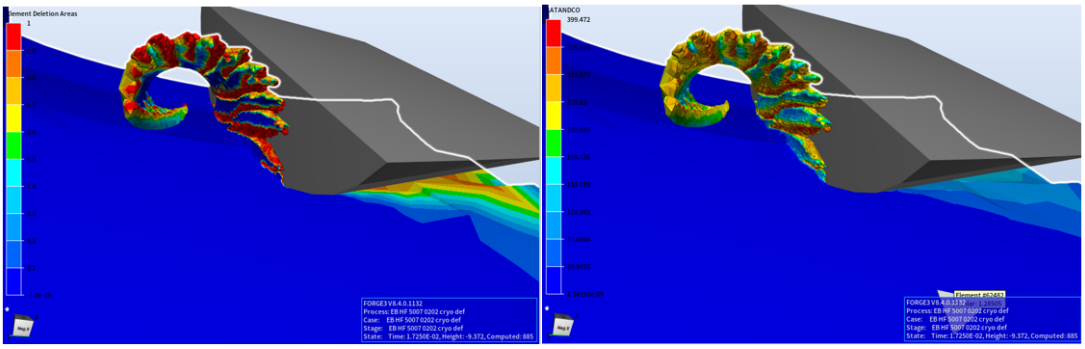

Figure 12.13: Element deletion areas and LATANDCO.

Cryo with Vc=70 m/min, fz=0.7 mm/rev*tooth, ap=0.4 mm, ae=13 mm. Now it is interesting to understand which is the influence of an increment of cutting speed in case of cryogenic machining.

Looking at the cutting forces it is possible to notice that the force in feed direction is well predicted in its first part even if an underestimation of the negative peak is present, but the rest of the profile lies inside the confidence interval even if it is really narrow in this case and can be considered a satisfactory result after the change of such a crucial parameter as cutting speed. For the force directed perpendicularly to the feed the problem

is the presence of evident oscillations in the profile of experimental forces. Once again this effect does not allow more detailed investigations taking as reference this force component. Percentage peak error on F_x = $\mathrm{Err}_{\mathrm{peak}}$ % = −21.63%, it becomes -13.47% if referred to the superior confidence interval.

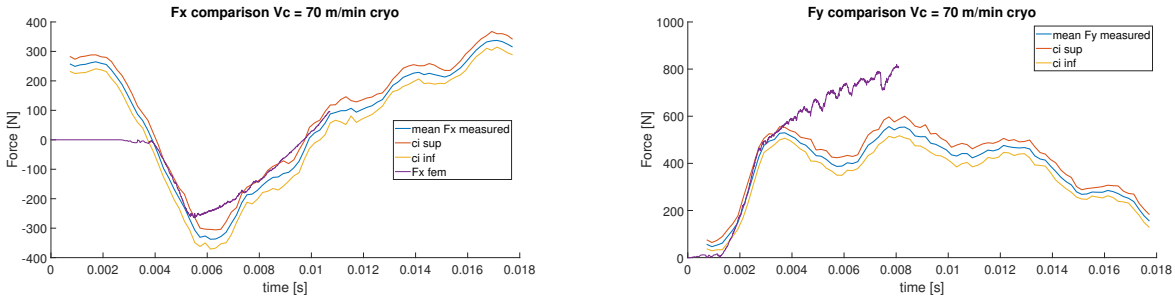

Figure 12.14: comparison between experimental and FEM forces in x and y direction.

The zone where the maximum temperature arises is always the same, the part of secondary deformation zone more distant from the centre of the tool. Here the amount of material in contact with the tool forbids an exposure to the ambient (cooling) media and the relative speed is higher resulting in a higher temperature build up due to friction phenomenon. Looking at the behaviour of the maximum temperature, after a fast rise up phase it stays above 1000°C never reaching 1100°C. The friction coefficients are the same adopted in the simulation with lower cutting speed (with flood cooling) but the heat generated by friction is also directly proportional to the relative speed between workpiece and tool, thus increasing the cutting speed this quantity grows up resulting in higher temperature.

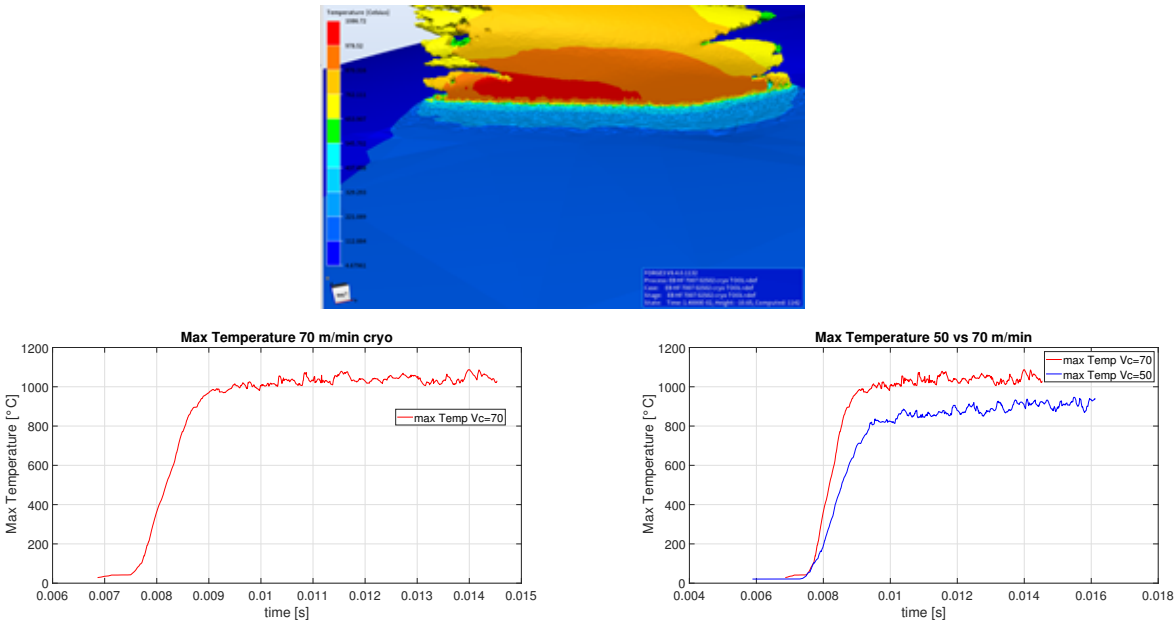

Figure 12.15: Maximum temperature location, maximum temperature profile, temperature comparison changing cutting speed.

The heat exchange mechanism as expected is not changed, with negligible heat exchanged between dies and through radiation, the most important role is played by the thermal power generated through friction entering in the piece that in absolute value is not distant from the one exchanged with ambient media but it is more localized. All the other considerations are the same of the cases analysed before.
Once again the higher cutting speed determines an enhancement of the friction influence, this is noticeable in the plot of comparison with the simulation at lower speed. The heat exchanged with ambient media is higher because it is proportional to the difference between the temperatures of ambient medium and workpiece. The first is always the same, the latter is higher in this case.

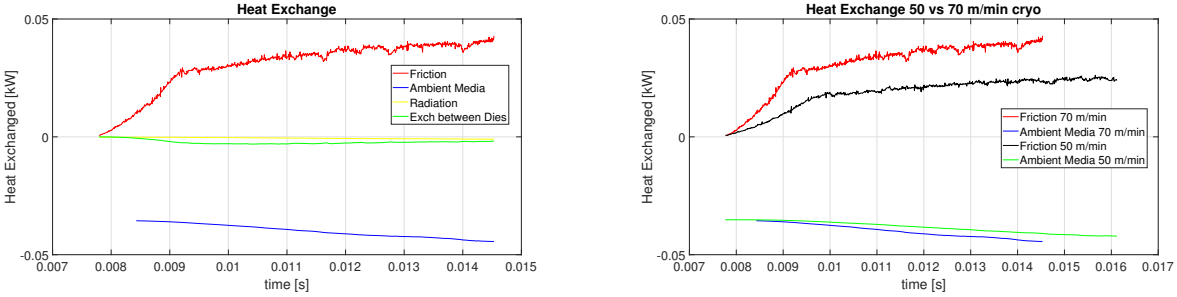

Figure 12.16: Heat exchange mechanisms and comparison with different cutting speeds.

Also for the mechanical power the mechanism are unchanged with elastic and friction power negligible with respect to plastic power. It is remarkable the consistent increment of plastic power with respect to the simulation with lower cutting speed.

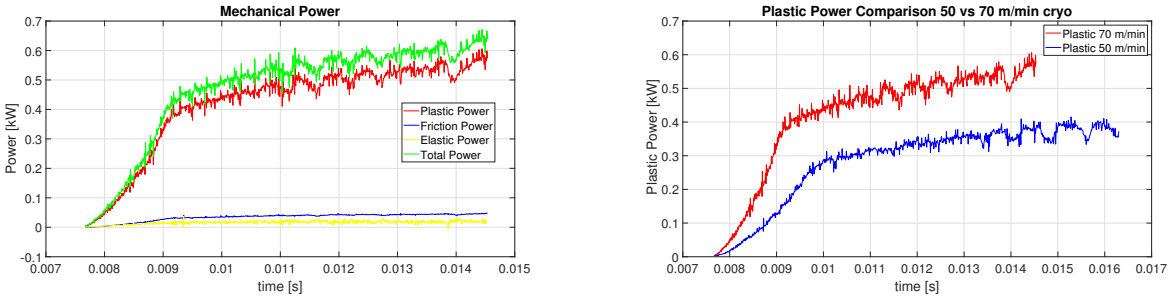

Figure 12.17: Mechanical power contributions and comparison with different cutting speeds.

The maximum effective strain is substantially unchanged with respect to the simulation with lower cutting speed since it ranges between 6 and 7 with maxima of 7.4. While logically with higher speed the strain rate increases ranging between 25000 and 55000 s^{-1} with peaks above 68000 s^{-1} enlarging the gap with the strain rate at which the material model has been determined.

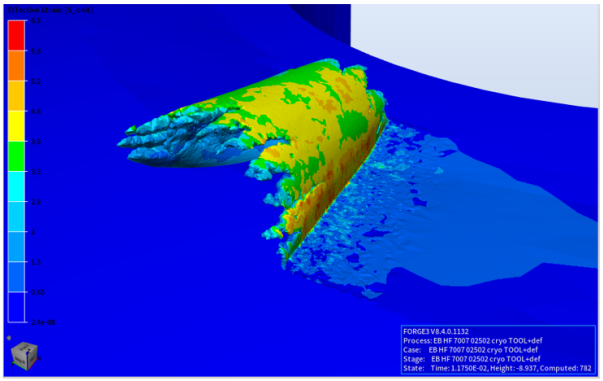

Figure 12.18: Effective strain.

Cryo with Vc=125 m/min, fz=0.7 mm/rev*tooth, ap=0.4 mm, ae=13 mm.
Further increasing the cutting speed the same problem is encountered with the force perpendicular to feed direction while the force in feed direction is better estimated with the finite element analysis. After the peak the force value is overestimated (in absolute value) but still acceptable.
Percentage peak error on F_x = Err_{peak} % = +27.29%, it becomes -9.21% if referred to the inferior confidence interval.

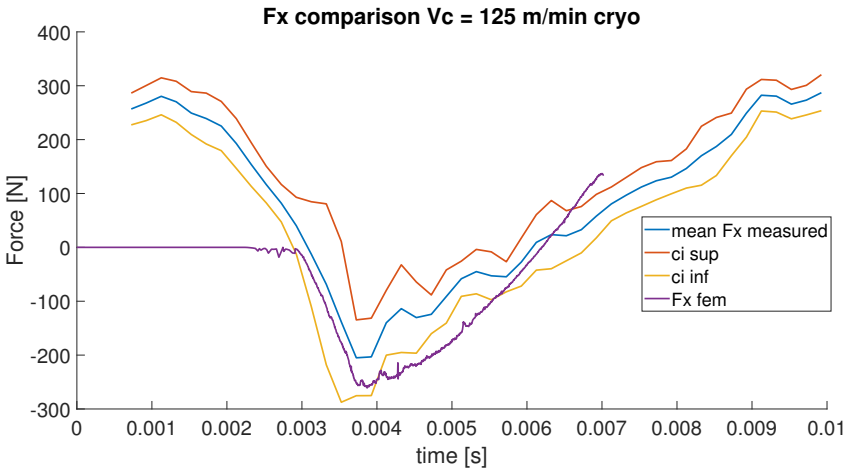

Figure 12.19: Fx comparison between experimental and FEM forces.

The maximum temperature location is always the same and the higher velocity increases this value. Its profile fastly rises above 1000°C and touches constantly 1200°C that is the maximum temperature experienced by now as shown in the comparative plot with the data coming from the other simulations in cryogenic conditions (70 and 50 m/min respectively).

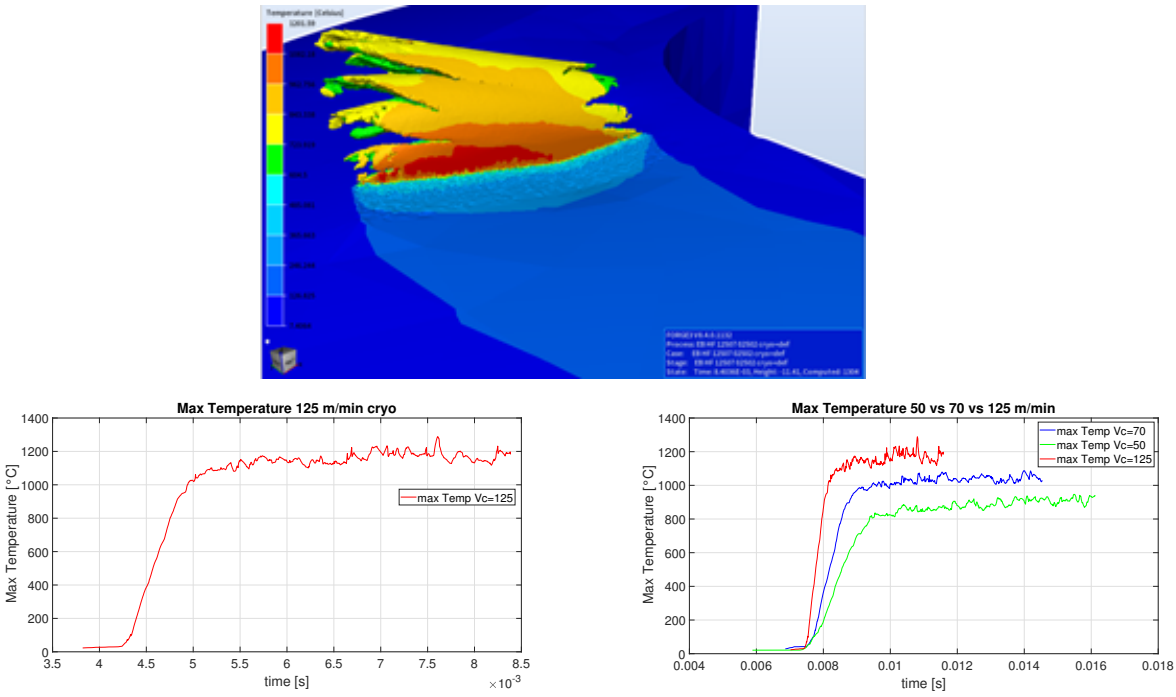

Figure 12.20: Maximum temperature location, maximum temperature profile, temperature comparison changing cutting speed.

The maximum effective strain is always located in the secodary deformation zone and it has value ranging between 5.5 and 7.5, similar to all the others simulations with cryogenic set up.

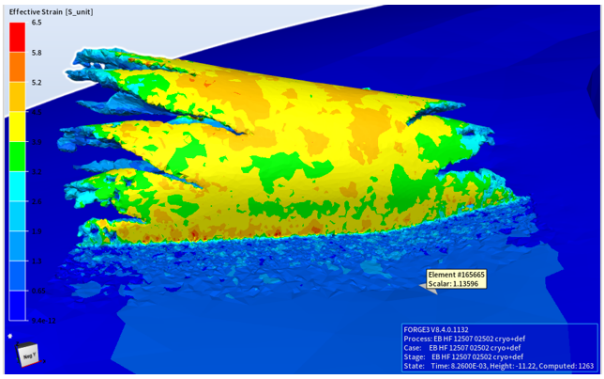

Figure 12.21: Effective strain.

The heat exchange finds once again its major contributions in the thermal power generated by friction entering in the workpiece and heat exchange with ambient media. This one has a positive trend in its second part because there a fracture in the chip occures and a considerable portion of material at high temperature is delated from the computation. In the comparative plot it is appreciable how cutting speed is influent in the magnitude of heat exchanged with friction while the influence on heat exchanged with ambient media is much lower.
The radiative contribution is slightly negative since the arbitrarly selected tool's skin temperature results slightly lower than the temperature developed on the tool-chip interface.

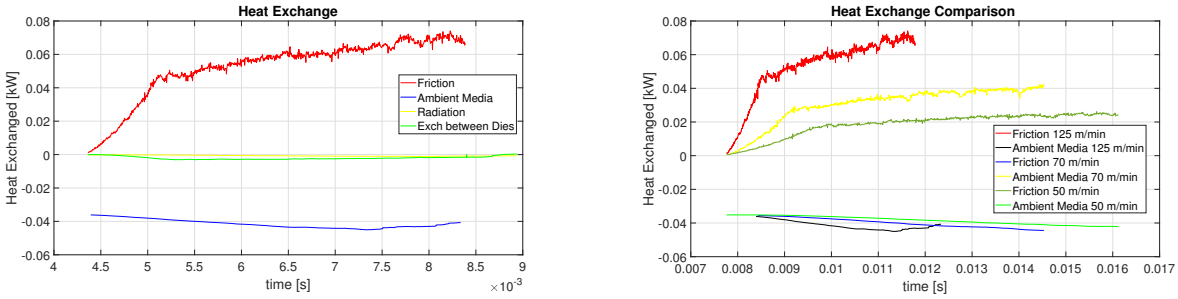

Figure 12.22: Heat exchange mechanisms and comparison between different cutting speeds in cryogenic conditions.

Also the plastic power is considerably increased by the cutting speed while other powers are still negligile in the whole computation.

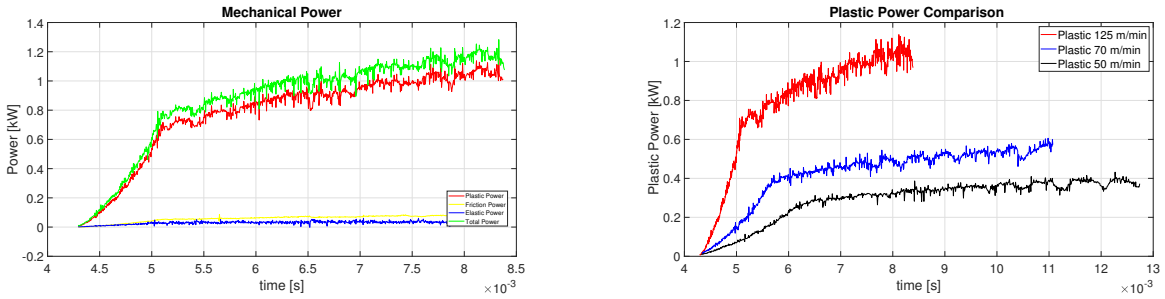

Figure 12.23: Mechanical power contributions and plastic power comparison between different cutting speeds in cryogenic conditions.

Wet with Vc=70 m/min, fz=0.7 mm/rev*tooth, ap=0.4 mm, ae=13 mm.
The force in feed direction is satisfacoty predicted also in this case since the fem results lies in the confidence interval of the experimentsl results, while high divergence is present in case of force perpendicular to feed direction.
Percentage peak error on F_x = Err_{peak} % = -9.27%, it becomes $+1.42\%$ if referred to the superior confidence interval.

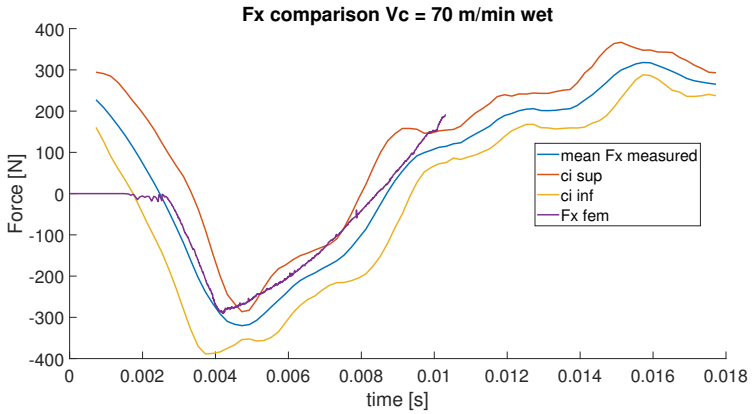

Figure 12.24: Fx comparison between experimental and FEM forces.

The maximum temperature location is always the same (secondary defromation zone) and as expected also in wet enviroment the cutting speed has a noticeble influence on the temperature build up as shown in the comparative plot between the case at Vc=70 m/min and Vc=50 m/min. Now the maximum temperature lies between 1100°C and 1180°C.

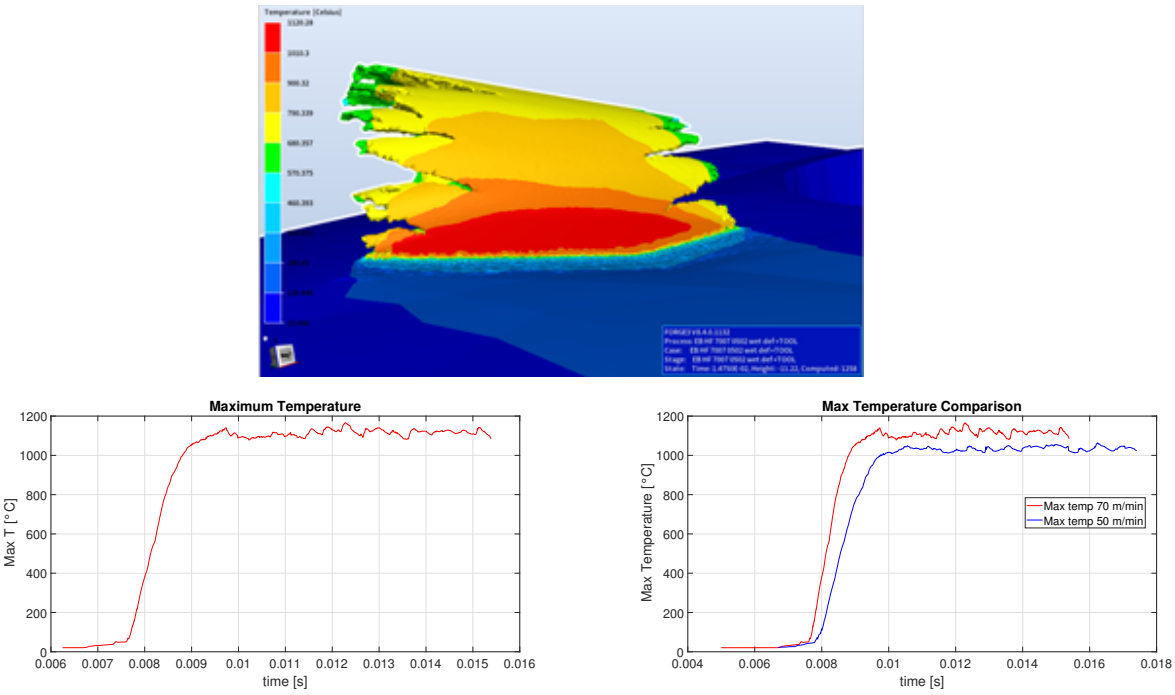

Figure 12.25: Maximum temperature location, maximum temperature profile, temperature comparison changing cutting speed.

The maximum effective strain once again is increased with respect to the cryogenic case, with peaks above 8.

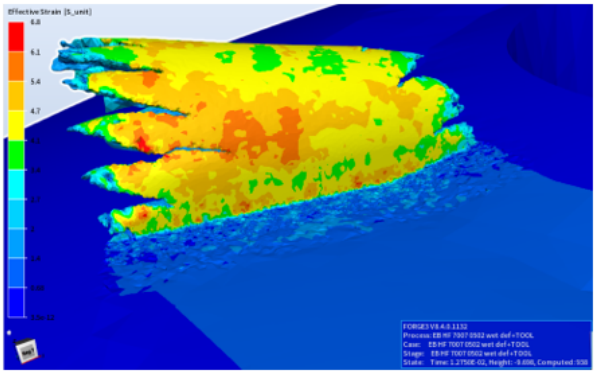

Figure 12.26: Effective strain.

The higher portion of thermal power is generated through friction and exchanged with the ambient media (flood), while the heat exchanged between dies (tool and workpiece) and the heat exchanged through radiation are rather limited mainly due to the low amount of time characterizing the cutting arc of one single tooth.
The thermal power exchaged with ambient media has a different shape if compared with

the one in cryogenic environment since the starting temperature of the two cooling media is very diferent (30 vs -195 °C).

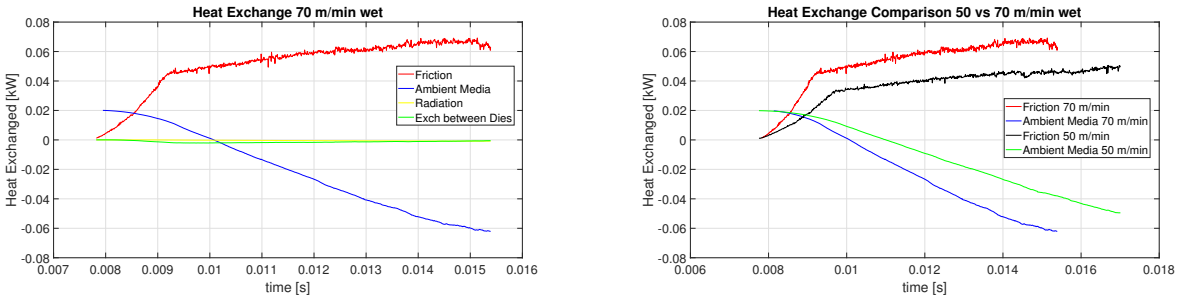

Figure 12.27: Heat exchange mechanisms and heat exchange comparison with lower cutting speeds.

The higher amount of mechanical power is used for the plastic deformation of the material (responsible of the shearing action) and as noticed also in for the cryogenic case this power increses for higer cutting speeds, as logic suggets. Once again friction power and elastic power play a secondary role.

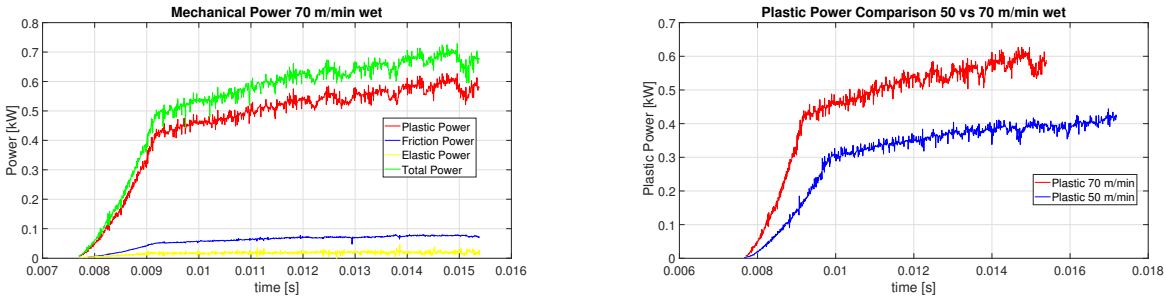

Figure 12.28: Mechanical power contributions and plastic power comparison with lower cutting speeds.

Wet with Vc=125 m/min, fz=0.7 mm/rev*tooth, ap=0.4 mm, ae=13 mm.
In this case the force in feed direction is not well predicted by the finite element simulation, but this was predictable since the experimental data show an evident oscillation that decreases their reliability and it is not repeatable by the finite element model.
Percentage peak error on F_x = $\mathrm{Err}_{\mathrm{peak}}$ % = +80.52%, it becomes +2.63% if referred to the inferior confidence interval.

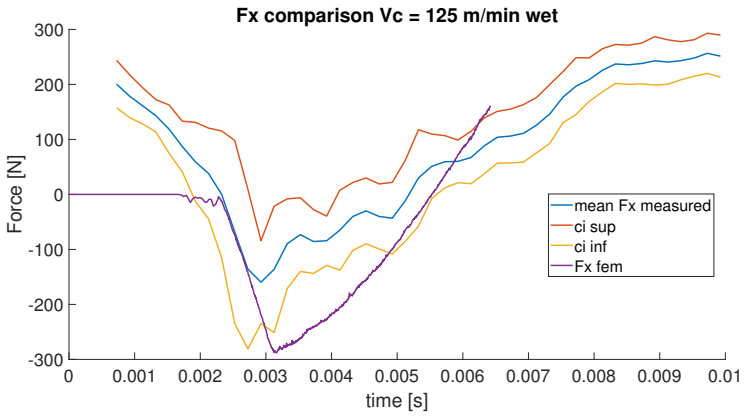

Figure 12.29: Fx comparison between experimental and FEM forces.

As expected,here the highest temperatures are reached with values touching 1300°C.

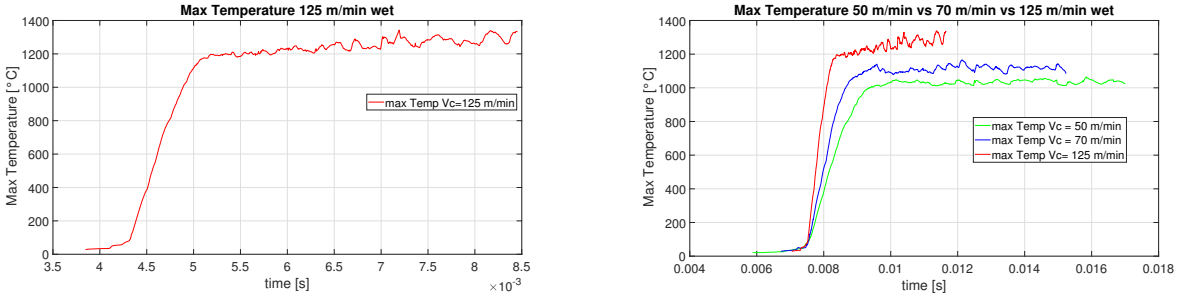

Figure 12.30: Maximum temperature and maximum temperature at different cutting speeds.

The thermal power exchanged by friction is very high since the friction coefficients are higher if compared with cryogenic case and the cutting speed is equal to 125 m/min. Also the heat exchagend with the ambient medium is high because the temperature in the cutting zone is the highest of the 6 analised cases. Its decresing behaviour (in absolute value) in the last part is given by the brackage of the chip and consequent deletion of a portion of hot material by the computation.

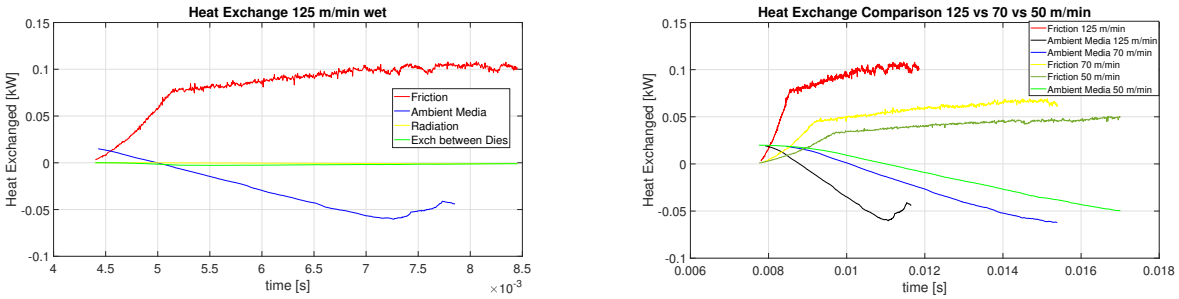

Figure 12.31: Heat exchange mechanisms and heat exchange comparison with lower cutting speeds.

Once again the effective strain is higher if compared to the cryogenic case and the strain rate is comparable with the one of the cryogenic case at 125 m/min.
The mechanical power is primarly influenced by the plastic power but in this case also the friction power becomes considerable due to the effect of high friction coefficients and high cutting speed.

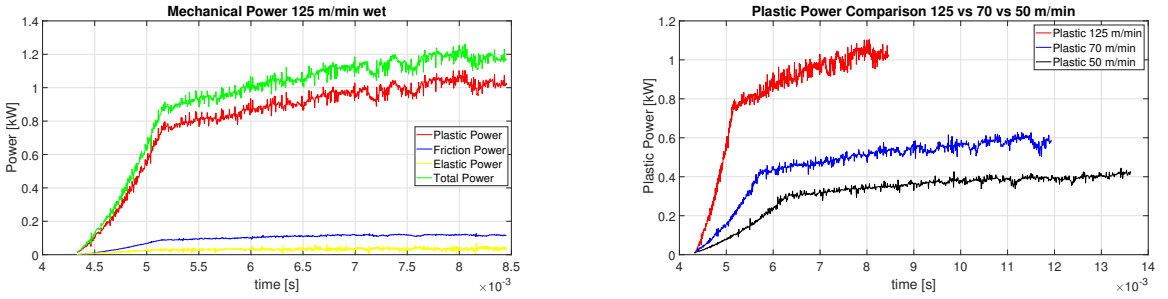

Figure 12.32: Mechanical power contributions and plastic power comparison with lower cutting speeds.

12.1. Differences between high feed and square shoulder milling

In this section the differences between high feed and square shoulder milling are underlined and investigated on the basis of the results of the FE simulations. In particular it is necessary to understand why with the application of cryogenic coolant (LN2) the square shoulder cutters show short life, resulting not competitive against more conventional wet machining. On the contrary using the same system for the delivery of the cryogenic fluid in the cutting zone, high feed cutters exhibit an increment of their life if compared to the

wet approach, especially at high cutting speeds.

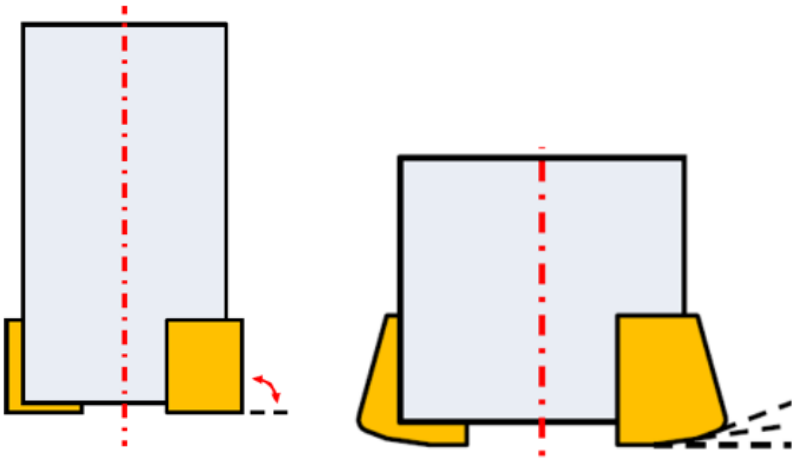

Figure 12.33: Square shoulder (left) vs High feed (right) mill.

First of all there is a geometrical response to this problem, evident in the engagement phase between cutter and workpiece. Square shoulder inserts with lead angle = 90° in wall milling are subjected to intense hammering action when approaching the cut. The whole insert edge is engaged at once, the engagement is sudden, not gradual thus square shoulder concentrates immediately the load on a thin rake area. The situation can also be worsened if largely positive rake angles are present; the action of the cryogenic fluid can overharden the workpiece and (with this geometry) reduce the toughness of the cutter drastically decreasing its life.
In high feed the engagement phase is much more gradual and the value of depth of cut is generally higher than the feed per tooth adopted with square shoulder. This allows the high feed, that is also geometrically more robust, to distribute the stresses on a wider area. In the following plot, the comparison of simulated F_y profiles for the two different milling strategies at the same cutting speed are reported. In the figure there is a zoom on the engagement phases of the two different approaches.

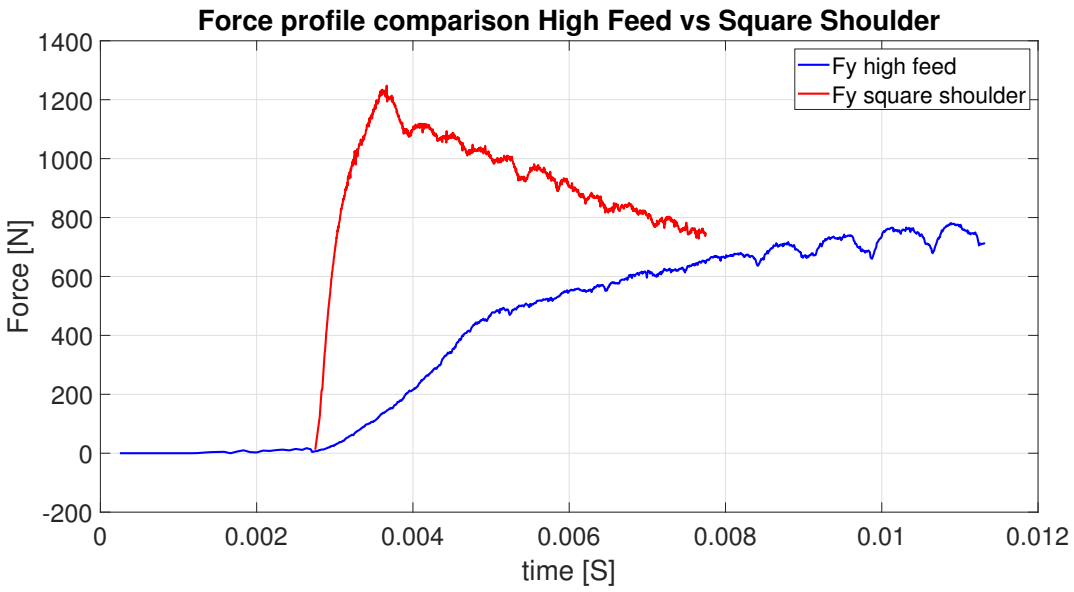

Figure 12.34: Force profile (Fy) comparison Square shoulder vs High feed.

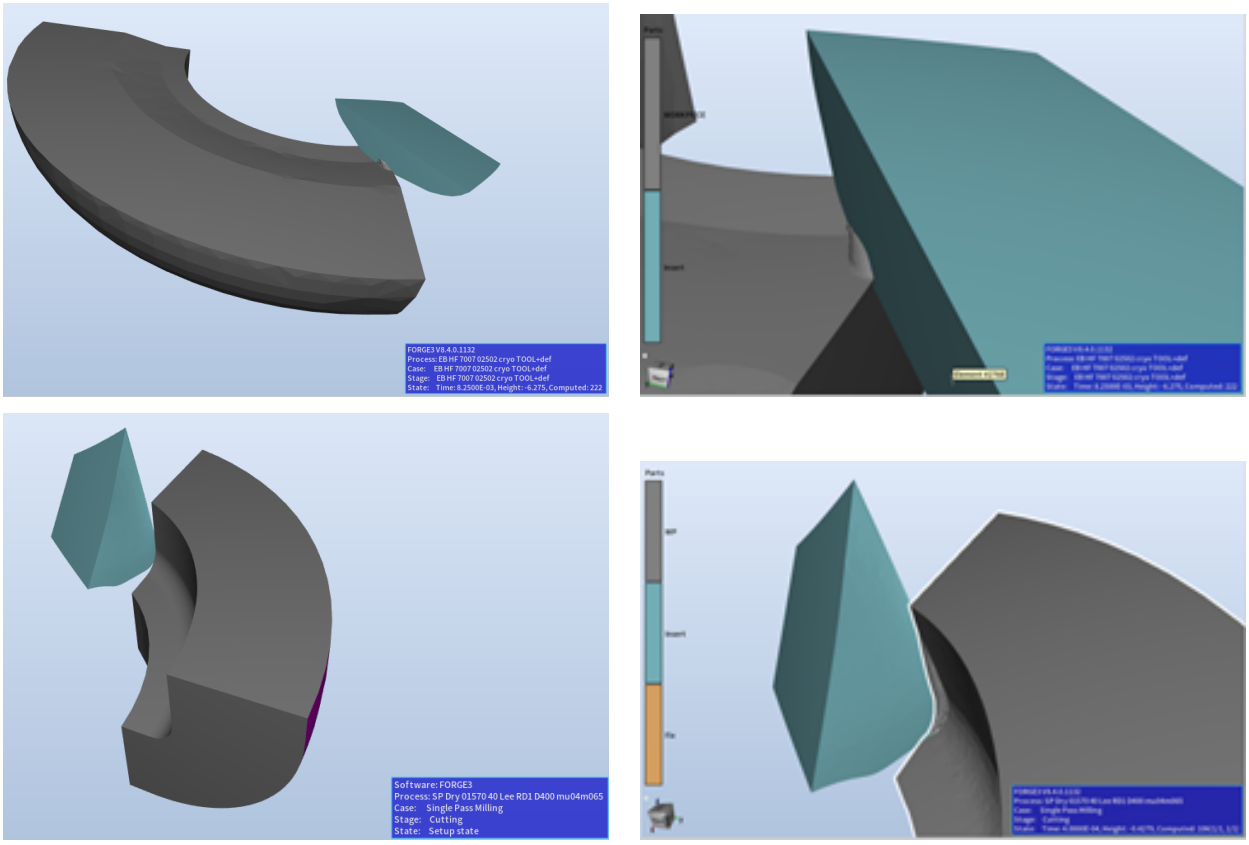

Figure 12.35: Zoom on the first part of engagement High feed (above) vs Square shoulder (below) model.

The plot compares two cutting operations with very different parameters:
- High Feed, cryogenic environment Vc = 50 m/min, fz = 0.7 mm/rev*tooth, ap = 0.4 mm, ae = 13 mm
- Square Shoulder, cryogenic environment Vc = 50 m/min, fz = 0.2 mm/rev*tooth, ap = 3 mm, ae = 5 mm
so it is not correct to make specific comparisons on the magnitude of the force, but it is meaningful to notice the slope in the first part of the plot. In square shoulder it is a sort of hammering, in high feed the profile is more gradual (confirming the considerations done before). This difference is fundamental, especially if the tool is embrittled by the cryogenic fluid. The hammering on an embrittled tool leads to fast chipping of the cutting profile with obvious bad consequences on the life of the tool.

On Forge it is possible to activate the computation also on a rigid die (tool in this case) in order to obtain quantities useful for a deepening of this comparison between different milling strategies. The price of this operation is the doubling of the computation time, so it is not affordable for all the cutting conditions; it has been activated for the cryogenic environment at Vc = 70 m/min.

It is possible to quantify the contact time, in the first image the thin part on the left should be neglected since in reality it is not in contact with the workpiece but its distance from it is under the tolerance factor of the software so it is displayed as a contact zone. The zone where the tool is in contact with the workpiece for a longer time is the spot where engagement starts, then the contact zone progressively enlarges toward right (reference is image on the left).

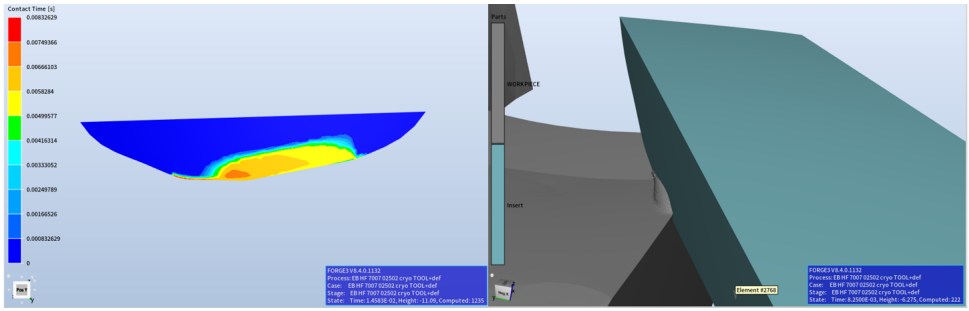

Figure 12.36: Contact time visualization and detail on initial engagement of high feed simulation.

It is possible to display the normal stress on the insert, with a maximum (compressive value) of -2360 MPa. From the front view on the rake, loking at the combination of tangent (along x,y,z) relative velocities between tool and workpiece it is possible to notice

how the maximum values are localized in the more distant part from the centre of the tool because here the tool has a higher tangent velocity. This is also the spot where the maximum temperature is likely to arise on the tool skin.
Note that the more compressed spot and the maximum temperature one are not coincident in this case!

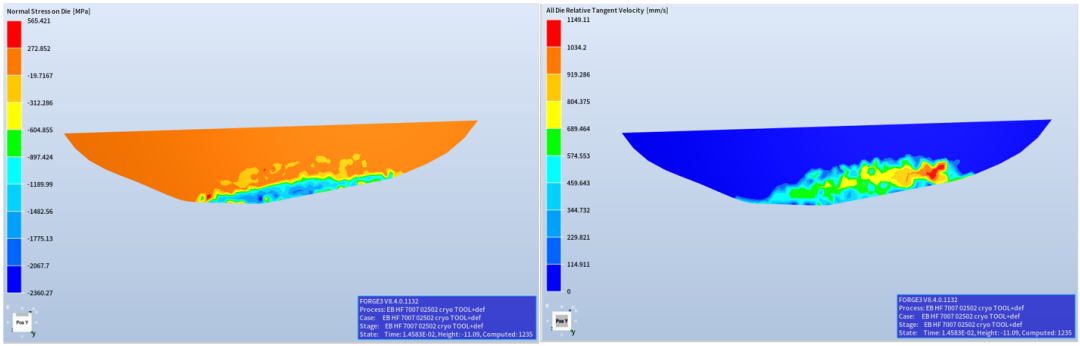

Figure 12.37: Normal stress [MPa] on tool and combination of tangent velocietis [mm/s] in the three directions in high feed simulation.

Then it is possible to visualize the "Die Abrasion Wear" (index) which is the integral in time of the product between pressure and relative speed between tool and workpiece, expressed in [mm*MPa]. Die abrasion index $= \int (P * v_{sl})\, dt$. This value alone can only give an idea of where it is more likely to develop wear due to abrasion, but if compared with the same quantity coming from other operations can give interesting results.

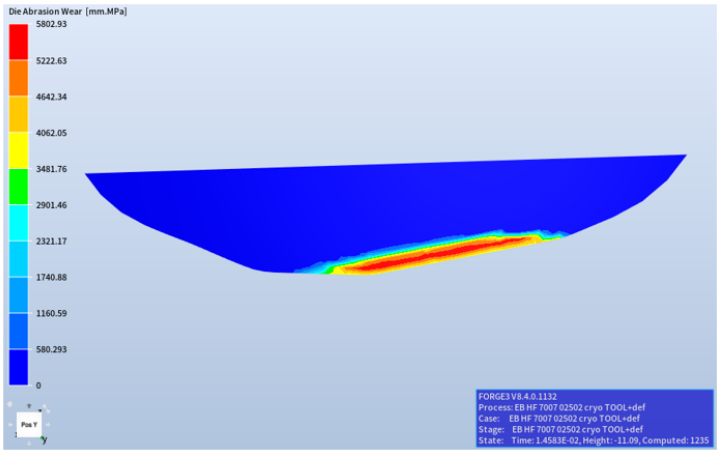

Figure 12.38: Die Abrasion Wear, cryo, Vc = 70 m/min.

For instance, a comparison is possible with data coming from a simulation of sqaure shoulder milling always at Vc= 70 m/min [credits to L.Losa] (dry machining, fz=0.15

mm/rev*tooth, ap=3 mm , ae=5 mm). At a contact time of 0.0044 s the maximum normal stress on the tool is -4041 MPa, the combination of tangential speeds is 1476.57 mm/s and the Die abrasion wear is 5874.7 mm*MPa.
For the high feed configuration (cryogenic condionits), after 0.0044 s of contact, the normal stress is -2292.17 MPa, the combination of tangential speeds 1098.77 mm/s and the Die abrasion wear 2223.03 mm*MPa. Each quantity is largely decreased in case of high feed milling, obviously the cutting parameters are not identical and the comparison between these values is not an absolute law, but the Die Abrasion Wear index indicates that between the two approches a big difference on wear basis is present.
Moreover, as underlined before, in case of high feed milling in the first part of the cutting arc just a small portion of material is in contact with the tool, neglecting this entering phase and starting the calculation of the contact time when the entire chip section is encountered for the first time, at 0.0044 s the the normal stress on the tool is -3415.5 MPa, the combination of tangential speeds 1004.89 mm/s and the Die Abrasion Wear index 4035.38 mm*MPa. Also in this case the abrasion wear is substantially decreased. In addition (see next section), with cryogenic environment the abrasion index can increase so this gap may have been larger if instead of dry environment also for the sqaure shoulder case cryogenic environment would have been considered.

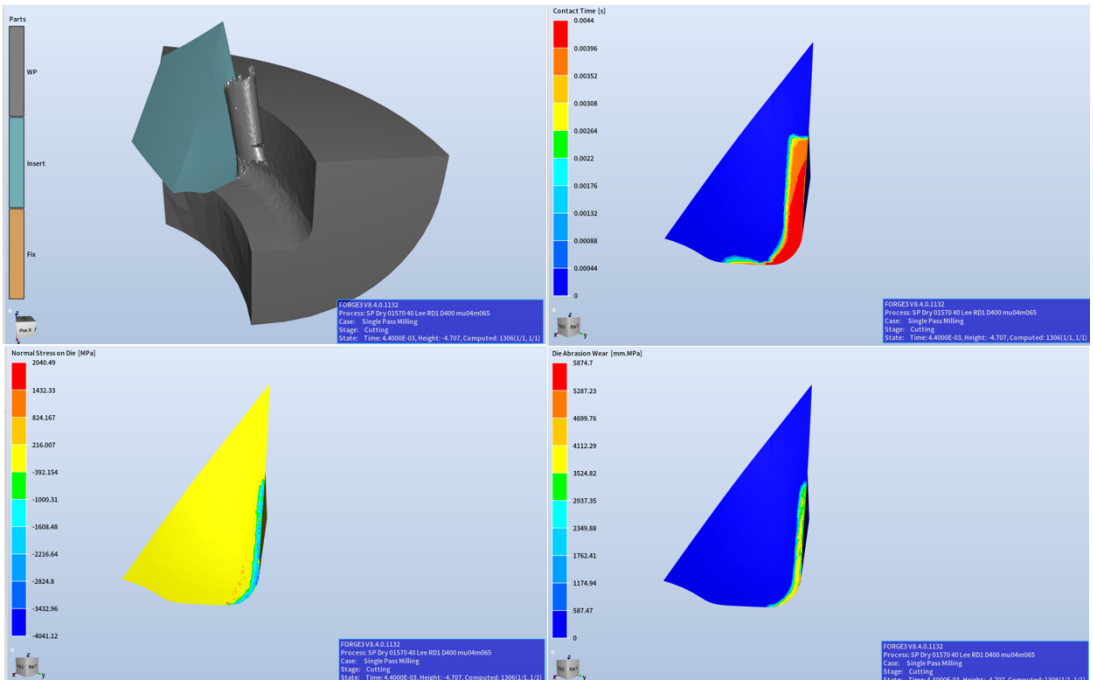

Figure 12.39: Square shoulder milling, contact time, normal stress and die abrasion wear.

It is also possible to make hypothesis on the superiority, on tool life basis, of the high feed

approach because with square shoulder the zone of maximum temperature and maximum normal stress are coincident, while for high feed milling the maximum temperature spot (considering it coincident with the spot of maximum tangent velocity) is shifted outward (far from the centre) with respect to the zone with maximum normal stress.

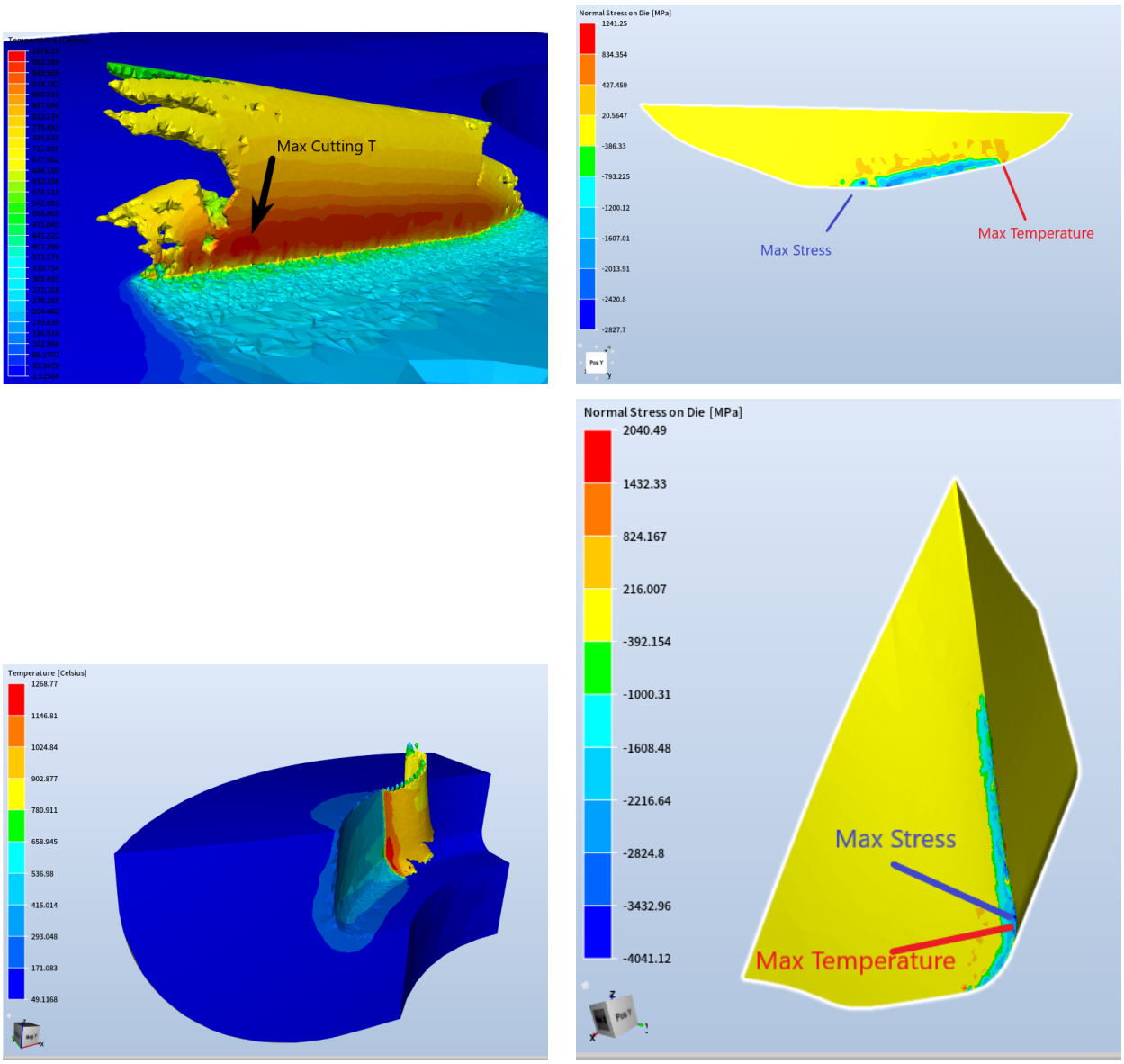

Figure 12.40: Maximumum temperature in the cutting zone and display of maximum stress on the tool both for high feed (above) and square shoulder (below).

In sqaure shoulder approach, the cut takes place on the external profile. Comparing two tools with same nominal diameter, at the same rotational speed (so with same nominal Vc) for the square shoulder one the cut takes place in a zone with higer tangent speed. In high feed the cut takes place in the lower part of the insert (not on the external diameter),

where the tangent speed is lower and this speed plays a crucial role in friction/abrasion phenomena (this topic is discussed in detail in the next section).
These are qualitative considerations, more specific results can be extracted only comparing more similar operations (for example with same radial engagement).
Another non negligible factor is that with a square shoulder mill low values of feed per tooth must be adopted. As consequence, cutting materials with low thermal conductivity as Ti6Al4V a large amount of heat remains localized in a small area around the cutting zone, and without high feed values the cutter insists on a zone already at high temperature and this can induce higher skin temperature on the tool, favouring wear mechanisms.

The following plots are very important, they report the comparison of the maximum temperature profiles between the cryogenic cases simulated in high feed at two different cutting speeds Vc_1 = 50 m/min, Vc_2 = 70 m/min, fz = 0.7 mm/rev*tooth, ap = 0.4 mm and ae = 13 mm and the cryogenic cases simulated in square shoulder at Vc_1 = 50 m/min, Vc_2 = 70 m/min,, fz = 0.2 mm/rev*tooth, ap = 3 mm and ae = 5 mm.
The results confirm that the maximum temperature profiles developed on the workpiece and reasonably also on the tool are much steeper and higher in case of square shoulder milling, with obvious detrimental effects on the tool life. Between the two profiles on average there is a difference of 100°C, even if the square shoulder simulations start with the workpiece at 0°C and the high feed one at 20°C.

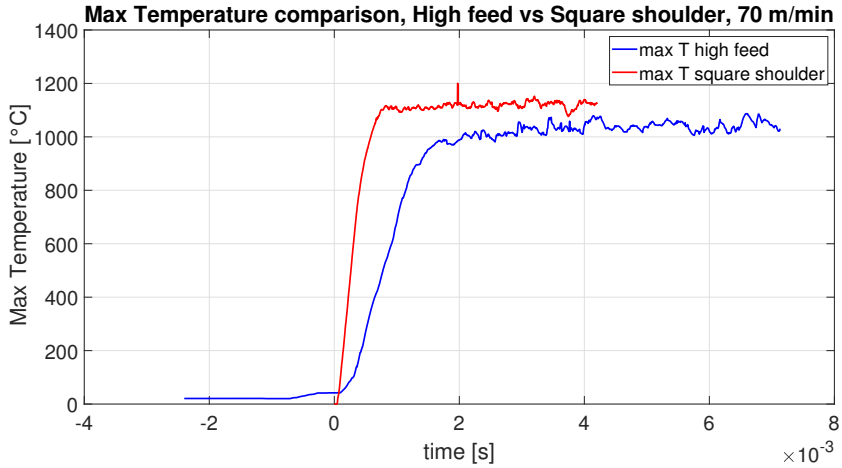

Figure 12.41: Difference in Max temperature between High Feed and Square Shoulder at 70 m/min.

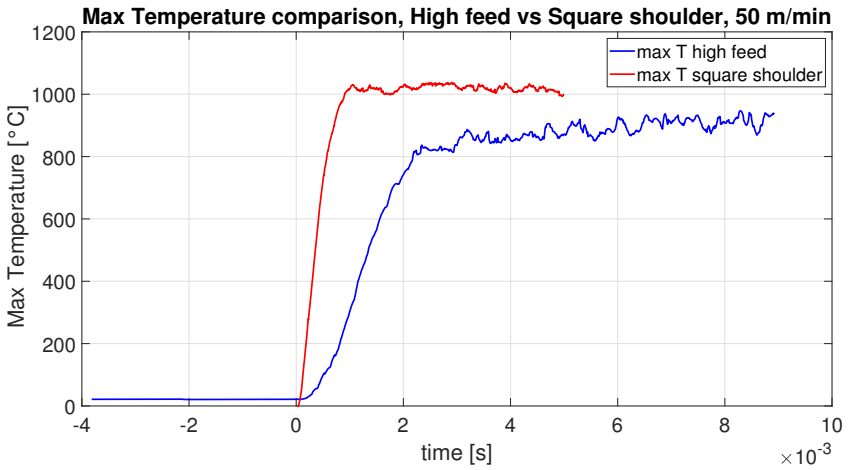

Figure 12.42: Difference in Max temperature between High Feed and Square Shoulder at 50 m/min.

12.2. Different wear depending on cooling lubrication strategies

Also for the simulation in high feed and wet environment at 70 m/min the computation on the tool has been activated with a sensible increment of the computational burden. The collected data are compared with the correspondent data of the case featured by Vc = 70 m/min in cryogenic environment. In particular the comparison is made at normal stress and tangent velocity level, which are at the basis of the abrasion wear index computation. Actually no clear differences are appreciable comparing this kind of results even if a lower maximum normal stress is present almost at every step of the result displayed in case of wet machining. However this is just a local value that characterizes a single node or few nodes concentrated in small areas and it is not enough to justify clear differences under the wear point of view.

In wet conditions the wear abrasion index is lower with respect to cryogenic machinig for the same cutting speed, and a more solid explanation can come from another quantity: the contact area between tool and workpiece. What is evident is that the contact area decreases with cryogenic machining. Thus a comparable cutting force acts on a smaller area (in cryogenic case) giving more reliability to the hypothesis of increased pressure acting on the cutting edge thus higher wear abrasion index. The workpiece also is at a lower temperature in the cryogenic case, so an hardening of the material even if small is present and also this factor can influence the abrasion phenomenon.

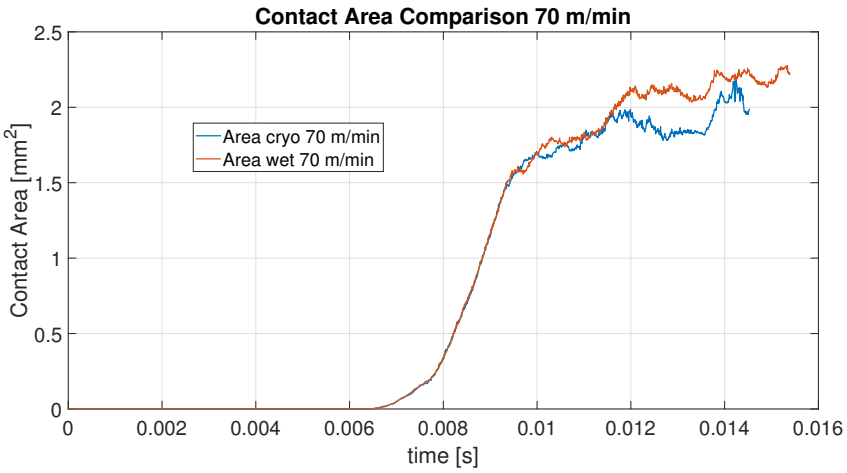

Figure 12.43: Contact area comparison in high feed cryogenic vs wet at 70 m/min.

Is this enough to justify a differnet overall wear behaviour between the two cases?
No, because the abrasion is just one of the wear causes of a tool and the hardening can take place also on the tool side enhancing its resistence to abrasion, but from the FE results no further considerations can be done. What can be said about the other wear causes?
- Atomic diffusion: higher temperatures promote this phenomenon of net atomic transport from the tool to the workpiece thus the higher temperatures of wet machining could facilitate it.
- Adhesion: in the experimental tests at 50 and 70 m/min with cryogenic cooling has been experienced a sort of built-up edge (BUE), with obvious negative effects on the tool life. This phenomenon is typical of ductile materials worked at medium-low cutting speed. Usually the friction between tool and chip favours the adhesion of a part of the worked material on the rake of the tool near the cutting edge. The BUE formation is cyclical, it appears in small quantities, it grows up, becomes unstable and detaches from the rake. The major portion of BUE flows away with the chip, but since it is adherent to the rake it is able to remove small portions of it. Smaller parts of the BUE do not flow away with the chip but remain on the new worked surface of the workpiece, drastically increasing its roughness.
But in this case we are dealing with Ti6Al4V that can not be considered a ductile material, it is difficult to imagine on it a phenomenon of BUE like the one experienceable with Aluminium for instance. More likely is the hypothesis that the cryogenic fluid in this case complicates the engagement (that with Ti6Al4V is not easy) especially in the very first part of the cutting arc where the uncut chip thickness is minimal, promoting rubbing and not a real cut between the tool and the workpiece that favours a sort of "BUE" formation.

As analysed before the spot on the tool where the cut starts is shifted towards the centre of the mill with respect to the external diameter.

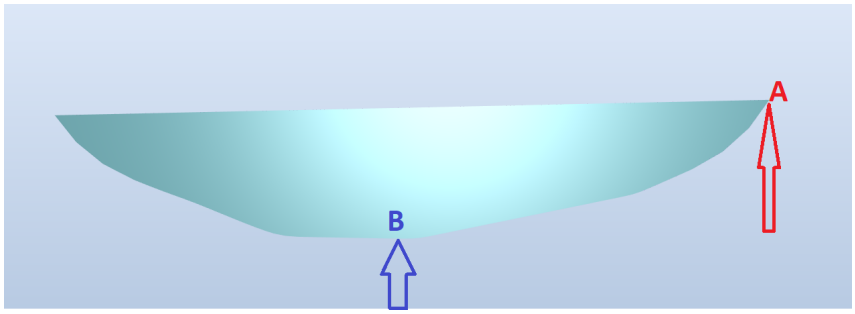

Figure 12.44: Detail on external edge (A) and actual engagement point (B) in high feed.

In this case it is 4 mm far from the external ideal circumference, so at a radial quote of 6 mm instead of 10 mm from the centre, being the total diameter D = 20 mm. The cutting speed Vc = 50 m/min is calculated on the nominal external diameter once fixed the rotational speed.

$$n = \frac{V_c * 1000}{\pi * D}$$

At 795 rpm, but considering the diameter at which the cut starts D = 12 mm the actual cutting speed is decreased of the 40% resulting Vc'=50*(1-0.4)=30 m/min that is a really low cutting speed potentially able to promote BUE formation or at least rubbing and not cut between tool and workpiece. In the case of Vc = 70 m/min the actual cutting speed in the interested spot is 42 m/min, once again a low value for the industrial practice. The wear tests in [3] also evidenced that at 125 m/min the adhesion phenomenon does not take place anymore, here the cutting speed in the most stressed spot goes down from 125 m/min to 125*(1-0.4) = 75 m/min which is a medium value for the industrial practice.
Anyway it is not clear why the "BUE" is not present with flood cooling for all the considered cutting speed, the cryogenic fluid evidently promotes this phenomenon but from the FE simulations it is not possible to determine in which way.
- Oxidation: higher temperatures promote oxidation phenomena on the insert, the oxidized layers are easy to be removed promoting wear. In cryogenic conditions this phenomenon is limited since the liquid nitrogen in contact with hot surfaces evaporates and the nitrogen vapour surrounds the cutting zone preventing oxidation of the tool. The water-oil emulsion used in wet environment has not the same insulative effect, but this aspect should be deeply investigated case by case. Looking at the chips' colour it is evident that in wet condition they face higher temperature and they change colour, but it is not straightforward to evaluate if also oxidation is present. And if it is present on the chips it is not said that the same happens on the tool.

- Plastic deformation: also this wear modality is promoted by higher temperatures so theoretically it is more likely in case of wet machining.
- Fatigue: during a milling operation every insert undergoes a cyclical solicitation both on mechanical and thermal point of view, the insert can be damaged under coupled non-isothermal fatigue. The cryogenic approach in this case brings the positive contribution of avoiding excessive temperature build up but at the same time it is capable of drastically decreasing the cutter skin temperature during the idle phase (phase in which the cutter is not engaged with the workpiece) keeping very high the difference between maximum and minimum temperature and also risking the embrittlement of the cutter.

Future CFD studies will be done trying to determine which is the temperature of the cutter at the beginning of the engagement under different parameters as radial engagement and cutting speed, and with different cooling strategies. The starting temperature in this case is not particularly relevant for the total temperature build up since the low time of contact between tool and workpiece avoids relevant heat exchange through conduction, but it is relevant under a thermal fatigue or embritlement point of view.

In literature it is often experienced a superiority of cryogenic approach only at high cutting speeds if compared with wet machining and one reason could be that at higher speeds not only excessive temperaure built up is avoided but also the idle phase is reduced and probably the cutter has not time to be cooled at low temperatures that may enhance embrittlement or thermal fatigue. From a mechanical point of view the cryogenic delivery system should avoid the overhardening of the workpiece and ideally allow only the friction, plastic power and temperature reduction, reducing the thermo-mechanical stress on the cutter.

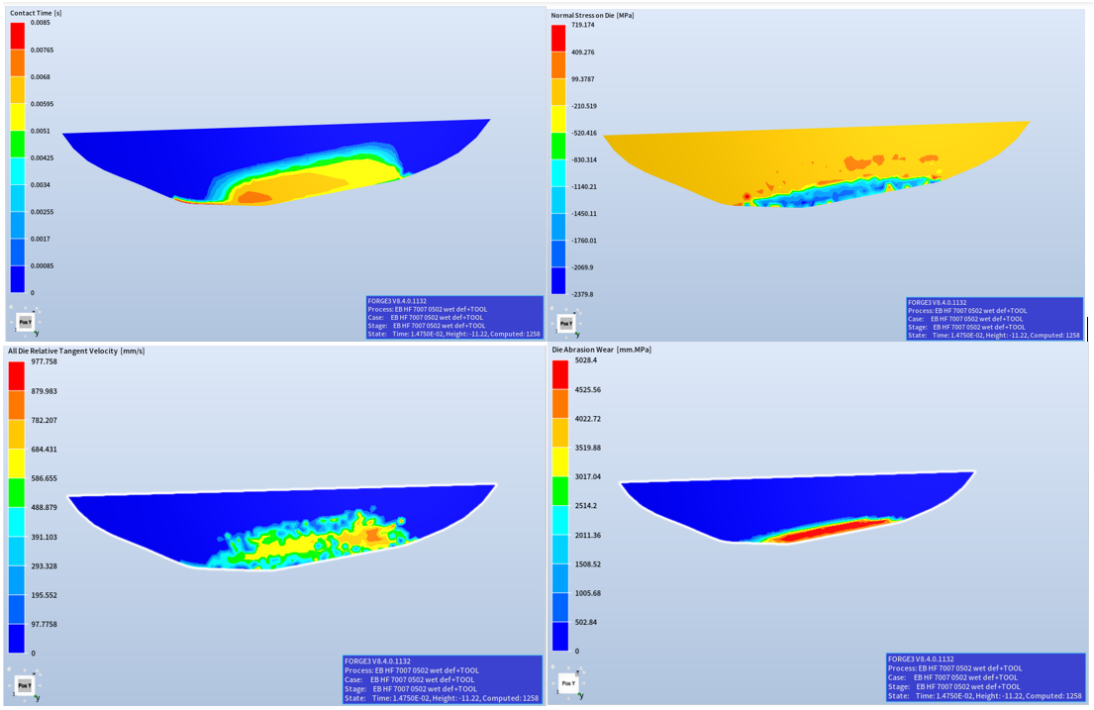

Figure 12.45: Contact time, normal stress, tangent velocicties, abrasion wear index for wet machinign at 70 m/min.

12.3. Overall Comparison of Results

It is useful to compare all the six simulated conditions in order to better evaluate the influence of the cooling environment and of the cutting speed.

As underlined many times in this work the temperature reached by the tool is a crucial factor when wear phenomenon is considered. According to literature, the use of cryogenic fluid (LN2 or CO2) lowers the measured (or estimated) temperatures in the cutting zone, if compared with dry or wet machining. Moreover, the cutting speed is the most influent parameter on the cutting temperature, higher cutting speeds lead to higher cutting temperatures. Following these considerations, logic suggests that the lower cutting temperature will be experienced for the lowest cutting speed (50 m/min) coupled with the cryogenic cooling, while the highest cutting temperature will be experienced for the higher cutting speed (125 m/min) coupled with the flood cooling. And also, between tests at the same cutting speed the one with cryogenic cooling will be featured by the lower tempearture. Looking at the comparative plot below these sentences are verified with finite element simulations, giving reliability to the results.
These maximum temperature values are referred to the workpiece, but are useful to have

also an indication of the tool skin maximum temperature.

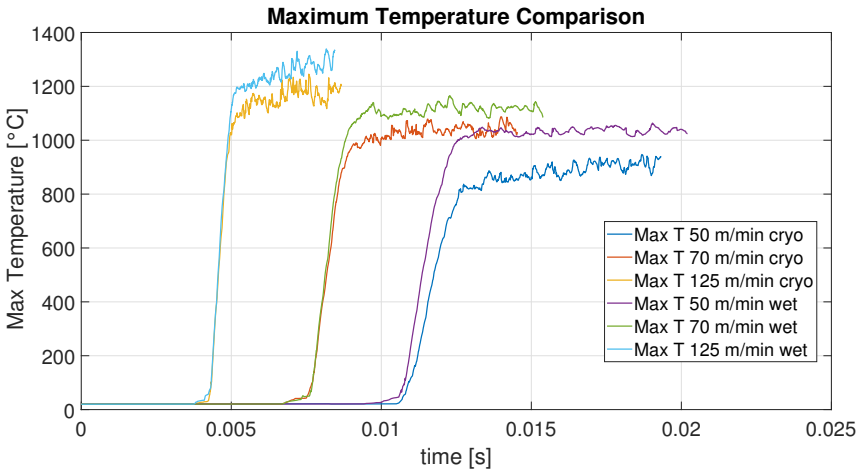

Figure 12.46: Overall maximum temperature comparison.

From the analysis of each case it is evident that the higher amount of thermal power exchanged during the cutting process is generated by friction in correspondence of the tool-workpiece interface. This also underlines the importance of a reliable contact/friction model in a finite element simulation. In the plot below it is visible that the heat generated by friction is strictly correlated to the cutting speed. The high difference of values between tests at the same cutting speed with different cooling strategies is justified by the lower friction coefficient adopted in the cryogenic setup, choice driven by experimental results as in [2].

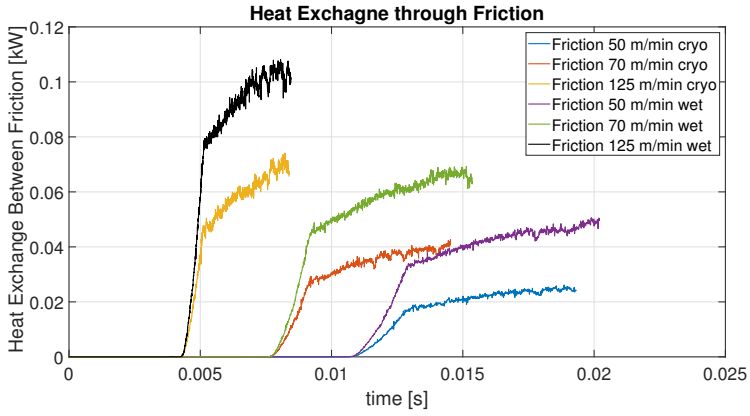

Figure 12.47: Overall comparison of thermal power generated by friction that flows into the workpiece.

The second major contribution (in absolute value) in the thermal problem is given by the heat exchanged with ambient media. In cryogenic conditions this quantity starts at high

values (always in absolute value) if compared with flood cooling since the temperature of the gaseous nitrogen surrounding the cutting zone (-150°C) or the temperature of the window of enhanced heat exchange (-195°C) is much lower with respect to the temperature of the flood environment (30°C). In the second part of the cutting arc the thermal power extracted by the workpiece is higher in case of flood cooling and this is explained by the fact that the flood has an higher heat exchange coefficient if compared with the gaseous nitrogen and they both interacts also with the hot surface left behind by the cutter which has a considerable area. And also the average temperature in the cutting zone in case of flood cooling is much higher than in case of cryogenic cooling so the term (Tambient -Tworkpiece) is higher.
For the cases at 125 m/min the curve changes its sign because the chip breaks in half at a certain point and the broken part is delated by the computation.

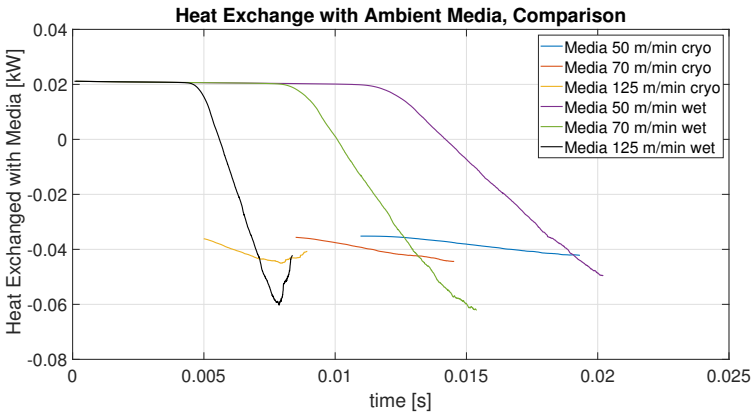

Figure 12.48: Overall comparison of thermal power exchanged with the ambient media from workpiece side.

The thermal power exchanged by conduction between tool and workpiece is rather limited. The contact time is really short and the tool workpiece interface conductance is quite low if considered the averege of machining simulations. The majority of simulations in litereture are turning simulations in which the necessity is to simulate a steady state condition for the thermal problem, thus the tool workpiece interface conductance is brought to unphisical values in oder to reach rapidly high tempereature values and a sort of steady state condition. In milling there is not a steady state value to reach due to the unsteady nature of the process, thus the interface conductance value is lowered to physical values which anyway are not easy to be determined. Also the temperature profile of the tool influences the thermal power exchanged through conduction, for the cryogenic cases I adopted lower tool skin temperatures with respect to flood cooling, a colder tool will extraxt more heat from the workpiece but these values are microscopic if compared to

the values presented above, so their discussion becomes marginal. Also the heat exchaged through radiation is very small and it depends on the surface temperature of tool and workpiece.

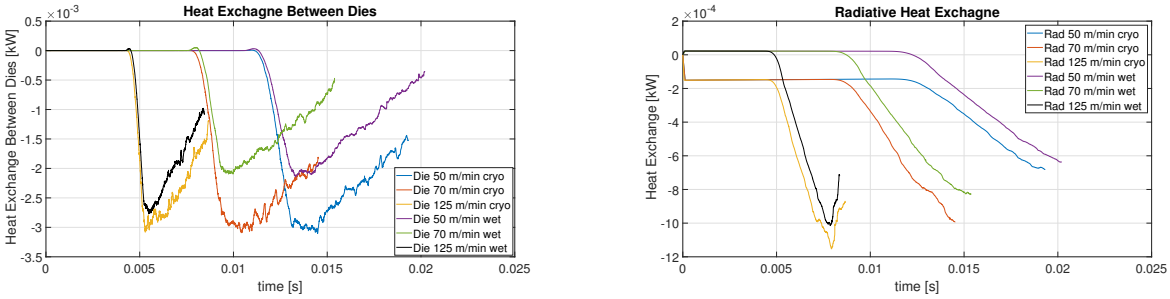

Figure 12.49: Overall comparison of thermal power exchanged thorugh conduction and radiation between tool and workpiece.

Passing from the thermal power to the mechanical one it is evident that the major contribution is given by the plastic power, as expected for a chip removal operation, since it is responsible of the shearing action. If for the thermal problem the most important factor was the friction model, now for the mechanical one the most important factor is the material model.
Increasing the cutting speed the plastic power increases in a considerable way. It is also important to notice that passing from flood cooling to cryogenic cooling the plastic power decreases. Reasonably the material shows less ductility at lower temperatures, this result finds confirmation in literature and also looking at the effective strain of each simulation, it is decreased in case of cryogenic cooling.

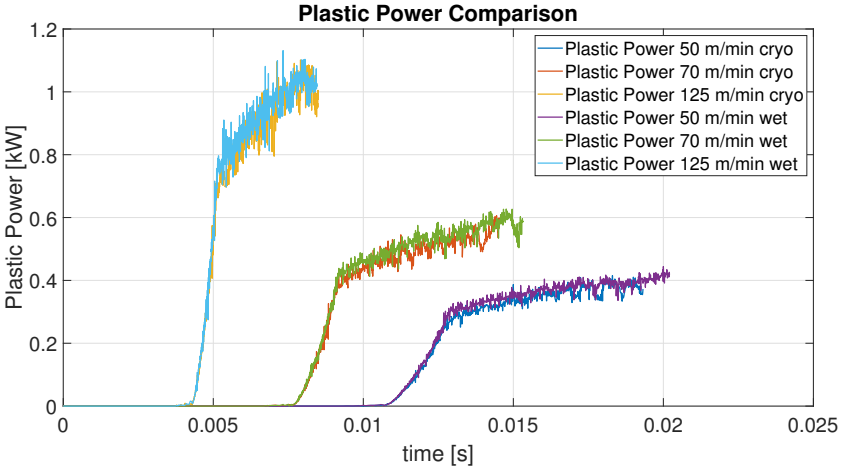

Figure 12.50: Overall comparison of plastic power.

The second major contribution to the mechanical power is the friction power which is influenced by the friction coefficients adopted and by the cutting speed as the comparative plot shows below.
The lower contribution is given by the elastic power, which is particularly small and noisy, it can be neglected. In the cutting phase the material is cut under the shearing action given by a strong plastic deformation, in this mechanism the elastic contribution will be really small/negligible.

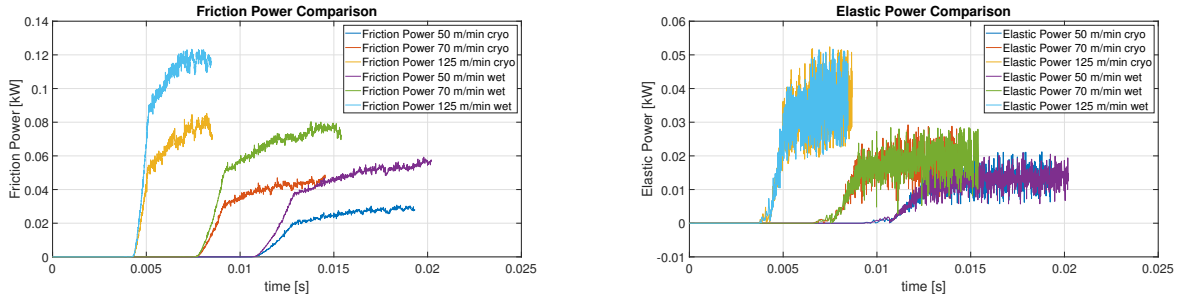

Figure 12.51: Overall comparison of friction power and elastic power.

Summing up all the three contributions it is possible to evaluate the total mechanical power which has a shape completely similar to the one of plastic power with lower values in case of cryogenic cooling, a result in agreement with experimental findings [2], giving reliability to the finite element results.
This underlines how the cryogenic approach can give environmental benefits not only because of the absence of dangerous substances released in the ambient but also because it is capable of decreasing the cutting power requested in chip removal operations, thus reducing the energy required at machine level, in addition to the advantage of avoiding the use of pumps for the feeding and recirculation of the conventional metal cutting fluids.

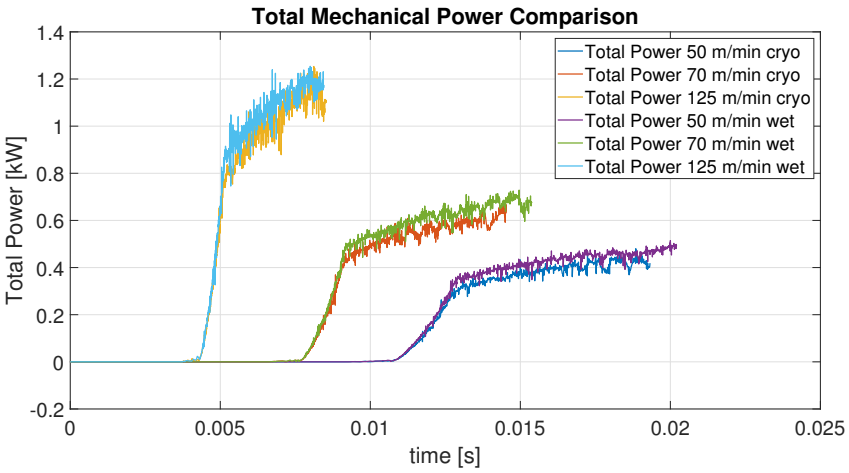

Figure 12.52: =Overall comparison of total mechanical power.

Another common observation in literature is the contact area reduction between tool and workpiece passing from dry or flood machining to cryogenic machining. This aspect was previously investigated for the cases at 70 m/min while now a complete comparison is presented, showing that the contact area reduction takes place at every cutting speed.

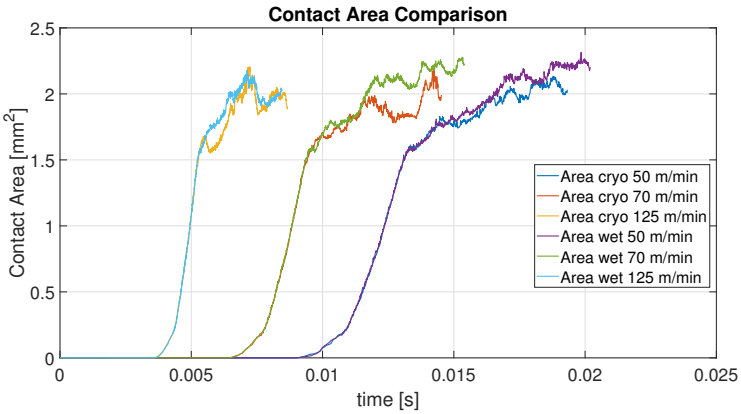

Figure 12.53: Overall comparison of tool workpiece contact area.

13 | Summary of results, critical discussion and future developments

Both the conditions (wet and cryogenic) are run with the same Johnson-Cook material model with coefficients determined by Lee and Lin in 1998 [76]. The damage model is a Latham-Cockcroft with D = 400 MPa and the tool-workpiece interface conductance is $10 kW/m^2K$. In the table below are summarized other parameters of each set up:

Cutting Environment	Wet	Cryogenic
Friction coefficients	$\mu = 0.2, m = 0.5$	$\mu = 0.2, m = 0.25$
Workpiece initial temperature	20°C	20°C
Ambient temperature	30°C	−150°C
HTC with Ambient media	5000 W/m^{2}K	1500 W/m^{2}K
HTC jet window	–	Variable with Tsurf
HTC jet window temperature	–	−195°C
Tool skin Temperature	Rising in time	Rising in time

Table 13.1: Parameters of FE set up for different cutting environments.

In the high feed model, passing from wet to cryogenic machining the results of the simulations say:

Parameter	Finding
Max T	Decreased for every cutting speed
Contact Area	Decreased for every cutting speed
Normal Stress on Tool	Increased
Tool Abrasion Index	Increased
Effective Strain	Decreased for every cutting speed
Thermal Power due to Friction	Decreased for every cutting speed
Heat exch by Conduction	Incresed for every cutting speed (abs value)
Heat exch by Radiation	Increased for every cutting speed (abs value)
Friction Power	Decreased for every cutting speed
Plastic Power	Decreased for every cutting speed
Total Mechanical Power	Decreased for every cutting speed

Table 13.2: Differences in the results between wet and cryogenic environment.

Passing from square shoulder to high feed milling the results of the simulations say:

Parameter	Finding
Max T	Decreased
Normal Stress on Tool	Decreased
Tool-WP relative Tangential Speed	Decreased
Tool Abrasion Index	Decreased

Table 13.3: Differences in the results passing from square shoulder to high feed milling.

The tables above resumes the results of the FE simulations, now it is time to critically analyse them and the parameters used in the modelling phase.

First of all substantial differences between high feed and square shoulder cutters have been discussed justifing different results in terms of tool life when applying LN2 as coolant. High feed tools are more robust (thanks to new geometries developed in the last years), promote lower/smoother temperature build up and smoother force profiles if compared with square shoulder tools.
In my opinion the main limitation of this analysis and of the data on the tool life is that the data about high feed come from tests with radial engagement corresponding to the 65% of the mill's diameter, while the data about square shoulder come from test with radial

engagement corresponding to the 25% of the mill's diameter. The square shoulder cutter during the idle phase has more time to be frozen and a frozen tool increases drastically the possibility of developing chipping between rake and flank, especially if, as in case of sqaure shoulder, the stresses are concentrated in a thin area, extremally stressed under a mechanical and thermal point of view. And also, if the tool is frozen during the idle phase the difference between maximum and minimum temperature increases, high temperature drops are responsible of thermal fatigue and can cause problems to the external coating layer of the tool; repeated cycles of thermal expansion ad contraction not followed by the substrate can lead to the detachment of the coating.
Future CFD studies will be done in order to determine which is the temperature drop during the idle phase with different cooling strategies and cutting parameters. Possibly the outputs of these simulations will be helpful boundary conditions for future FEM simulations and will give an idea of the complete thermal cycle seen by the tool.
As discussed in the state of the art of this thesis work, it is not available a standard and reliable instrumentation for the measurement of temperatures at the tool-workpiece interface in milling, thus the simulated temperature can not be precisely validated. Anyway there are different temperatures easier to be measured, not available for this work, that in future experimental tests should be acquired (because precious initial conditions) as temperature of the environment inside the machine, temperature of the cutting fluid (emulsion), temperature of the workpiece during the instant before the passage of the tool.

Between the results coming from the two models (square shoulder and high feed) a big difference is present; in the square shoulder simulations the only comparable force between FEM and experimental results was the force in y direction (perpendicular to feed) while in the high feed model the comparison is better along x direction (parallel to feed). Probably the main limitation is the effect of the machine tool and dynamometric table's dynamics on the force profiles. When oscillations are evident, they can not be reproduced by the FE model and the simulated forces diverge with respect to the measured ones. In both the cases the experimental tests were conceived as wear tests, the starting block of material had a big mass that complicates the forces' acquisition and the system's dynamics. Probably data acquired on smaller workpieces with a more stable system would be easier to be replicated with a FE simulation and a validation of the models based on the comparison of forces in two directions (instead of one) would be possible. Anyway the results of forces' comparison obtained in both the cases are satisfactory, validating and giving reliability to the FE models.

This work suggests that previously developed models of square shoulder milling are adaptable to different machining strategies, obtaining good results. As said before the model designed by L.Losa has been adapted to the new geometries and in case of cryogenic milling the majority of its parameters have been used also in the high feed set up. Material model, damage model, heat exchange properties with ambient media and tool-workpiece interface conductance are the same. The material model has been conserved because its choice comes from a wide literature review and FE comparative tests with other models which demonstrate its superiority and reliability in case of Ti6Al4V machining. The same holds for the choice of a simple Latham-Cockcroft damage model, able to approximate the proper chip morphology without an excessive complication of the model. Also the friction model is the same Coulomb-Tresca (obviously with different μ and m parameters), this is a choice driven by literature since it is evident how more complicated friction models do not bring satisfactory improvements to the results. The cooling medium (LN2) is the same, as the tool-workpiece material pair, so heat exchange properties with ambient media and tool-workpiece interface conductance are the same in the two models.
One problem experienced is that many material models in literature are tested in very simple orthogonal cutting operations, in which the kinematics is very simple and the cutting zone is really small; in these cases also with a very small mesh size the simulations last a reasonable time. Passing to real cutting operations with more complex kinematics and wider cutting zones, such a small mesh size increases exponentially the simulation time, forcing the choice of a coarser mesh. Larger meshes can prevent some material (or damage) models from showing their real potentialities. On the other side, without the availability of more powerful hardware resources, heavier simulations are not affordable.
Another complication on the material model side is the fact that the flow stress equations are derived from tests at strain rates way smaller with respect to the one experienced in cutting simulations. In my opinion it is not a case that the best reproduced condition in this work is the one with Vc=50 m/min in wet environment, that is the lower cutting speed of the test campaign, and the strain rate is the one closest to the strain rate in which the material model has been developed. At low cutting speeds the material model coupled with the damage model is also able to reproduce the typical segmented chip morphology, increasing the speed with the same damage model the shear bands fastly evolves in fractures on the chip, while at 125 m/min it is not rare to find continous chips between the collected ones, also in cryogenic conditions in which the chips' defectiveness should be higher. Increasign the Damage value D of the damage model is possible to avoid the fragmentation of the chips in the simulations but shear bands are not formed in the first part of the cut. The easiest condition for a more precise validation of the chip morphology would have been the lowest cutting speed (50 m/min) but unfortunately no chips were

collected under 125 m/min.

The friction model and its parameters are the most influent factors for the thermal problem, but an increment of friction coefficients increases the magnitude of the forces too, so the friction coefficients are also a precious tool for the calibration of the cutting forces. Here a problem rises up: as underlined in the state of the art, it is not possible to separate exactly the effects of the material and the friction models. For their correct calibration are required extremely precise measurements of cutting forces and temperatures, and the latter are not measureable with precision in milling. In turning the cutting temperature is much easier to the be measured and it is not a casuality that in literature only FE simulations of turning operations are available. In this scenario a simple friction model is a good choiche, it is worth giving more attention to the material model and one assessed its goodness also an higher effort can be spent on the friction model.

For the thermal problem also the heat transfer coefficients with ambient media are fundamental. In my opinion (for the cryogenic case) the choice of creating a window of enhanced heat exchange in the zone where the LN2 is present is a good approximation, but it has some limitations that probably decrease its effectiveness with respect to the real case. All the boling/evaporation phenomena, liquid stagnation or gaseous cushion formation are summarized with a mean behaviour in a single window. It would be intersting to understand through CFD simulations which is the dominant phenomenon among them (as function of the cutting parameters) and adjust the heat transfer coefficients as consequence. Anyway the obtained results, also when compared with wet machining, are in line with what is reported in literature on this topic.

The reulsts of the finte element simluations confirms what has been experienced in experimental tests: in cryogenic conditions the total mechanical power requested for the cut is lower if compared with wet conditions. The main contribution to this power reduction is given by the reduction of the plastic power since the material at low temperatures is sheared without reaching the same values of plastic deformations typical of wet machining. The second relevant contribution is given by the reduction of the friction power. These results underline that the cryogenic approach at shop floor level reduces the energy demand of the machines if compared to wet approach, and this gap is hugely enlarged considering the absence of recirculating or suction pumps in the cryogenic equipment. Assessed this, now the environmental challenge is the necessity of finding less pollutant processes for the liquefaction of nitrogen.

In this work a superiority of high feed milling over square shoulder as strategy to couple with cryogenic cooling has been assessed. Future works should aim at the validation of

the FE models according to the forces in more than one direction and at the completion of an entire cutting arc with refined mesh size. Then it is important to introduce the deformability of the tool that in this work is considered rigid. This will allow a deeper investigation of stresses on it, with the possibility to extract interesting results for the future developement of tools specifically dedicated to cryogenic machining. Consider that the tools available on the market are designed to keep their mechanical properties high at high temperatures but not the same attention is given for the performances at really low temperatures. An optimization of the properties in cryogenic condition would be a big step for enlarging the potentialities of cryogenic machining. These steps require more powerful hardware resources to be carried out in resonable time (under one week at least).

All the attention here is given to power consumption or tool life but for every manufacturing process the quality of the produced parts is fundamental. In particuar, Ti6Al4V is largely used in aerospace industry where extremely strict regulations on the quality of the manufactured pieces are present. Future works will be done with the aim of extimating through FE simulations the mechanical properties of cryogenically manufactured parts, with particular attention on sufrace quality, hardness and residual stresses. The hope is to have one more proof of the superiority of this approach over more conventinal and pollutant/harmful technologies like wet machining. Doing this through FEA allows the reduction of time and costs of the research in this complicated but important field.

Bibliography

[1] N. Abukhshim, P. Mativenga, and M. A. Sheikh. Heat generation and temperature prediction in metal cutting: A review and implications for high speed machining. *International Journal of Machine Tools and Manufacture*, 46(7-8):782–800, 2006.

[2] P. Albertelli and M. Monno. Energy assessment of different cooling technologies in ti-6al-4v milling. *The International Journal of Advanced Manufacturing Technology*, 112(11):3279–3306, 2021.

[3] P. Albertelli, V. Mussi, M. Strano, and M. Monno. Experimental investigation of the effects of cryogenic cooling on tool life in ti6al4v milling. *The International Journal of Advanced Manufacturing Technology*, pages 1–13, 2021.

[4] S. Anurag and Y. Guo. A modified micromechanical approach to determine flow stress of work materials experiencing complex deformation histories in manufacturing processes. *International Journal of Mechanical Sciences*, 49(7):909–918, 2007.

[5] P. Arrazola and T. Özel. Investigations on the effects of friction modeling in finite element simulation of machining. *International Journal of Mechanical Sciences*, 52 (1):31–42, Jan. 2010. ISSN 0020-7403. doi: 10.1016/j.ijmecsci.2009.10.001.

[6] P. Arrazola, D. Ugarte, and X. Dominguez. A new approach for the friction identification during machining through the use of finite element modeling. *International Journal of Machine Tools and Manufacture*, 48(2):173–183, 2008.

[7] T. Augspurger, M. Koch, F. Klocke, and B. Döbbeler. Investigation of transient temperature fields in the milling cutter under co2 cooling by means of an embedded thermocouple. *Procedia CIRP*, 79:33–38, 2019.

[8] T. Augspurger, G. Da Silva, D. Schraknepper, P. Mattfeld, and T. Bergs. Model-based monitoring of temperatures and heat flows in the milling cutter. *The International Journal of Advanced Manufacturing Technology*, 107(9):4231–4238, 2020.

[9] M. Bacci da Silva and J. Wallbank. Cutting temperature: prediction and measurement methods—a review. *Journal of Materials Processing Tech-*

nology, 88(1):195–202, 1999. ISSN 0924-0136. doi: https://doi.org/10.1016/S0924-0136(98)00395-1. URL https://www.sciencedirect.com/science/article/pii/S0924013698003951.

[10] V. A. Balogun and P. T. Mativenga. Impact of un-deformed chip thickness on specific energy in mechanical machining processes. *Journal of Cleaner Production*, 69:260–268, 2014.

[11] J. Barry, G. Byrne, and D. Lennon. Observations on chip formation and acoustic emission in machining ti–6al–4v alloy. *International Journal of Machine Tools and Manufacture*, 41(7):1055–1070, 2001.

[12] M. Bermingham, J. Kirsch, S. Sun, S. Palanisamy, and M. Dargusch. New observations on tool life, cutting forces and chip morphology in cryogenic machining ti-6al-4v. *International Journal of Machine Tools and Manufacture*, 51(6):500–511, 2011.

[13] M. Bermingham, S. Palanisamy, D. Kent, and M. Dargusch. A comparison of cryogenic and high pressure emulsion cooling technologies on tool life and chip morphology in ti–6al–4v cutting. *Journal of Materials Processing Technology*, 212 (4):752–765, 2012.

[14] R. Bertolini, S. Bruschi, A. Ghiotti, G. Haugou, H. Morvan, and L. Dubar. Material behaviour at low temperatures for calibrating cryogenic machining numerical simulations. *Procedia CIRP*, 82:344–349, 2019.

[15] D. Biermann and M. Heilmann. Improvement of workpiece quality in face milling of aluminum alloys. *Journal of Materials Processing Technology*, 210(14):1968–1975, 2010.

[16] C. Bonnet, F. Valiorgue, J. Rech, C. Claudin, H. Hamdi, J. Bergheau, and P. Gilles. Identification of a friction model—application to the context of dry cutting of an aisi 316l austenitic stainless steel with a tin coated carbide tool. *International Journal of Machine Tools and Manufacture*, 48(11):1211–1223, 2008.

[17] C. Bonnet, F. Valiorgue, J. Rech, and H. Hamdi. Improvement of the numerical modeling in orthogonal dry cutting of an aisi 316l stainless steel by the introduction of a new friction model. *CIRP Journal of Manufacturing Science and Technology*, 1(2):114–118, 2008.

[18] A. Bordin, S. Imbrogno, G. Rotella, S. Bruschi, A. Ghiotti, and D. Umbrello. Finite

element simulation of semi-finishing turning of electron beam melted ti6al4v under dry and cryogenic cooling. *Procedia CIRP*, 31:551–556, 2015.

[19] M. Calamaz, D. Coupard, and F. Girot. A new material model for 2d numerical simulation of serrated chip formation when machining titanium alloy ti–6al–4v. *International Journal of Machine Tools and Manufacture*, 48(3-4):275–288, 2008.

[20] M. Calamaz, D. Coupard, and F. Girot. Numerical simulation of titanium alloy dry machining with a strain softening constitutive law. *Machining Science and Technology*, 14(2):244–257, 2010.

[21] M. Calamaz, D. Coupard, M. Nouari, and F. Girot. Numerical analysis of chip formation and shear localisation processes in machining the ti-6al-4v titanium alloy. *The International Journal of Advanced Manufacturing Technology*, 52(9):887–895, 2011.

[22] G. M. Calvert, E. Ward, T. M. Schnorr, and L. J. Fine. Cancer risks among workers exposed to metalworking fluids: a systematic review. *American journal of industrial medicine*, 33(3):282–292, 1998.

[23] E. Ceretti, L. Filice, D. Umbrello, and F. Micari. Ale simulation of orthogonal cutting: a new approach to model heat transfer phenomena at the tool-chip interface. *CIRP annals*, 56(1):69–72, 2007.

[24] G. Chen, C. Ren, X. Yang, X. Jin, and T. Guo. Finite element simulation of high-speed machining of titanium alloy (ti–6al–4v) based on ductile failure model. *The International Journal of Advanced Manufacturing Technology*, 56(9):1027–1038, 2011.

[25] W. Cheng, J. Outeiro, J.-P. Costes, R. M'saoubi, H. Karaouni, L. Denguir, V. Astakhov, and F. Auzenat. Constitutive model incorporating the strain-rate and state of stress effects for machining simulation of titanium alloy ti6al4v. *Procedia CIRP*, 77:344–347, 2018.

[26] K. Chipasa. Best practice guide for the disposal of water-mix metalworking fluids. *UKLA, UK*, pages 1–6, 2011.

[27] C. Courbon, F. Pusavec, F. Dumont, J. Rech, and J. Kopac. Tribological behaviour of ti6al4v and inconel718 under dry and cryogenic conditions—application to the context of machining with carbide tools. *Tribology International*, 66:72–82, 2013.

[28] A. Davoudinejad, E. Chiappini, S. Tirelli, M. Annoni, and M. Strano. Finite element

simulation and validation of chip formation and cutting forces in dry and cryogenic cutting of ti–6al–4v. *Procedia manufacturing*, 1:728–739, 2015.

[29] M. Dhananchezian and M. P. Kumar. Cryogenic turning of the ti–6al–4v alloy with modified cutting tool inserts. *Cryogenics*, 51(1):34–40, 2011.

[30] N. Dhar, M. W. Islam, S. Islam, and M. A. H. Mithu. The influence of minimum quantity of lubrication (mql) on cutting temperature, chip and dimensional accuracy in turning aisi-1040 steel. *Journal of materials processing technology*, 171(1):93–99, 2006.

[31] V. Dhokia, S. Newman, R. Imani-Asrai, et al. An initial study of the effect of using liquid nitrogen coolant on the surface roughness of inconel 718 nickel-based alloy in cnc milling. *Procedia CIRP*, 3:121–125, 2012.

[32] J. Duplak, M. Hatala, D. Duplakova, and J. Steranka. Comprehensive analysis and study of the machinability of a high strength aluminum alloy (en aw-alzn5. 5mgcu) in the high-feed milling. *Advances in Production Engineering & Management*, 13 (4):455, 2018.

[33] J. Duplák, M. Hatala, D. Dupláková, and J. Steranka. Evaluation of time efficiency of high feed milling. *TEM Journal*, 7(1):13, 2018.

[34] A. Egana, J. Rech, and P. Arrazola. Characterization of friction and heat partition coefficients during machining of a tial6v4 titanium alloy and a cemented carbide. *Tribology Transactions*, 55(5):665–676, 2012.

[35] N. El-Tayeb, T. C. Yap, V. Venkatesh, and P. Brevern. Modeling of cryogenic frictional behaviour of titanium alloys using response surface methodology approach. *Materials & Design*, 30(10):4023–4034, 2009.

[36] E. Ezugwu and Z. Wang. Titanium alloys and their machinability—a review. *Journal of Materials Processing Technology*, 68(3):262–274, 1997. ISSN 0924-0136. doi: https://doi.org/10.1016/S0924-0136(96)00030-1. URL `https://www.sciencedirect.com/science/article/pii/S0924013696000301`. Superplasticity and Superplastic Technology in Japan.

[37] D. Fernández, A. Sandá, and I. Bengoetxea. Cryogenic milling: Study of the effect of co2 cooling on tool wear when machining inconel 718, grade ea1n steel and gamma tial. *Lubricants*, 7(1):10, 2019.

[38] L. Filice, F. Micari, S. Rizzuti, and D. Umbrello. A critical analysis on the friction modelling in orthogonal machining. *International Journal of Machine*

Tools and Manufacture, 47(3):709–714, 2007. ISSN 0890-6955. doi: https://doi.org/10.1016/j.ijmachtools.2006.05.007. URL `https://www.sciencedirect.com/science/article/pii/S0890695506001386`.

[39] P. Golda, R. Schießl, and U. Maas. Heat transfer simulation of a cryogenic cooling stream in machining operation. *International Journal of Heat and Mass Transfer*, 144:118616, 2019.

[40] M. P. Groover. *Tecnologia meccanica / Mikell P. Groover*. CittàStudi, Milano, edizione italiana. edition, 2014. ISBN 978-88-251-7389-5.

[41] Y. Guo, Q. Wen, and K. Woodbury. Dynamic material behavior modeling using internal state variable plasticity and its application in hard machining simulations. 2006.

[42] T. Gutowski, J. Dahmus, and A. Thiriez. Electrical energy requirements for manufacturing processes. In *13th CIRP international conference on life cycle engineering*, volume 31, pages 623–638. Leuven, Belgium, 2006.

[43] A. Haglund, H. Kishawy, and R. Rogers. An exploration of friction models for the chip–tool interface using an arbitrary lagrangian–eulerian finite element model. *Wear*, 265(3-4):452–460, 2008. doi: 10.1016/j.wear.2007.11.025.

[44] C. Herrmann, S.-H. Suh, G. Bogdanski, A. Zein, J.-M. Cha, J. Um, S. Jeong, and A. Guzman. Context-aware analysis approach to enhance industrial smart metering. In *Glocalized Solutions for Sustainability in Manufacturing*, pages 323–328. Springer, 2011.

[45] S. Y. Hong. Economical and ecological cryogenic machining. *J. Manuf. Sci. Eng.*, 123(2):331–338, 2001.

[46] S. Y. Hong. Lubrication mechanisms of ln2 in ecological cryogenic machining. *Machining science and technology*, 10(1):133–155, 2006.

[47] S. Y. Hong and M. Broomer. Economical and ecological cryogenic machining of aisi 304 austenitic stainless steel. *Clean Products and Processes*, 2(3):157–166, 2000.

[48] S. Y. Hong and Y. Ding. Cooling approaches and cutting temperatures in cryogenic machining of ti-6al-4v. *International Journal of Machine Tools and Manufacture*, 41(10):1417–1437, 2001.

[49] S. Y. Hong and Z. Zhao. Thermal aspects, material considerations and cooling

strategies in cryogenic machining. *Clean Products and Processes*, 1(2):107–116, 1999.

[50] S. Y. Hong, Y. Ding, and W. cheol Jeong. Friction and cutting forces in cryogenic machining of ti–6al–4v. *International Journal of Machine Tools and Manufacture*, 41(15):2271–2285, 2001. ISSN 0890-6955. doi: https://doi.org/10.1016/S0890-6955(01)00029-3. URL https://www.sciencedirect.com/science/article/pii/S0890695501000293.

[51] S. Y. Hong, I. Markus, and W. cheol Jeong. New cooling approach and tool life improvement in cryogenic machining of titanium alloy ti-6al-4v. *International Journal of Machine Tools and Manufacture*, 41(15):2245–2260, 2001. ISSN 0890-6955. doi: https://doi.org/10.1016/S0890-6955(01)00041-4. URL https://www.sciencedirect.com/science/article/pii/S0890695501000414.

[52] S. Y. Hong, I. Markus, and W.-c. Jeong. New cooling approach and tool life improvement in cryogenic machining of titanium alloy ti-6al-4v. *International journal of machine tools and manufacture*, 41(15):2245–2260, 2001.

[53] S. Y. Hong, Y. Ding, and J. Jeong. Experimental evaluation of friction coefficient and liquid nitrogen lubrication effect in cryogenic machining. *Machining Science and Technology*, 6(2):235–250, 2002.

[54] M. Hribersek, V. Sajn, F. Pusavec, J. Rech, and J. Kopac. The procedure of solving the inverse problem for determining surface heat transfer coefficient between liquefied nitrogen and inconel 718 workpiece in cryogenic machining. *Procedia CIRP*, 58:617–622, 2017.

[55] J. Hua and R. Shivpuri. Prediction of chip morphology and segmentation during the machining of titanium alloys. *Journal of Materials Processing Technology*, 150(1):124–133, 2004. ISSN 0924-0136. doi: https://doi.org/10.1016/j.jmatprotec.2004.01.028. URL https://www.sciencedirect.com/science/article/pii/S0924013604000846.

[56] S. Imbrogno, S. Sartori, A. Bordin, S. Bruschi, and D. Umbrello. Machining simulation of ti6al4v under dry and cryogenic conditions. *Procedia CIRP*, 58:475–480, 2017.

[57] I. Inagaki, T. Takechi, Y. Shirai, and N. Ariyasu. Application and features of titanium for the aerospace industry. *Nippon steel & sumitomo metal technical report*, 106(106):22–27, 2014.

[58] S. Ingle and D. Raut. Challenges in machining of titanium alloys with proper tooling & machining parameters-a review.

[59] I. Jawahir, H. Attia, D. Biermann, J. Duflou, F. Klocke, D. Meyer, S. Newman, F. Pusavec, M. Putz, J. Rech, et al. Cryogenic manufacturing processes. *CIRP annals*, 65(2):713–736, 2016.

[60] J. Jeswiet and S. Kara. Carbon emissions and ces™ in manufacturing. *CIRP annals*, 57(1):17–20, 2008.

[61] F. Jiang, Z. Liu, Y. Wan, and Z. Shi. Analytical modeling and experimental investigation of tool and workpiece temperatures for interrupted cutting 1045 steel by inverse heat conduction method. *Journal of Materials Processing Technology*, 213 (6):887–894, 2013.

[62] D. Jianxin, L. Yousheng, and S. Wenlong. Diffusion wear in dry cutting of ti–6al–4v with wc/co carbide tools. *Wear*, 265(11-12):1776–1783, 2008.

[63] S.-C. Jun. Lubrication effect of liquid nitrogen in cryogenic machining friction on the tool-chip interface. *Journal of mechanical science and technology*, 19(4):936–946, 2005.

[64] U. Karaguzel, M. Bakkal, and E. Budak. Modeling and measurement of cutting temperatures in milling. *Procedia CIRP*, 46:173–176, 2016.

[65] Y. Karpat. Temperature dependent flow softening of titanium alloy ti6al4v: An investigation using finite element simulation of machining. *Journal of Materials Processing Technology*, 211(4):737–749, 2011.

[66] T. Kato and H. Fujii. Pvd film method for measuring the temperature distribution in cutting tools. 1996.

[67] T. Kato and H. Fujii. Temperature measurement of workpiece in surface grinding by pvd film method. 1997.

[68] Y. Kaynak. Evaluation of machining performance in cryogenic machining of inconel 718 and comparison with dry and mql machining. *The International Journal of Advanced Manufacturing Technology*, 72(5):919–933, 2014.

[69] A. M. Khan, N. He, M. Jamil, and S. M. Raza. Energy characterization and energy-saving strategies in sustainable machining processes: A state-of-the-art review. *Journal of Production Systems and Manufacturing Science*, 2(1):3–3, 2021.

[70] F. Klocke and G. Eisenblätter. Dry cutting. *Cirp Annals*, 46(2):519–526, 1997.

[71] F. Klocke, A. Krämer, H. Sangermann, and D. Lung. Thermo-mechanical tool load during high performance cutting of hard-to-cut materials. *Procedia CIRP*, 1: 295–300, 2012.

[72] J. Koelsch. Beyond titanium nitride: New tool coatings pick up where titanium nitride left off. *Manufacturing Engineering(USA)*, 109(4):27–32, 1992.

[73] R. Komanduri. Some clarifications on the mechanics of chip formation when machining titanium alloys. *Wear*, 76(1):15–34, 1982.

[74] E. Kuljanic and M. Sortino. Twem, a method based on cutting forces—monitoring tool wear in face milling. *International Journal of Machine Tools and Manufacture*, 45(1):29–34, 2005.

[75] L. Laperrière and G. Reinhart. *CIRP encyclopedia of production engineering*. Springer Berlin, 2014.

[76] W.-S. Lee and C.-F. Lin. High-temperature deformation behaviour of ti6al4v alloy evaluated by high strain-rate compression tests. *Journal of Materials Processing Technology*, 75(1):127–136, 1998. ISSN 0924-0136. doi: https://doi.org/10.1016/S0924-0136(97)00302-6. URL `https://www.sciencedirect.com/science/article/pii/S0924013697003026`.

[77] P. Lequien, G. Poulachon, J. Outeiro, and J. Rech. Hybrid experimental/modelling methodology for identifying the convective heat transfer coefficient in cryogenic assisted machining. *Applied Thermal Engineering*, 128:500–507, 2018.

[78] C. Leyens and M. Peters. *Titanium and titanium alloys: fundamentals and applications*. Wiley Online Library, 2006.

[79] R. Liu, S. Melkote, R. Pucha, J. Morehouse, X. Man, and T. Marusich. An enhanced constitutive material model for machining of ti–6al–4v alloy. *Journal of Materials Processing Technology*, 213(12):2238–2246, 2013.

[80] J. Longbottom and J. Lanham. Cutting temperature measurement while machining–a review. *Aircraft Engineering and Aerospace Technology*, 2005.

[81] L. LOSA. Comprehensive analysis of cryogenic machining application through the development of a finite element model for ti6al4v milling. 2021.

[82] V. M. Luchesi and R. T. Coelho. Experimental investigations of heat transfer coefficients of cutting fluids in metal cutting processes: analysis of workpiece phenomena in a given case study. *Proceedings of the Institution of Mechanical Engi-*

neers, Part B: Journal of Engineering Manufacture, 226(7):1174–1184, 2012. doi: 10.1177/0954405412442459. URL https://doi.org/10.1177/0954405412442459.

[83] S. Madhukar, A. Shravan, P. V. Sai, and D. V. Satyanarayana. A critical review on cryogenic machining of titanium alloy (ti-6al-4v). *International Journal of Mechanical Engineering and Technology*, 7(5):38–45, 2016.

[84] P. Mativenga and M. Rajemi. Calculation of optimum cutting parameters based on minimum energy footprint. *CIRP annals*, 60(1):149–152, 2011.

[85] S. N. Melkote, W. Grzesik, J. Outeiro, J. Rech, V. Schulze, H. Attia, P.-J. Arrazola, R. M'Saoubi, and C. Saldana. Advances in material and friction data for modelling of metal machining. *Cirp Annals*, 66(2):731–754, 2017.

[86] A. Molinari, R. Cheriguene, and H. Miguelez. Numerical and analytical modeling of orthogonal cutting: The link between local variables and global contact characteristics. *International Journal of Mechanical Sciences*, 53(3):183–206, 2011. ISSN 0020-7403. doi: https://doi.org/10.1016/j.ijmecsci.2010.12.007. URL https://www.sciencedirect.com/science/article/pii/S0020740310002821.

[87] A. Molinari, R. Cheriguene, and H. Miguelez. Contact variables and thermal effects at the tool–chip interface in orthogonal cutting. *International Journal of Solids and Structures*, 49(26):3774–3796, 2012. ISSN 0020-7683. doi: https://doi.org/10.1016/j.ijsolstr.2012.08.013. URL https://www.sciencedirect.com/science/article/pii/S0020768312003502.

[88] A. Moufki, A. Molinari, and D. Dudzinski. Modelling of orthogonal cutting with a temperature dependent friction law. *Journal of the Mechanics and Physics of Solids*, 46(10):2103–2138, 1998. ISSN 0022-5096. doi: https://doi.org/10.1016/S0022-5096(98)00032-5. URL https://www.sciencedirect.com/science/article/pii/S0022509698000325.

[89] J. A. Mountford. Titanium-properties, advantages and applications solving the corrosion problems in marine service. In *CORROSION 2002*. OnePetro, 2002.

[90] A. Nordgren, B. Z. Samani, and R. M. Saoubi. Experimental study and modelling of plastic deformation of cemented carbide tools in turning. *Procedia CIRP*, 14: 599–604, 2014.

[91] A. Oudin, P. Lamesle, L. Penazzi, S. Le Roux, and F. Rézaï-Aria. Thermomechanical fatigue behaviour and life assessment of hot work tool steels. In *European structural integrity society*, volume 29, pages 195–201. Elsevier, 2002.

[92] T. Özel. The influence of friction models on finite element simulations of machining. *International Journal of Machine Tools & Manufacture*, 46:518–530, 2006.

[93] T. Özel and E. Zeren. A methodology to determine work material flow stress and tool-chip interfacial friction properties by using analysis of machining. 2006.

[94] T. Özel, S. Yildiz, and J. Ciurana. Influence of material models on serrated chip formation in simulation of machining ti-6al-4v titanium alloy. In *Proceedings of 12th CIRP Conference on Modeling of Machining Operations*, pages 123–130, 2009.

[95] T. Ozel, I. Llanos, J. Soriano, and P.-J. Arrazola. 3d finite element modelling of chip formation process for machining inconel 718: comparison of fe software predictions. *Machining Science and Technology*, 15(1):21–46, 2011.

[96] D. O'Sullivan and M. Cotterell. Temperature measurement in single point turning. *Journal of materials processing technology*, 118(1-3):301–308, 2001.

[97] K.-H. Park, G.-D. Yang, M. Suhaimi, D. Y. Lee, T.-G. Kim, D.-W. Kim, and S.-W. Lee. The effect of cryogenic cooling and minimum quantity lubrication on end milling of titanium alloy ti-6al-4v. *Journal of Mechanical Science and Technology*, 29(12):5121–5126, 2015.

[98] A. Patil, S. Ingle, and Y. More. Machining challenges in ti-6al-4v.-a review. *International Journal of Innovations in Engineering and Technology (ISSN:2319-1058)*, 5:6–23, 08 2015.

[99] G. Pittalà and M. Monno. A new approach to the prediction of temperature of the workpiece of face milling operations of ti-6al-4v. *Applied Thermal Engineering*, 31(2):173–180, 2011. ISSN 1359-4311. doi: https://doi.org/10.1016/j.applthermaleng.2010.08.027. URL `https://www.sciencedirect.com/science/article/pii/S1359431110003704`.

[100] H. Puls, F. Klocke, and D. Lung. A new experimental methodology to analyse the friction behaviour at the tool-chip interface in metal cutting. *Production engineering*, 6(4-5):349–354, 2012.

[101] F. Pusavec, D. Kramar, P. Krajnik, and J. Kopac. Transitioning to sustainable production–part ii: evaluation of sustainable machining technologies. *Journal of Cleaner Production*, 18(12):1211–1221, 2010.

[102] F. Pusavec, T. Lu, C. Courbon, J. Rech, U. Aljancic, J. Kopac, and I. Jawahir. Analysis of the influence of nitrogen phase and surface heat transfer coefficient on

cryogenic machining performance. *Journal of Materials Processing Technology*, 233: 19–28, 2016.

[103] S. Rawal, J. Brantley, and N. Karabudak. Additive manufacturing of ti-6al-4v alloy components for spacecraft applications. In *2013 6th international conference on recent advances in space technologies (RAST)*, pages 5–11. IEEE, 2013.

[104] J. Rech, P. Arrazola, C. Claudin, C. Courbon, F. Pusavec, and J. Kopac. Characterisation of friction and heat partition coefficients at the tool-work material interface in cutting. *CIRP Annals*, 62(1):79–82, 2013.

[105] G. Reitz. *Die Grösse des geistlichen und ritterschaftlichen Grundbesitzes im ehemaligen Kur-Trier*. Görresdruckerei, 1919.

[106] M. I. Sadik and S. Isakson. The role of pvd coating and coolant nature in wear development and tool performance in cryogenic and wet milling of ti-6al-4v. *Wear*, 386:204–210, 2017.

[107] M. I. Sadik, S. Isakson, A. Malakizadi, and L. Nyborg. Influence of coolant flow rate on tool life and wear development in cryogenic and wet milling of ti-6al-4v. *Procedia CIRP*, 46:91–94, 2016.

[108] M. Sato, N. Tamura, and H. Tanaka. Temperature variation in the cutting tool in end milling. *Journal of Manufacturing Science and Engineering*, 133(2), 2011.

[109] M. N. Sharif, S. Pervaiz, and I. Deiab. Potential of alternative lubrication strategies for metal cutting processes: a review. *The International Journal of Advanced Manufacturing Technology*, 89(5-8):2447–2479, 2017.

[110] A. K. Sharma, A. K. Tiwari, and A. R. Dixit. Progress of nanofluid application in machining: a review. *Materials and Manufacturing Processes*, 30(7):813–828, 2015.

[111] A. K. Sharma, A. K. Tiwari, and A. R. Dixit. Effects of minimum quantity lubrication (mql) in machining processes using conventional and nanofluid based cutting fluids: A comprehensive review. *Journal of cleaner production*, 127:1–18, 2016.

[112] V. S. Sharma, M. Dogra, and N. Suri. Cooling techniques for improved productivity in turning. *International Journal of Machine Tools and Manufacture*, 49(6):435–453, 2009.

[113] M. Shaw and A. Vyas. The mechanism of chip formation with hard turning steel. *CIRP Annals*, 47(1):77–82, 1998. ISSN 0007-8506. doi: https://doi.org/10.

1016/S0007-8506(07)62789-9. URL https://www.sciencedirect.com/science/article/pii/S0007850607627899.

[114] B. Shi and H. Attia. Modeling the thermal and tribological processes at the tool-chip interface in machining. *Machining Science and Technology*, 13(2):210–226, 2009. doi: 10.1080/10910340903007605. URL https://doi.org/10.1080/10910340903007605.

[115] B. Shi, A. Elsayed, A. Damir, H. Attia, and R. M'Saoubi. A hybrid modeling approach for characterization and simulation of cryogenic machining of ti–6al–4v alloy. *Journal of Manufacturing Science and Engineering*, 141(2), 2019.

[116] S. Shimada, H. Tanaka, M. Higuchi, T. Yamaguchi, S. Honda, and K. Obata. Thermo-chemical wear mechanism of diamond tool in machining of ferrous metals. *CIRP Annals*, 53(1):57–60, 2004.

[117] A. Shokrani, V. Dhokia, and S. T. Newman. Environmentally conscious machining of difficult-to-machine materials with regard to cutting fluids. *International Journal of machine Tools and manufacture*, 57:83–101, 2012.

[118] A. Shokrani, V. Dhokia, P. Muñoz-Escalona, and S. T. Newman. State-of-the-art cryogenic machining and processing. *International Journal of Computer Integrated Manufacturing*, 26(7):616–648, 2013.

[119] A. Shokrani, V. Dhokia, and S. T. Newman. Comparative investigation on using cryogenic machining in cnc milling of ti-6al-4v titanium alloy. *Machining science and Technology*, 20(3):475–494, 2016.

[120] A. Shokrani, V. Dhokia, and S. T. Newman. Investigation of the effects of cryogenic machining on surface integrity in cnc end milling of ti–6al–4v titanium alloy. *Journal of Manufacturing Processes*, 21:172–179, 2016.

[121] M. Sima and T. Özel. Modified material constitutive models for serrated chip formation simulations and experimental validation in machining of titanium alloy ti–6al–4v. *International Journal of Machine Tools and Manufacture*, 50(11):943–960, 2010.

[122] H. Simon, M. Thoma, and K. Maier. Cooling lubricants with chlorine high pressure additives. *Werkstattstechnik;(Germany, Federal Republic of)*, 69(2), 1979.

[123] B. Stampfer, P. Golda, F. Zanger, R. Schießl, U. Maas, and V. Schulze. Thermomechanically coupled numerical simulation of cryogenic orthogonal cutting. *Procedia CIRP*, 82:438–443, 2019.

[124] L. Sterle, F. Pušavec, and M. Kalin. Determination of friction coefficient in cutting processes: comparison between open and closed tribometers. *Procedia CIRP*, 82: 101–106, 2019.

[125] M. Strano, E. Chiappini, S. Tirelli, P. Albertelli, and M. Monno. Comparison of ti6al4v machining forces and tool life for cryogenic versus conventional cooling. *Proceedings of the Institution of Mechanical Engineers, Part B: Journal of Engineering Manufacture*, 227(9):1403–1408, 2013.

[126] M. A. Suhaimi, G.-D. Yang, K.-H. Park, M. J. Hisam, S. Sharif, and D.-W. Kim. Effect of cryogenic machining for titanium alloy based on indirect, internal and external spray system. *Procedia Manufacturing*, 17:158–165, 2018.

[127] S. Sun, M. Brandt, and M. S. Dargusch. Characteristics of cutting forces and chip formation in machining of titanium alloys. *International Journal of Machine Tools and Manufacture*, 49(7-8):561–568, 2009.

[128] I. Svenningsson and K. Tatar. On the mechanism of three-body adhesive wear in turning. *The International Journal of Advanced Manufacturing Technology*, 113 (11):3457–3472, 2021.

[129] E. Tahmasebi, P. Albertelli, T. Lucchini, M. Monno, and V. Mussi. Cfd and experimental analysis of the coolant flow in cryogenic milling. *International Journal of Machine Tools and Manufacture*, 140:20–33, 2019.

[130] C. Tahri, P. Lequien, J. Outeiro, and G. Poulachon. Cfd simulation and optimize of ln2 flow inside channels used for cryogenic machining: application to milling of titanium alloy ti-6al-4v. *Procedia CIRP*, 58:584–589, 2017.

[131] N. Tapoglou, M. I. A. Lopez, I. Cook, and C. M. Taylor. Investigation of the influence of co2 cryogenic coolant application on tool wear. *Procedia CIRP*, 63: 745–749, 2017.

[132] D. Ulutan and T. Özel. Determination of tool friction in presence of flank wear and stress distribution based validation using finite element simulations in machining of titanium and nickel based alloys. *Journal of Materials Processing Technology*, 213(12):2217–2237, 2013. ISSN 0924-0136. doi: https://doi.org/10.1016/j.jmatprotec.2013.05.019. URL `https://www.sciencedirect.com/science/article/pii/S0924013613001751`.

[133] D. Umbrello. Finite element simulation of conventional and high speed machining of ti6al4v alloy. *Journal of materials processing technology*, 196(1-3):79–87, 2008.

[134] D. Umbrello, L. Filice, S. Rizzuti, F. Micari, and L. Settineri. On the effectiveness of finite element simulation of orthogonal cutting with particular reference to temperature prediction. *Journal of materials processing technology*, 189(1-3):284–291, 2007.

[135] C. Veiga and J. P. Davim. Review on machinability of titanium alloys: The process perspective. 2013.

[136] K. Venugopal, S. Paul, and A. Chattopadhyay. Growth of tool wear in turning of ti-6al-4v alloy under cryogenic cooling. *Wear*, 262(9-10):1071–1078, 2007.

[137] Z. Wang and K. Rajurkar. Cryogenic machining of hard-to-cut materials. *Wear*, 239(2):168–175, 2000.

[138] P. Wanigarathne, A. Kardekar, O. Dillon, G. Poulachon, and I. Jawahir. Progressive tool-wear in machining with coated grooved tools and its correlation with cutting temperature. *Wear*, 259(7-12):1215–1224, 2005.

[139] Y. Yang and W. Zhu. Study on cutting temperature during milling of titanium alloy based on fem and experiment. *The International Journal of Advanced Manufacturing Technology*, 73(9-12):1511–1521, 2014.

[140] E. Yasa, S. Pilatin, and O. Çolak. Overview of cryogenic cooling in machining of ti alloys and a case study. *Journal of Production Engineering*, 15(2):1–9, 2012.

[141] Y. Yildiz and M. Nalbant. A review of cryogenic cooling in machining processes. *International Journal of Machine Tools and Manufacture*, 48(9):947–964, 2008.

[142] M. Yousfi, J. Outeiro, C. Nouveau, B. Marcon, and B. Zouhair. Tribological behavior of pvd hard coated cutting tools under cryogenic cooling conditions. *Procedia CIRP*, 58:561–565, 2017.

[143] H. Zhen-Bin and R. Komanduri. On a thermomechanical model of shear instability in machining. *CIRP Annals*, 44(1):69–73, 1995. ISSN 0007-8506. doi: https://doi.org/10.1016/S0007-8506(07)62277-X. URL `https://www.sciencedirect.com/science/article/pii/S000785060762277X`.

[144] C. Zhong, J. Liu, T. Zhao, T. Schopphoven, J. Fu, A. Gasser, and J. H. Schleifenbaum. Laser metal deposition of ti6al4v—a brief review. *Applied Sciences*, 10(3): 764, 2020.

[145] Z. Zurecki, J. Frey, and R. Ghosh. Finish-turning of hardened powder-metallurgy

steel using cryogenic cooling. *Advances in Powder Metallurgy and Particulate Materials*, (7):7–185, 2003.

List of Figures

List of Tables

Appendix, Mesh on Forge

The precision of the solution of every finite element analysis is intrinsically linked to the quality of the mesh used. Forge software applies spatial triangulations, its meshes are composed by 2D triangles and 3D tetrahedra (so the mesh size of an element = average length of its edges). The mesher in particular applies the Delaunay triangulation algorithm (Delaunay criterion = empty circumcircle criterion):
let $\check{T}$ be a triangulation, $\check{T}$ is a Delaunay triangulation if for every couple of triangles adjacent to T (3D tetrahedra) no node of any element (triangle or tetrahedron) is contained within the circumcircle (sphere) associated with the other element.

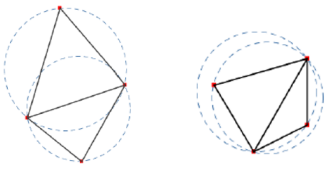

Figure 1: examples of triangular elements

On the left triangles the Delaunay criterion is satisfied, on the right one it is not.
A triangulation that satisfies Delaunay criterion maximizes the minimums of the angles between the edges, it is possible to obtain triangles (tetrahedra) as close as possible to the equiangular triangle (regular tetrahedron). This is what guarantees a high-quality isotropic mesh. The classic technique involves the use of a scatter plot to produce a set of triangles or tetrahedra, their apexes are the scatter plot dots. Other methods have appeared that involve integrating an imposed domain (contour), that is, 2D peaks and edges and, possibly, 3D triangles. Usually, the result is no longer strictly a Delaunay triangulation and it is consequently called a constrained Delaunay triangulation.

Classic technique, Delaunay Kernel: it is a method used to insert a point in a Delaunay triangulation by locally modifying the topology of the existing triangulation while maintaining the Delaunay criterion:

$$T_{i+1} = T_i - C_p + B_p$$

T_i = triangulation already constructed, P = point to be inserted, T_{i+1} = triangulation after point p has been inserted, C_p = the set of T_i triangles the associated circumcircle of which contains p, B_p = the set of triangles constructed by joining p to the endpoints of each edge visible from p.

-If p is outside the initial triangulation (C_p = empty)

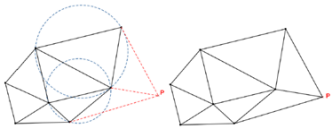

Figure 2: insertion of a point p located outside the initial triangulation

- If p is inside the initial triangulation (C_p = not empty)

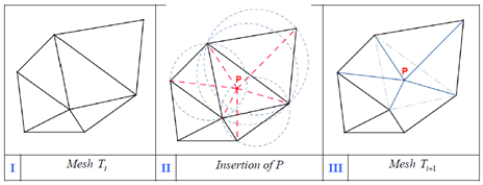

Figure 3: examples of triangular elements

Constrained Delaunay triangulation: the Delaunay kernel is used to compute the Delaunay triangulation for a convex hull of a scatter plot. The domain to be meshed is usually limited by a boundary that is either a 2D contour or a closed set of 3D facet. It is necessary to insert the edges and facets of the boundary into the existing triangulation. This can be done by computing the intersection of the edge (facet) to be inserted with the edges (facets) of the mesh. A precautionary measure can be taken beforehand on the edges of the boundary so that the circumcircles that have these edges as their diameter contain no other peaks than the endpoints of that edge. The edges that don't satisfy this property are recursively divided until they do [Source: Forge Software Guide, cap.3]. In the majority of practical applications the meshing algorithm has to face complex geometries and in these cases it is better to use topology meshers especially for operations such as remeshing, mesh adaptation and variable mesh size imposition. More in detail: all the

elements of a triangulation form a mesh topology if all edges (facets) of each triangulation element belong to no more than two triangles (tetrahedra). For a mesh topology to be a mesh it must satisfy the minimal volume criterion: the sum of the volumes of the elements in the mesh topology must be equal to the volume of the domain to be meshed. The steps followed generally are:

- Construction of initial topology, based on the discretization of the boundary of the domain to be meshed, this stage consists of connecting a node via a starring operator to all the other nodes except those attached to the same facet.

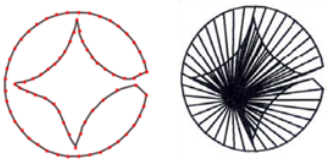

Figure 4: initial topology construction

- Improvement of current topology via iterative sweeping. From each node and each edge the local starred topology is removed and replaced by another obtained topology obtained by sweeping edges, by adding or removing nodes or by barycentring. Among the possible topologies the selected is the one that minimizes the total volume (to satisfy better the minimal volume criterion).

Figure 5: iterative improvement starting from the initial topology

In 3D, the equivalent of the edge swap in 2D is the transformation of two tetrahedra that have one common facet into three tetrahedra. In the case several possible topologies have the same volume it is necessary to give special weights that promotes the topologies with better geometric quality of the elements.

$$C\left(e, h_e\right) = C_0 \frac{|\Omega_e|}{h_e^3}$$

$|\Omega_e|$ = volume of the element "e", h_e = average length of the edges of the tetrahedron "e", C_0 = constant used to normalise the shape factor to 1 for an equiangular tetrahedron.

$C(e, h_e)$ is maximum for an equiangular tetrahedron and it is equal to 0 for a flat tetrahedron. In case of anisotropic meshes the characteristic size is no longer a scalar but a matrix $M = metric$ used to define the size of the element in different directions of the space. Referring to a diagonalised form

$$M = R \begin{pmatrix} \frac{1}{h_1^2} & \cdots & 0 \\ \vdots & \ddots & \vdots \\ 0 & \cdots & \frac{1}{h_d^2} \end{pmatrix} R^T$$

With d = dimension of the space, R = rotation matrix formed by eigenvectors of M and $\left(\frac{1}{h_i^2}\right)_{1 \leq i \leq d}$ the corresponding eigenvalues. So M accounts for the principal directions (columns of R) and the mesh size h_i in each principal direction. In the end the shape criterion of an anisotropic mesh is slightly modified with respect to the isotropic case resulting in

$$C_M(e, h_e) = C_0 \frac{|\Omega_e|_M}{h_M^d}$$

$|\Omega_e|_M$ = euclidean volume of the element in the metric M.
h_M^d = average size of the edges in the metric M, C_0 = constant used to normalise the shape factor to 1 for an equiangular tetrahedron as it applies to the metric M, $C_M(e, h_e)$ = maximal for an equiangular tetrahedron in the metric M (it is equal to 0 for a flat tetrahedron).

Mesh refinement/mesh boxes/remeshing: during the simulations, in order to accurately observe phenomena in precise areas of interest a really fine mesh is needed. At the same time to reduce the computational cost is not reasonable to finely mesh the entire parts of the simulated model.
On Forge, Mesh boxes allow the user to prescribe a different mesh size within it than the mesh size prescribed for the rest of the object; they are defined by cartesian space coordinates and specific mesh size must be applied. Boxes can be either Lagrangian or Eulerian. The latter remains fixed in space throughout the process while a Lagrangian mesh box will move according to the object (or better its barycentre) to which it is connected. Deformations encountered during the simulations may be such that it is necessary to regularly remesh the parts. With a Lagrangian description of motion the mesh is "covected" with the material, it undergoes the same deformation but does not support it and it degenerates. Or the geometry of the contact may need adaptations to prevent facets of the mesh from crossing the angular points of the die surfaces. The remeshing techniques and the associated thresholds will be encountered in the sections regarding the practical part of this work.